

Integrated By Design: An Investigation into
Solid-State Battery Processing & the
Elucidation of Reaction Mechanisms

By

Matteo P. Hogan

A thesis submitted to the University of Kent as part of the
requirement in the subject of Physics for the degree of

Doctor of Philosophy

School of Physical Sciences

March 2020

University of
Kent

Contents

List of Figures.....	vii
List of Tables.....	xiii
List of Abbreviations.....	xiii
Declarations.....	xv
Acknowledgements.....	xvi
Abstract.....	xvii
1 Introduction.....	1
1.1 Integrated Design.....	1
1.2 Aims of the Research.....	3
1.3 Energy Storage.....	4
1.4 The Li-ion Battery.....	7
1.5 Improving the Li-ion Battery.....	8
1.6 The Cathode.....	9
1.6.1 LiCoO ₂ (LCO).....	10
1.6.2 LiMn ₂ O ₄ (LMO).....	12
1.6.3 LiNi _{0.8} Co _{0.15} Al _{0.05} O ₂ & LiNi _x Co _y Mn _z O ₂ (NCA & NMC).....	12
1.6.4 LiFePO ₄	12
1.6.5 Li ₂ MSiO ₄ (L(M)S).....	13
1.7 The Electrolyte.....	15
1.7.1 Non-aqueous Electrolytes.....	16
1.7.2 Aqueous Electrolytes.....	17
1.7.3 Ionic Liquids.....	19
1.7.4 Gel Electrolytes.....	20
1.7.5 Solid Electrolytes.....	21
1.8 The Anode.....	25
1.8.1 Intercalation Anodes.....	26
1.8.2 Alloying Anodes.....	27

1.8.3 Conversion Anodes.....	28
1.8.4 Another Approach – Polymeric Anodes.....	29
1.9 Additive Manufacturing.....	32
1.9.1 Deposition Techniques.....	32
1.9.1.1 <i>Chemical Vapour Deposition (CVD)</i>	32
1.9.1.2 <i>Atomic Layer Deposition (ALD)</i>	32
1.9.1.3 <i>Pulsed Laser Deposition (PLD)</i>	33
1.9.1.4 <i>Magnetron Sputtering</i>	34
1.9.1.5 <i>Tape Casting (Doctor Blade)</i>	35
1.9.1.6 <i>Screen Printing</i>	36
1.9.1.7 <i>Ink-Jet Printing</i>	37
1.9.1.8 <i>Spray Coating</i>	38
1.10 Summary.....	39
1.11 References.....	41
2 Materials, Methods and Characterisation Techniques.....	65
2.1 $\text{Li}_2\text{FeSiO}_4$	65
2.1.1 Solid State Synthesis.....	65
2.1.1 Sol-Gel Synthesis.....	65
2.2 Cell Preparation.....	66
2.2.1 Electrode Preparation.....	66
2.2.2 Electrolyte Preparation.....	68
2.2.3 Separator Preparation.....	68
2.2.4 Coin Cell Assembly.....	68
2.2.5 Pouch Cell Assembly.....	69
2.3 Materials Characterisation.....	70
2.3.1 X-Ray Diffraction (XRD).....	70
2.3.2 XRD Sample Preparation.....	71
2.3.3 Scanning Electron Microscopy (SEM).....	72
2.3.3.1 <i>Auger Electrons</i>	73

2.3.3.2 Secondary Electrons.....	73
2.3.3.3 Backscattered Electrons.....	73
2.3.3.4 Energy Dispersive X-Rays.....	73
2.3.4 ThermoGravimetric Analysis (TGA).....	74
2.3.5 Differential Scanning Calorimetry (DSC).....	74
2.4 X-ray Absorption Spectroscopy.....	75
2.4.1 The Basic Principles of XAS.....	75
2.4.2 X-ray Absorption Spectroscopy Measurements.....	76
2.4.2.1 The Background.....	76
2.4.2.2 X-Ray Absorption Near-Edge Structure.....	77
2.4.2.3 Extended X-Ray Absorption Fine Structure.....	77
2.4.3 X-Ray Absorption Spectroscopy Experiments.....	78
2.4.4 The Beamline.....	79
2.5 X-Ray Raman Scattering Spectroscopy.....	80
2.6 Electrochemical Measurements.....	82
2.6.1 Electrochemical Impedance Spectroscopy (EIS).....	82
2.6.2 Cyclic Voltammetry (CV).....	83
2.6.3 Galvanostatic Cycling (Charge and Discharge Curves).....	84
2.7 References.....	85
3 Positive Electrode – $\text{Li}_2\text{FeSiO}_4$	88
3.1 Synthesis and Characterisation.....	91
3.1.1 Solid State.....	91
3.1.1.1 XRD.....	92
3.1.2 Sol-Gel.....	92
3.1.2.1 Sol-Gel XRD.....	93
3.1.3 SEM.....	95
3.2 Cycling.....	97
3.3 X-ray Absorption Spectroscopy (XAS).....	99
3.3.1 Electrolyte Effect.....	100

3.4 The Elusive Fe ⁴⁺ : In-Operando XANES.....	102
3.4.1 Fe K-edge XANES.....	103
3.4.2 Oxygen K-edge Contribution.....	107
3.5 Elevated Temperature Cycling.....	117
3.6 Conclusion.....	119
3.7 References.....	121
4 Negative Electrode – PEDOT:PSS.....	127
4.1 Introduction.....	127
4.2 Deposition Methods.....	129
4.2.1 Tape Casting (Doctor Blade).....	129
4.2.2 Spray-Coating.....	131
4.2.3 Inkjet Printing.....	132
4.3 Results.....	133
4.3.1 Thermal Stability.....	133
4.3.2 Chemical and Mechanical Properties of the Films.....	135
4.3.2.1 Doctor Blade.....	135
4.3.2.2 Spray-Coating.....	138
4.3.2.3 Inkjet Printing.....	140
4.3.3 Electrochemical Properties of the Films.....	142
4.3.3.1 Deposition Dependent Battery Cycling.....	142
4.3.3.1.1 Manufacturing Dependent Electrochemical Performance.....	143
4.3.3.1.2 Doctor Blade.....	144
4.3.3.1.3 Spray-Coating.....	144
4.3.3.1.4 Inkjet Printing.....	145
4.3.3.1.5 Comparison of Electrochemical Behaviours.....	145
4.3.4 Chemical Reaction Mechanism and “Lithium Trapping”.....	146
4.3.4.1 Cyclic Voltammetry (CV).....	146
4.3.4.2 Galvanostatic Cycling Curves.....	148
4.3.4.3 FTIR.....	151

4.3.4.4 Proposed Mechanism – Deposition Dependent Reactions.....	154
4.3.5 Post Mortem SEM.....	156
4.4 Conclusion.....	159
4.5 References.....	161
5 Solid State Electrolyte – PEGDA PEM.....	164
5.1 Introduction.....	164
5.2 Why Solid State.....	164
5.3 What is a Polymer Electrolyte.....	165
5.4 Polymer Electrolytes and Ionic Conductivity.....	165
5.5 Lithium ion Transport Mechanism in Solid Polymer Electrolytes.....	166
5.6 Selecting a Host Polymer.....	169
5.7 Aims.....	170
5.8 Synthesis.....	170
5.9 Characterisation.....	172
5.9.1 XRD.....	172
5.9.2 TGA.....	174
5.9.3 DSC.....	177
5.10 Mechanical Properties.....	178
5.11 Conductivity (Impedance Spectroscopy).....	180
5.12 Electrochemical Stability vs Li/Li ⁺	181
5.13 SEM.....	182
5.14 Galvanostatic Cycling.....	187
5.15 Conclusion.....	193
5.16 References.....	195
6 Integrated Design.....	207
6.1 The Concept.....	207
6.2 The Antenna.....	207
6.3 Battery Integration.....	208

6.4 The IBAS.....	209
6.5 IBAS Performance.....	211
6.6 Battery Cycling.....	213
6.7 Conclusion.....	214
6.8 References.....	217
7 Conclusions and Future Works.....	219
7.1 Conclusions.....	219
7.2 Future Works.....	221

List of Figures

1.1 An example of a wearable, body conforming electronics product (adapted with permission from AAAS [3]).....	2
1.2 : Radar plots showing the defining properties of $\text{Li}_2\text{FeSiO}_4$, PEDOT:PSS and PEGDA PEM selected for this study.....	4
1.3 A comparison of gravimetric and volumetric energy densities of various battery technologies (Adapted with permission [179]).....	6
1.4 A schematic diagram of a Li-ion battery in a state of charging.....	7
1.5 Crystal structures of olivine, layered and spinel compounds (adapted with permission [180]).....	9
1.6 Figure showing pristine and NaAlO_2 coated LCO capacity retention (adapted with permission [19]).....	11
1.7 Figure showing pure LCO vs Ti-doped LCO capacity retention (adapted with permission [20]).....	11
1.8 Theoretical and Practical energy densities of various cathode materials (adapted with permission [181]).....	14
1.9 Multiple cycles of $\text{Li}_2\text{FeSiO}_4$ cathode indicating high reversible capacity (adapted with permission [182]).....	15
1.10 Electrochemical stability windows of aqueous electrolyte and working potentials of various electrode materials (reprinted with permission [40]).....	18
1.11 A diagram indicating various anode chemistries and their respective gravimetric capacities and operating potentials (adapted with permission [186]).....	25
1.12 A schematic diagram of the reaction processes of the main types of anode materials (reprinted with permission [184]).....	26
1.13 A schematic diagram of a proposed metal-free all-polymer Li-ion battery.....	31
1.14 A schematic of a PLD apparatus (reprinted with permission [187]).....	33
1.15 A schematic diagram of magnetron sputtering (reprinted with permission [158]).....	34

1.16 A schematic diagram of the screen-printing process (reprinted with permission [188]).....	36
1.17 A schematic diagram showing continuous and drop on demand inkjet printing processes (reprinted with permission [189]).....	37
2.1 A schematic diagram illustrating the electrode preparation process.....	67
2.2 Schematic diagram of a CR2032 coin half-cell stack.....	68
2.3 Images of the individual components and at various stages of the pouch cell assembly.....	69
2.4 A schematic demonstrating the principles of XRD (reproduced with permission [20]).....	71
2.5 Schematic diagram of the reaction processes which occur in SEM.....	72
2.6 Schematic representation of A) X-ray Absorption B) Fluorescence Emission C) Auger Emission.....	76
2.7 Annotated example XAS spectrum.....	78
2.8 Schematic Diagram of BM26A beamline optics.....	79
2.9 A schematic of the XAS and XRS process whilst probing the O K-edge (reprinted with permission [12]).....	80
2.10 Schematic representation of an IXS experiment (reprinted with permission [15]).....	81
2.11 A representation of a typical Nyquist plot.....	82
2.12 A) A CV curve of LiFePO_4 and B) its corresponding galvanostatic cycling curve (reprinted with permission [21]).....	83
3.1 Diagrams of $\text{Li}_2\text{FeSiO}_4$ polymorphs (reprinted with permission [41]).....	90
3.2 Diagrams of $\text{Li}_2\text{FeSiO}_4$ pristine and cycled structures (reprinted with permission [41]).....	90
3.3 XRD of $\text{Li}_2\text{FeSiO}_4$ synthesised via solid state reaction with corresponding peak lists A) $\text{Li}_2\text{FeSiO}_4$ B) Fe_3O_4 C) Li_2SiO_3	92
3.4 XRD of $\text{Li}_2\text{FeSiO}_4$ synthesised via Sol-Gel method with corresponding peak lists A) $\text{Li}_2\text{FeSiO}_4$ B) Metallic Fe.....	93
3.5 XRD of $\text{Li}_2\text{FeSiO}_4$ synthesised via Sol-Gel method with corresponding peak lists A) $\text{Li}_2\text{FeSiO}_4$ B) Fe_3O_4	94

3.6 XRD of $\text{Li}_2\text{FeSiO}_4$ synthesised via Sol-Gel method with corresponding peak list for A) $\text{Li}_2\text{FeSiO}_4$ B) Fe_3O_4 C) Li_2SiO_3	94
3.7 Low magnification SEM image of $\text{Li}_2\text{FeSiO}_4$	95
3.8 High magnification SEM images of $\text{Li}_2\text{FeSiO}_4$	96
3.9 Galvanostatic cycling of $\text{Li}_2\text{FeSiO}_4$ showing a 1Li^+ extraction and insertion.....	97
3.10 Room temperature cycling performance of $\text{Li}_2\text{FeSiO}_4$ synthesised via a sol-gel method showing a greater than 1Li^+ removal.....	98
3.11 XANES data showing pre-cycling oxidation of $\text{Li}_2\text{FeSiO}_4$	99
3.12 XANES data of the Electrolyte Effect study a) freshly prepared samples b) the same samples after 14 days storage under an argon atmosphere.....	101
3.13 XANES data showing: A) a clear progressive change in oxidation state from Fe^{2+} to Fe^{3+} during the first charge B) A zoomed in image of the pre-edge feature showing the same progressive change from Fe^{2+} to Fe^{3+} C) a zoomed in image of the main Fe K-edge indicating no further progression beyond Fe^{3+} is achieved.....	104
3.14 Galvanostatic cycling profile for $\text{Li}_2\text{FeSiO}_4$	105
3.15 XAS data showing a partially reversed Fe oxidation state going from Fe^{3+} to Fe^{2+} upon first discharge A) main edge B) magnified pre-edge.....	106
3.16 A) an image showing the beamline setup and position of moveable sensors B) An example of a sample pouch with aluminium windows C) A close up of sample holder and sensor position, as well as beam position.....	108
3.17 An image of a y-plane scan of the sample pouch and holder.....	109
3.18 A graphical representation of $\text{Li}_2\text{FeSiO}_4$ samples' state of charge used for this experiment, dashed line denotes 1Li^+ removal.....	110
3.19 An example of the full-range XRS scan, with indicated Li, O and Fe edges...	111
3.20 Fe L-edge XRS scans through $\text{Li}_2\text{FeSiO}_4$ first charge (A) and discharge (B).....	113
3.21 Oxygen edge XRS spectrum of $\text{Li}_2\text{FeSiO}_4$ during first charge.....	114
3.22 Oxygen edge XRS spectrum of $\text{Li}_2\text{FeSiO}_4$ during first discharge.....	115
3.23 Galvanostatic cycling profiles of $\text{Li}_2\text{FeSiO}_4$ cycled at various rates.....	117
3.24 Room temperature vs elevated temperature Galvanostatic cycling curves for $\text{Li}_2\text{FeSiO}_4$	118

4.1	Chemical structure of PEDOT:PSS [7].....	128
4.2	PEDOT:PSS doctor blade coating A) wet B) after drying.....	130
4.3	Spray-coated PEDOT:PSS on copper foil after A) one coat and B) final coat....	131
4.4	A) Inkjet printer used to deposit PEDOT:PSS onto copper foil B) coated copper foil.....	132
4.5	TGA of dried, pure PEDOT:PSS with an indicator showing 5% mass loss.....	133
4.6	XRD of pure PEDOT:PSS.....	134
4.7	SEM image of A) doctor bladed PEDOT:PSS/CMC coating B) EDX sulfur mapping C) EDX copper mapping.....	136
4.8	Magnified SEM image of A) Doctor Bladed PEDOT:PSS B) EDX mapping of Sulphur C) EDX mapping of Copper.....	137
4.9	SEM image of A) spray coated PEDOT:PSS B) EDX copper mapping.....	138
4.10	SEM images of spray-coated PEDOT:PSS at varying magnifications.....	139
4.11	SEM image of inkjet printed PEDOT:PSS film.....	140
4.12	SEM images of inkjet printed PEDOT:PSS film, at varying magnifications....	141
4.13	Discharge Capacities and Coulombic Efficiencies across 50 cycles of A) Doctor Blade B) spray-coted C) Inkjet Printed PEDOT:PSS films.....	143
4.14	CV curve of PEDOT:PSS vs Li/Li.....	147
4.15	Schematic diagram of the proposed second lithium insertion mechanism into PSS.....	147
4.16	A typical PEDOT:PSS cycling curve with redox plateaus indicated.....	148
4.17	Multiple cycling curves of PEDOT:PSS.....	149
4.18	CV curves of initial (blue) and subsequent (green) PEDOT:PSS cycles.....	150
4.19	FTIR spectrum of pure and lithiated PEDOT:PSS (reprinted with permission [27]).....	152
4.20	Model of PSS monomer indicating preferred Li ⁺ site.....	153
4.21	Galvanostatic cycling profiles of Inkjet Printed, Spray Coated and Doctor Blade cast PEDOT:PSS, indicating first and second reaction plateaus.....	154
4.22	Schematic diagram of the proposed mechanism for performance variations in A) Doctor Blade B) Spray Coated C) Spray Coated post-cycling D) Inkjet Printed PEDOT:PSS films.....	156

4.23	SEM images of post-mortem PEDOT:PSS cells A)B) pristine C)D) after 1st discharge E)F) after 20 cycles G)H) after 100+ cycles.....	158
5.1	A diagram depicting the most common ion transport mechanisms found in crystalline materials (reprinted with permission [6]).....	167
5.2	Schematic diagram of the PEGDA PEM synthesis process.....	171
5.3	XRD spectra for the PEGDA PEM's constituent components (PEGDA8000, LiTFSI and SCN).....	172
5.4	XRD pattern of Pegda PEM.....	173
5.5	TGA results for PEM constituent components PEGDA8000, SCN and LiTFSI.....	174
5.6	TGA results for PEGDA8000 based PEM with a 5% mass loss indication.....	175
5.7	TGA results of PEGDA PEM vs LiPF ₆ liquid electrolyte.....	176
5.8	DSC scan for PEGDA PEM.....	177
5.9	Freestanding PEGDA PEM being flexed, rolled and twisted.....	178
5.10	PEGDA PEM being stretched.....	179
5.11	EIS spectrum of PEGDA8000 PEM.....	180
5.12	Electrochemical stability window of PEGDA8000 PEM.....	182
5.13	A) SEM image of PEGDA8000 PEM B)C)D)E) EDX elemental mapping of carbon, oxygen, fluorine and sulphur respectively.....	183
5.14	Cross-sectional SEM image of PEGDA8000 PEM cast onto an LNMO electrode on an aluminium foil current collector.....	184
5.15	A) high magnification SEM image of PEGDA8000 PEM/LNMO electrode interface B)C)D) EDX mappings of manganese, carbon and sulphur respectively.....	185
5.16	Cycling profile of LFS/PEM/LTO full cell at room temperature. Inset: Cycling profile of LFS/LTO using LiPF ₆ EC/DEC liquid electrolyte.....	187
5.17	Initial cycling profile for LFP/PEM/Li half-cell at room temperature.....	189
5.18	A) Initial cycling profile of LFP/PEM/Li half-cell at 60°C and B) A comparison of galvanostatic cycling performance of LFP half-cells using PEGDA8000 PEM at room temperature (red) and at 60°C (blue) and using liquid electrolyte at room temperature (green).....	190

5.19 A) First 5 cycle curves of LFP/PEM/LTO full cell, cycled at a C-rate of 1C B) Cycling profiles of various cycles of a LFP/PEM/LTO full cell at various rates C) Discharge capacities of all cycles of LFP/PEM/LTO full cell at various C-rates....	192
6.1 Layout of the nested slot line RFID antenna Size in mm: $L = 65$, $W = 20$, $l = 25$, $w = 2.2$, $t = 0.5$; and $L_{tail} = 40$ (reprinted with permission [8]).....	207
6.2 Schematic view of the IBAS layers (reprinted with permission [8]).....	209
6.3 IBAS prototype stages A) antenna etching B) Chip soldering C) spray coated PEDOT:PSS D) final product on body for testing (reprinted with permission [8]).....	210
6.4 Theoretical read distances using a 3.2W EIRP interrogating power (reprinted with permission [8]).....	211
6.5 IBAS turn-ON powers for passive, BAP integrated and BAP coin-cell (reprinted with permission [8]).....	212
6.6 IBAS battery first charge curve.....	213
6.7 Cycling data for a PEDOT:PSS vs LNMO pouch cell.....	214

List of Tables

1.1	Categorised Energy Storage Systems (adapted with permission [1]).....	4
1.2	Advantages and Disadvantages of Primary and Secondary Batteries.....	5
1.3	A table showing common carbonates and esters used in electrolytes for Li-ion batteries (reprinted with permission from [183]).....	16
3.1	Cells assembled for the study of the Electrolyte Effect using XANES.....	100

List of Abbreviations

ALD	Atomic Layer Deposition
AM	Active Material
BSE	Backscattered Electrons
CB	Carbon Black
CMC	Carboxymethylcellulose
CV	Cyclic Voltammetry
CVD	Chemical Vapour Deposition
DBP	Dibutyl phthalate
DEC	Diethyl Carbonate
DMC	Dimethyl Carbonate
DSC	Differential Scanning Calorimetry
EC	Ethylene Carbonate
EDX	Energy Dispersive X-rays
EIS	Electrochemical Impedance Spectroscopy
EMI	1-Ethyl-3-methylimidazolium
EV	Electric Vehicle
EXAFS	Extended X-ray Absorption Fine Structure
GPE	Gel Polymer Electrolyte
IBAS	Integrated Battery Antenna System
ID	Integrated Design
IL	Ionic Liquids
IXS`	Inelastic X-ray Scattering
LCO	LiCoO ₂
LFP	LiFePO ₄
LFS	Li ₂ FeSiO ₄
LiBOB	Lithium bis(oxolato)borate
LiPF ₆	Lithium hexafluorophosphate
LIPON	Li ₂ PO ₂ N
LISICON	Lithium Super Ionic Conductor
LiTFSI	Lithium bis(trifluoromethanesulfonyl)imide

LLTO	Lanthanum Titanate
LLZO	$\text{Li}_7\text{La}_3\text{Zr}_2\text{O}_{12}$
LMO	LiMn_2O_4
LNMO	$\text{LiNi}_{0.5}\text{Mn}_{1.5}\text{O}_4$
LTO	$\text{Li}_4\text{Ti}_5\text{O}_{12}$
NASICON	Sodium Super Ionic Conductor
NCA	$\text{LiNi}_{0.8}\text{Ca}_{0.15}\text{Al}_{0.05}\text{O}_2$
NMC	$\text{LiNi}_x\text{Co}_y\text{Mn}_z\text{O}_2$
NMP	N-methyl-2-pyrrolidone
OCV	Open Circuit Voltage
OLED	Organic Light Emitting Diode
PC	Propylene Carbonate
PE	Polyethylene
PEDOT:PSS	Poly(3,4-ethylenedioxythiophene):poly(styrenesulfonate)
PEGDA	Poly(ethylene glycol) diacrylate
PEGDME	Polyethyleneglycol dimethylether
PEM	Polymer Electrolyte Membrane
PEO	Poly(ethylene oxide)
PLD	Pulsed Laser Deposition
PP	Polypropylene
PV	Photovoltaic
PVDF	Polyvinylidene fluoride
SAXS	Small Angle X-ray Scattering
SCN	Succinonitrile
SE	Secondary Electrons
SEI	Solid Electrolyte Interface
SEM	Scanning Electron Microscopy
SOFC	Solid Oxide Fuel Cell
SPE	Solid Polymer Electrolyte
SS	Stainless Steel
TEOS	Tetraethyl orthosilicate
TGA	ThermoGravimetric Analysis
VC	Vinylene Carbonate
XANES	X-ray Absorption Near-Edge Structure
XAS	X-ray Absorption Spectroscopy
XRD	X-Ray Diffraction
XRS	X-ray Raman Scattering

Declarations

I, Matteo Hogan, declare that this Thesis has been written by me and confirm that the work presented in this thesis is my own. I also confirm that any part which are the works of others have been clearly stated, including the use of figures and quotations. This work has not been previously submitted for any academic degree.

Matteo Hogan

March 2020

Acknowledgements

Firstly, I would like to express my deepest appreciation and gratitude to my supervisor, Dr. Maria Alfredsson, for her support, motivation and knowledge throughout my PhD.

Also the DSTL for their funding, in particular Dr Darren Browning, Professor Jim Wilson and Rebecca Mangham for their guidance.

Thank you also, to the EPSRC for the funding received for these studies.

I am grateful to Frans Ooms and Professor Erik Kelder from TUDelft, for the use of their equipment and their support and assistance with beamline experiment preparations.

To Alessandro Longo, Giannantonio Cibin and Chiara Cavallari for their help and support at their respective beamlines.

I would like to thank my fellow PhD student colleagues in Maria Alfredsson's group, Dr. Nanami Yokota, Dr. Marcus Bertuzzo, Jimmel Stewart, Dr. Rebecca Tanney and Sally Pang for their support and assistance during my PhD.

I would also like to thank my family and friends for their constant support and understanding throughout my PhD.

Finally, a special thank you to my fiancée Siân, for her constant love and support, and without whom this would not have been possible.

Abstract

Among the portable electronics market, Li-ion batteries remain the preferred choice for many applications, due to their high specific energy. However, current battery technologies have flaws associated with both their chemistries, manufacturing methods and architecture. Battery and device architectures are regularly kept as separate entities during product design, and only put together in the final design, unnecessarily increasing device footprint, costs and weight. Herein, we explore an alternative approach to these limitations, by developing an integrated battery antenna system. The three main components of the battery: the cathode, the electrolyte and the anode are investigated with an aim to design an all-solid-state flexible, wearable, body conformable antenna battery system.

$\text{Li}_2\text{FeSiO}_4$ is explored as a high capacity, environmentally benign cathode material. Utilizing in-operando XAS and ex-situ XRS to explore the origin of the materials' additional capacity associated with the removal of $>1\text{Li}^+$ per unit formula. It is found that oxygen contributes, reversibly, as a charge compensation mechanism to the additional capacity.

A PEGDA based solid polymer electrolyte membrane (PEM) is explored as a high performance, high conductivity, flexible, stretchable and thermally stable alternative to liquid electrolytes. The PEM is found to be stable up to 4.7V vs Li/Li⁺ and yield a conductivity of $1.4 \times 10^{-3} \text{Scm}^{-1}$, which places it securely into the "superionic" region. . For the first time, this system has been applied to a full-cell configuration, yielding strong cycling performance throughout, with full-cell capacities reaching as high as 151mAhg^{-1} at room temperature.

PEDOT:PSS is a mixed conductive polymer, assessed as a potential anode material. The material was deposited using three different techniques: (I) tape casting (II) spray-coating (III) inkjet printing. It was found that cycling performance was heavily dependent on the manufacturing technique employed. Inkjet printed, binder free films exhibited the greatest performance with capacities stable across all 50 cycles tested.

Finally, the PEDOT:PSS anode was incorporated into an on-body electronic device – an RFID antenna, utilizing the antenna architecture as a dual purpose component. The antenna powered by the integrated battery exhibited strong performance characteristics, matching those of a commercial coin cell battery.

1 Introduction

1.1 Integrated Design

Integrated Design (ID) refers to the use of product architecture to fully integrate a battery within a product. Most products are designed first and foremost, for their primary functionality, however, their form is often dictated by component dimensions e.g. the battery. This is largely due to current battery technologies standardised design, i.e. rectangular or cylindrical blocks. This can greatly affect the final products' shape and size. For many static technologies, this may not be an issue. However, its importance grows when considering portable and/or wearable technologies.

Wearable technology is a rapidly emerging market, with manufacturers looking to design body-conformable devices such as wrap-around displays, wearable heart-rate monitors, fitness trackers, smart watches and other wearable devices. Thus far, all commercialised products have been relatively bulky and blocky, not because the technology of the electronics demands this, but due to the design constraints imposed by the battery to power the electronics. These products can benefit greatly from ID; take the "smart watch" concept, current products are typically thicker than 1cm and are housed in blocky casings. However, many of the manufacturers of these watches have demonstrated their capability of producing low profile, curved and even flexible displays. The reason products have been limited to bulky housing is due to the battery and its inability to flex, or easily conform to 3D architectures. With ID and the use of the novel deposition technologies (section 1.7), battery design can be modified to enable wrap around, body conformable energy storage. For example, watch straps could become multifunctional by integrating a battery, therefore reducing the overall profile whilst retaining functionality.

The concept of ID is not a new one; many research groups have investigated the use of novel battery technologies and electronics with the aim of developing products with lower profiles, reduced weight, body conformability and flexibility [1] [2] [3] [4] [5]. However, these products usually focus on either the electronics or the battery, often referencing potential applications rather than developing a truly integrated product.

Nonetheless, these novel battery technologies are a promising step towards truly integrated devices. These novel technologies often implement the use of solid-state electrolytes (Section 1.5.5), for their potential flexible characteristics, mechanical strengths and safety which is of paramount importance when designing close to skin wearable technologies, encouraging further research on solid polymer electrolytes.

Figure 1.1 shows an example of a body conformable, potentially low-profile device designed for temperature sensing and data logging with Bluetooth wireless operation [3]. However, despite using flexible PCB and hydrogel substrates, their power source is a large bulky LiPo battery. This detracts from the devices low profile nature and significantly increases the weight of the product.

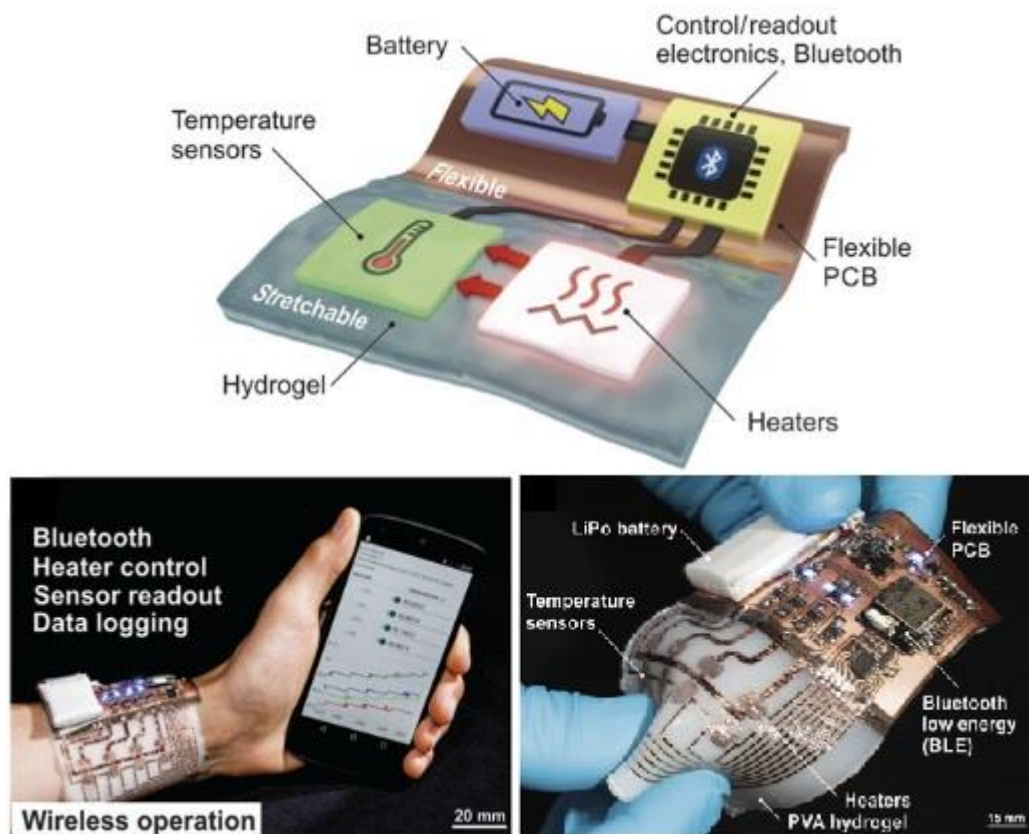


Figure 1.1: An example of a wearable, body conforming electronics product (adapted with permission from AAAS [3])

Another approach to this would be to implement ID and incorporate a low profile, flexible battery, making use of the devices large surface area. Using a larger surface area for the battery allows for a reduction in profile whilst maintaining the necessary capacity to power the device. This is the approach investigated in this study, to design

a low profile fully integrated battery antenna system (IBAS), taking it a step further by utilising the antenna itself as a major component of the battery (current collector), further reducing the devices profile, weight, cost and complexity [6].

1.2 Aims of the Research

The aim of this research is to investigate various pathways to creating a better battery and exploring manufacturing techniques with the aim of creating an integrated battery antenna system (IBAS). The IBAS is designed to be an on-the-skin wearable and body conformable device, this means it is necessary to explore chemistries that exhibit low toxicity, improved safety, allows for cell flexibility (body conformability), has a high enough capacity and voltage to power the devices electronics, also, due to the integrated design, must be rechargeable and reliable as the battery will not be removable. The thesis explores many components of a battery and ranges from synthesising and characterising low cost, non-toxic and environmentally friendly electrode materials, using a variety of in-house and national facility synchrotron radiation techniques (chapter 3), to exploring mixed conducting polymer electrodes and different approaches to manufacturing, by investigating a variety of deposition techniques and their implications for battery technologies (chapter 4). Battery safety and versatility is taken into consideration in chapter 5, where solid polymer electrolytes are investigated for use in an all-solid-state full-cell battery, the system explored exhibits high room temperature ionic conductivity, high thermal stability, high flexibility and stretchability. Finally, chapter 6 presents the low profile, body conformable IBAS and details its performance characteristics, comparing the antenna performance using the integrated battery with that of a traditional coin cell.

Figure 1.2 illustrates the strengths and weaknesses of each of the materials chosen for this study, where a higher number signifies better performance e.g. lower toxicity, higher capacity, lower cost etc. Looking at the $\text{Li}_2\text{FeSiO}_4$ we see strong performance in terms of safety, cost, toxicity and capacity. Whilst PEDOT:PSS exhibits good performance regarding toxicity, safety, conductivity, flexibility and cost. Lastly the PEGDA PEM shows strong performance in safety, stretchability and flexibility. These are all essential attributes when considering materials for use in the IBAS and justifies their selection for this study.

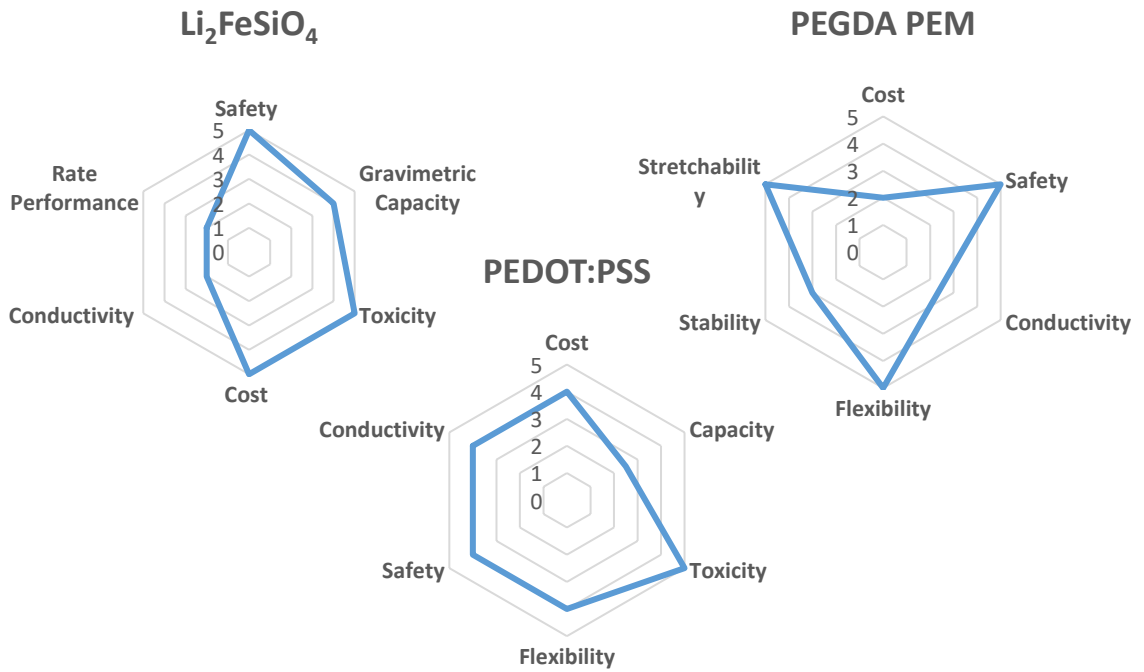


Figure 1.2: Radar plots showing the defining properties of $\text{Li}_2\text{FeSiO}_4$, PEDOT:PSS and PEGDA PEM selected for this study

1.3 Energy Storage – The Humble Battery

The World we live in today has become dependent on energy. Electrical energy generated using multiple methods, from a host of sources – fossil fuels, nuclear, wind, hydroelectric and solar are among the largest providers. This energy is needed to feed our lifestyles. Today’s world runs because of the energy we are able to generate. Industrial production, electronic appliances in the work place or at home, portable electronic devices, electrical vehicles etc. are all tasks that are dependent on electricity. Many of our common energy sources produce power within limited time intervals, however, energy is in demand 24 hours a day, 7 days a week. It has, therefore, become essential to store energy for use when needed. There are several ways to store energy, which can be categorised as shown in Table 1.1 [7].

Table 1.1: Categorized Energy Storage Systems (adapted with permission [1])

Mechanical	Thermal	Electrical	Chemical	Electrochemical
Pumped Hydro	Latent Heat Storage	Capacitor	Hydrogen Fuel cells	Secondary Batteries
Compressed Air		Supercapacitor		Flow Cells
Flywheel		Superconducting Magnetic		

Whilst many of the solutions shown are effective methods of energy storage, many require large areas or specific environmental scenarios e.g. pumped hydro and latent heat storage. Few of the aforementioned storage systems are suitable for applications such as portable electronics, and are therefore, more suited to grid applications. It is for these reasons that no other system has become as intimately integrated into our lives as batteries.

Batteries have played a part in our lives for many years; there is even evidence to suggest that batteries were in use thousands of years ago, in the form of the Parthian battery [8]. Of course, these batteries were primitive, and therefore, unable to produce a significant amount of current or voltage. The first “modern” battery was invented by the Italian scientist, Alessandro Volta in 1800. He piled up layers of copper and zinc electrodes, separated by layers of cloth soaked in sulphuric acid, which acted as an electrolyte. This battery is today known as the “voltaic cell” [9]. One major drawback of this type of battery is that once the energy is used it cannot be recharged, known as a “primary” battery.

The rechargeable, “secondary”, battery was invented in 1859, by the French scientist Gaston Planté. This was lead acid based, similar to lead acid systems currently used in a number of applications, including vehicles. There are both advantages and disadvantages to “primary” and “secondary” type batteries, a few of which are listed in Table 1.2.

Table 1.2: Advantages and Disadvantages of Primary and Secondary Batteries

	Advantages	Disadvantages
Primary	Low initial cost of materials High capacity High initial voltage Low self-discharge rate	More expensive long term High waste when disposing Not suitable for “high drain” applications
Secondary	Low cost over long periods Long life Suitable for “high drain” applications	High initial cost High self-discharge rate May require maintenance

The importance of the “secondary” battery is huge as it made the invention of portable electronic devices possible. It would now be almost unthinkable to introduce a portable electronic device without a secondary battery powering it due to our demand for convenience and due to the huge long-term cost of powering these devices with primary batteries.

As demand for energy storage and portability increases so does the need for better performing batteries. This has led to a vast number of battery types being invented. Figure 1.3 shows the gravimetric and volumetric energy densities of different types of batteries.

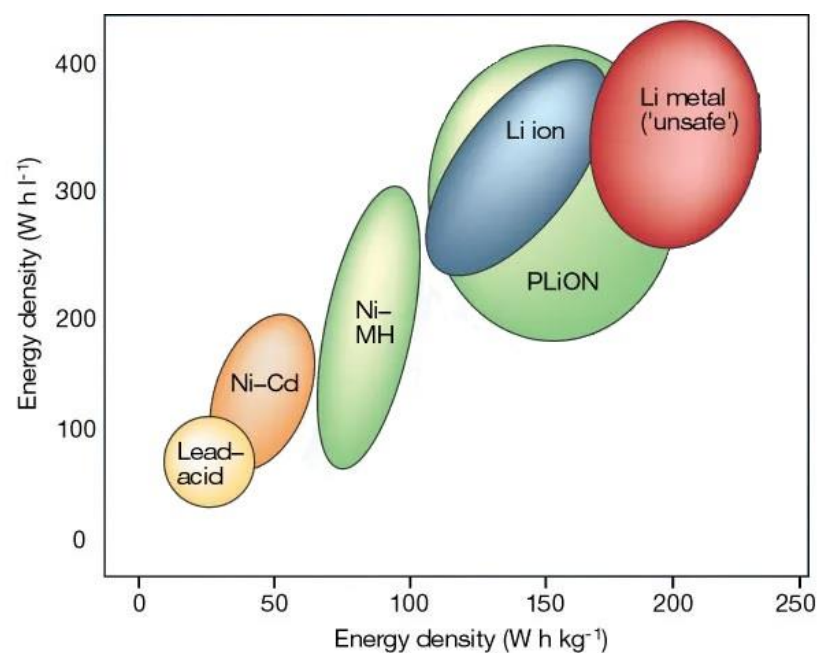


Figure 1.3: A comparison of gravimetric and volumetric energy densities of various battery technologies (Adapted with permission [179])

Each battery technology has its advantages and disadvantages; it can be seen that the aforementioned lead-acid battery has the lowest gravimetric as well as volumetric energy density, therefore eliminating its suitability in portable electronics based on the required battery size. Instead lead-acid batteries are better suited to applications such as vehicles with combustion engines, due to their rugged dependability and affordability. This is where Lithium-ion batteries excel, whilst being expensive and more fragile than other chemistries; they have a high specific energy, leading to a smaller and lighter battery than other comparable technologies.

Figure 1.3 shows Li-ion batteries as a strong option with only lithium metal outperforming it. However, there are numerous concerns with lithium metal batteries

due to lithium dendrite formation on the lithium metal surface during repeated cycling, resulting in the battery short circuiting, making it unsafe as it may lead to thermal runaway and, eventually, cell combustion. As dendrite formation is a slower process in Li-ion batteries, this technology is well positioned as the frontrunner of energy storage. The reason Li-ion batteries dominate this sector is, in part, due to their high specific energy (energy density Wh/kg), but also because of their low maintenance and high specific power (W/kg).

1.4 The Li-ion Battery

Since its first commercialisation by Sony in 1991 [10], vast amounts of research has taken place on improving every component of the Li-ion battery. However, the basic

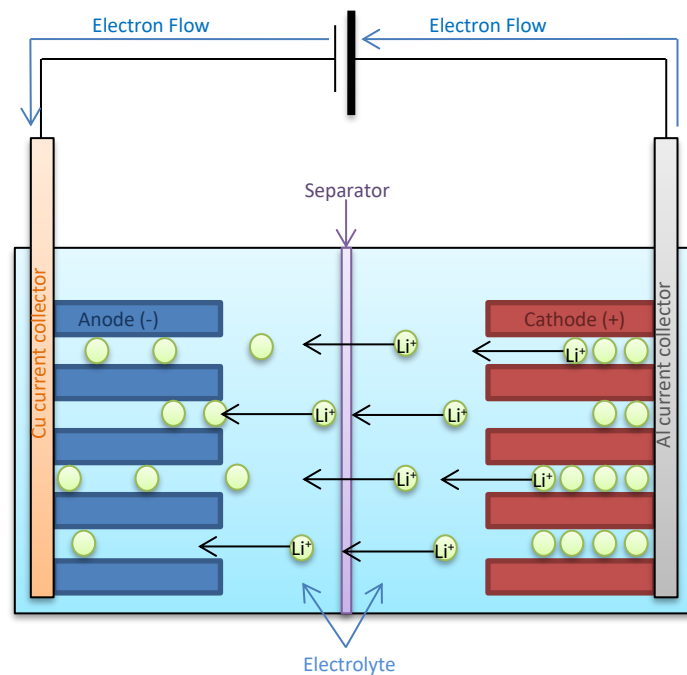


Figure 1.4: A schematic diagram of a Li-ion battery in a state of charging

principles have remained unchanged. Figure 1.4 shows a schematic of the workings within a Li-ion battery, indicating each component.

There are three main components to a Li-ion battery: A positive electrode (cathode) typically formed of a lithium containing metal oxide e.g. LiCoO_2 or LiFePO_4 , a negative electrode (anode) typically a porous carbon e.g. graphite, and an electrolyte (ionically conducting medium) which incorporates a lithium salt e.g. LiPF_6 dissolved into an organic solvent, often carbonate based, solvents e.g. ethylene carbonate:diethyl

carbonate (EC:DEC). In addition to the three main components are other essential components which do not actively contribute to the chemistry of the battery, e.g. casing to prevent leakages and protect the battery from oxygen and water contamination, current collectors (Al and Cu foils) to act as an electrically conducting medium for positive and negative electrodes and the separator, to prevent internal short circuits between the anode and cathode.

A battery stores and generates electrical energy through repeated redox (reduction/oxidation) reactions. Oxidation is when the oxidation state of an ion is increased by the removal of an electron, whereas reduction is when it is decreased by the addition of an electron. When the battery is being charged the Li^+ ions are extracted from the cathode through the electrolyte transport medium to the graphite anode, which has a layered structure for efficient Li-ion storage. During charging, electrons pass through the external circuit from the cathode to the anode. Resulting in an oxidation of the transition metal ion in the cathode e.g. $\text{Co}^{3+} \rightarrow \text{Co}^{4+}$. Now this energy is stored to be used when needed. During discharge, this process is reversed and the oxidation state of the cathode is reduced i.e. $\text{Co}^{4+} \rightarrow \text{Co}^{3+}$. These two processes are repeated upon cycling (charging and discharging) of the battery.

1.5 Improving the Li-ion Battery

Upon closer inspection of the individual components of a Li-ion battery, there are many paths which can be taken to improve each one of them. The paths explored in this study will be briefly introduced and a justification will be presented according to current literature.

When considering on how to improve a technology, many things must be considered, including the target customer, manufacturing methods, material costs, environmental implications and safety. For the Li-ion battery, the target audience is very broad due to a range of applications. However, the main applications are portable electronics and electric vehicles.

Electronics with integrated battery solutions is an enticing prospect, enabling manufacturers to reduce size whilst maintaining capacity, or designing products with less restriction on battery form-factor. This requires advanced manufacturing

techniques giving greater control over material placement than the conventional methods currently used in industry such as tape casting (doctor blade).

The automotive industry is heavily investing in post-combustion technologies due to growing concern over greenhouse gasses and other environmental issues, leading to a push toward electric vehicles. However, whilst this is a positive change, it has led to a closer inspection on the environmental costs of the lithium battery industry, and so, more environmentally friendly and cost-effective battery materials are desirable. In addition to this, alternatives to the currently used, harmful materials in electrode processing, such as, hazardous solvent N-Methyl-2-Pyrrolidone (NMP) have been sought out. High voltage and high capacity materials have also been heavily researched in an attempt to increase vehicle power and range.

1.6 The Cathode

Cathodes are a vital component in a battery; they must hold many essential characteristics to be considered for further research and potential commercialisation. A diverse selection of compounds have been considered for use as the positive electrode in Li-ion batteries. Among these, transition metal-oxides have stood above most other competitors, due to their redox abilities at elevated potentials (>3V). These transition metal-oxides are split into three main structure groups: layered, spinel and olivine, with examples shown in Figure 1.5.

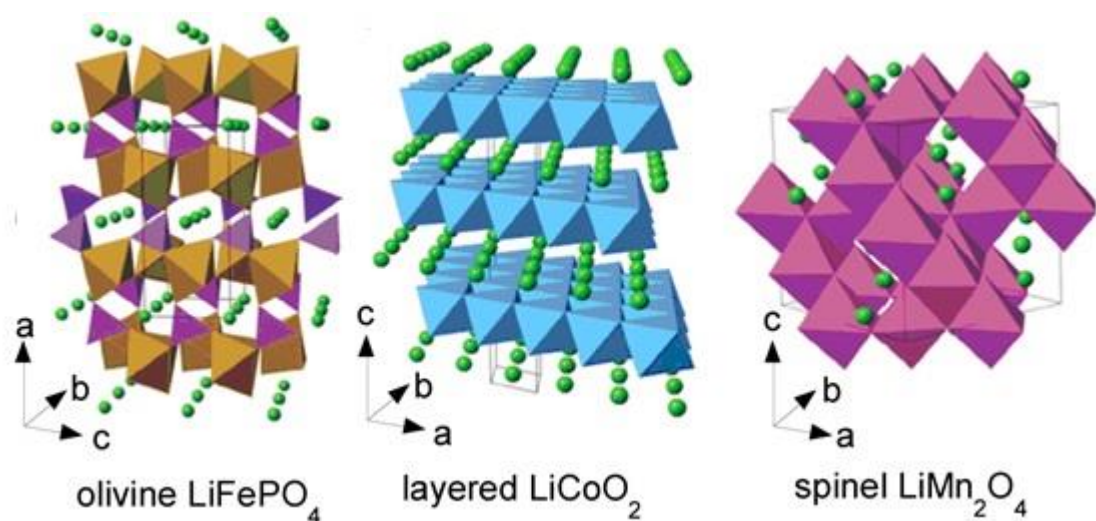


Figure 1.5: Crystal structures of olivine, layered and spinel compounds (adapted with permission [180])

These crystal structures possess 1D tunnels (olivine), 2D layers (layered) or 3D networks (spinel) where Li^+ ions are inserted and extracted. These structures and pathways allow for high reversibility and minimal volume expansion upon cycling.

1.6.1 LiCoO_2 (LCO)

Layered LiCoO_2 (LCO) was the first commercialised cathode material used in Li-ion batteries. Despite its success, LCO has shortcomings. LCO has a theoretical capacity of 248mAhg^{-1} , but in commercial cells, the material only achieves around 140mAhg^{-1} due to limiting the operating potential window below 4.2V [11]. This is due to severe side reactions and lattice distortions experienced during deep cycling ($\text{Li}_{1-x}\text{CoO}_2$ where $x > 0.5$) [12]. Cycling above this point, therefore, leads to high capacity fading of the material. For this reason, LCO is typically cycled to $x \leq 0.5$, this reduces its energy density. In addition, LCO experiences transition metal (cobalt) dissolution into the electrolyte, due to small amounts of HF formation, which in turn, reacts with LCO further increasing capacity fade [13].

Many methods have been employed to reduce/eliminate these lattice distortions and suppress Co dissolution. Thin layer, chemically resistant coatings, have been deposited by chemical vapour deposition (CVD), sol-gel and atomic layer deposition (ALD) to act as a barrier between LCO and the electrolyte [14] [15] [16]. These coatings not only reduce direct contact between LCO and the electrolyte, creating a more stable interface and reducing Co dissolution, they may also increase electron mobility and suppress oxygen formation. In addition, they are also designed to react with HF to form more stable compounds [17] [18]. Figure 1.6 shows how such coatings affect capacity retention. It can be seen that, upon coating, capacity retention is greatly increased, with the coated sample exhibiting $\approx 13\%$ increased capacity retention after 50 cycles [19].

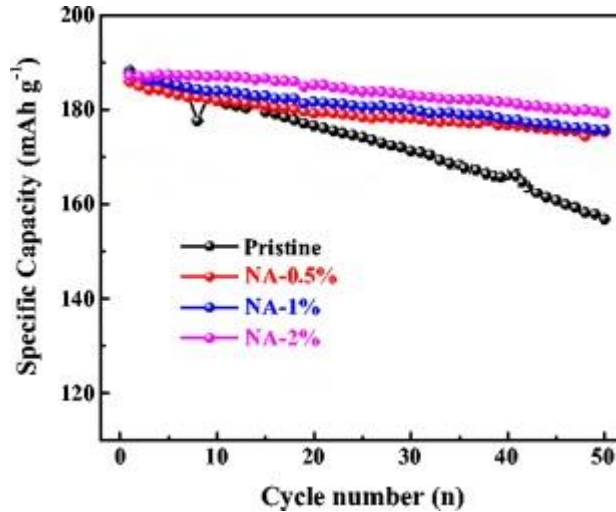


Figure 1.6: Figure showing pristine and NaAlO₂ coated LCO capacity retention (adapted with permission [19])

Doping is another widely used method for increasing LCO performance. Here, doping is used to alter LCO's capacity and/or increase structural stability, allowing for cycling beyond $x=0.5$ without the aforementioned lattice distortion. Figure 1.7 shows the capacity retention of LCO doped with Ti [20].

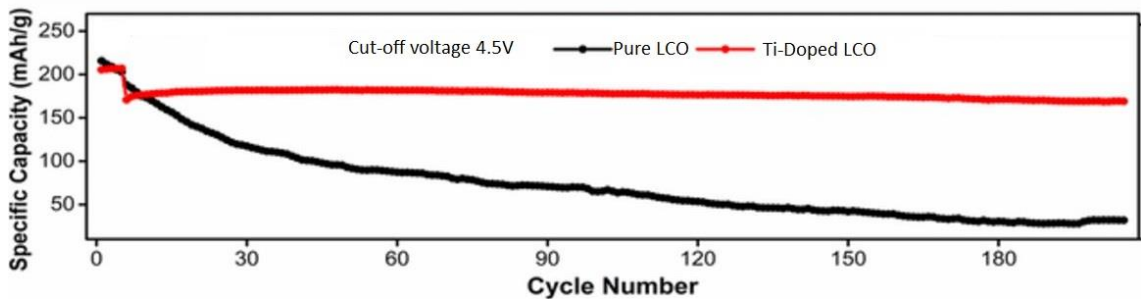


Figure 1.7: Figure showing pure LCO vs Ti-doped LCO capacity retention (adapted with permission [20])

A marked improvement is visible, the doped material exhibits high capacity retention and stable cycling even with the higher cut-off voltage of 4.5V, whereas the pure LCO exhibits rapid capacity degradation caused by structural instability.

Whilst many groups have shown the potential to improve LCO as a cathode material and harness more capacity than a typical commercial LCO cell, they cannot change the fact LCO has other inherent flaws. Namely, high toxicity and high costs due to the high levels of cobalt.

1.6.2 LiMn₂O₄ (LMO)

As a result, alternative materials have been sought out. One candidate proposed was spinel LiMn₂O₄ (LMO). LMO immediately solves two of LCOs major flaws, the removal of cobalt and the introduction of manganese reduces both cost and toxicity. LMO also exhibits strong high rate performance, however, LMO suffers from many of the same issues as LCO. Manganese dissolution and structural instabilities are among the numerous reasons LMO exhibit high capacity fading [21]. In addition, LMO has a low theoretical capacity of 148mAhg⁻¹. Similar to LCO, multiple methods have been employed to improve LMOs characteristics, including doping and coatings [22] [23]. However, its low capacity limits its potential growth.

1.6.3 LiNi_{0.8}Co_{0.15}Al_{0.05}O₂ & LiNi_xCo_yMn_zO₂ (NCA & NMC)

In the search for more structurally stable cathodes which exhibit both high capacity and high capacity retention, it was proposed that combining cobalt with other transition metals would improve these characteristics. Not only can the addition of other transition metals improve structural stability, but also reduce cost by reducing the effective cobalt content (when compared to LCO). Layered compounds, such as, LiNi_{0.8}Co_{0.15}Al_{0.05}O₂ (NCA) is a strong candidate which has been commercialised due to high discharge capacity (≈200mAhg⁻¹). However, it has the potential of high capacity fading at elevated temperatures caused by large, unstable solid electrolyte interface (SEI) growth [24]. Another layered compound, LiNi_xCo_yMn_zO₂ (NMC) also achieves high capacities, and operating voltages, whilst also having much higher stability than LCO. In addition, by controlling the amounts of Ni, Mn, and Co, NMC can largely be tailored to specific applications, with compositions favouring either high power or high energy. However, both NCA and NMC still contain environmentally unfriendly, costly and toxic materials (cobalt and nickel), which, when EV production expands, may become unviable.

1.6.4 LiFePO₄ (LFP)

Therefore, cathode materials with a much lower economic and environmental impact have been researched. Olivine LiFePO₄ (LFP) is one such material. Composed of environmentally benign and cost effective materials, LFP also exhibits high thermal and electrochemical stability, and reactions produce flat voltage plateaus, LFP was readily

commercialised. Issues with low ionic mobility and electronic conductivity were remedied by nanosizing and carbon coating, improving upon its rate performance [25] [26]. However, low operative voltages ($\approx 3.3\text{V}$) and unremarkable capacities (170mAhg^{-1}) limit its potential in high capacity applications.

1.6.5 Li_2MSiO_4 (L(M)S)

The need for higher energy density and larger capacities has led to researching materials which can reversibly remove and reinsert $>1 \text{Li}^+$ per unit formula. There are multiple options for this. One of the most promising is a lithium containing silicate, following the formula: Li_2MSiO_4 ($\text{M}=\text{Fe}, \text{Mn}, \text{Co}, \text{Ni}$). These materials offer the potential for the removal of 2Li^+ per unit formula, therefore increasing energy density. Aside from the cost and toxicity of Co and Ni, the silicates synthesised using Co and Ni have very high redox potentials, with first reaction plateaus occurring above 4V and the second believed to occur above 5V . These voltages are beyond current electrolytes stability windows, therefore, poor cycling performance is typically observed in these materials, meaning that they are currently only accessing the first Li^+ plateau, often achieving a reversible Li^+ extraction of <0.5 [27]. Zhang et al. observed an LCS discharge capacity of 144mAhg^{-1} , however, a sharp decline in capacity was observed in further cycling [28].

Alternatively, $\text{Li}_2\text{MnSiO}_4$ has been extensively researched due to its positive characteristics, including large capacities at relatively high potentials. However, it undergoes large structural rearrangements, introducing an amorphous phase upon first charge, leading to rapid capacity drop-off and poor reversibility [29] [30].

$\text{Li}_2\text{FeSiO}_4$ has gained a lot of attention. The material composition is cheap and environmentally benign, meaning that it would be well suited to the ever-expanding Li-ion battery industry. It exhibits very good structural stability (after an initial structural rearrangement during the first cycle [31]) and strong thermal stability, leading to a safe cathode material. With regards to energy density Figure 1.8 shows experimental and theoretical energy densities vs operating voltages.

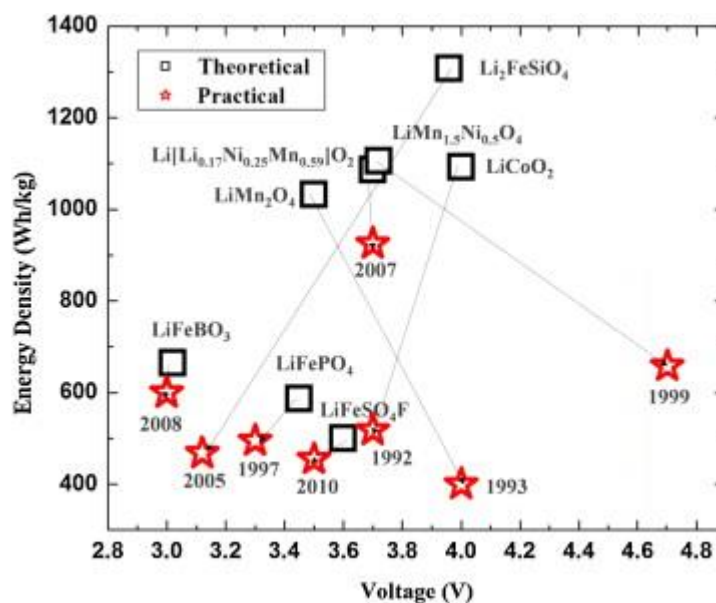


Figure 1.8: Theoretical and Practical energy densities of various cathode materials (adapted with permission [181])

It can be seen that LFS scores strongly on theoretical energy density (1300Whkg^{-1}) and working potential (4V). However, LFS performed relatively poorly experimentally in 2005. Since then, performance of LFS cathode materials have been greatly improved [32] [33]. Achieving reversible, greater than a 1 electron reaction per unit formula even at room temperature, early cycling of LFS was undertaken at elevated temperatures to compensate for poor ionic and electronic conductivities inherent of silicate cathodes [34]. The potential for high energy density is attributed to LFS's high theoretical capacity of 330mAhg^{-1} (accounting for a full 2Li^+ extraction and reinsertion) whilst early studies showed reversibly capacities of $<165\text{mAhg}^{-1}$ indicating up to a 1Li^+ removal, more recent studies have achieved a greater than 1Li^+ reaction. Figure 1.9 shows multiple cycles exhibiting a greater than 165mAhg^{-1} . This shows promise for LFS as a high capacity cathode material.

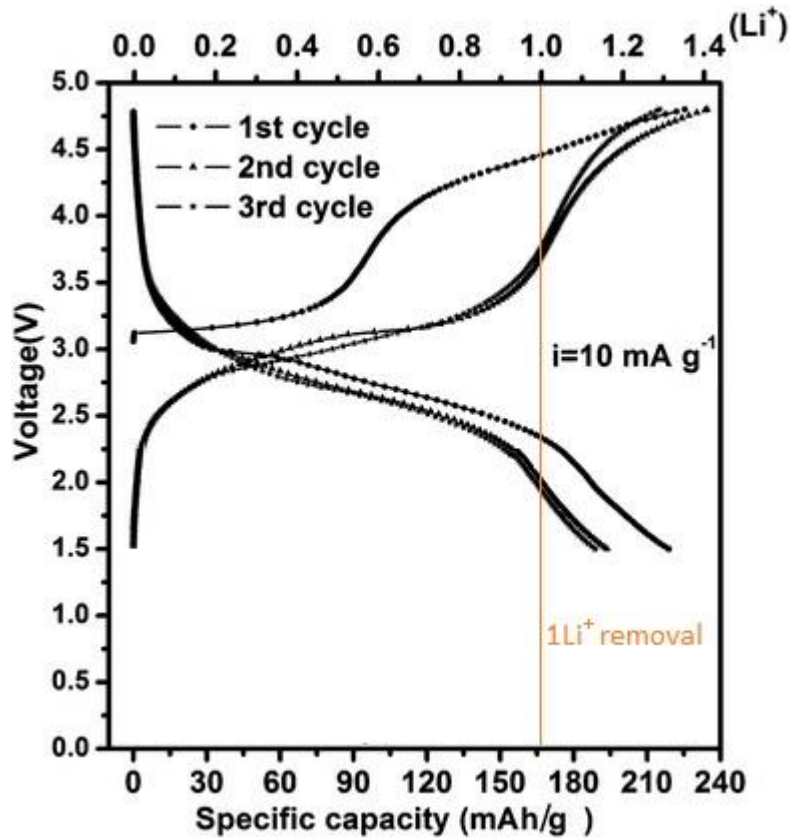


Figure 1.9: Multiple cycles of $\text{Li}_2\text{FeSiO}_4$ cathode indicating high reversible capacity (adapted with permission [182])

However, the operating voltage is still in the 3V region, which may make it unsuitable for high power applications. For the purposes of integrated electronics, high voltage systems are not of paramount importance, for this, LFS remains a strong candidate. It is for these environmental, stability and performance characteristics, that this material was chosen for this project.

1.7 The Electrolyte

The electrolyte is an essential component in a lithium ion battery; it is the ionically conducting medium providing Li^+ transport between the anode and cathode, thereby completing the cell. An electrolyte must possess these attributes [35] [36]:

- 1 It should exhibit high ionic conductivity to enable high rate capability and facile lithium insertion and removal.
- 2 It should be an electronic insulator to avoid short circuits and prevent self-discharge.

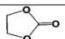
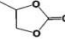
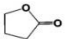
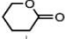
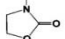
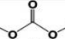
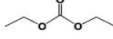
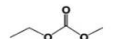
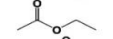
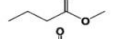
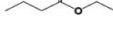

- 3 It should be electrochemically stable vs electrode materials in both the anodes and cathodes working potentials, to prevent both electrolyte degradation and reactions with the electrode materials.
- 4 It should be inert to all other cell components, including packaging.
- 5 It should exhibit good thermal stability at regular battery operation temperatures

In addition to these essential attributes, there are other criteria which are desirable. Materials and production methods should be sustainable and low cost to allow for large-scale production. Materials should also be environmentally friendly, or at least, limit toxicity, recyclable and/or biodegradable. There have been many types of electrolytes, which can be categorised broadly into 5 categories: 1) Non-aqueous liquid (organic solvents) 2) Aqueous liquid 3) Ionic Liquid 4) Gel electrolytes and 5) Solid electrolytes.

1.7.1 Non-aqueous Electrolytes

Commercial Li-ion batteries use organic solvents as electrolytes, in which a lithium salt is dissolved. The most commonly used salt is LiPF₆, typically in a 1M solution. The organic solvents are largely carbonate based organic solvents listed in Table 1.3. These solvents are used due to their low viscosities and wide-range liquid phases (low melting points T_m and high boiling points T_b), high flashpoints are also preferred due to safety concerns. It can be seen that not many of the solvents hold all desired attributes, so it is common to combine more than one solvent.

Table 1.3: A table showing common carbonates and esters used in electrolytes for Li-ion batteries (reprinted with permission from [183])

Solvent	Structure	M. Wt	T _m / °C	T _b / °C	η/cP 25 °C (40 °C)	ε 25 °C	Dipole Moment/debye	T _f / °C	d/gcm ⁻³ , 25 °C
EC		88	36.4	248	1.90, (40 °C)	89.78	4.61	160	1.321
PC		102	-48.8	242	2.53	64.92	4.81	132	1.200
BC		116	-53	240	3.2	53	4.23	97	1.199
γBL		86	-43.5	204	1.73	39	4.29	81	1.057
γVL		100	-31	208	2.0	34	4.52	110	1.17
NMO		101	15	270	2.5	78			
DMC		90	4.6	91	0.59 (20 °C)	3.107	0.76	18	1.063
DEC		118	-74.3 ^a	126	0.75	2.805	0.96	31	0.969
EMC		104	-53	110	0.65	2.958	0.89		1.006
EA		88	-84	77	0.45	6.02		-3	0.902
MB		102	-84	102	0.6			11	0.898
EB		116	-93	120	0.71			19	0.878

Propylene carbonate (PC) was the main solvent used in early Li-ion batteries, including the LCO cell first commercialised by Sony [10]. However, it was soon realised that PC forms unstable solid electrolyte interphase (SEI) and it co-intercalated with Li⁺ into the graphite anodes, eventually leading to exfoliation and, therefore, a reduction in capacity and continued electrolyte decomposition [37]. Ethylene carbonate (EC) was chosen as a combination solvent, due to its stable SEI forming properties. EC exhibits other strong electrolyte properties, readily solvation of lithium salts and high ionic conductivity, however, it has a high melting temperature of 36.4°C meaning it is unsuitable as the sole solvent in Li-ion batteries. It is, therefore, often mixed with other thinning solvents such as DEC, DMC and EMC. This combination of solvents mixed with a lithium salt such as LiPF₆ yields an electrolyte with high ionic conductivity, a high reduction voltage ≈1.3V vs Li/Li⁺ allowing for early SEI formation on the graphite anode so it stabilises quickly [38].

Whilst carbonate based electrolytes remain a standard in Li-ion batteries today, they have many intrinsic flaws, namely: poor thermal stability, narrow electrochemical stability window (for high voltage applications, compared to some chemistries), volatile, high flammability, poor mechanical stability and have the potential to leak. For these reasons there is constant research into alternative electrolyte compositions.

1.7.2 Aqueous Electrolytes

One such alternative comes in the form of aqueous electrolytes. There are multiple advantages to the use of aqueous electrolytes including: low cost, low environmental impact, non-flammability, intrinsic cooling properties, very high ionic conductivities (up to 2 orders of magnitude higher than carbonate based equivalent), simplified processing (no humidity control is required) and low toxicity. These attributes show potential as a much safer alternative electrolyte to the standard carbonate based systems for use in integrated consumer electronics, where many applications involve wearable or close-to-skin technology and therefore, safety is paramount.

Aqueous electrolytes have been considered as an alternative electrolyte since first proposed by Li et al. in 1994 [39]. However, owing to the narrow stability window of water (≈1.2V) and the potential for both O₂ and H₂ evolution upon cycling, its

applications have been, somewhat limited. However, Luo et al. showed that by adjusting the electrolytes pH, some control over the positioning of this window could be gained, as depicted in Figure 1.10 [40].

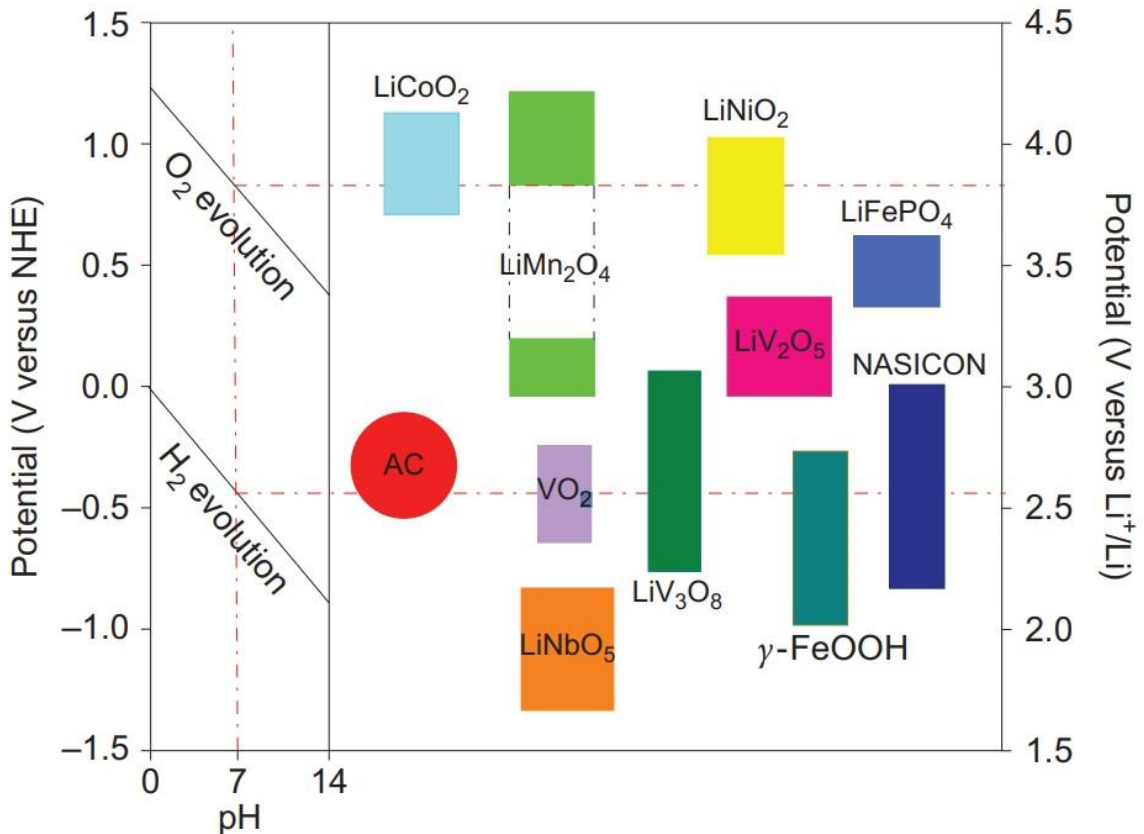


Figure 1.10: Electrochemical stability windows of aqueous electrolyte and working potentials of various electrode materials (reprinted with permission [40])

This allowed some full cells to be cycled using electrodes which fit within this window. However, whilst the window can be shifted, it remains narrow and so, any resulting batteries would have relatively low potentials, typically in the 1V region [40] [41]. This would greatly limit their usage, in addition, the main candidate for anode materials were environmentally unfriendly vanadium based anodes [42].

However, it has been shown that the electrochemical stability window can be widened by the use of a “water-in-salt” electrolyte which, in turn, forms a stable SEI and enabling a voltage window of $\approx 3V$ [43]. This “water-in-salt” electrolyte consisted of highly concentrated LiTFSI salt ($>20M$) in water. At these concentrations the salt outnumbers the solvent in both weight and volume. Suo et al. found, using quantum chemistry calculations, that at these concentrations LiTFSI reduction at higher voltages than the hydrogen evolution, thus passivating and eventually suppressing H_2 evolution,

by changing its onset voltage from 2.63V down to 1.9V [43]. The access to larger stability window allows for a wider variety of chemistries to be used, increasing working voltages and enhancing energy density of aqueous Li-ion batteries. This was further improved by Yamada et al. [44] using a “hydrate-melt” electrolyte. Though these electrolytes contain very little water content, their voltage stability window was widened to $\approx 3.8\text{V}$ and enabled the use of lower voltage anode materials, such as, $\text{Li}_4\text{Ti}_5\text{O}_{12}$ (LTO) producing cells with overall potentials around 3.1V.

Other methods to further enhance aqueous electrolyte cells, include enabling the use of Li-metal and graphite anodes, which are considered unsuitable for aqueous cells. In both cases, Li-metal or graphite anodes have been firstly coated in a gel-polymer electrolyte then further coated in a LISICON ceramic electrolyte layer to protect the anode and prevent contact with the aqueous electrolyte [45], or coated with a hydrophobic SEI additive to promote a stable SEI formation prior to any contact with water, these methods have enabled the use of aqueous electrolytes in cells exhibiting potentials as high as 4V [46].

Whilst these are positive strides into supporting safer, more environmentally friendly batteries, their cycling stability and coulombic efficiencies still need great improvement. In addition to this, aqueous electrolytes still do not allow the use of high voltage cathode materials.

1.7.3 Ionic Liquids

Another proposed chemistry for electrolytes is that of ionic liquids (IL). Ionic liquids are ionic compounds (i.e. salts) with a melting temperature below 100°C . However, the main focus is on room temperature ionic liquids. They have become an interest in Li-ion research due to their positive attributes: non-volatile, non-flammable, high thermal stability, high room-temperature ionic conductivities, high oxidation resistance (high voltage electrochemical windows) and no need for solvents. However, ILs often suffer from much higher viscosities than carbonate alternatives, therefore effectively reducing ionic conductivities.

In addition, poor SEI forming properties and relatively high reduction potentials vs Li/Li^+ ($\approx 1.0\text{V}$) of early ILs, such as those based on 1-Ethyl-3-methylimidazolium (EMI),

once again limited their use with graphite and metallic lithium anodes [47]. It is for this reason that the addition of small amounts of carbonate based additives, such as vinylene carbonate (VC), was explored to enable the formation of a stable SEI, protecting the graphite and allowing continued Li^+ insertion and removal [48] [49]. It has also been shown that the addition of LiTFSI salt can change the stability windows of ILs, by passivating the graphite anodes [50]. In addition, it has been shown that some IL's have enhanced stability vs Li-metal or graphite anodes and also exhibit large voltage stability windows $>5.5\text{V}$ [51]. IL's can, therefore, be used in high voltage cells using cathode materials such as $\text{LiNi}_{0.5}\text{Mn}_{1.5}\text{O}_4$ (LNMO) exhibiting redox potentials as high as 4.8V [52]. However, the long-term stability of such a cell is limited, therefore further improvement is necessary.

Ionic liquids are a promising step towards safer Li-ion batteries, however, due to their inherent downfalls, further research is necessary to improve cyclability, anode side electrochemical stability, and poor kinetics, which arise due to high viscosities. It has been proposed that ILs show promise as an electrolyte additive in standard carbonate based electrolytes to help improve safety and enhance upper-limit voltage windows [53].

1.7.4 Gel Electrolytes

Thus far, due to their liquid nature, all aforementioned electrolytes suffer from one major issue, leakage. Batteries with leaking electrolyte will eventually kill the cell, but this can also lead to a host of safety issues, including environmental and flammability problems. To remedy this, polymer based electrolytes were proposed and have since gained a lot of attention and been commercialised. Polymer electrolytes were investigated as early as the 1970s [54]. These systems consisted of a lithium containing salt dissolved into a polymer matrix, these so called "salt complexes" are classified as a "dry polymer" electrolyte, which will be discussed further in the solid electrolyte (section 1.7.5). The inherent issue with dry polymer electrolytes is the very low room temperature ionic conductivity. This led to investigating methods to enhance ionic conductivities. As early as 1974 gel polymer electrolytes (GPE) have been investigated [55]. GPEs consist of a host polymer, swollen with liquid electrolytes, typically carbonate based, to form a gel. The liquid electrolyte acts as a plasticizer within the

polymer matrix, effectively suppressing crystallinity of the host polymer, thus promoting ionic conductivities. As opposed to a dry polymer electrolyte, where a polymer host is used for both structural support and an ionically conducting matrix, a GPE largely uses a polymer host for structural scaffolding alone, however, some groups have reported a considerable contribution of the polymer network to ionic conductivity values [56] [57].

In addition to improved mechanical stability, GPEs exhibit many of the positive traits associated with liquid electrolytes: high ionic conductivity, strong stability characteristics vs both positive and negative electrodes and wide stability windows. It is for these reasons that GPEs were readily commercialised, with the first commercial cell being produced by Bellcore in the 1990s, consisting of a poly(vinylidene fluoride)-hexafluoropropylene (PVDF-HFP) host polymer, soaked with LiPF_6 in EC:DMC liquid electrolyte with a SiO_2 filler to enhance electrolyte uptake [58].

The introduction of GPEs to the commercialised market was a positive step towards flexible electronics design, the nature of GPEs allows for “lithium-polymer” batteries to be formed into a desired shape, enabling differently shaped cells to be used and allowing for any available space in a product design to be utilised. However, due to a lack of difference in the fundamental chemistry when compared to standard liquid electrolytes, many of the negative attributes associated with them remain: Poor thermal stability, no dendritic suppression, flammability and poor high voltage stability [53] [58].

However, due to the obvious strengths exhibited by GPEs they are still widely available in the commercial market and are still heavily researched with many groups researching GPEs in combination with not only carbonate based liquid electrolytes, but also other chemistries such as the aforementioned ionic-liquids [59] [60] [61].

1.7.5 Solid Electrolytes

Another approach to Li-ion electrolytes is that of the all-solid-state electrolyte. Solid state electrolytes hold many advantages over their liquid and gel counterparts. Namely, no chance of leaking, greatly improved thermal stability, strong stability window characteristics, non-combustible, less restrictive battery formation, dendritic

suppression and excellent mechanical properties [62] [63]. However, not all solid electrolytes exhibit all of these characteristics at once. Solid electrolytes come in multiple forms, typically categorised as: glass, ceramic and polymeric. Each has their advantages and disadvantages:

1. Glass and glassy ceramic materials have no long range periodic ordering, this open structure is ideal when considering ionic conductivity as ions can move more freely due to multiple “defects” – sometimes purposefully engineered to create structural disorder. In addition, glass electrolytes can be absent of grain boundaries, which reduces internal resistance and can suppress inter-grain dendritic formation. However, the conductivities of many studied systems, such as $\text{Li}_2\text{PO}_2\text{N}$ (LIPON) are still far too low to be comparable to liquid electrolytes, or suffer from stability issues [64, 65, 66, 67]. However, it has been shown that upon crystallisation of some glass electrolytes such as $(\text{Li}_2\text{S})_5(\text{GeS}_2)(\text{P}_2\text{S}_5)$ conductivities can be increased due to a large drop in ion mobility activation energies E_A [68].
2. Crystalline ceramic materials have been studied extensively as potential candidates for replacing liquid electrolytes. Ceramic electrolytes exhibit wide electrochemical windows ($\geq 5.5\text{V}$) and are thermally stable at temperatures in excess of 300°C [69, 70, 71].

Structures with multiple defects such as Sodium Super Ionic Conductor-type (NASICON) as LATP which follows the structure template: $A_xB_y(\text{PO}_4)_3$ where A is an alkali metal ion (Li, Na) and B is a multivalent metal ion (Ti, Fe) [72]. Lithium Super Ionic Conductor-type (LISICON), such as Li_4SiO_4 , where doping through cationic substitution is used, such that Si^{4+} ions are substituted with Al^{3+} ions, creating larger tetrahedra and organised structure defects, allowing Li^+ ions to sit interstitially which, in turn, promotes greater interstitial ionic movement. Changing from locally oscillating Li^+ ions to interstitially hopping Li^+ ions and even enabling “superionic flow”, hence, increasing ionic conductivity [73]. Garnet-type materials such as $\text{Li}_7\text{La}_3\text{Zr}_2\text{O}_{12}$ (LLZO) are highly stable vs lithium and can accommodate excess Li^+ giving it potential as a solid electrolyte [74] and Perovskites e.g. lanthanum titanate (LLTO), show high bulk ionic

conductivity allowing for high lithium diffusion within the system [75]. However, due to very low grain boundary conductivity of LLTO its use as a solid electrolyte has been hindered [76].

In fact, grain boundaries and electrolyte:electrode contact is often an issue with crystalline ceramic electrolytes. If there is no ionic connection between the electrode material and the electrolyte then the capacity cannot be harnessed or if the conductivity between materials is low, then the cycle rate performance drops dramatically, restricting its use as an electrolyte. To improve the contact issues, many methods have been attempted, sintering is sometimes used to ensure a connected interface [77, 78]. However, this can affect the active materials themselves, creating new phases at the interfaces, changing its structure or chemical composition [79]. In addition, ceramic electrolytes may limit the thickness of the active material layer as the solid electrolyte does not percolate into the material as a liquid electrolyte would, thus reducing potential energy density. To try and remedy this, ceramic electrolyte coatings have been applied to electrode materials during synthesis [80] or ALD has been used for thin uniform coatings [81]. Whilst these methods can improve the performance of the electrolytes dramatically and increase both ionic conductivity and interfacial contact, they can also reduce electronic conductivity within the cast electrodes, thus increasing cell impedance [82]. Ceramic electrolytes can also be brittle, making them more suited to flat, thin film batteries [36].

Due to these issues, processing costs associated with ceramic electrolytes' synthesis, deposition and high temperature post deposition treatments can be high. Ceramic electrolytes show great promise as an alternative to liquid electrolytes, however, fundamental issues need resolving to fully realise their potential.

3. Solid Polymer Electrolytes (SPE) resolve many of the issues associated with ceramic electrolytes, whilst retaining many of their positive attributes. SPEs can be synthesised as free standing, flexible and stretchable films [83] [84]. They can exhibit broad temperature stability windows and wide electrochemical stability windows [85] [86]. They can be synthesised using quick, simplified and

cost-effective processing techniques such as solution casting and UV curing [87] [88]. However, SPEs have been plagued by low room temperature ionic conductivities.

As previously mentioned, polymer-salt complexes were investigated in the 1970s where Fenton et al. found that polyethylene oxide (PEO) complexed with a lithium salt became ionically conductive [54]. However, it was not until 1979 that the first battery using a solid polymer electrolyte was made [89]. PEO and PEO-based electrolytes are still among the most actively researched SPEs today, owing to its high ionic conductivities (compared to other polymer host alternatives). However, conductivities of single polymer-salt complexes fall far short of the conductivities necessary to achieve a viable solid-state battery without further improvements. It has been suggested that the low room temperature conductivities stem from the rigid structure of the highly crystalline nature of the PEO polymer indicating that ionic conductivity takes place in the amorphous regions of a SPE [90] [91].

Since then a multitude of methods have been proposed in an effort to raise SPEs ionic conductivity, namely, suppressing polymer chain crystallinity via: cross-linking, co-polymerisation, the use of large anions and plasticisation, or a combination thereof [92] [93] [94] [95]. This has given rise to a range of highly stable, highly flexible and highly conductive, amorphous SPEs.

It has been shown that whilst a very simple and cost-effective process, solution casting can lead to unwanted side reactions upon cycling, due to residual solvent within a cell [96]. Hence, it is often considered beneficial to be able to process SPEs without the use of solvents, resulting in research based on solvent free processing techniques, e.g. hot-pressing, melt-compounding and UV curing [97] [98]. Of these techniques the simplest, most cost-effective method is UV curing. Not only does this technique allow for large area, roll-to-roll processing, but also ensures good interfacial contact between electrolyte and electrode.

SPEs show great promise as an alternative to standard liquid electrolytes. They surpass liquid electrolytes on many factors, the main factors being safety, processability, the possibility of 3D structural deposition and environmental impact. They are well suited

to printed electronics due to their liquid-solid transition, they are also suitable for wearable consumer electronics due to their potential for bio-compatibility and even biodegradability [99] [100]. It is a combination of these reasons that this study focusses on poly(ethylene glycol) diacrylate (PEGDA) as the host polymer. It holds many of the previously mentioned characteristics and can be synthesised into a plasticised, crosslinked, solvent free and UV curable solid polymer electrolyte as an alternative to liquid electrolytes.

1.8 The Anode

Another essential component in the Li-ion battery, the anode is the negative electrode in a Li-ion battery. Like the cathode, there is a wide variety of available materials being researched, but unlike the cathode, where multiple different materials have been successfully commercialised, the anode almost exclusively consists of graphite or other carbon based materials. However, as shown in Figure 1.11, there are many options when it comes to anode materials; the reason for minimal commercialisation of alternative chemistries is discussed here.

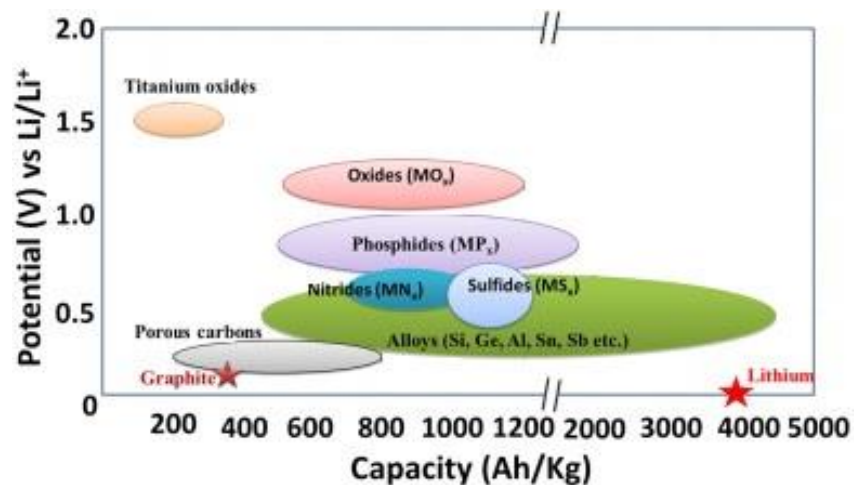


Figure 1.11: A diagram indicating various anode chemistries and their respective gravimetric capacities and operating potentials (adapted with permission [186])

As battery technologies advance, new anode materials which are tailored to more specific applications are required. This may not necessarily mean anodes with higher energy densities or larger capacities. For example, applications such as integrated battery-antenna systems or printed electronics often require batteries with specific

voltages, processability options and safety characteristics, whilst batteries for electric vehicles (EV) need larger capacities or higher operating voltages. Research on anode materials has focused on three main technologies: intercalation, alloying and conversion anodes. Figure 1.12 shows a schematic of the typical process associated with each of these anode types.

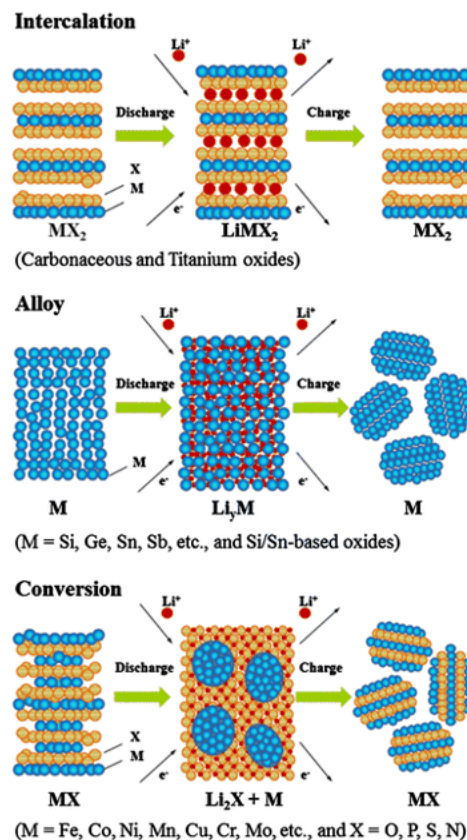


Figure 1.12: A schematic diagram of the reaction processes of the main types of anode materials (reprinted with permission [184])

1.8.1 Intercalation Anodes

Intercalation anodes are materials that allow Li^+ ions into and out of their structures by electrochemically intercalating into a space between its layered structure. Graphite is the best known of all intercalation anodes. The material has a relatively high theoretical capacity (when compared to cathode materials) of 372mAhg^{-1} , and achieves between $330\text{-}360\text{mAhg}^{-1}$ experimentally. However, graphite exhibits poor stability characteristics upon cycling in certain electrolytes due to a previously mentioned exfoliation process, which removes graphene layers from the anode,

resulting in irreversible capacity fading. As mentioned in section 1.5.1, this is addressed by the use of electrolytes which are specifically tailored to decompose and form a stable SEI on the graphite surface during the initial cycle. Whilst this generates an irreversible capacity loss, the graphite is then stabilised for future cycling. The intercalation of Li^+ ions is a highly reversible process allowing for long cycle life. Other advantages of graphite include a low reaction potential of $<0.25\text{V}$ vs Li/Li^+ and high intrinsic conductivities, which enables relatively high-power batteries. However, the low reaction potential of graphite can also be considered a disadvantage, as it can promote dendritic formation, therefore giving rise to safety issues and shortening battery life [101].

Another well-known and commercialised group of intercalation anode materials are titanium oxides, namely $\text{Li}_4\text{Ti}_5\text{O}_{12}$ (LTO). Whilst LTO has a relatively low theoretical capacity (175mAhg^{-1}) it exhibits excellent safety characteristics, owing to its high operating voltage ($\approx 1.55\text{V}$), which ensures no dendrite formation. The operating voltage is above the decomposition voltages of carbonate electrolytes. It is also regarded as a “zero strain” material due to its very low volume expansion upon lithiation [102] [103] [104] [105]. In addition, LTO is composed of inexpensive materials with a low environmental impact.

Due to its low capacity, high operating potential and low electronic conductivities, LTO has limited use in applications where high or high power is required. However, due to the aforementioned safety characteristics and very flat reaction plateau. Instead, it is very well suited to applications in integrated electronics and antenna systems, as many chips used in such electronics often have an activation voltage $\approx 1.2\text{-}1.8\text{V}$ and a pairing of LTO and LFP produces a battery with very flat voltage plateaus of 1.9V . This study utilises this combination of electrodes for stable cycling with the SPE.

1.8.2 Alloying Anodes

In alloying anode materials, lithium is inserted into the materials structure by creating a Li-M alloy ($\text{M} = \text{Si}, \text{Sn}, \text{Ge}, \text{Al}, \text{Sb}$ etc.). This reversible alloying can yield a very high capacity (4200mAhg^{-1} in the case of Si [106]) which is a very attractive attribute for an anode material. It is for this reason, along with the drive for highly energy dense

batteries from the electric vehicle (EV) sector, that a lot of research on alloying anodes has been undertaken.

In addition to high capacities, many alloying anodes exhibit low reaction potentials (≈ 0.4 vs Li/Li^+ for Si [107]) and abundant materials with a low environmental impact (Si, Al). However, along with these positive attributes there are some fundamental flaws with alloying-type anodes. Volume expansion is the major flaw, upon lithium insertion, alloying anodes exhibit large volume changes (300-400% in the case of Si) [108] [109]. This volume change not only requires unique cell design to cope with the expansion, but it also leads to structural degradation of the anode material itself, breaking up the material (pulverisation) depicted in Figure 1.12, this eventually leads to a breakdown of the electronic contact in the electrode and a large irreversible capacity loss within the cell and thus, reduces cycle life [110]. In addition, the volume expansion inhibits stable SEI formation, as Si expands, any formed SEI cracks and is broken down, therefore initiating more SEI formation, further degrading the electrolyte [111].

To remedy these issues, a large variety of methods have been employed, focusing on areas such as graphene incorporation, composites, particle size, morphology and encapsulation [112] [113] [114] [115] [116]. Whilst these methods have seen vast improvements in cyclability and reversible capacities, alloying anodes still require further research and development before becoming viable for large scale commercialisation. Due to the large volume expansion, alloy compounds are currently unsuitable for integrated electronics applications.

1.8.3 Conversion Anodes

Conversion anodes, are anode materials which undergo a conversion reaction upon lithiation. Following the general formula:



Where M is a transition metal (Fe,Co,Cu etc.) and X is an anion (O,N,F,S,P) [117]. As indicated in this equation, upon lithiation, lithium combines with the anion whilst the transition metal is reduced down to its metallic state. Theoretical capacities of

conversion-based anodes range from 350mAhg^{-1} to 1800mAhg^{-1} , making them an enticing prospect for anode materials [118].

Another potential benefit of conversion anodes is that their operating voltages are highly tailorable by careful selection of materials used due to their broad reaction voltage windows ranging from $\approx 1.3\text{V}$ to $< 0.5\text{V}$. In addition, environmentally friendly, low cost, non-toxic and abundant materials are available such iron oxides. Similarly to alloying anodes, conversion anodes suffer from volume expansions and effective pulverisation (Figure 1.12), this occurs as the transition metal is reduced to its metallic state, effectively reducing particle sizes to the nanometre scale, which then fail to fully reversibly react upon de-lithiation. This leads to a large voltage hysteresis stemming from poor kinetics, poor recovery of the segregated transition-metal+anion back to the original compound leads to capacity loss, poor coulombic efficiencies and poor cyclability [119].

Similarly to alloying anodes, many approaches have been employed to resolve these issues. Nano-sizing, and other morphological adjustments to reduce lithium and electron pathways, whilst also reducing the strains associated with the conversion reactions [120]. Carbon coating and graphene networks were introduced in an attempt to improve the conductive network, promoting faster, more reversible reactions [121] [122]. Encapsulation, to better cope with volume expansions and control pulverisation [123] [124]. These methods show promise in improving conversion anodes performance, but these anodes need further investigation before a larger introduction into the rechargeable Li-ion battery market. A Sn based composite has been commercialised by Sony, though cycle life was poor [125]. It should be noted that some of these chemistries have been commercialised as primary batteries [126].

1.8.4 Another Approach – Polymeric Anodes

Thus far, the three main anode types have been introduced, their advantages and disadvantages discussed, and no single technology was found to hold all desirable attributes for the next generation of Li-ion batteries. In addition to the three commonly presented solutions, there is another proposed anode technology which shows promise: polymeric anodes.

These organic anode materials come in many forms and have been widely researched for use in various energy storage technologies [127] [128]. Organic polymers as Li-ion battery electrodes is an attractive concept, showing benefits from environmental benignity, to low-cost energy storage and many polymers are processable without the use of harmful solvents, instead, using aqueous solvents [129] [130]. Organic polymers have been explored as both anode and cathode materials due to their well-known redox characteristics [131] [132] [133].

Polymer anodes performances vary dramatically, with capacities ranging from 2mAh^{-1} to capacities in excess of 1000mAhg^{-1} [134] [135]. Polymer electrodes show highly stable characteristics vs electrolytes and highly reversible reactions with good coulombic efficiencies [136] [137] [138]. In addition to the aforementioned benefits of using organic polymers as electrode materials, polymers give rise to a multitude of possibilities in terms of battery design, integrated electronics and wearable technologies.

Polymers can exhibit strong adhesion properties, allowing the use of polymer electrodes without additional binder, increasing energy density. Polymers can also be mixed conductors, that is to say, they are both electronically and ionically conducting [139] [140]. This attribute is a huge benefit in electrode materials, as it reduces or removes the need for conductive additives (such as carbon black) which, in turn, further increases energy density, in fact, some conducting polymers have been used as an alternative to carbon black and binder combination in electrode preparation in Li-ion batteries due to their high conductivities and electrochemical stabilities, offering protection to electrode materials from unstable SEI formation [138] [141] [142].

Aside from these attributes, conducting polymers hold potential for less restrictive cell design than their inorganic counterparts. Polymers are well-known for their film-forming ability, this, in combination with their electronically conducting nature, paves the way towards metal-free cell design. Electrically conductive, free-standing polymer sheets, which may also act as active material in a Li-ion cell would remove the need for metallic current collectors; not only does this have uses in defence/security applications (energy storage devices invisible to scanning devices) but also allows for

1.9 Additive Manufacturing

A major part of this project is focussed on the manufacturing and engineering side of batteries and integrated electronics. From deposition techniques and processability, to battery architecture and product design. Here a brief overview of both current and novel techniques and applications are presented.

1.9.1 Deposition Techniques

There are many methods that have been employed to deposit electrode materials onto their respective current collectors. Methods include: tape casting (doctor blade), screen printing, spray coating, ink-jet printing, chemical vapour deposition (CVD), atomic layer deposition (ALD), pulsed laser deposition (PLD) and magnetron sputtering. Each technique has its advantages and disadvantages which makes them better suited to various applications.

1.9.1.1 Chemical Vapour Deposition (CVD)

Chemical vapour deposition (CVD) is a technique involving material deposition from a chemical reaction of one or more volatile precursors onto a substrate, with deposition controlled. Reactions in CVD are most commonly thermally driven, requiring elevated temperatures in excess of 600°C [145]. This technique provides highly uniform films over large areas. This technique can also be used to deposit on 3D architectures, allowing for use in non-uniformly shaped cell designs. However, due to the high temperature requirements and equipment, this technique is costly. In addition, layer thicknesses are relatively low, being in the nanometre range. These attributes suggest that CVD may not be suitable for large scale battery production, instead being more suited to niche products, or microbatteries [146]. In addition, CVD has been widely studied for protective layer deposition, or a surface modification technique, for example, carbon coating [147] [148] [149].

1.9.1.2 Atomic Layer Deposition (ALD)

Atomic layer deposition (ALD) technique is closely related to CVD, however, ALD separates precursors so no gas-phase reactions take place. ALD is a self-terminating technique, that is to say, reactions occur between gaseous precursors and surface groups, once all surface groups have reacted the deposition process stops, a second

material can then be deposited allowing for very thin, to be deposited and stacked [150]. ALD allows for highly uniform, conformal films, allowing for potential use in non-standard battery architectures. Deposited layers are also pin-hole free and chemically bonded to the target substrate. This makes them particularly useful for protective coatings, such as, artificial SEI layers [151] [152]. Similarly to CVD, ALD layer thicknesses are in the nanometre range, which restricts their use in large scale battery production.

1.9.1.3 Pulsed Laser Deposition

Pulsed laser deposition (PLD) is a physical vapour deposition technique, which allows effective deposition of material onto a substrate. A high intensity, pulsed laser is fired at a target (consisting of the desired deposition material). The laser vaporises the target material, forming a “plasma plume” containing, among other components, the desired deposition material. The material is then deposited onto the substrate. This deposition is undertaken using controlled environments, using background gas atmospheres at various vacuum pressures, depending on the desired film composition. Figure 1.14 shows a schematic of the process.

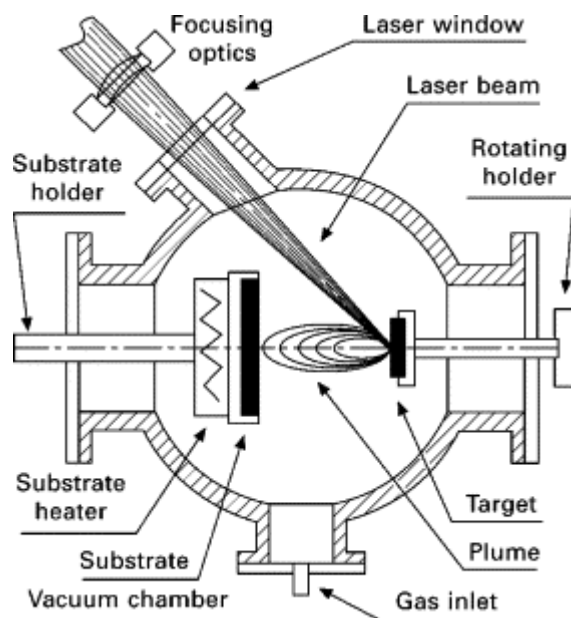


Figure 1.14: A schematic of a PLD apparatus (reprinted with permission [187])

PLD has been used to deposit a wide variety of battery materials, including anodes, cathodes and electrolytes, showing the potential for all-solid-state batteries deposited solely by PLD [153] [154] [155] [156] [157] [158]. Whilst PLD can be used for the

deposition of these battery components, its use is again limited, to niche, or small-scale cell builds due to the expensive set-up and running costs. Another limiting factor is that the deposition requires enclosed chambers for operation, making this process unsuitable for roll-to-roll processing.

1.9.1.4 Magnetron Sputtering

Sputtering is a process where materials (metals, polymer or ceramics) are deposited onto a substrate, using a high vacuum environment ejected atoms are condensed before deposition onto the target substrate. Magnetron sputtering further improves this system by the use of powerful magnets on the material source side, which traps electrons in magnetic fields, increasing the plasma density and confining it to near the target and decreasing damage caused to the deposited films. This results in uniform films that can be deposited much faster than a traditional sputtering process [159]. Figure 1.15 shows a schematic of the magnetron sputtering deposition technique.

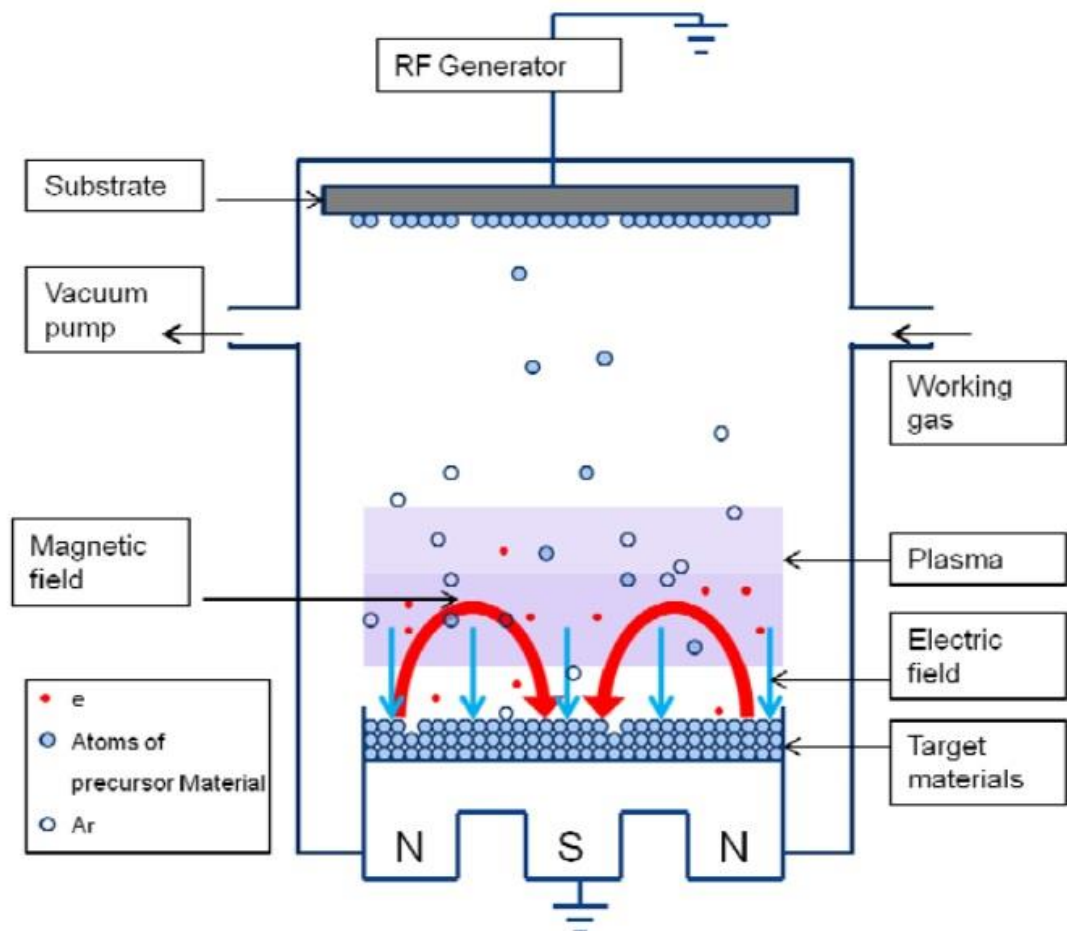


Figure 1.15: A schematic diagram of magnetron sputtering (reprinted with permission [158])

The magnetron sputtering technique is limited when compared to ALD and CVD in terms of conformity, being a technique that depends on line-of-sight deposition. Magnetron sputtering technique is also limited in terms of deposition speeds and film thicknesses when compared to other techniques [160]. Magnetron sputtering has been used to deposit a variety of electrode materials [161] [162] [163]. However, similarly to the other, aforementioned physical vapour deposition techniques, magnetron sputtering is better suited to niche applications for thin film and microbatteries [164] [165] [166].

1.9.1.5 Tape Casting (Doctor Blade)

Thus far, the deposition techniques mentioned, have all been used as novel, lab-scale battery material deposition techniques. More suited to thin-film and microbatteries, due to the inherent constraints of the techniques they are not well-suited to mass production or roll-to-roll processing. This, of course, is a necessity to keep up with the demand of modern technology; not only in terms of deposition speed, but also the volume of deposited material (the aforementioned techniques deposit films in the nanometre – a few micrometres scale).

This is where the tape casting (doctor blade) technique excels. It consists of a flat blade, set at a specific distance from the deposition substrate, with a deposition well filled with the slurry. Either the blade is pulled along the substrate depositing an even layer of the desired thickness onto the substrate, or in large scale production, the substrate is pulled past a fixed blade for the same effect. The wetted substrate is then pulled through a furnace to dry the film, evaporating any solvents, with the finished substrate rolled at the end of the production line. The films produced are uniform (to a micrometre scale), with thicknesses ranging from one or a few hundred μm . The technique does not restrict the types of materials which can be deposited; if a slurry can be made, it can be deposited with this technique.

Doctor blading is the most common technique used in major battery manufacturing due to its coating speed, adjustable deposition thicknesses and low cost of equipment. However, the doctor blade technique is somewhat limited in terms of cell design, due to the nature of the technique, material is constantly deposited in a continuous film

until material runs out of production is halted. This is ideal for mass production of standard cell designs (pouch cells or rolled cells) where long sheet electrodes are stacked, rolled or folded to produce regularly shaped (rectangular or cylindrical) cells. However, if an irregularly shaped cell is desired, or a cell for integrated electronics, doctor blading is unsuitable, shaped electrodes can be punched out of electrode sheets, producing large amounts of waste. Instead, other techniques with greater control may be desired.

1.9.1.6 Screen Printing

Screen printing is a widely used technique for printing on a variety of substrates. The technique uses a selective (patterned) mesh screen with ink on top and the deposition substrate underneath, a squeegee is then pulled across the screen, therefore depositing the ink onto the substrate in the pattern determined by the mask. Figure 1.16 depicts this process.

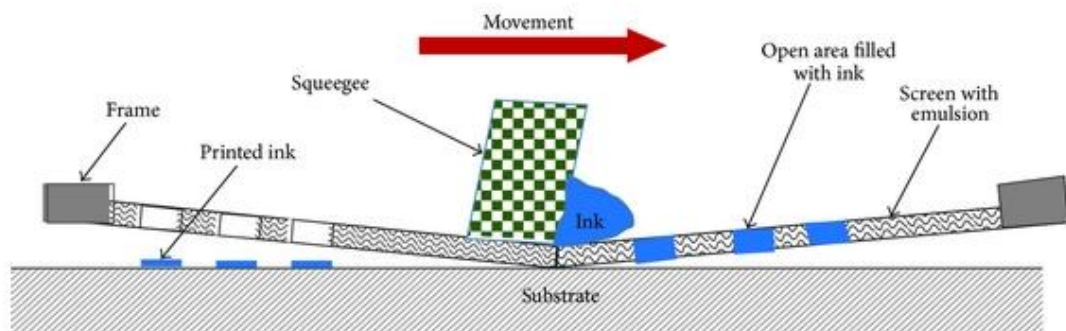


Figure 1.16: A schematic diagram of the screen-printing process (reprinted with permission [188])

The technique allows for printing of all material types, with thicknesses varying from 20-100 μm , sometimes more or less. Thickness is easily controlled by changing the thickness of the stencil and mesh sizes [167]. An adaptation of simple screen printing can also make the technique suitable for roll-to-roll printing. Limitations come in the form of design intricacies, restrictions on printed feature widths and the potential for material waste. Furthermore, with increasing mesh thickness, there is a reduction in print resolution. Lastly, this technique can be suitable for long print runs; but adjusting print designs requires new screens, which can make the process more costly than other alternatives if new designs are frequently required. Nonetheless, screen printing is a promising technology for affordable, design specific, Li-ion electrode deposition

with potential in integrated electronics. Many groups have investigated the technique for Li-ion batteries, with promising results [168] [169] [170].

1.9.1.7 Ink-Jet Printing

Ink-jet Printing is a highly controllable direct writing technique, commonly used in a variety of manufacturing industries. Ink-jet printing can be used to deposit material in a desired pattern with a high degree of precision, due to the ability of depositing minute quantities of material (pL per droplet) without the need of a mask or screen, instead opting for a CAD design patterning system [171]. This allows for immediate design changes without the additional costs and time constraints associated with ordering new masks or screens. There are two main types of ink-jet printing: continuous or drop-on-demand (depicted in Figure 1.17).

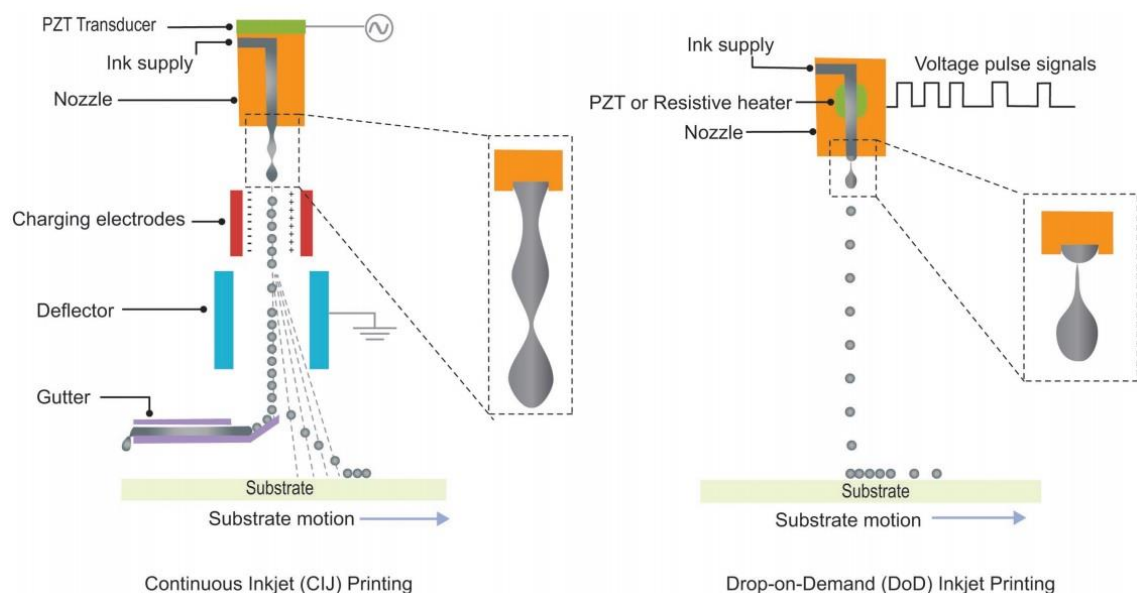


Figure 1.17: A schematic diagram showing continuous and drop on demand inkjet printing processes (reprinted with permission [189])

Ink-jet printing is sometimes referred to as a “zero-waste” manufacturing technique making ink-jet printing a cost effective and highly versatile technique. However, due to the very low volumes deposited, ink-jet printing often requires multiple passes to achieve the desired volume or thickness of film, this is a time consuming process slowing down production causing unwanted effects, such as, increasing film resistance and breaking up on electronic contact within the films. There are methods which can

be employed to mitigate this, for example, multi-nozzle printing or adjusting printer parameters allowing a greater material flow. In addition, other ink-jet restrictions include limitations on particle size and potential nozzle clogging during printing.

However, ink-jet printing allows its use to print highly intricate patterns onto a wide variety of rigid and flexible substrates whilst maintaining suitability for roll-to-roll manufacturing, making it a desirable technique for selective deposition manufacturing [172]. Whilst patterning is possible using ink-jet printing, the process is for use on planar surfaces and is not a conformable printing technique. Ink-jet printing is widely used in the printing of electronically conductive tracks, as well as various Li-ion electrode materials [173] [174]. This suggests promise for ink-jet printings' implementation in integrated battery products.

1.9.1.8 Spray Coating

Spray Coating is a versatile technique, widely used in industries, e.g. in the automotive industry for paint and protective layer applications. There are many types of spray coating which vary in complexity, equipment, cost and materials which can be deposited. Among the most cost effective, spraying methods include electrostatic and air-fed spraying methods. These techniques are suitable for large area coverage of both thin and thick film deposition, which can be tuned by varying ink composition, air pressures or applied voltages. The basic principles of spray coating involves the atomization of an ink via methods such as an electrostatic process or compressed carrier gas, the atomized droplets make impact onto the desired substrate, depositing a film [175].

Films produced via spray coating methods are often dense (low porosity) with relatively high surface roughness (though these can be mitigated) due to the high velocity of particle deposition. This technique is heavily susceptible to surface tension properties due to the potentially large droplet size and volume of material deposited in one sweep (as opposed to Ink-Jet Printing where volumes are much lower, therefore, less susceptible).

Other advantages of the spray coating technique include high flexibility afforded to ink formulation which allows the technique to be used to deposit a wide array of materials

including metals, ceramics and polymers. In addition, unlike the aforementioned techniques capable of depositing large scale, roll-to-roll, high volume films (doctor blade, screen printing and ink-jet printing) spray coating is a shape conformable technique, allowing coating on 3D architectures [176]. The techniques' deposition resolution is very poor; however, patterning can be achieved via the use of masking [177]. Spray coatings' main draw backs include high wastage (material is deposited on the masks not just on the desired substrates) and variations in film uniformity [175].

Nonetheless, the use of spray coating has been widely implemented in the deposition of various materials [178] [179], to the extent that full cells deposited solely by spray coating have been achieved [180].

Of all the mentioned deposition techniques, only doctor blading, screen printing, ink-jet printing and spray coating are suitable for efficient upscaling of Li-ion batteries. Due to equipment available, the doctor blading, ink-jet printing and spray coating techniques were further investigated for the deposition of polymer anode candidate PEDOT:PSS.

1.10 Summary

Based on this literature review, multiple areas were chosen for further exploration. Discussed in section 1.6, many issues were raised with current cathode technologies, ranging from environmental and monetary costs of using elements such as cobalt in cathodes to limited capacities exhibited by more environmentally friendly and cheaper alternatives such as LiMn_2O_4 and LiFePO_4 . With these considerations, $\text{Li}_2\text{FeSiO}_4$ was chosen for investigation in this study. Consisting of affordable, abundant and environmentally benign elements whilst also giving the potential for high theoretical capacities (330mAhg^{-1}), placing it as a prime candidate as a future cathode material.

Next in section 1.7 electrolytes were discussed, raising concerns with current technologies in terms of both safety and mechanical limitations. It was mentioned that electrolyte combustibility and leakage problems are improved with the use of solid-state electrolytes. In particular, polymer electrolytes are of interest due to their allowance for low temperature processability and liquid-to-solid transition, potentially leading to a "soaking effect" giving the ability to form a good electrode-electrolyte

interface before curing takes place. These are some of the reasons a PEGDA based electrolyte has been chosen for investigation in this study.

Anodes were discussed in section 1.8, the advantages and disadvantages of each technology were mentioned and an alternative technology was proposed: polymeric anodes. Bringing advantages such as environmental benignity and facile processability. In particular, mixed conducting polymers were mentioned due to their potential for additive free electrode films and even the potential for current collector free and less restrictive cell design. Of the potential candidates, PEDOT:PSS is considered in this study, due to its promising conductivity attributes, water processability and commercial availability in bulk. This is coupled with the manufacturing (deposition) techniques discussed in section 1.9 where two techniques are determined as promising alternatives to the commercially used doctor blade coating. These techniques are used in this study and directly compared for film forming and adhesion properties, as well as battery performance characteristics.

1.11 References

- [1] S.-H. Kim, K.-H. Choi, S.-J. Cho, S. Choi, S. Park and S.-Y. Lee, "Printable Solid-State Lithium-Ion Batteries: A New Route toward Shape-Conformable Power Sources with Aesthetic Versatility for Flexible Electronics," *Nano Letters*, vol. 15, pp. 5168 - 5177, 2015.
- [2] X. Chen, H. Huang, L. Pan, T. Liu and M. Niederberger, "Fully Integrated Design of a Stretchable Solid-State Lithium-Ion Full Battery," *Advanced Materials*, p. 1904648, 2019.
- [3] D. Wirthl, R. Pichler, M. Drack, G. Kettlguber, R. Moser, R. Gerstmayr, F. Hartmann, E. Bradt, R. Kaltseis, C. M. Siker, S. E. Schausberger, S. Hild, S. Bauer and M. Kaltenbrunner, "Instant tough bonding of hydrogels for soft machines and electronics," *Science Advances*, vol. 3, 2017.
- [4] G. Zhou, F. Li and H.-M. Cheng, "Progress in flexible lithium batteries and future prospects," *Energy & Environmental Science*, vol. 7, p. 1307, 2014.
- [5] J. A. Rogers, T. Someya and Y. Huang, "Materials and Mechanics for Stretchable Electronics," *Science*, vol. 327, no. 5973, pp. 1603 - 1607, 2010.
- [6] M. C. Caccami, M. P. Hogan, M. Alfredsson, G. Marrocco and J. C. Batchelor, "A Tightly Integrated Multilayer Battery Antenna for RFID Epidermal Applications," *IEEE*, vol. 66, no. 2, pp. 609 - 617, 2018.
- [7] X. Luo, J. Wang, M. Dooner and J. Clarke, "Overview of current development in electrical energy storage technologies and the application potential in power system operation," *Applied Energy*, vol. 137, pp. 511 - 536, 2015.
- [8] P. Keyser, "The Purpose of the Parthian Galvanic Cells: A First-Century A.D. Electric Battery Used for Analgesia," *Journal of Near Eastern Studies*, vol. 52, pp. 81-89, 1993.

- [9] P. Brenni, R. Galdi, F. Peitra and A. Savini, "From Volta onwards: a variety of electrical batteries in the Pavia Museum of Electrical Technology," in *in HISTory of ELeCtro-technology CONference (HISTELCON)*, 2012.
- [10] G. E. Blomgren, "The Development and Future of Lithium Ion Batteries," *JOURNAL OF THE ELECTROCHEMICAL SOCIETY*, vol. 164, no. 1, pp. 5019 - 5025, 2017.
- [11] J. Xie, J. Zhao, Y. Liu, H. Wang, C. Liu, T. Wu, P.-C. Hsu, D. Lin, Y. Jin and Y. Cui, "Engineering the surface of LiCoO₂ electrodes using atomic layer deposition for stable high-voltage lithium ion batteries," *Nano Research*, 2017.
- [12] J. Reimers and J. Dahn, "Electrochemical and In Situ X-Ray Diffraction Studies of Lithium Intercalation in Li_xCoO₂," *The Electrochemical Society*, vol. 139, no. 8, pp. 2091 - 2097, 1992.
- [13] X. Dai, A. Zhou, J. Xu, B. Yang, L. Wang and J. Li, "Superior electrochemical performance of LiCoO₂ electrodes enabled by conductive Al₂O₃-doped ZnO coating via magnetron sputtering," *Journal of Power Sources*, vol. 298, pp. 114 - 122, 2015.
- [14] M. Xie, T. Hu, L. Yang and Y. Zhou, "Synthesis of high-voltage (4.7 V) LiCoO₂ cathode materials with Al doping and conformal Al₂O₃ coating by atomic layer deposition," *RSC Advances*, vol. 6, no. 68, pp. 63250 - 63255, 2016.
- [15] Z. Jian, W. Wang, M. Wang, Y. Wang, N. AuYeung, M. Liu and Z. Feng, "Al₂O₃ coated LiCoO₂ as cathode for high-capacity and long-cycling Li-ion batteries," *Chinese Chemical Letters*, vol. 29, no. 12, pp. 1768 - 1772, 2018.
- [16] W. Chang, J.-W. Choi, J.-C. Im and J. K. Lee, "Effects of ZnO coating on electrochemical performance and thermal stability of LiCoO₂ as cathode material for lithium-ion batteries," *Journal of Power Sources*, vol. 195, no. 1, pp. 320 - 326, 2010.

- [17] X. Li, J. Liu, X. Meng, Y. Tang, M. N. Banis, J. Yang, R. Hu, M. Cai and X. Sun, "Significant impact on cathode performance of lithium-ion batteries by precisely controlled metal oxide nanocoatings via atomic layer deposition," *Journal of Power Sources*, vol. 247, pp. 57 - 69, 2014.
- [18] C. M. Julien and A. Mauger, "Functional behavior of AlF₃ coatings for high-performance cathode materials for lithium-ion batteries," *Materials Science*, vol. 6, no. 3, pp. 406 - 440, 2019.
- [19] B. Shen, P. Zuo, P. Fan, J. Yang, G. Yin, Y. Ma, X. Cheng, C. Du and Y. Gao, "Improved electrochemical performance of NaAlO₂-coated LiCoO₂ for lithium-ion batteries," *Journal of Solid State Electrochemistry*, vol. 21, no. 4, pp. 1195 - 1201, 2017.
- [20] L. Sun, Z. Zhang, X. Hu, H. Tian, Y. Zhang and X. Yang, "Realization of Ti Doping by Electrostatic Assembly to Improve the Stability of LiCoO₂ Cycled to 4.5 V," *Journal of the Electrochemical Society*, vol. 166, no. 10, pp. 1793 - 1798, 2019.
- [21] H. Xia, Z. Luo and J. Xie, "Nanostructured LiMn₂O₄ and their composites as high-performance cathodes for lithium-ion batteries," *Progress in Natural Science: Materials International*, vol. 22, no. 6, pp. 572 - 584, 2012.
- [22] M. Michalska, D. A. Ziolkowska, J. B. Jasinski, P. -H. Lee, P. Lawniczak, B. Andrzejewski, A. Ostrowski, W. Bednarski, S. -H. Wu and L. J. -Y, "Improved electrochemical performance of LiMn₂O₄ cathode material by Ce doping," *Electrochimica Acta*, vol. 276, pp. 37 - 46, 2018.
- [23] C. Zhang, X. Liu, Q. Su, J. Wu, T. Huang and Y. Aishui, "Enhancing Electrochemical Performance of LiMn₂O₄ Cathode Material at Elevated Temperature by Uniform Nanosized TiO₂ Coating," *ACS Sustainable Chemistry & Engineering*, vol. 5, no. 1, pp. 640 - 647, 2017.
- [24] N. Nitta, F. Wu, J. T. Lee and G. Yushin, "Li-ion battery materials: present and future," *Materials Today*, vol. 18, no. 5, pp. 252 - 264, 2015.

- [25] K. Saravanan, P. Balaya, M. V. Reddy, B. V. R. Chowdari and J. J. Vittal, "Morphology controlled synthesis of LiFePO₄/C nanoplates for Li-ion batteries," *Energy & Environmental Science*, vol. 3, no. 4, 2010.
- [26] S. Yang, X. Zhou, J. Zhang and Z. Liu, "Morphology-controlled solvothermal synthesis of LiFePO₄ as a cathode material for lithium-ion batteries," *Journal of Materials Chemistry*, vol. 20, no. 37, 2010.
- [27] Z. L. Gong and L. Y. Yang, "Synthesis and electrochemical performance of Li₂CoSiO₄ as cathode material for lithium ion batteries," *Journal of Power Sources*, vol. 174, no. 2, pp. 524 - 527, 2007.
- [28] Z. Zhang, Z. Chen, X. Zhang, D. Wu and J. Li, "P-doping Li₂CoSiO₄/C cathode material: A joint experimental and theoretical study," *Electrochimica Acta*, vol. 264, pp. 166 - 172, 2018.
- [29] R. Dominko, "Li₂MSiO₄ (M = Fe and/or Mn) cathode materials," *Journal of Power Sources*, vol. 184, no. 2, pp. 462 - 468, 2008.
- [30] Y. L. Gong, Y. X. Li and Y. Yang, "Synthesis and Characterization of Li₂MnxFe_{1-x}SiO₄ as a Cathode Material for Lithium-Ion Batteries," *Electrochemical and Solid-State Letters*, vol. 9, no. 12, pp. 542 - 544, 2006.
- [31] T. Muraliganth, K. R. Stroukoff and A. Manthiram, "Microwave-Solvothermal Synthesis of Nanostructured Li₂MSiO₄/C (M = Mn and Fe) Cathodes for Lithium-Ion Batteries," *Chemistry of Materials*, vol. 22, no. 20, pp. 5754 - 5761, 2010.
- [32] D. Lv, J. Bai, P. Zhang, S. Wu, Y. Li, W. Wen, Z. Jiang, J. Mi, Z. Zhu and Y. Yang, "Understanding the High Capacity of Li₂FeSiO₄: In Situ XRD/XANES Study Combined with First-Principles Calculations," *Chemistry of Materials*, vol. 25, no. 10, pp. 2014 - 2020, 2013.
- [33] H. Gao, Q. Wu, M. Guo, S. Yang, Y. Zhao and Y.-U. Kwon, "Rationally fabricating nitrogen-doped carbon coated nanocrystalline Li₂FeSiO₄@N-C with excellent Li-

- ion battery performances," *Electrochimica Acta*, vol. 318, pp. 720 - 729, 2019.
- [34] A. Nyten, A. Abouimrane, M. Armand, T. Gustafsson and J. O. Thomas, "Electrochemical performance of $\text{Li}_2\text{FeSiO}_4$ as a new Li-battery cathode material," *Electrochemistry Communications*, vol. 7, no. 2, pp. 156 - 160, 2005.
- [35] Z. Xu, J. Yang, H. Li, Y. Nuli and J. Wang, "Electrolytes for advanced lithium ion batteries using silicon-based anodes," *Journal of Materials Chemistry A*, vol. 7, 2019.
- [36] J. L. Schaefer, Y. Lu, S. S. Moganty, P. Agarwal, N. Jayaprakash and L. A. Archer, "Electrolytes for high-energy lithium batteries," *Applied Nanoscience*, vol. 2, no. 2, pp. 91 - 109, 2012.
- [37] H. Zhao, S.-J. Park, F. Shi, Y. Fu, V. Battaglia, P. N. Ross Jr and G. Liu, "Propylene Carbonate (PC)-Based Electrolytes with High Coulombic Efficiency for Lithium-Ion Batteries," *Journal of The Electrochemical Society*, vol. 161, no. 1, pp. 194 - 200, 2014.
- [38] S. J. An, J. Li, C. Daniel, D. Mohanty, S. Nagpure and D. L. Wood, "The state of understanding of the lithium-ion-battery graphite solid electrolyte interphase (SEI) and its relationship to formation cycling," *Carbon*, vol. 105, pp. 52 - 76, 2016.
- [39] W. Li, J. R. Dahn and D. S. Wainwright, "Rechargeable lithium batteries with aqueous electrolytes," *Science*, vol. 264, no. 5162, pp. 1115 - 1118, 1994.
- [40] J.-Y. Luo, W.-J. Cui, P. He and Y.-Y. Xia, "Raising the cycling stability of aqueous lithium-ion batteries by eliminating oxygen in the electrolyte," *Nature Chemistry*, vol. 2, pp. 760 - 765, 2010.
- [41] H. Kim, J. Hong, K.-Y. Park, H. Kim, S.-W. Kim and K. Kang, "Aqueous Rechargeable Li and Na Ion Batteries," *Chemical Reviews*, vol. 114, no. 23, pp. 11788 - 11827, 2014.

- [42] W. Tang, Y. Zhu, L. Liu, Y. Wu, K. P. Loh, H. Zhang and K. Zhu, "Aqueous rechargeable lithium batteries as an energy storage system of superfast charging," *Energy and Environmental Science*, vol. 6, no. 7, 2013.
- [43] L. Suo, O. Borodin, T. Gao, M. Olguin, J. Ho, X. Fan, C. Luo, C. Wang and K. Xu, "'Water-in-salt' electrolyte enables high-voltage aqueous lithium-ion chemistries," *Science*, vol. 350, no. 6263, pp. 938 - 943, 2015.
- [44] Y. Yamada, K. Usui, K. Sodeyama, S. Ko, Y. Tateyama and A. Yamada, "Hydrate-melt electrolytes for high-energy-density aqueous batteries," *Nature Energy*, vol. 1, 2016.
- [45] Z. Chang, C. Li, Y. Wang, B. Chen, L. Fu, Y. Zhu, L. Zhang, Y. Wu and W. Huang, "A lithium ion battery using an aqueous electrolyte solution," *Scientific Reports*, vol. 6, 2016.
- [46] C. Yang, J. Chen, T. Qing, X. Fan, W. Sun, A. v. Cresce, M. S. Ding, O. Borodin, J. Vatamanu, M. A. Schroeder, N. Edison, C. Wang and K. Xu, "4.0 V Aqueous Li-Ion Batteries," *Joule*, vol. 1, no. 1, pp. 122 - 132, 2017.
- [47] M. Holzapfel, C. Jost, A. Prodi-Schwab, F. Krumeich, A. Wursig, H. Buqa and P. Novak, "Stabilisation of lithiated graphite in an electrolyte based on ionic liquids: an electrochemical and scanning electron microscopy study," *Carbon*, vol. 43, pp. 1488 - 1498, 2005.
- [48] A. Farnicola, F. Croce, B. Scrosati, T. Watanabe and H. Ohno, "LiTFSI-BEPyTFSI as an improved ionic liquid electrolyte for rechargeable lithium batteries," *Journal of Power Sources*, vol. 174, no. 1, pp. 342 - 348, 2007.
- [49] T. Sato, T. Maruo, S. Marukane and K. Takagi, "Ionic liquids containing carbonate solvent as electrolytes for lithium ion cells," *Journal of Power Sources*, vol. 138, pp. 253 - 261, 2004.
- [50] E. Markevich, V. Baranchugov, G. Salitra, D. Aurbach and M. A. Schmidt,

- “Behavior of Graphite Electrodes in Solutions Based on Ionic Liquids in In Situ Raman Studies,” *Journal of the Electrochemical Society*, vol. 155, no. 2, pp. 132 - 137, 2008.
- [51] S. K. Martha, E. Markevich, V. Burgel, G. Salitra, E. Zinigrad, B. Markovsky, H. Sclar, Z. Pramovich, O. Heik, D. Aurbach, I. Exnar, H. Buqa, T. Drezen, G. Semrau, M. Schmidt, D. Kovacheva and N. Saliyski, “A short review on surface chemical aspects of Li batteries: A key for a good performance,” *Journal of Power Sources*, vol. 189, no. 1, pp. 288 - 296, 2009.
- [52] V. Borgel, E. Markevich, D. Aurbach, G. Semrau and M. Schmidt, “On the application of ionic liquids for rechargeable Li batteries: High voltage systems,” *Journal of Power Sources*, vol. 189, no. 1, pp. 331 - 336, 2009.
- [53] M. Marinek, J. Syzdek, M. Marczewski, M. Piszcz, L. Niedzicki, M. Kalita, A. Plewa-Marczewska, A. Bitner, P. Wieczorek, T. Trzeciak, M. Kasprzyk, P. Leziak, Z. Zukowska, A. Zalewska and W. Wieczorek, “Electrolytes for Li-ion transport,” *Solid State Ionics*, vol. 276, pp. 107 - 126, 2015.
- [54] D. E. Fenton, J. M. Parker and P. V. Wright, “COMPLEXES OF ALKALI-METAL IONS WITH POLY(ETHYLENE OXIDE),” *Polymer*, vol. 14, no. 11, p. 589, 1973.
- [55] G. Feuillade and P. Perche, “Ion-conductive macromolecular gels and membranes for solid lithium cells,” *Journal of Applied Electrochemistry*, vol. 5, no. 1, pp. 63 - 69, 1975.
- [56] L. T. Costa and M. C. C. Ribeiro, “Molecular dynamics simulation of polymer electrolytes based on poly(ethylene oxide) and ionic liquids. I. Structural properties,” *Journal of Chemical Physics*, vol. 124, no. 18, 2006.
- [57] W. Fan, N.-W. Li, X. Zhang, S. Zhao, R. Cao, Y. Yin, Y. Xing, J. Wang, Y.-G. Guo and C. Li, “A Dual-Salt Gel Polymer Electrolyte with 3D Cross-Linked Polymer Network for Dendrite-Free Lithium Metal Batteries,” *Advanced Science*, vol. 5, no. 9, 2018.

- [58] J.-M. Tarascon, A. S. Gozdz, C. Schmutz, F. Shokoohi and P. C. Warren, "Performance of Bellcore's plastic rechargeable Li-ion batteries," *Solid State Ionics*, Vols. 86 - 88, pp. 49 - 54, 1996.
- [59] X. Liu, Y. Ren, L. Zhang and S. Zhang, "Functional Ionic Liquid Modified Core-Shell Structured Fibrous Gel Polymer Electrolyte for Safe and Efficient Fast Charging Lithium-Ion Batteries," *Frontiers in Chemistry*, vol. 7, no. 421, 2019.
- [60] H. Porthault, G. Piana, M. Cesbron, V. Armel, A. Bazin, S. Franger and S. Oukassi, "Photo-Initiated Cross-Linking of a Methacrylate/Ionic Liquid Based Gel Polymer Electrolyte: Effect of the Curing Sequence on the Electrochemical Properties," *Journal of Physical Chemistry C*, vol. 123, pp. 18171 - 18179, 2019.
- [61] B. Rupp, M. Schmuck, A. Balducci, M. Winter and W. Kern, "Polymer electrolyte for lithium batteries based on photochemically crosslinked poly(ethylene oxide) and ionic liquid," *European Polymer Journal*, vol. 44, no. 9, pp. 2986 - 2990, 2008.
- [62] M. Motoyama, M. Ejiri and Y. Iriyama, "Modeling the Nucleation and Growth of Li at Metal Current Collector/LiPON Interfaces," *Journal of the Electrochemical Society*, vol. 162, no. 13, pp. 7067 - 7071, 2015.
- [63] Q. Li, J. Chen, L. Fan, X. Kong and Y. Lu, "Progress in electrolytes for rechargeable Li-based batteries and beyond," *Green Energy & Environment*, vol. 1, no. 1, pp. 18 - 42, 2016.
- [64] A. Varzi, R. Raccichini, S. Passerini and B. Scrosati, "Challenges and prospects of the role of solid electrolytes in the revitalization of lithium metal batteries," *Journal of Materials Chemistry A*, vol. 4, pp. 17251 - 17259, 2016.
- [65] B. V. Lotsch and J. Maier, "Relevance of solid electrolytes for lithium-based batteries: A realistic view," *Journal of Electroceramics*, vol. 38, no. 2-4, pp. 128 - 141, 2017.
- [66] "Ion Conduction in Superionic Glassy Electrolytes: An Overview," *Journal of*

Materials Science & Technology, vol. 29, no. 3, pp. 193 - 208, 2013.

- [67] L. L. Van-Jodin, A. Claudel, C. Secouard, F. Sabary, J.-P. Barnes and S. Martin, "Role of the chemical composition and structure on the electrical properties of a solid state electrolyte: Case of a highly conductive LiPON," *Electrochimica Acta*, vol. 259, pp. 742 - 751, 2018.
- [68] K. Mori, T. Kasai, K. Iwase, F. Fujisaki, Y. Onodera and T. Fukunaga, "Structural origin of massive improvement in Li-ion conductivity on transition from (Li₂S)₅(GeS₂)(P₂S₅) glass to Li₁₀GeP₂S₁₂ crystal," *Solid State Ionics*, vol. 301, pp. 163 - 169, 2017.
- [69] H. W. Kim, P. Manikandan, Y. J. Lim, J. H. Kim, S.-c. Nam and Y. Kim, "Hybrid solid electrolyte with the combination of Li₇La₃Zr₂O₁₂ ceramic and ionic liquid for high voltage pseudo-solid-state Li-ion batteries," *Journal of Materials Chemistry A*, vol. 43, 2016.
- [70] K. B. Dermenci, E. Cekic and S. Turan, "Al stabilized Li₇La₃Zr₂O₁₂ solid electrolytes for all-solid state Li-ion batteries," *International Journal of Hydrogen Energy*, vol. 41, no. 23, pp. 9860 - 9867, 2016.
- [71] X. Yu, J. Bates, G. Jellison and F. Hart, "A stable thin-film lithium electrolyte: lithium phosphorus oxynitride," *Journal of the Electrochemical Society*, vol. 144, no. 2, pp. 524 - 532, 1997.
- [72] H. Bai, J. Hu, Y. Duan, T. Kozawa, M. Naito, J. Zhang and S. Dong, "Surface modification of Li_{1.3}Al_{0.3}Ti_{1.7}(PO₄)₃ ceramic electrolyte by Al₂O₃-doped ZnO coating to enable dendrites-free all-solid-state lithium-metal batteries," *Ceramics International*, vol. 45, no. 12, pp. 14663 - 14668, 2019.
- [73] Y. Deng, C. Eames, B. Fleutot, R. David, J.-N. Chotard, E. Suard, C. Masquelier and M. S. Islam, "Enhancing the Lithium Ion Conductivity in Lithium Superionic Conductor (LISICON) Solid Electrolytes through a Mixed Polyanion Effect," *ACS Applied Material Interfaces*, vol. 9, no. 8, pp. 7050 - 7058, 2017.

- [74] S. Song, B. Chen, Y. Ruan, J. Sun, L. Yu, Y. Wang and J. Thokchom, "Gd-doped $\text{Li}_7\text{La}_3\text{Zr}_2\text{O}_{12}$ garnet-type solid electrolytes for all-solid-state Li-Ion batteries," *Electrochimica Acta*, vol. 270, pp. 501 - 508, 2018.
- [75] Y. Inaguma, C. Liqun, M. Itoh, T. Nakamura, T. Uchida, H. Ikuta and M. Wakihara, "High ionic conductivity in lithium lanthanum titanate," *Solid State Communications*, vol. 86, no. 10, pp. 689 - 693, 1993.
- [76] J.-F. Wu and X. Guo, "Origin of the low grain boundary conductivity in lithium ion conducting perovskites: $\text{Li}_3\text{xLa}_{0.67-x}\text{TiO}_3$," *Physical Chemistry Chemical Physics*, vol. 19, no. 8, 2017.
- [77] Y. Lai, Z. Sun, L. Jiang, X. Hao, M. Jia, L. Wang and F. Liu, "Rapid sintering of ceramic solid electrolytes $\text{LiZr}_2(\text{PO}_4)_3$ and $\text{Li}_{1.2}\text{Ca}_{0.1}\text{Zr}_{1.9}(\text{PO}_4)_3$ using a microwave sintering process at low temperatures," *Ceramics International*, vol. 45, no. 8, pp. 11068 - 11072, 2019.
- [78] "Three-Dimensional Bicontinuous Nanocomposite from a Self-Assembled Block Copolymer for a High-Capacity All-Solid-State Lithium Battery Cathode," *Chemistry of Materials*, vol. 28, pp. 4453 - 4459, 2016.
- [79] K. Nie, Y. Hong, J. Qui, Q. Li, X. Yu, H. Li and L. Chen, "Interfaces Between Cathode and Electrolyte in Solid State Lithium Batteries: Challenges and Perspectives," *Frontiers in Chemistry*, vol. 6, no. 616, 2018.
- [80] Q. Zhang, W. Jiang, Z. Zhou, S. Wang, X. Guo, S. Zhao and G. Ma, "Enhanced electrochemical performance of Li_4SiO_4 -coated LiFePO_4 prepared by sol-gel method and microwave heating," *Solid State Ionics*, vol. 218, pp. 31 - 34, 2012.
- [81] X. Han, Y. Gong, K. Fu, X. He, G. T. Hitz, J. Dai, A. Pearse, B. Liu, H. Wang, G. Rubloff, Y. Mo, V. Thangardurai, E. D. Wachsman and L. Hu, "Negating interfacial impedance in garnet-based solid-state Li metal batteries," *Nature Materials*, vol. 16, pp. 572 - 579, 2017.

- [82] X. Li, J. Liu, M. N. Banis, A. Lushington, R. Li, M. Cai and X. Sun, "Atomic layer deposition of solid-state electrolyte coated cathode materials with superior high-voltage cycling behavior for lithium ion battery application," *Energy & Environmental Science*, vol. 7, no. 2, 2014.
- [83] S. Berg, T. Kelly, I. Porat, B. Moradi-Ghadi and H. Ardebili, "Mechanical deformation effects on ion conduction in stretchable polymer electrolytes," *Applied Physics Letters*, vol. 113, 2018.
- [84] P. Lv, J. Yang, G. Liu, H. Liu, S. Li, C. Tang, J. Mei, Y. Li and D. Hui, "Flexible solid electrolyte based on UV cured polyurethane acrylate/succinonitrile-lithium salt composite compatibilized by tetrahydrofuran," *Composites Part B: Engineering*, vol. 120, pp. 35 - 41, 2017.
- [85] S. Chen, J. Wang, Z. Wei, Z. Zhang, Y. Deng, X. Yao and X. Xu, "One-pot synthesis of crosslinked polymer electrolyte beyond 5V oxidation potential for all-solid-state lithium battery," *Journal of Power Sources*, vol. 431, pp. 1 - 7, 2019.
- [86] C. Li, Y. Huang, X. Feng, Z. Zhang and P. Liu, "High electrochemical performance poly(ethylene oxide)/2,4-toluene diisocyanate/polyethylene glycol as electrolytes for all-solid-state lithium batteries," *Journal of Membrane Science*, vol. 587, 2019.
- [87] Z. Wang, S. Chen, Z. Huang, Z. Wei, L. Shen, H. Gu, X. Xu and X. Yao, "High conductivity polymer electrolyte with comb-like structure via a solvent-free UV-cured method for large-area ambient all-solid-state lithium batteries," *Journal of Materiomics*, vol. 5, no. 2, pp. 195 - 203, 2019.
- [88] M. Sasikumar, A. Jagadeesan, M. Raja, R. Hari Krishna and P. Sivakumar, "The effects of PVAc on surface morphological and electrochemical performance of P(VdF-HFP)-based blend solid polymer electrolytes for lithium ion-battery applications," *Ionics*, vol. 25, no. 5, pp. 2171 - 2181, 2019.
- [89] M. B. Armand, J. M. Chabagno and M. J. Dulcot, "Fast ion transport in solids:

electrodes and electrolytes," P. Vashista, J. N. Mundy and G. K. Shenroy, Eds., New York, United States: Elsevier North Holland, 1979, p. 131.

- [90] A. Arya and A. L. Sharma, "Insights into the use of polyethylene oxide in energy storage/conversion devices: a critical review," *Journal of Physics D: Applied Physics*, vol. 50, 2017.
- [91] W. H. Meyer, "Polymer Electrolytes for Lithium-Ion Batteries," *Advanced Materials*, vol. 10, no. 6, 1998.
- [92] J. F. Le Nest, S. Callens, A. Gandini and M. Armand, "A new polymer network for ionic conduction," *Electrochimica Acta*, vol. 37, no. 9, pp. 1585 - 1588, 1992.
- [93] R. Khurana, J. L. Schaefer, L. A. Archer and G. W. Coates, "Suppression of Lithium Dendrite Growth Using Cross-Linked Polyethylene/Poly(ethylene oxide) Electrolytes: A New Approach for Practical Lithium-Metal Polymer Batteries," *Journal of the American Chemical Society*, vol. 136, pp. 7395 - 7402, 2014.
- [94] H. Saxena, B. Bhattacharya, N. A. Jadhav, V. K. Singh, S. Shukla, M. Dubey and P. K. Singh, "Multiwall carbon-nanotube-doped ion conducting polymer electrolyte for electrochemical application," *Journal of Experimental Nanoscience*, vol. 9, no. 5, pp. 444 - 451, 2014.
- [95] Y.-T. Kim and E. S. Smotkin, "The effect of plasticizers on transport and electrochemical properties of PEO-based electrolytes for lithium rechargeable batteries," *Solid State Ionics*, vol. 149, pp. 29 - 37, 2002.
- [96] L. Liu, X. Qi, S. Yin, Q. Zhang, X. Liu, L. Suo, H. Li, L. Chen and Y.-S. Hu, "In Situ Formation of a Stable Interface in Solid-State Batteries," *American Chemical Society Energy Letters*, vol. 4, no. 7, pp. 1650 - 1657, 2019.
- [97] H. Graebe, A. Netz and A. Kwade, "A Solvent-Free Electrode Coating Technique for All Solid State Lithium Ion Batteries," in *Symposium on Plasma Nano Science and Technology held during the 231st Meeting of the Electrochemical-Society*

(ECS), New Orleans, 2017.

- [98] V. Gregorio, N. Garcia and P. Tiemblo, "Solvent-Free and Scalable Procedure to Prepare PYR13TFSI/LiTFSI/PVDF-HFP Thermoplastic Electrolytes with Controlled Phase Separation and Enhanced Li Ion Diffusion," *Membranes*, vol. 9, no. 50, 2019.
- [99] Y. Lin, Y. Cheng, J. Li, J. D. Miller, J. Liu and X. Wang, "Biocompatible and biodegradable solid polymer electrolytes for high voltage and high temperature lithium batteries," *RSC Advances*, vol. 7, no. 40, 2017.
- [100] E. Yulianti, Deswita, Sudaryanto and Mashadi, "Study of solid polymer electrolyte based on biodegradable polymer polycaprolactone," *Malaysian Journal of Fundamental and Applied Sciences*, vol. 15, no. 3, pp. 467 - 471, 2019.
- [101] Q. Zhang, C. Zhang, B. Li, D. Jiang, S. Kang, X. Li and Y. Wang, "Preparation and characterization of W-doped $\text{Li}_4\text{Ti}_5\text{O}_{12}$ anode material for enhancing the high rate performance," *Electrochimica Acta*, vol. 107, pp. 139 - 146, 2013.
- [102] J. Wang, Y. Li, X. Zhang, H. Deng, Y. Zhao, Q. Cheng, X. Gao, S. Tang and Y.-C. Cao, "Study on sucrose modification of anode material $\text{Li}_4\text{Ti}_5\text{O}_{12}$ for Lithium-ion batteries," *Results in Physics*, vol. 13, 2019.
- [103] P. A. Medina IV, H. Zheng, B. D. Fahlman, P. Annamalai, A. Swartbooi, L. Le Roux and M. K. Mathe, " $\text{Li}_4\text{Ti}_5\text{O}_{12}$ /graphene nanoribbons composite as anodes for lithium ion batteries," *Springer Plus*, vol. 4, no. 643, 2015.
- [104] T. P. Zhou, X. Y. Feng, X. Guo, W. W. Wu, S. Cheng and H. F. Xiang, "Solid-state synthesis and electrochemical performance of Ce-doped $\text{Li}_4\text{Ti}_5\text{O}_{12}$ anode materials for lithium-ion batteries," *Electrochimica Acta*, vol. 174, pp. 369 - 375, 2015.
- [105] B. Vikram Babu, K. Vijaya Babu, G. Tewodros Aregai, L. Seeta Devi, B. Madhavi

- Latha, M. Sushma Reddi, K. Samatha and V. Veeraiah, "Structural and electrical properties of Li₄Ti₅O₁₂ anode material for lithium-ion batteries," *Results in Physicas*, vol. 9, pp. 284 - 289, 2018.
- [106] W. Li, R. Yang, X. Wang, T. Wang, J. Zheng and X. Li, "Intercalated Si/C films as the anode for Li-ion batteries with near theoretical stable capacity prepared by dual plasma deposition," *Journal of Power Sources*, vol. 221, pp. 242 - 246, 2013.
- [107] D. Ma, Z. Cao and A. Hu, "Si-Based Anode Materials for Li-Ion Batteries: A Mini Review," *Nano-Micro Letters*, vol. 6, no. 4, pp. 347 - 358, 2014.
- [108] C.-Y. Chou, H. Kim and G. S. Hwang, "A Comparative First-Principles Study of the Structure, Energetics, and Properties of Li-M (M = Si, Ge, Sn) Alloys," *Journal of Physical Chemistry C*, vol. 115, no. 40, pp. 20018 - 20026, 2011.
- [109] Y. Jin, B. Zhu, Z. Lu, N. Liu and J. Zhu, "Challenges and Recent Progress in the Development of Si Anodes for Lithium-Ion Battery," *Advanced Energy Materials*, vol. 7, no. 23, 2017.
- [110] J. Sakabe, N. Ohta, T. Ohnishi, K. Mitsuishi and K. Takada, "Porous amorphous silicon film anodes for high-capacity and stable all-solid-state lithium batteries," *Communications Chemistry*, vol. 1, 2018.
- [111] Y. Jin, B. Zhu, Z. Lu, N. Liu and J. Zhu, "Challenges and Recent Progress in the Development of Si Anodes for Lithium-Ion Battery," *Advanced Energy Materials*, vol. 7, 2017.
- [112] X. Liu, X. Zhu and D. Pan, "Solutions for the problems of silicon-carbon anode materials for lithium-ion batteries," *Royal Society Open Science*, vol. 5, no. 6, 2018.
- [113] J. R. Szczech and S. Jin, "Nanostructured silicon for high capacity lithium battery anodes," *Energy & Environmental Science*, vol. 4, no. 56, 2011.

- [114] C. Wu, X. Tong, Y. Ai, D.-S. Liu, P. Yu, J. Wu and Z. M. Wang, "A Review: Enhanced Anodes of Li/Na-Ion Batteries Based on Yolk-Shell Structured Nanomaterials," *Nano-Micro Letters*, vol. 10, no. 40, 2018.
- [115] N. Liu, H. Wu, M. T. McDowell, Y. Yao, C. Wang and Y. Cui, "A Yolk-Shell Design for Stabilized and Scalable Li-Ion Battery Alloy Anodes," *Nano Letters*, vol. 12, no. 6, pp. 3315 - 3321, 2012.
- [116] M.-H. Park, M. G. Kim, J. Joo, K. Kim, J. Kim, S. Ahn, Y. Cui and J. Cho, "Silicon Nanotube Battery Anodes," *Nano Letters*, vol. 9, no. 11, pp. 3844 - 3847, 2009.
- [117] E. K. Heidari, A. Kamyabi-Gol, M. H. Sohi and A. Ataie, "Electrode Materials for Lithium Ion Batteries: A Review," *Journal of Ultrafine Grained and Nanostructured Materials*, vol. 51, no. 1, pp. 1-12, 2018.
- [118] J. Cabana, L. Monconduit, D. Larcher and M. R. Palacin, "Beyond Intercalation-Based Li-Ion Batteries: The State of the Art and Challenges of Electrode Materials Reacting Through Conversion Reactions," *Advanced Energy Materials*, vol. 22, no. 35, 2010.
- [119] N. Nitta and G. Yushin, "High-Capacity Anode Materials for Lithium-Ion Batteries: Choice of Elements and Structures for Active Particles," *Particle & Particle Systems Characterization*, vol. 31, pp. 317 - 336, 2014.
- [120] N. Wu, Y. R. Shi, C. Ma, X. Zhang, J.-M. Zhou, Y. Wei, H. Liu, Y. Yan and H.-T. Liu, "High performance nano- α -Fe₂O₃ electrode materials synthesized by facile and green approaches for lithium-ion batteries," *Materials Letters*, vol. 238, pp. 155 - 158, 2019.
- [121] J. Wang, M. Gao, D. Wang, X. Li, Y. Dou, Y. Liu and H. Pan, "Chemical vapor deposition prepared bi-morphological carbon-coated Fe₃O₄ composites as anode materials for lithium-ion batteries," *Journal of Power Sources*, vol. 282, pp. 257 - 264, 2015.

- [122] J. Han, D. Kong, W. Lv, D.-M. Tang, D. Han, C. Zhang, D. Liu, Z. Xiao, X. Zhang, J. Xiao, X. He, F.-C. Hsia, C. Zhang, Y. Tao, D. Golberg, F. Kang, L. Zhi and Q.-H. Yang, "Caging tin oxide in three-dimensional graphene networks for superior volumetric lithium storage," *Nature Communications*, vol. 9, 2018.
- [123] B. Luo, T. Qiu, D. Ye, L. Wang and L. Zhi, "Tin nanoparticles encapsulated in graphene backboned carbonaceous foams as high-performance anodes for lithium-ion and sodium-ion storage," *Nano Energy*, vol. 22, pp. 232 - 240, 2016.
- [124] C. Li, A. Sarapulova, Z. Zhao, Q. Fu, V. Trouillet, A. Missiul, E. Welter and S. Dsoke, "Understanding the Lithium Storage Mechanism in Core-Shell Fe₂O₃@C Hollow Nanospheres Derived from Metal-Organic Frameworks: An In operando Synchrotron Radiation Diffraction and in operando X-ray Absorption Spectroscopy Study," *Chemistry of Materials*, vol. 31, no. 15, pp. 5633 - 5645, 2019.
- [125] D. Foster, J. Wolfenstine, J. Read and J. L. Allen, "Performance of Sony's Alloy Based Li-ion Battery," *Army Research Laboratory*, 2008.
- [126] P. J. Masset and R. A. Guidotti, "Thermal activated ("thermal") battery technology: Part IIIa: FeS₂ cathode material," *Journal of Power Sources*, vol. 177, no. 2, pp. 595 - 609, 2008.
- [127] J. Cao, F. Ding, H. Chen, H. Wang, W. Wang, Z. Chen and J. Xu, "A new redox-active conjugated polymer containing anthraquinone pendants as anode material for aqueous all-organic hybrid-flow battery," *Journal of Power Sources*, vol. 423, pp. 316 - 322, 2019.
- [128] B. Xu and J. Hou, "Solution-Processable Conjugated Polymers as Anode Interfacial Layer Materials for Organic Solar Cells," *Advanced Energy Materials*, vol. 8, no. 20, 2018.
- [129] K. Wijeratne, U. Ail, R. Brooke, M. Vagin, X. Liu, M. Fahlman and X. Crispin, "Bulk electronic transport impacts on electron transfer at conducting polymer

electrode–electrolyte interfaces,” *Proceedings of the National Academy of Sciences*, vol. 115, no. 47, pp. 11899 - 11904, 2018.

- [130] J. R. Reynolds, B. C. Thompson and T. A. Skotheim, *Conjugated Polymers: Properties, Processing and Applications*, CRC Press, 2019.
- [131] J. Xie, Z. Wang, Z. J. Xu and Q. Zhang, “Toward a High-Performance All-Plastic Full Battery with a Single Organic Polymer as Both Cathode and Anode,” *Advanced Energy Materials*, vol. 8, 2018.
- [132] J. Zhao, T. Kang, Y. Chu, P. Chen, F. Jin, F. Jin, Y. Shen and L. Chen, “A polyimide cathode with superior stability and rate capability for lithium-ion batteries,” *Nano Research*, vol. 12, no. 6, pp. 1355 - 1360, 2019.
- [133] R. L. Belanger, B. Commarieu, A. Paoletta, J.-C. Daigle, S. Bessette, A. Vijn, J. P. Claverie and K. Zaghib, “Diffusion Control of Organic Cathode Materials in Lithium Metal Battery,” *Scientific Reports*, vol. 9, 2019.
- [134] L. Yang, V.-A. Mihali, D. Brandell, M. Stromme and M. Sjodin, “Conjugated Pyridine-Based Polymers Characterized as Conductivity-Carrying Components in Anode Materials,” *Journal of Physical Chemistry C*, vol. 118, pp. 25956 - 25963, 2014.
- [135] S. Zhang, W. Huang, P. Hu, C. Huang, C. Shang, C. Zhang, R. Yang and G. Cui, “Conjugated microporous polymers with excellent electrochemical performance for lithium and sodium storage,” *Journal of Materials Chemistry A*, vol. 3, pp. 1896 - 1901, 2015.
- [136] H. Numazawa, K. Sato, H. Imai and Y. Oaki, “Multistage redox reactions of conductive-polymer nanostructures with lithium ions: potential for high-performance organic anodes,” *NPG Asia Materials*, vol. 10, pp. 397 - 405, 2018.
- [137] Z. Li, W. Zhong, A. Cheng, Z. Li, L. Li and H. Zhang, “Novel hyper-crosslinked polymer anode for lithium-ion batteries with highly reversible capacity and long

- cycling stability,” *Electrochimica Acta*, vol. 281, pp. 162 - 169, 2018.
- [138] J. Lee and W. Choi, “Surface Modification of Over-Lithiated Layered Oxides with PEDOT:PSS Conducting Polymer in Lithium-Ion Batteries,” *Journal of the Electrochemical Society*, vol. 162, no. 4, pp. 743 - 748, 2015.
- [139] A. Malti, J. Edberg, H. Granberg, Z. U. Khan, J. W. Andreason, X. Liu, D. Zhao, H. Zhang, Y. Yao, J. Brill, E. Isak, M. Fahlman, L. Wagberg, X. Crispin and M. Berggren, “An organic mixed ion–electron conductor for power electronics,” *Advanced Science*, vol. 3, 2016.
- [140] J. Rivnay, S. Inal, B. A. Collins, M. Sessolo, E. Stavrinidou, X. Strakosas, C. Tassone, D. M. DeLongchamp and G. G. Malliaras, “Structural control of mixed ionic and electronic transport in conducting polymers,” *Nature Communications*, vol. 7, 2016.
- [141] D. Bresser, D. Buchholz, A. Moretti, A. Varzi and S. Passerini, “Alternative binders for sustainable electrochemical energy storage – the transition to aqueous electrode processing and bio-derived polymers,” *Energy & Environmental Science*, vol. 11, 2018.
- [142] H. Wang, J. Lin and Z. X. Shen, “Polyaniline (PANi) based electrode materials for energy storage and conversion,” *Journal of Science: Advanced Materials and Devices*, vol. 1, no. 3, pp. 225 - 255, 2016.
- [143] F. Greco, A. Zucca, S. Taccola, A. Menciassi, T. Fujie, H. Haniuda, S. Takeoka, P. Dario and V. Mattoli, “Ultra-thin conductive free-standing PEDOT/PSS nanofilms,” *Soft Matter*, no. 22, 2011.
- [144] S. Ahmed, M. Rafat, M. K. Singh and S. A. Hashmi, “A free-standing, flexible PEDOT:PSS film and its nanocomposites with graphene nanoplatelets as electrodes for quasi-solid-state supercapacitors,” *Nanotechnology*, vol. 29, 2018.
- [145] X. Wang and G. Yushin, “Chemical vapor deposition and atomic layer deposition

- for advanced lithium ion batteries and supercapacitors," *Energy & Environmental Science*, vol. 8, pp. 1889 - 1904, 2015.
- [146] C. Chen, R. A. Eichel and P. H. L. Notten, "Metal-organic chemical vapor deposition enabling all-solid-state Li-ion microbatteries: A short review," *Journal of Electroceramics*, vol. 38, no. 2-4, pp. 230 - 247, 2017.
- [147] I. H. Son, J. H. Park and J. Mun, "Surface modification of over-lithiated layered oxide by low-temperature chemical vapor deposition for high energy lithium-ion batteries," *Energy Storage Materials*, vol. 4, pp. 137 - 144, 2016.
- [148] C. Li, H. P. Zhang, L. J. Fu, H. Liu, Y. P. Wu, E. Rahm, R. Holze and H. Q. Wu, "Cathode materials modified by surface coating for lithium ion batteries," *Electrochimica Acta*, vol. 51, no. 19, pp. 3872 - 3883, 2006.
- [149] H. Omanda, T. Brousse, C. Marhic and D. M. Schleich, "Improvement of the thermal stability of LiNi_{0.8}Co_{0.2}O₂ cathode by SiO_x particle coating," *Journal of the Electrochemical Society*, vol. 151, no. 6, pp. 922 - 929, 2004.
- [150] M. Mantymaki, M. Ritala and M. Leskela, "Metal Fluorides as Lithium-Ion Battery Materials: An Atomic Layer Deposition Perspective," *Coatings*, vol. 8, no. 277, 2018.
- [151] L. A. Riley, S. V. Atta, A. S. Cavanagh, Y. Yan, S. M. George, P. Liu, A. C. Dillon and S.-H. Lee, "Electrochemical effects of ALD surface modification on combustion synthesized LiNi_{1/3}Mn_{1/3}Co_{1/3}O₂ as a layered-cathode material," *Journal of Power Sources*, vol. 196, pp. 3317 - 3324, 2011.
- [152] H.-Y. Wang and F.-M. Wang, "Electrochemical investigation of an artificial solid electrolyte interface for improving the cycle-ability of lithium ion batteries using an atomic layer deposition on a graphite electrode," *Journal of Power Sources*, vol. 233, pp. 1 - 5, 2013.
- [153] W. C. West, Z. D. Hood, S. P. Adhikari, C. Liang, A. Lachgar, M. Motoyama and Y.

- Iriyama, "Reduction of charge-transfer resistance at the solid electrolyte – electrode interface by pulsed laser deposition of films from a crystalline Li₂PO₂N source," *Journal of Power Source*, vol. 312, pp. 116 - 122, 2016.
- [154] S. Shiraki, H. Oki, Y. Takagi, T. Suzuki, A. Kumatani, R. Shimizu, M. Haruta, T. Ohsawa, Y. Sato, Y. Ikuhara and T. Hitosugi, "Fabrication of all-solid-state battery using epitaxial LiCoO₂ thin films," *Journal of Power Sources*, vol. 267, pp. 881 - 887, 2014.
- [155] X. Q. Yu, Y. He, J. P. Sun, K. Tang, H. Li, L. Q. Chen and X. J. Huang, "Nanocrystalline MnO thin film anode for lithium ion batteries with low overpotential," *Electrochemistry Communications*, vol. 11, no. 4, pp. 791 - 794, 2009.
- [156] A. Rambabu, B. Senthilkumar, A. Dayamani, S. B. Krupanidhi and P. Barpanda, "Preferentially oriented SrLi₂Ti₆O₁₄ thin film anode for Li-ion micro-batteries fabricated by pulsed laser deposition," *Electrochimica Acta*, vol. 269, pp. 212 - 216, 2018.
- [157] B. Yan, B. Song, P. Xiao and L. Lu, "Li-rich Thin Film Cathode Prepared by Pulsed Laser Deposition," *Scientific Reports*, vol. 3, 2013.
- [158] C. M. Julien and A. Mauger, "Pulsed Laser Deposited Films for Microbatteries," *Coatings*, vol. 9, no. 6, p. 386, 2019.
- [159] D. K. Maurya, A. Sardarinejad and K. Alameh, "Recent Developments in R.F. Magnetron Sputtered Thin Films for pH Sensing Applications—An Overview," *Coatings*, vol. 4, pp. 756 - 771, 2014.
- [160] R. Bosco, J. V. D. Beucken, S. Leeuwenburgh and J. Jansen, "Surface Engineering for Bone Implants: A Trend from Passive to Active Surfaces," *Coatings*, vol. 2, pp. 95 - 119, 2012.
- [161] V. A. Sugiawati, F. Vacandio, C. Perrin-Pellegrino, A. Galeyeva, A. P. Kurbatov and

- T. Djenizian, "Sputtered Porous Li-Fe-P-O Film Cathodes Prepared by Radio Frequency Sputtering for Li-ion Microbatteries," *Scientific Reports*, vol. 9, 2019.
- [162] M. V. Reddy, B. Pecquenard, P. Vinatier and A. Levasseur, "Effect of Substrate Temperature on Morphology and Electrochemical Performance of Radio Frequency Magnetron Sputtered Lithium Nickel Vanadate Films Used as Negative Electrodes for Lithium Microbatteries," *Journal of Physical Chemistry B*, vol. 110, no. 9, pp. 4301 - 4306, 2006.
- [163] X.-J. Zhu, L.-B. Cheng, C.-G. Wang, Z.-P. Guo, P. Zhang, G.-D. Du and H.-K. Liu, "Preparation and Characteristics of LiFePO₄ Thin Film by Radio Frequency Magnetron Sputtering for Lithium Microbatteries," *Journal of Physical Chemistry C*, vol. 132, no. 32, pp. 14518 - 14522, 2009.
- [164] E. Evshchik, D. Novikov, A. Levchenko, S. Nefedkin, A. V. Shikhovtseva, O. V. Bushkova and Y. A. Dobrovolski, "Magnetron Sputtering Silicon Thin Film Electrodes for Lithium-Ion Batteries," *International Journal of Electrochemical Science*, vol. 13, pp. 2860 - 2874, 2018.
- [165] C. L. Wang, Y. C. Liao, F. C. Hsu, N. H. Tai and M. K. Wua, "Preparation and characterization of thin film Li₄Ti₅O₁₂ electrodes by magnetron sputtering," *Journal of the Electrochemical Society*, vol. 152, no. 4, pp. 653 - 657, 2005.
- [166] H. Y. Park, S. R. Lee, Y. J. Lee, B. W. Cho and W. I. Cho, "Bias sputtering and characterization of LiCoO₂ thin film cathodes for thin film microbattery," *Materials Chemistry and Physics*, vol. 93, no. 1, pp. 70 - 78, 2005.
- [167] J. P. Matters, R. O. Kadara and C. E. Banks, "New directions in screen printed electroanalytical sensors: an overview of recent developments," *Analyst*, vol. 136, pp. 1067 - 1076, 2011.
- [168] R. E. Sousa, J. Oliveira, A. Goren, D. Miranda, M. M. Silva, L. Hilliou, C. M. Costa and S. Lanceros-Mendez, "High performance screen printable lithium-ion battery cathode ink based on C-LiFePO₄," *Electrochimica Acta*, vol. 196, pp. 92 - 100,

2016.

- [169] M. S. Park, S. H. Hyun and S. C. Nam, "Characterization of a LiCoO₂ thick film by screen-printing for a lithium ion micro-battery," *Journal of Power Sources*, vol. 159, pp. 1416 - 1421, 2006.
- [170] S. Ohta, S. Komagata, J. Seki, T. Saeki, S. Morishita and T. Asaoka, "All-solid-state lithium ion battery using garnet-type oxide and Li₃BO₃ solid electrolytes fabricated by screen-printing," *Journal of Power Sources*, vol. 238, pp. 53 - 56, 2013.
- [171] C. L. Cobb and C. C. Ho, "Additive Manufacturing: Rethinking Battery Design," *The Electrochemical Society Interface*, vol. 25, no. 1, pp. 75 - 78, 2016.
- [172] Z. Bao, J. A. Rogers and H. E. Katz, "Printable organic and polymeric semiconducting materials and devices," *Journal of Materials Chemistry*, vol. 9, pp. 1895 - 1904, 1999.
- [173] Y.-T. Kwon, Y.-I. Lee, S. Kim, K.-J. Lee and Y.-H. Choa, "Full densification of inkjet-printed copper conductive tracks on a flexible substrate utilizing a hydrogen plasma sintering," *Applied Surface Science*, vol. 396, pp. 1239 - 1244, 2017.
- [174] G. G. Rozenberg, E. Bresler, S. P. Speakman, C. Jeynes and J. H. G. Steinke, "Patterned low temperature copper-rich deposits using inkjet printing," *Applied Physics Letters*, vol. 81, pp. 5249 - 5251, 2002.
- [175] G. Barroso, Q. Li, R. K. Bordia and G. Motz, "Polymeric and ceramic silicon-based coatings – a review," *Journal of Materials Chemistry A*, vol. 7, pp. 1936 - 1963, 2019.
- [176] T. Carey, C. M. F. L. Jones, D. Deganello and F. Torrioni, "Spray-Coating Thin Films on Three-Dimensional Surfaces for a Semitransparent Capacitive-Touch Device," *ACS Applied Materials & Interfaces*, vol. 10, pp. 19948 - 19956, 2018.

- [177] K. S. Elassy, T. K. Akau, W. A. Shiroma, S. Seo and A. T. Ohta, "Low-Cost Rapid Fabrication of Conformal Liquid-Metal Patterns," *Applied Sciences*, vol. 9, p. 1565, 2019.
- [178] S. H. Lee, C. Huang and P. S. Grant, "Layer-by-layer printing of multi-layered heterostructures using Li₄Ti₅O₁₂ and Si for high power Li-ion storage," *Nano Energy*, vol. 61, pp. 96 - 103, 2019.
- [179] A. F. Leonard and N. Job, "Safe and green Li-ion batteries based on LiFePO₄ and Li₄Ti₅O₁₂ sprayed as aqueous slurries with xanthan gum as common binder," *Materials Today Energy*, vol. 12, pp. 168 - 178, 2019.
- [180] N. Singh, C. Galande, A. Miranda, A. Mathkar, W. Gao, A. L. M. Reddy, A. Vlad and P. M. Ajayan, "Paintable Battery," *Scientific Reports*, vol. 2, 2012.
- [181] J.-M. Tarascon and M. Armand, "Issues and challenges facing rechargeable lithium batteries," *Nature*, vol. 414, pp. 359 - 367, 2001.
- [182] C. M. Julien, A. Mauger, K. Zaghib and H. Groult, "Comparative Issues of Cathode Materials for Li-Ion Batteries," *Inorganics*, vol. 2, no. 1, pp. 132 - 154, 2014.
- [183] B. Xu, D. Qian, Z. Wang and Y. S. Meng, "Recent progress in cathode materials research for advanced lithium ion batteries," *Materials Science and Engineering: R: Reports*, vol. 73, no. 5-6, pp. 51 - 65, 2012.
- [184] D. Lv, W. Wen, X. Huang, J. Bai, J. Mi, S. Wu and Y. Yang, "A novel Li₂FeSiO₄/C composite: Synthesis, characterization and high storage capacity," *Journal of Materials Chemistry*, vol. 21, no. 26, pp. 9506 - 9512, 2011.
- [185] K. Xu, "Nonaqueous liquid electrolytes for lithium-based rechargeable batteries," *Chemical Reviews*, vol. 104, no. 10, 2004.
- [186] J. Lu, Z. Chen, F. Pan, Y. Cui and K. Amine, "High-Performance Anode Materials for Rechargeable Lithium-Ion Batteries," *Electrochemical Energy Reviews*, vol. 1,

no. 1, pp. 35 - 53, 2018.

- [187] P. V. Nikitin, S. Ramamurthy, R. Martinez and K. V. S. Rao, "Passive Tag-to-Tag Communication," *IEEE International Conference on RFID*, pp. 224 - 231, 2012.
- [188] S. Goriparti, E. Miele, F. De Angelis, E. Di Fabrizio, R. P. Zaccaria and C. Capiglia, "Review on recent progress of nanostructured anode materials for Li-ion batteries," *Journal of Power Sources*, vol. 257, pp. 421 - 443, 2014.
- [189] J. Pou, F. Lusquinos, R. Comesana and M. Boutinguiza, "14 - Production of biomaterial coatings by laser-assisted processes," in *Advances in Laser Materials Processing*, Woodhead Publishing, 2010, pp. 394 - 425.
- [190] S. Ahmadi, N. Asim, M. A. Alghoul, F. Y. Hammadi, K. Saeedfar, N. A. Ludin, S. H. Zaidi and K. Sopian, "The Role of Physical Techniques on the Preparation of Photoanodes for Dye Sensitized Solar Cells," *International Journal of Photoenergy*, vol. 2014, p. 19, 2014.
- [191] X. Peng, J. Yuan, S. Shen, M. Gao, A. S. R. Chesman, H. Yin, J. Cheng, Q. Zhang and D. Angmo, "Perovskite and Organic Solar Cells Fabricated by Inkjet Printing: Progress and Prospects," *Advanced Functional Materials*, vol. 27, p. 1703704, 2017.

2 Materials, Methods and Characterisation Techniques

2.1 $\text{Li}_2\text{FeSiO}_4$ Synthesis

2.1.1 Solid State Synthesis

Stoichiometric amounts of lithium carbonate (Li_2CO_3), silicon dioxide (SiO_2) and iron(II) oxalate dihydrate ($\text{FeC}_2\text{O}_4 \cdot 2\text{H}_2\text{O}$) (All purchased from Sigma Aldrich) were weighed out, Super P (Alpha Aesar) or sucrose (Sigma Aldrich) was also added as a carbon source, corresponding to 10-14% carbon in the end product, the mixture was ball milled under ethanol at 400rpm for 6hours then dried, pressed into a pellet and placed in a tube furnace under constant argon flux. The tube furnace was heated at a rate of $2^\circ\text{C}/\text{min}$ to 800°C , where it dwelled for 6 hours before cooling back to room temperature at a rate of $2^\circ\text{C}/\text{min}$. The resulting pellet was immediately transferred into an argon filled glovebox and ground lightly into a powder, where it remained until the point of use.

2.1.2 Sol-Gel Synthesis

This method was based on a sol-gel synthesis published by Brownrigg et.al. [1]. Stoichiometric amounts of lithium acetate dihydrate ($\text{CH}_3\text{COOLi} \cdot 2\text{H}_2\text{O}$) (Sigma Aldrich), Iron(II) acetate ($\text{Fe}(\text{CO}_2\text{CH}_3)_2$) (STREM) and tetraethyl orthosilicate (TEOS – $\text{Si}(\text{OC}_2\text{H}_5)_4$) (Sigma Aldrich) were mixed in ethanol with 1ml acetic acid (Sigma Aldrich). The suspension was placed in a Teflon lined autoclave and heated to 130°C for 12 hours. The resulting gel was dried at 80°C in an oven. The dried powder was mixed with sucrose, corresponding to a carbon content between 7-12%, and ball milled under acetone for 30 minutes. Once dried the powder was pressed into a pellet and placed in a tube furnace under constant argon or nitrogen flux. The furnace was heated to 600°C at a rate of $10^\circ\text{C}/\text{min}$, and held for 10 hours, then cooled to room temperature at the same rate. The resulting sample was immediately transferred into an argon filled glovebox where it remained until point of use.

It should be noted that whilst the Brownrigg paper suggests drying the gel in a vacuum oven, this, in combination with synthesis under an argon/nitrogen flux and the carbon content appeared to reduce the iron significantly to cause metallic iron impurities. Hence, the amount of carbon used was reduced in an attempt to inhibit its reductive

effects. However, this allowed for iron oxide impurities to occur in the material. The synthesis was attempted multiple times using a vacuum oven or a standard oven and varying the carbon content until a balance was found and impurities were minimised. The best results were found to be using a standard oven and a carbon content corresponding stoichiometrically, to 10 wt.% of the $\text{Li}_2\text{FeSiO}_4/\text{C}$ produced.

2.2 Cell Preparation

2.2.1 Electrode Preparation

Aside from PEDOT:PSS, all electrode materials have been processed with a standardised preparation technique designed to give consistent and directly comparable results. Firstly, a 6wt% polyvinylidene fluoride (PVDF) in *N*-Methyl-2-pyrrolidone (NMP) (Both purchased from Sigma Aldrich) solution is made. This involved heating NMP to 80°C under constant stirring and adding the appropriate amount of PVDF binder slowly, stirring continues until fully dissolved (circa 1 hour). If electrode materials have not previously been used or have been exposed to air and moisture they are firstly dried under vacuum at 120°C to remove any moisture. Next, the active material (AM) (e.g. $\text{Li}_2\text{FeSiO}_4$) and conductive additive (e.g. Super P or carbon black (CB)) are weighed out in a ratio of 8:1, respectively. These powders are combined and wet ball-milled (Fritsch pulverisette 7) under ethanol for 1hr at 600rpm in zirconia vials. This ensures a homogeneous mixture where the AM and CB are well incorporated. This mixture is dried under vacuum for 12hrs. Once dried, the AM/CB mixture is weighed out into a small vial with a stir bar inserted. The PVDF/NMP solution is added so that the resulting suspension is AM:CB:PVDF in a ratio of 8:1:1 respectively. This suspension is stirred for 12hrs, and cast onto its corresponding metal foil (aluminium for cathode, copper for anode) using a “doctor blade”. The cast wet-electrode is then immediately under vacuum at 120°C for 12hrs, removing all NMP solvent. The resulting dry-electrode is cut into the desired shape and size (e.g. $\frac{1}{2}$ " diameter disks for use in CR2032 coin cells. In industry, electrodes would be calendared to control porosity, increase electronic conductivity and create uniform films. Here the cut disks are pressed using a pellet press to achieve a similar result. Figure 2.1 shows the process described above.

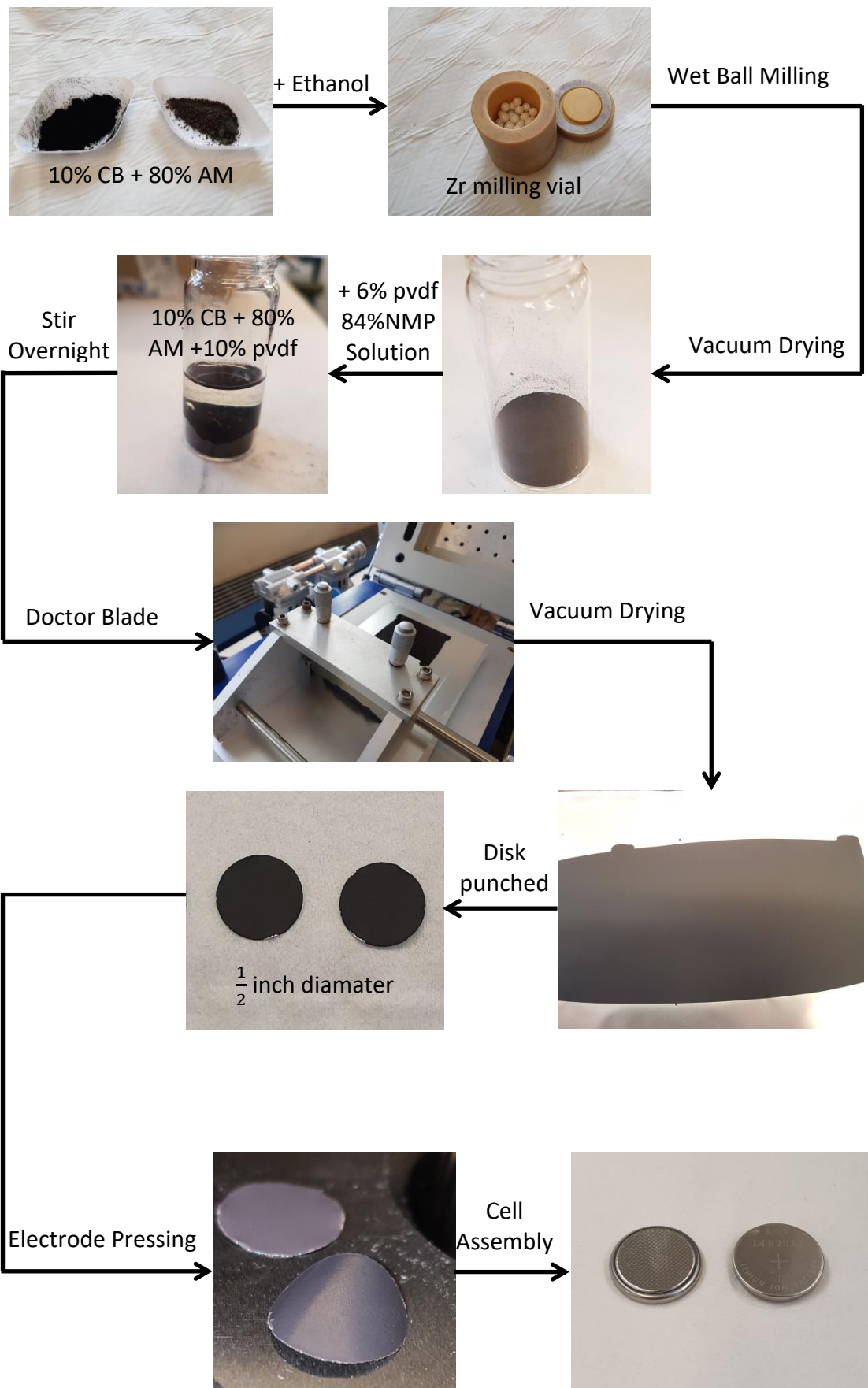


Figure 2.1: A schematic diagram illustrating the electrode preparation process

2.2.2 Electrolyte Preparation

Unless otherwise stated, all cells in this study were made using 1M LiPF₆ in ethylene carbonate/diethylene carbonate in a 1:1 volume ratio purchased from Sigma Aldrich [2]. Electrolytes were stored and used in an argon filled glovebox O₂ and H₂O <0.5ppm.

2.2.3 Separator Preparation

Two separators were used in this study. Firstly, was a tri-layer polypropylene/polyethylene/polypropylene (PP/PE/PP) Celgard separator purchased from MTI [3]. This separator was used for all coin cells in this study. The separator film is punched into disks $\frac{5}{8}$ " in diameter so that it is larger than the electrode disks and covers the entire inner diameter of the CR2032 coin cells. The disks are briefly rinsed with ethanol to remove any debris and then dried thoroughly under vacuum. Once dried, separators are placed in a vial and stored in an argon filled glovebox until used. Secondly a single layer PE Solupor separator was used [4]. This separator was used for all pouch cells in this study. The separator film was cut into 8x4cm strips and folded in half to form a double layer square of 4cm.

2.2.4 Coin Cell Assembly

The main cell type used in this study was in the form of CR2032 coin cells from MTI [5]. All cell components are dried at 80° under vacuum before storing in an Argon filled glovebox. Electrodes are prepared as described above before cell assembly. Figure 2.2 below shows a schematic diagram of a half-cell stack before crimping.

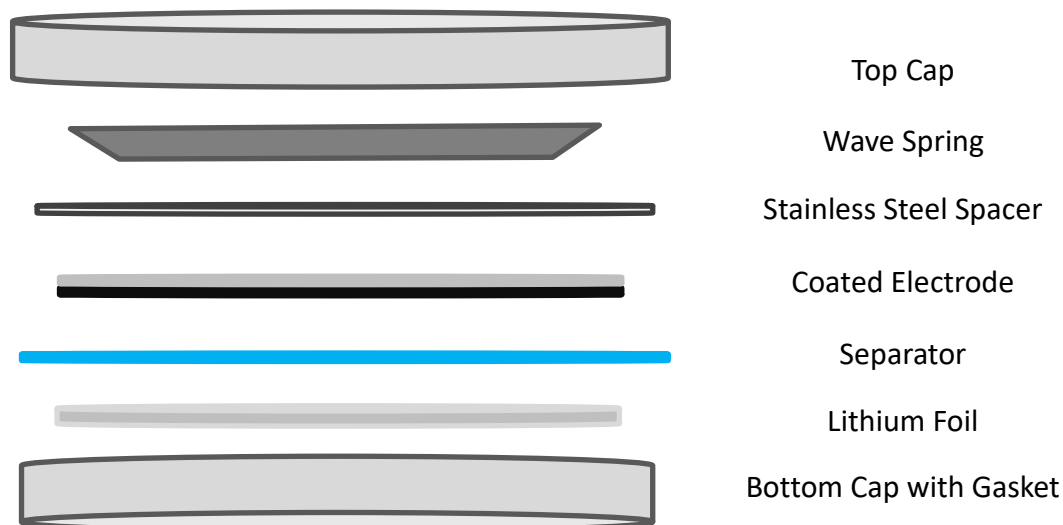


Figure 2.2: Schematic diagram of a CR2032 coin half-cell stack

2.2.5 Pouch Cell Assembly

Pouch cells were used when coin cells were not appropriate for the experiment e.g. XAS measurements. Due to the coin cells casing and internal components being made out of stainless steel, they were not suitable for XAS measurements as the beam would not penetrate the cell. In addition to this, the XAS study looks at the Fe K-edge with which the stainless steel could interfere with. Pouch cells were assembled using laminated aluminium pouch material [6], copper and aluminium tabs for anode and cathode respectively [7] and Solupor separator [4]. Hot-melt tape glue was used to seal the side with the tabs to ensure a hermetic seal [8]. Figure 2.3 shows images of the individual components and various stages, leading up to the finished product.



Figure 2.3: Images of the individual components and at various stages of the pouch cell assembly

Figure 2.3 shows pouch cells both with and without cut out windows. The type of pouch cell was tailored to its specific experiment and application, various window materials have been used, in this study either no window or aluminium/copper windows were used. For standard Fe K-edge XAS measurements the windows are unnecessary, however when using techniques such as small angle X-ray scattering (SAXS) or X-ray Raman scattering (XRS) where any additional scattering caused by additional layers and/or polymer coatings of the pouch cells may interfere, windows are cut from the pouch and the current collector tabs are heat sealed onto the pouch itself so as to fully seal the pouch. In a standard pouch cell, electrodes and lithium metal disks are inserted into the pouch cell in an argon filled glovebox, electrolyte added and all sides are heat sealed under vacuum in an argon filled glovebox.

2.3 Materials Characterisation

2.3.1 X-Ray Diffraction (XRD)

X-ray diffraction (XRD) is a powerful tool widely used for the structural characterisation of crystalline solids. X-rays of a fixed wavelength are generated by bombarding a target material (e.g. copper) with electrons. This excites the core electrons of the target material, creating an electron hole. This is an excited state, which leads to a transition of a higher level electron to “fall down” into the electron hole. In this process, the excited element finds a lower energy state resulting in the emission of a photon. The energy of these photons correspond to X-rays of the desired wavelength (λ). For crystalline materials, the crystal lattice has interatomic distances (d) similar to the wavelength of the supplied X-rays (λ), resulting in an interaction between the material and the incident beam. The nature of these interactions can be expressed by Bragg’s law:

$$n\lambda = 2d_{hkl}\sin\theta \quad (2-1)$$

Describing the relationship between the order of reflection (n), the wavelength of incident X-rays (λ), the interplanar spacing (d) and the angle of incidence (θ). To better understand this relationship Figure 2.4 shows a representation of a crystal lattice with interplanar spacing d_{hkl} (h,k,l being Miller indices of crystal planes (h,k,l)) with incident beams being scattered by adjacent planes. When then path difference between these two

beams ($2d_{hkl}\sin\theta$) is equal to an integer (n) of the X-rays' wavelength (λ) they will constructively interfere. When the beams are diffracted at different angles to the Bragg angle then destructive interference is observed.

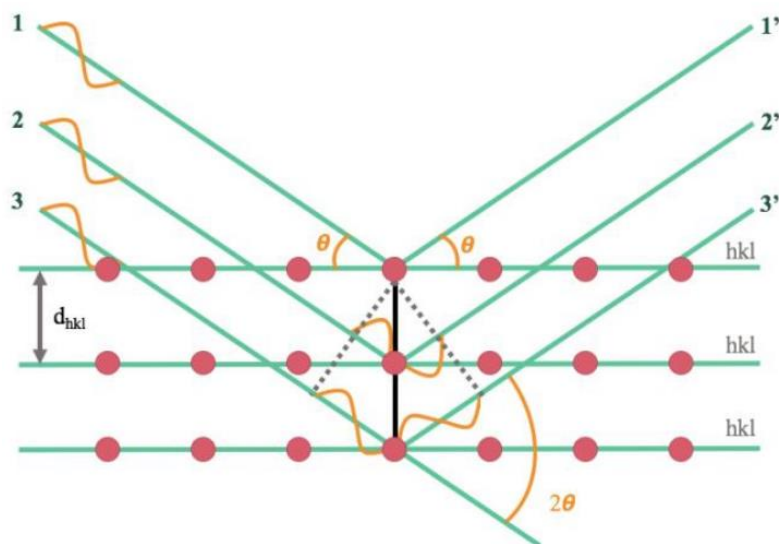


Figure 2.4: A schematic demonstrating the principles of XRD (reproduced with permission [20])

The diffractometer used in this study was the Rigaku MiniFlex using Cu- α radiation [6]. This diffractometer fires X-rays at the desired sample at a range of angles, the diffracted beam then hits the detector and the intensity is measured over the range of angles 2θ . These intensities are plotted versus 2θ and an XRD pattern is formed. In this study powder X-ray diffraction is used. This means that the materials lattice planes are randomly arranged, ensuring that some of the material is always orientated at the Bragg angle.

As will be demonstrated later in this thesis, XRD is not only used for structural analysis of crystalline materials, but it can also be a useful tool in determining whether a material is amorphous or not. In this case, a distinct lack of Bragg peaks – due to the lack of long range periodic order – would indicate an amorphous sample. Instead, the XRD pattern often exhibits a broad “hump”.

2.3.2 XRD Sample Preparation

Samples were ground into a fine powder using an agate pestle and mortar, ensuring no large grains and/or agglomerations. All samples were placed onto a zero background holder using some grease. Samples were scanned using the RIGAKU MiniFlex with a step size of 0.02° .

2.3.3 Scanning Electron Microscopy (SEM)

Scanning Electron Microscopy (SEM) is a widely used analytical technique for the purpose of obtaining high resolution, high magnification images of a material; yielding information on morphology and topography. Many systems combine SEM with Energy Dispersive X-rays (EDX), which are generated during use and give information about the samples elemental composition [7].

SEM utilises a high energy electron beam, generated by heating a filament e.g. Tungsten. These electrons are focused and targeted at the sample by using powerful magnetic lenses. SEM is normally carried out under high vacuum to avoid unwanted electron interactions with gaseous molecules, which may cause image distortions. However, under some circumstances gas is introduced into the sample chamber for the purpose of charge or thermodynamic stabilisation of samples, this is known as Variable Pressure SEM (VP-SEM). This has not been applied in this project.

Once the generated electron beam (known as the Primary Beam) hits the sample, there are multiple events which may occur. The main occurrences and zones in which they stem from are depicted in Figure 2.5. This study utilised the Hitachi S-3400N SEM.

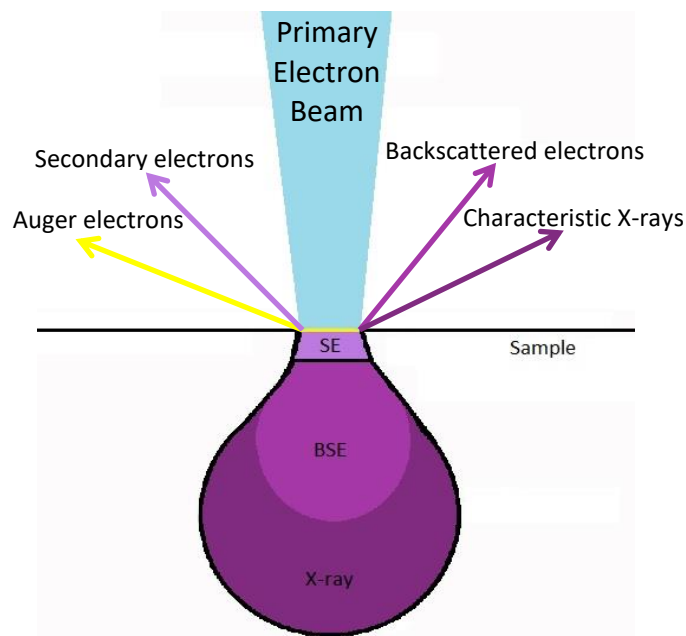


Figure 2.5: Schematic diagram of the reaction processes which occur in SEM

2.3.3.1 Auger Electrons

When an inner shell electron is removed, creating a vacancy, an electron from a higher shell “drops down” to fill this vacancy. This process releases excess energy associated with this “drop”, this energy may, in turn, eject a second higher shell electron, known as an “auger electron”. This is a surface sensitive process, with typical penetration depths of <5nm. Auger electron spectroscopy is used for surface composition and impurity information. The process is the same as auger electrons released in X-ray absorption spectroscopy (Figure 2.6 C), however, the inner shell electrons are released via an electron beam rather than an X-ray beam.

2.3.3.2 Secondary Electrons

Secondary electrons (SE) are the most commonly used event in SEM. Secondary electrons are generated when a K-shell electron is ejected from the target sample by either a primary electron or another secondary electron. Secondary electrons are low energy, so observed secondary electrons originate from near the surface of the material, secondary electrons from deeper within the material are released but are absorbed by the sample. Secondary electrons yield high resolution images and topographical information of a sample.

2.3.3.3 Backscattered Electrons

Backscattered electrons (BSE) are primary electrons which have interacted elastically with the samples atoms, in such a manner, that they have been reflected back (backscattered) out of the sample and into the detector. Aside from topographical information, BSE also give atomic density and phase information; as the materials atomic number increases, so does the amount of backscattered electrons, this can be useful in determining material separations, as materials with higher atomic numbers will appear brighter than lower atomic numbers due to the amount of backscattered electrons. Though it should be noted, when using BSE mode, resolution is reduced compared to SE mode.

2.3.3.4 Energy Dispersive X-rays

Energy Dispersive X-ray spectroscopy (EDX) is a powerful tool, allowing elemental information to be retrieved from a sample. When the primary beam electrons dislodge

electrons from the inner shells of the sample (K-shell), electrons from the outer shells replace it releasing energy in the form of X-rays. These X-rays have an element specific energy characteristic, allow for the determination of which element it originated from. This, in combination with SEM imaging allows for location specific elemental mapping, giving information on material composition and impurities.

2.3.4 ThermoGravimetric Analysis (TGA)

Thermogravimetric analysis (TGA) is an analysis technique used to monitor changes in a samples weight as a function of temperature. Increasing or decreasing temperature of a sample in a controlled atmosphere can induce physical or chemical changes within a sample. Atmospheres are controlled by using a purge gas; these can be inert or reactive gasses depending on the desired reactions, or intended applications for the observed material. TGA can be used to determine a materials thermal stability, which can be affected by reactions such as: solvent evaporation, material oxidation, thermal decomposition, sublimation and absorption. In addition to thermal stabilities, TGA can be used to determine carbon content and, in some cases, impurity content depending on decomposition temperatures. This study used the NETZSCH STA-409 TGA.

2.3.5 Differential Scanning Calorimetry (DSC)

Differential scanning calorimetry (DSC) is another thermal analysis technique, sometimes run in unison with TGA, or run as an individual technique. Similarly to TGA a samples physical and chemical changes are plotted as a function of temperature, however, instead of weight changes, DSC observes thermal flows associated with material reactions and transitions. A small amount of sample is heated in unison with a reference sample (often an empty crucible), in a controlled atmosphere, the required energy to retain thermal equilibrium between the sample and reference is measured. This allows for the observation and separation of endothermic and exothermic reactions within the material, that is to say, if a transition occurs within the material that requires the absorption or release of thermal energy this can be tracked using DSC. Types of reactions which are normally observed include: Glass transition (T_g), crystallisation temperature (T_c), melting temperature (T_m) and oxidation temperatures, as well as the reversibility of these reactions. These transitions appear as exothermic or endothermic peaks as a function of temperature. DSC is useful when selecting

materials for specific applications to ensure the material is in the correct phase during use.

2.4 X-ray Absorption Spectroscopy

X-ray Absorption Spectroscopy (XAS) is a powerful analytical technique which utilises synchrotron radiation capable of providing element specific electronic and structural properties.

2.4.1 The Basic Principles of XAS

In XAS, the sample of interest is bombarded with a highly intense beam of X-rays with a specific energy, normally between 500eV and 500KeV. This usually requires a synchrotron. When these X-rays enter a sample, one of three events will occur: 1) the X-ray may pass through the sample, unchanged; 2) the X-ray may interact with an atom, without enough energy to cause an excitation, but scatter (this process may be elastic or inelastic) or 3) the X-ray may become absorbed by an atoms (core) electrons, therefore, promoting the atom to an excited state. This absorption is expressed according to the Beer-Lambert Law:

$$I = I_0 e^{-\mu t} \quad (2-2)$$

Where I_0 is the intensity of the incident beam, I is the intensity of the transmitted beam, t is the sample thickness and the μ is the absorption coefficient, which gives the probability that X-rays will be absorbed.

This excitation, in turn, can lead to the ejection of the targeted atoms' core electrons. For this to happen, the binding energy of the core electron must be lower than that of the incident X-ray. Any excess energy from the X-ray is transferred to the ejected photoelectron. This process leaves behind an electron hole in the core energy level, which is then filled by electrons from higher energy levels, leading to one of multiple events, depicted in Figure 2.6.

There are two main events which lead to the decay of an atoms excited state. The first is that of X-ray fluorescence, where an electron from a higher orbital “falls” to fill the “core hole”, this process leads to the ejection of an X-ray (K_{α} or K_{β}) of a defined energy, characteristic of the atom it was ejected from, known as the fluorescence energies. The second mechanism is that of the auger effect, whereby an electron from a higher shell “falls” to fill the “core hole” and a second electron is ejected into the continuum, this second electron is known as an auger electron.

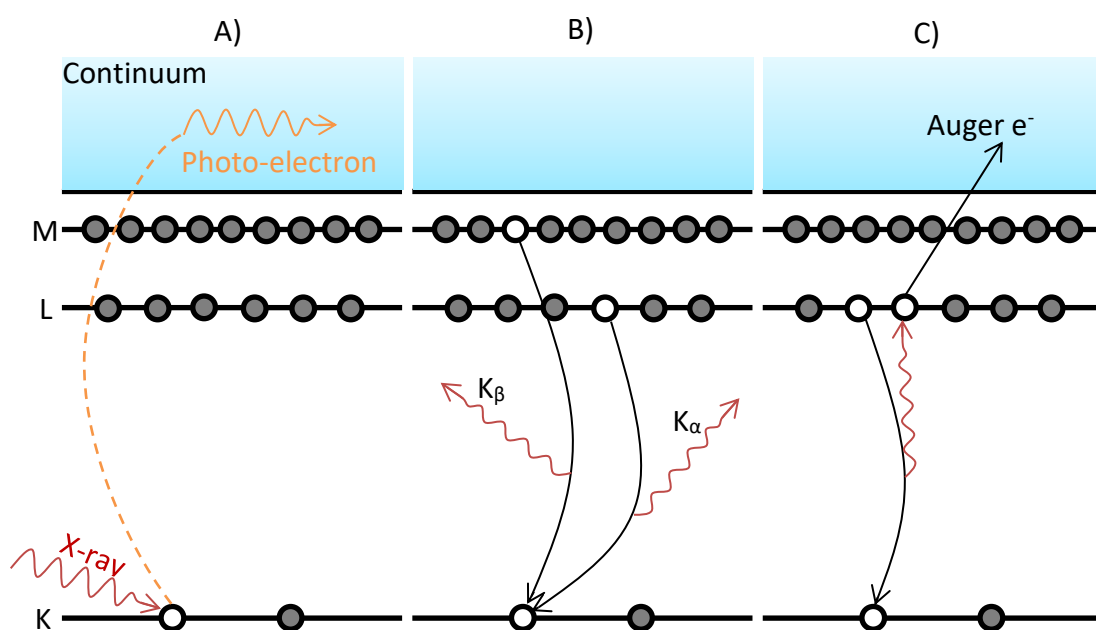


Figure 2.6: Schematic representation of A) X-ray Absorption B) Fluorescence Emission C) Auger Emission

2.4.2 X-ray Absorption Spectroscopy Measurements

XAS measurements are taken across a range of energies before and after the target materials absorption edges. Figure 2.7 shows a typical data plot received from an XAS measurement. Several distinct features can be observed: The background, pre-edge and main edge features, also highlighted are the XANES and EXAFS regions.

2.4.2.1 The Background

The gradual slope towards lower absorption as energy increases is a feature related to the properties of photon-matter interaction whereby the probability of an interaction decreases as a function of energy. This background is compensated for upon data fitting and analysis.

2.4.2.2 X-Ray Absorption Near-Edge Structure

X-ray absorption near-edge structure (XANES) is a region from around 20eV before and 50eV after the main absorption edge energy E_0 . The main edge is the most prominent feature, where the incident X-rays have sufficient energy to excite the electrons from the targeted orbital. Evidenced by a sharp rise in absorption, the edge position is assigned the distinct energy E_0 . The pre-edge feature highlighted in Figure 2.8 is a feature often associated with absorption from a localised electronic states and can be used to determine local coordination symmetry. XANES data yields information about the oxidation state and coordination chemistry. An increase in edge energy is characteristic of an oxidation process whilst a shift towards lower energies suggests a reduction of the target element. This is due to a higher energy requirement to excite electrons from the core shell, which are more tightly bound (higher oxidation state), the same can be said of atoms with increasing atomic numbers.

2.4.2.3 Extended X-Ray Absorption Fine Structure

The extended X-ray absorption fine structure (EXAFS) is a region from around 50eV to a few keV above E_0 and is characterised by the oscillating spectrum post-edge. These oscillations are caused by constructive and destructive interference created by the ejected photoelectron scattering caused by the atoms nearest neighbours. Constructive interference results in the absorbing atom to hold a higher electron density, whilst the opposite can be said of destructive interference, these constructive and destructive events create peaks and troughs respectively in the EXAFS regions. Therefore, EXAFS yields information such as coordination numbers and bond distances, as well as elemental information of nearest neighbours.

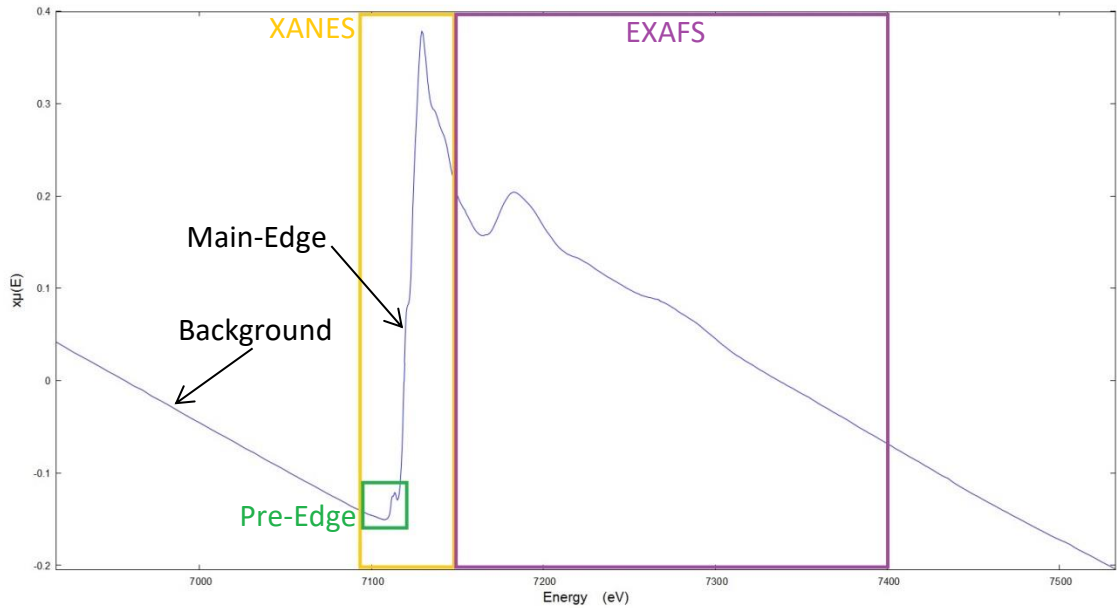


Figure 2.7: Annotated example XAS spectrum

2.4.3 X-Ray Absorption Spectroscopy Experiments

There are two main methods for conducting an XAS experiments, that is: Transmission mode and fluorescence mode. In transmission mode the X-ray beam intensity is measured after passing through the sample with the energy dependency of the absorption coefficient is calculated according to the relationship:

$$\mu(E) = -\ln \frac{I_0}{I} \quad (2-3)$$

Fluorescence mode, instead, relies on a secondary emission event such as the aforementioned fluorescence emission. With the energy dependence of the absorption coefficient instead, following the relationship:

$$\mu(E) \propto \frac{I_f}{I_0} \quad (2-4)$$

Where I_f is the intensity of a fluorescent emission line or electron emission. [8] [9]

2.4.4 The Beamline

As previously mentioned, XAS experiments most commonly require a synchrotron radiation facility. This study utilised two different facilities: European Synchrotron Radiation Facility (ESRF) and DIAMOND Light Source (DLS). All In-operando measurements were conducted at the ESRF on the BM26A beamline [10]. Figure 2.8 shows a schematic of the beamline.

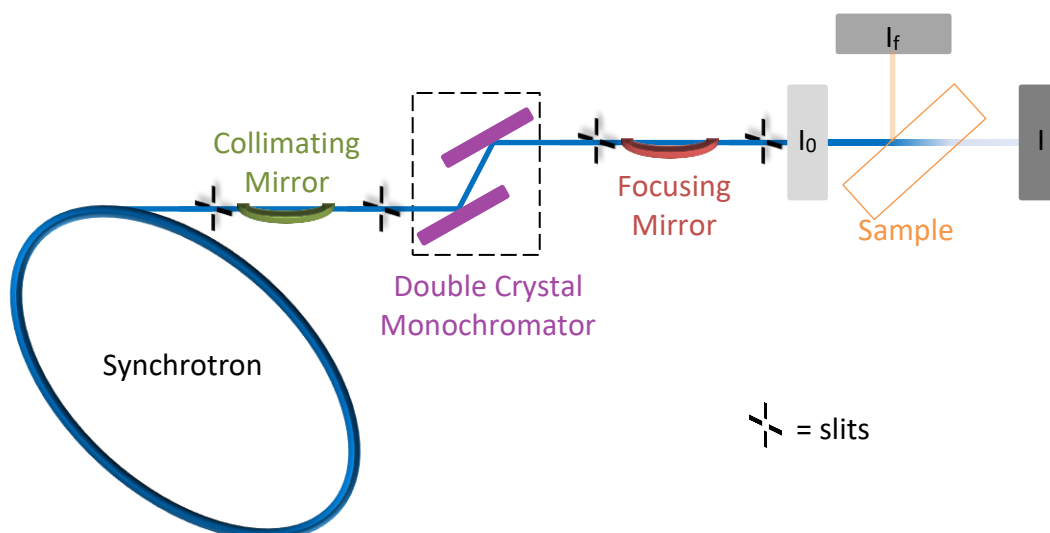


Figure 2.8: Schematic Diagram of BM26A beamline optics

The beam is collimated via the use of a Si or Si/Pt mirrors, the beam then passes through a double crystal monochromator which is used to filter the incoming beams energy band and narrow the X-rays to the desired wavelength. However, monochromators do not select a singular wavelength but also produce harmonics of said wavelength, which can cause spikes or “glitches” during data acquisition. Therefore, a focusing mirror is used for harmonic rejection and further focusing of the beam towards the sample. Along the way, the beam passes through a series of slits designed to control beam dimensions and angular spread, the final slit is user controlled to adjust final beam-size. Also indicated is the sample position and the Fluorescence and transmission detectors I_f and I respectively [8] [10]. All XAS data processing, including fitting and normalisation, was conducted via the use of Athena, under the IFEFFIT package [11].

2.5 X-Ray Raman Scattering Spectroscopy

X-ray Raman scattering (XRS) is a non-resonant inelastic X-ray scattering (IXS) by core electron excitations. Whilst XAS techniques are invaluable for material characterisation, XAS does have limitations. XAS uses X-rays of a broad range of energies, split into two classes: Hard X-rays (>5keV) and Soft X-rays (<5keV). Absorption edges which sit in the hard X-ray region can be easily observed using XAS with little impact from the sample environment. However, when energies sit in the soft X-ray region sample environment must be carefully considered. As the X-rays have low energy they can be affected by atmospheric absorption, cell absorption or scattering effects. This means, when using soft X-rays in XAS it is often a requirement to conduct experiments in a controlled atmosphere e.g. under helium or high vacuum. In addition, due to the samples internal absorption/scattering characteristics, soft X-ray techniques are often surface probing techniques and not capable of showing a materials bulk characteristics. XRS holds advantages over soft XAS in this respect; this is due to the use of hard X-rays for probing the material. Figure 2.9 shows a schematic comparing the XAS and XRS techniques probing the O K-edge (540eV) [12].

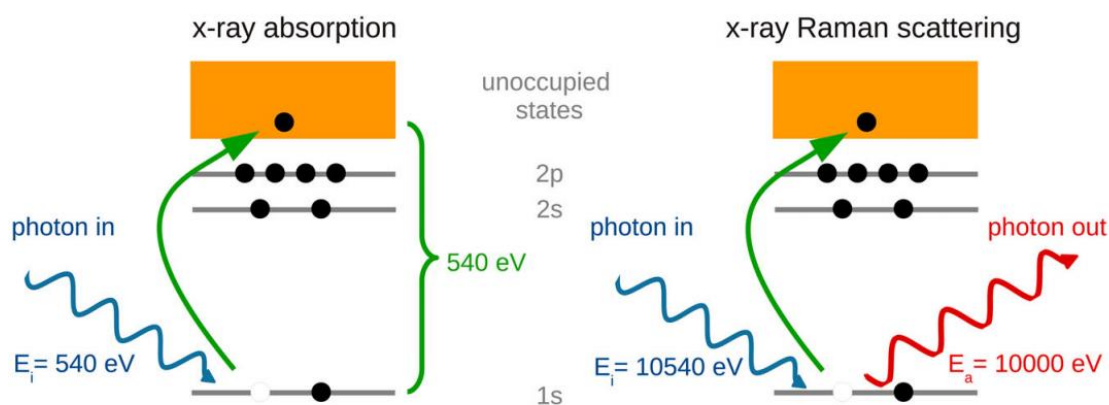


Figure 2.9: A schematic of the XAS and XRS process whilst probing the O K-edge (reprinted with permission [12])

It can be seen that, as previously described XAS utilises an incident beam of energy $E_i \approx 540 \text{ eV}$ (target edge energy) whilst in XRS, the inelastically scattered photons are analysed at a fixed energy (10keV) and the incident beam energy is tuned to: $E_i = E_a + 540 \text{ eV}$.

It should also be noted that, unlike XAS, XRS is not limited dipolar excitations and thus, can be used to probe dipole forbidden transitions. Figure 2.10 illustrates the principle

of IXS with respect to X-ray energy and momentum. A photon of energy ω_1 interacts with an electron within the sample, this leads to an inelastic scattering of the photon, reducing the energy to ω_2 . Upon this interaction, some of the photons energy ω ($\omega = \omega_1 - \omega_2$) and momentum q ($q = k_1 - k_2$) is imparted on the sample.

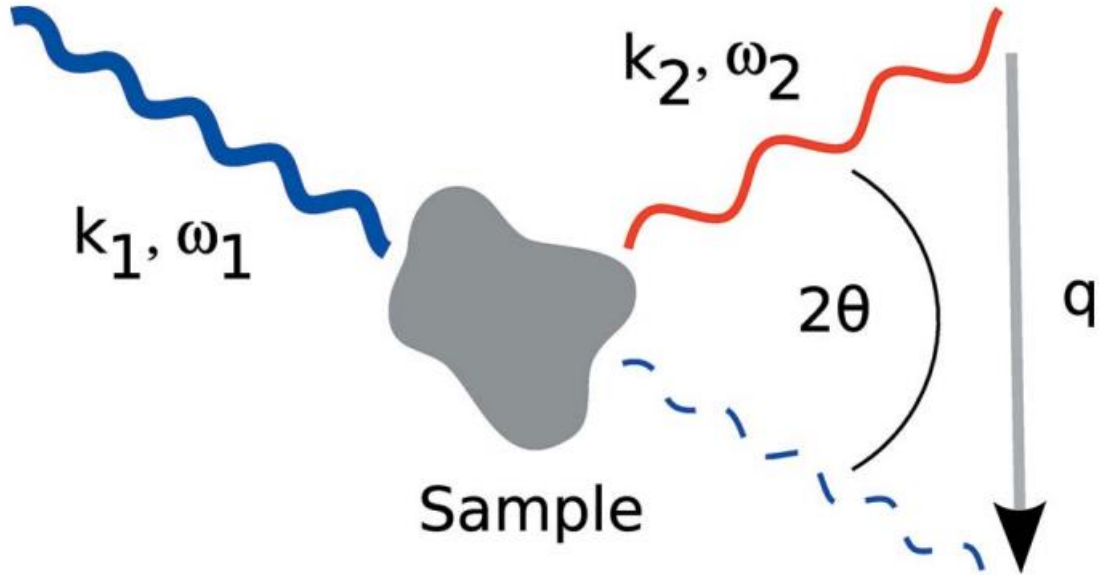


Figure 2.10: Schematic representation of an IXS experiment (reprinted with permission [15])

The measured quantity in IXS experiments is the double differential scattering cross section, expressed as:

$$\frac{d^2\sigma}{d\Omega d\omega} = \left(\frac{d\sigma}{d\Omega}\right)_{Th} S(\mathbf{q}, \omega) \quad (2-5)$$

Where $\left(\frac{d\sigma}{d\Omega}\right)_{Th}$ is the Thomson scattering cross-section and $S(\mathbf{q}, \omega)$ is the dynamic structure factor expressed:

$$S(\mathbf{q}, \omega) = \sum_f |\langle f | e^{i\mathbf{q}\cdot\mathbf{r}} | i \rangle|^2 \delta(E_i - E_f + \omega) \quad (2-6)$$

Where $|i\rangle$ expressing the systems initial state and $\langle f|$ is the final state. When momentum transfer \mathbf{q} is low, the spectrum is dominated by dipole excitations (e.g. $1s \rightarrow p$ transitions), providing information equivalent to XAS, albeit with bulk sensitivity. However, in high \mathbf{q} regions, the aforementioned dipole-forbidden excitations dominate (e.g. $1s \rightarrow d$ transitions) providing XRS with the ability to give information on partially unoccupied density of states. [12] [13] [14] [15] [16] The beamline used in this study was ID20 at the ESRF [17].

2.6 Electrochemical Measurements

2.6.1 Electrochemical Impedance Spectroscopy (EIS)

Impedance spectroscopy is a widely used tool for measuring a samples conductivity. This can include a combination of electronic and ionic conductivity, however, for the purpose of this study, only ionic conductivity is discussed. The material of interest is sandwiched between two electrodes (in a 2 electrode system), these electrodes are electrically conductive and can be ionically blocking, partially blocking or non-blocking to ions. This study makes use of ionically blocking stainless steel electrodes to remove ionically conducting effects stemming from electrode reactions. In impedance spectroscopy, the sample is subjected to a sinusoidal wave of a set frequency and the potential and current responses are collected. These responses can have phase differences depending on the nature of the material. The conventional method of representing impedance (complex resistance) is as a Nyquist plot (Figure 2.11) with two major impedance (Z) components: the in-phase (real) Z' and the out-of-phase (imaginary) Z'' components. These components are plotted to their limits $\omega \rightarrow \infty$ and $\omega \rightarrow 0$ where $Z'' \rightarrow 0$. At these limits, real resistances can be taken, therefore allowing conductivities to be calculated.

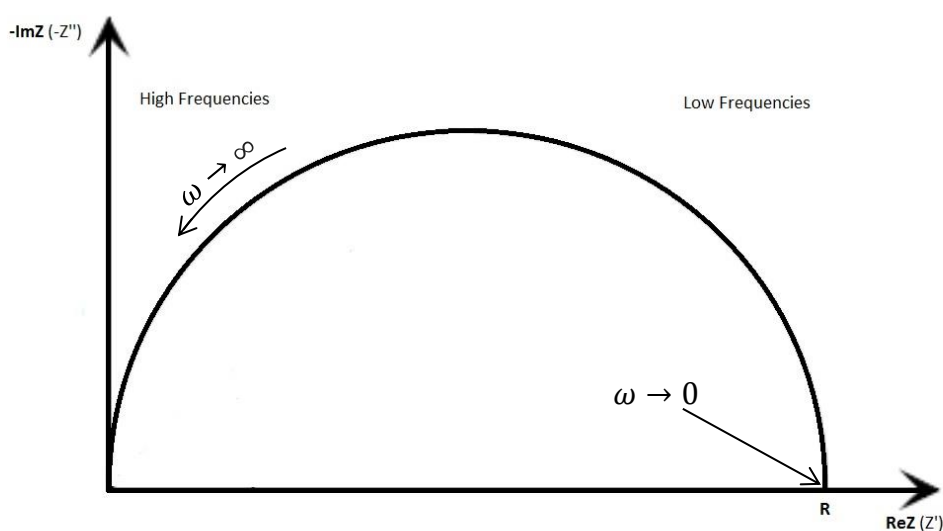


Figure 2.11: A representation of a typical Nyquist plot

All EIS measurements were undertaken using a Biologic VMP3 potentiostat [18].

2.6.2 Cyclic Voltammetry (CV)

Cyclic Voltammetry (CV) is a powerful technique which can be used in a multitude of ways. Here, CV has been used to gain a better understanding of redox potentials in electrode materials vs Li^+ . The technique involves submitting a half cell to a linear potential sweep between the desired voltages (typically the cycling voltages) starting at open circuit voltage (OCV). The current applied to achieve these potentials is mapped vs the voltage and thus a CV curve is formed. When little interaction is occurring, only low currents are necessary to achieve these voltages, however, as soon a redox potential is reached the current required to pass this voltage increases, therefore creating a peak in the CV curve. An example is shown in Figure 2.12, with the Galvanostatic cycling curve alongside, indicated are the CV anodic and cathodic peaks which correspond to the indicated cycling plateaus.

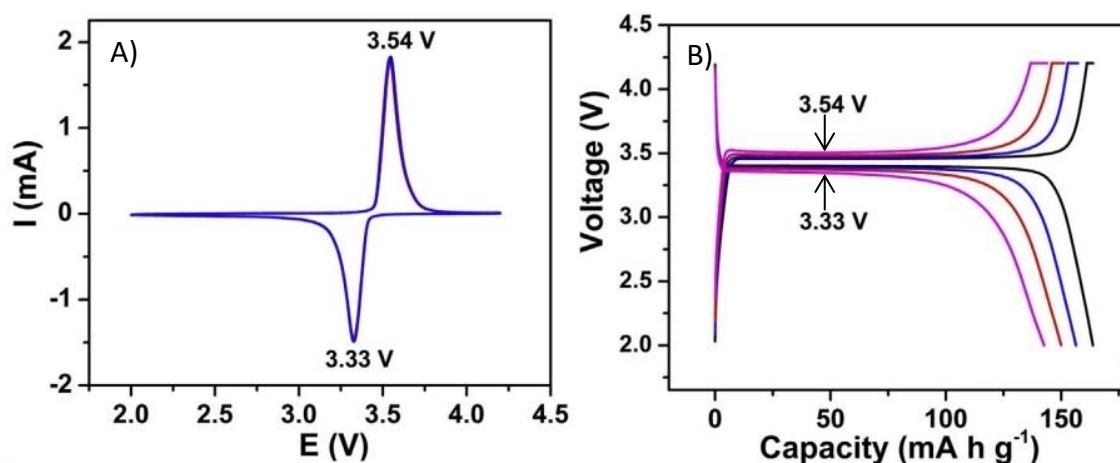


Figure 2.12: A) A CV curve of LiFePO_4 and B) its corresponding galvanostatic cycling curve (reprinted with permission [21])

CV curves can also yield other information and give insight to an electrodes' reactions, diffusion pathways and conductivity. For example, varying the sweep rate can yield information on the materials kinetics, as peak shifts may be observed in materials with poor conductivity and slow reaction times. Sharp peaks on a CV curve are indicative of a large, flat plateau associated with a redox reaction, as observed in Figure 2.12. Broad peaks on CV curves are more difficult to interpret. They can indicate that the galvanostatic cycling will show a sloped 'plateau', therefore, the reactions are taking place over a broader potential, they may also indicate slow kinetics, such as, diffusion

or conductivity within the cell. This can be further investigated by varying the scan speed or by combining with other characterisation techniques and/or simulations. All CV measurements in this study were undertaken using a Biologic VMP3 potentiostat [18].

2.6.3 Galvanostatic Cycling (Charge and Discharge Curves)

Galvanostatic cycling is the most common method for determining a materials specific capacity, coulombic efficiency, cycle lifetime and performance, often compared to literature or other materials cycled at various C-rates concerning battery research.

Specific capacity is how much energy a battery holds by weight, this is expressed in mAhg^{-1} and is often compared to the materials theoretical capacity as an indication of battery performance.

Coulombic efficiency is the percentage of capacity achieved in discharge (useable energy from the battery) compared to the capacity upon charging (amount of energy imparted unto the battery during charge). Coulombic efficiency is affected by various factors, such as, parasitic reactions, the formation of SEI, electrolyte decomposition, cycling C-rates and temperature. To calculate efficiency, equation 2-7 is used.

$$\text{Coulombic Efficiency (\%)} = \frac{\text{Discharge Capacity (mAhg}^{-1}\text{)}}{\text{Charge Capacity (mAhg}^{-1}\text{)}} \times 100 \quad (2-7)$$

C-rate refers to the rate at which the material is cycled. A C-rate of 1C indicates that the material is charged in 1 hour and discharged in 1 hour, a rate of 0.5C and 2C would indicate a charge or discharge in 2 hours or 0.5 hours respectively. This is a common way of referring to cycling speed as it allows for direct comparisons of different materials, material loadings or battery sizes independent of theoretical capacities.

Two systems were used for Galvanostatic cycling, all in-house cycling was conducted using the Biologic VMP3 potentiostat [18], whilst any cycling during in-operando beamline experiments used a Maccor system potentiostat [19].

2.7 References

- [1] A. W. Brownrigg, G. Mountjoy, A. V. Chadwick, M. Alfredsson, W. Bras, J. Billaud, A. R. Armstrong, P. G. Bruce, R. Dominko and E. M. Kelder, "In situ Fe K-edge X-ray absorption spectroscopy study during cycling of $\text{Li}_2\text{FeSiO}_4$ and $\text{Li}_{2.2}\text{Fe}_{0.9}\text{SiO}_4$ Li ion battery materials," *Journal of Materials Chemistry A*, vol. 3, pp. 7314 - 7322, 2015.
- [2] "Sigma Aldrich - Merck," [Online]. Available: <https://www.sigmaaldrich.com/catalog/product/aldrich/746746?lang=en®ion=GB>. [Accessed 18 03 2019].
- [3] "MTI Corporation," MTI Corporation, [Online]. Available: MTI Corporation. [Accessed 1 6 2018].
- [4] "Lydall," Solupor Membrane, [Online]. Available: <https://www.lydallpm.com/products/liquid-filtration/solupor-membrane/overview/>. [Accessed 1 12 2019].
- [5] "MTI corporation," MTI corporation, [Online]. Available: <https://www.mtixtl.com/304StainlessSteel-CR2032buttoncellscases20dx3.2mmforBatteryRes-2.aspx>. [Accessed 18 3 2019].
- [6] "ProfiTherm MIL - 131K - class 1," Brangs + Heinrich, [Online]. Available: <https://www.brangs-heinrich.de/en/products/corrosion-protection-export-packages/>. [Accessed 01 01 2020].
- [7] M. corporation, "MTI Corporation," [Online]. Available: <https://www.mtixtl.com/electrodesubstratecurrentcollector.aspx>. [Accessed 01 01 2020].
- [8] "MTI Corporation," [Online]. Available: <https://www.mtixtl.com/HotMeltAdhesivePolymerTapeforHeatSealingPouchCellT>

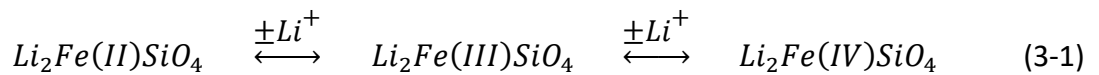
abs100mLx.aspx. [Accessed 01 01 2020].

- [9] "Rigaku," [Online]. Available: https://www.rigaku.com/en/products/xrd/miniflex?gclid=CjwKCAjwvnbBRA5Ei%20wAcRvnpjw6H1-%20apivMMWQ51b_MwvTeRcZLdYNWpRHHkApDrdiXv1r2uJ4R6RoCObwQAvD_Bw%20E.. [Accessed 30 09 2019].
- [10] M. Dunlap and J. E. Adaskaveg, "Introduction to the Scanning Electron Microscope. Theory, Practice, & Procedures.," *Facility for Advance Instrumentation*, p. 52, 1997.
- [11] M. Newville, "Fundamentals of XAFS," *Reviews in Minerology and Geochemistry*, vol. 78, pp. 33 - 74, 2014.
- [12] S. Calvin, XAFS for Everyone, CRC Press, 2013.
- [13] "BM26 Beamline (ESRF)," [Online]. Available: <https://www.esrf.eu/UsersAndScience/Experiments/CRG/BM26>. [Accessed 06 10 2019].
- [14] B. Ravel and M. Newville, "ATHENA, ARTEMIS, HEPHAESTUS: data analysis for X-ray absorption spectroscopy using IFEFFIT," *Journal of Synchrotron Radiation*, vol. 12, no. 4, pp. 537 - 541, 2005.
- [15] M. Wilke and C. Sternemann, "Spectroscopy of low and intermediate Z elements at extreme conditions: in situ studies of Earth materials at pressure and temperature via X-ray Raman scattering," *High Pressure Research*, vol. 36, no. 3, pp. 275 - 292, 2016.
- [16] C. J. Sahle, A. Mirone, T. Vincent, A. Kallonen and S. Huotari, "Improving the spatial and statistical accuracy in X-ray Raman scattering based direct tomography," *Journal of Synchrotron Radiation*, vol. 24, pp. 476 - 481, 2017.

- [17] Y. Joly, C. Cavallari, S. A. Guda and C. J. Sahle, "Full-Potential Simulation of X-ray Raman Scattering Spectroscopy," *Journal of Chemical Theory and Computation*, vol. 13, pp. 2172 - 2177, 2017.
- [18] C. J. Sahle, A. Mirone, J. Niskanen, J. Inkinen, M. Krisch and S. Huotari, "Planning, performing and analyzing X-ray Raman scattering experiments," *Journal of Synchrotron Radiation*, vol. 22, pp. 400 - 409, 2015.
- [19] R. A. Gordon, G. T. Seidler, T. T. Fister, M. W. Haverkort, G. A. Sawatzky, A. Tanaka and T. K. Sham, "High multipole transitions in NIXS: Valence and hybridization in 4f systems," *EPL*, vol. 81, 2008.
- [20] "ID20 Beamline ESRF," [Online]. Available: <http://www.esrf.eu/home/UsersAndScience/Experiments/EMD/ID20.html>. [Accessed 06 10 2019].
- [21] "Biologic VMP3," [Online]. Available: <https://www.biologic.net/products/potentiostat-galvanostat-eis/vmp3-modular-16-channels-potentiostat/>. [Accessed 07 10 2019].
- [22] "Maccor 4200," [Online]. Available: <http://www.maccor.com/Products/Model4200.aspx>. [Accessed 07 10 2019].
- [23] N. Yokota, "Design and Development of Lithium-Sulphur Batteries: In-operando Studies using X-ray Absorption Spectroscopy," University of Kent, Canterbury, 2018.
- [24] C. Qi, X. Ma, G. Ning, X. Song, B. Chen, X. Lan, Y. Li, X. Zhang and J. Gao, "Aqueous slurry of S-doped carbon nanotubes as conductive additive for lithium ion batteries," *Carbon*, vol. 92, pp. 245 - 253, 2015.

3 Positive Electrode – $\text{Li}_2\text{FeSiO}_4$

Commercially available lithium ion batteries use cathode materials, such as, LiFePO_4 (LFP) and LiCoO_2 (LCO) demonstrate theoretical capacities of 170 and 274 mAhg^{-1} , respectively. Experimentally they both achieve around 150 mAhg^{-1} [1]. Both materials demonstrate good lifetime performance/expectations, which is encouraging in most commercial applications. Despite the success of lithium-ion batteries in portable electronics, the constant advancements in electronic hardware means more power is required to support the higher energy demand. This, in turn, leads rise to a need for high power lithium-ion batteries. In principle, three techniques could be used to increase battery power: 1) Increase the amount of active electrode material 2) Introduce higher working voltage window 3) Increase the specific capacity of the electrode materials. The limiting component regarding specific capacity in lithium-ion batteries is the cathode (graphite anodes have a theoretical capacity of 372 mAhg^{-1} and an experimental capacity of 330 mAhg^{-1}). It has, therefore, been proposed that materials which have the ability to extract more than one Li per unit formula should be researched, thus increasing both capacity and voltage window. One of the proposed candidates is $\text{Li}_2\text{FeSiO}_4$, an orthosilicate with the general formula: Li_2MSiO_4 (M = Fe, Mn, Co). $\text{Li}_2\text{FeSiO}_4$ demonstrates a high theoretical capacity of 330 mAhg^{-1} accounting for a two-ion exchange [2]. Because of its ability to extract two Li-ions, $\text{Li}_2\text{FeSiO}_4$ is also a candidate for a high voltage cathode. The second Fe-ion oxidation is expected at 4.6V [3] [4]. The two-stage reaction equation for $\text{Li}_2\text{FeSiO}_4$ is as follows:



Room temperature cycling shows a complete, single Li-ion removal from the structure is possible. However, some sources have published papers stating that they have achieved the removal of more than one Li-ion. [5]

This single Li-ion removal, associated with the Fe^{2+} to Fe^{3+} redox reaction, which accounts for a specific capacity of 165 mAhg^{-1} . The additional capacity associated with a

>1Li⁺ removal has been proposed to originate from the iron redox couple Fe³⁺/Fe⁴⁺. However, this is a strongly debated topic, it has been reported in the literature that Fe⁴⁺ has been observed [5]. Whilst other groups, instead, propose the additional capacity could be associated with an oxygen redox reaction or electron redistribution rather than a second Fe redox couple.

Aside from the high theoretical capacity of Li₂FeSiO₄ the material also has the advantage of being composed of elements which are environmentally benign and some of the most abundant on earth: iron, silicon and oxygen [6]. The material is, therefore, sustainable for long term use including recycling and can be manufactured cheaply if scale-up processes should be required.

There are also negative properties associated with Li₂FeSiO₄, including very low intrinsic electronic conductivity [7] [8]. This is often found in silicate electrodes and is attributed to their large band gaps (>1.3eV) [9]. This has led other groups studying this material to improve electronic conductivity via carbon coating, synthesising carbon composites and mixing with larger amounts of additional carbon additives [10] [11] [12].

Li₂FeSiO₄ also exhibits poor ionic conductivity (diffusion rates) [13]. One solution to this restriction is to synthesise Li₂FeSiO₄ as nano-particles. The principle here is, by reducing particle size, lithium-ion diffusion pathways are shortened, increasing ion mobility throughout the electrode [14] [15]. Particle size reduction is widely used and has been shown, computationally, using first principle DFT calculations, to increase Li₂FeSiO₄ diffusion coefficients by up to 14 orders of magnitude [16].

Phase pure Li₂FeSiO₄ was first synthesised and researched as a cathode material by Nyttén et al., [17] where it was found that a structural rearrangement occurs during the first cycle resulting in a shift of the first charging plateau from 3.1V in the first cycle to 2.8V in subsequent cycles. Figure 3.1 shows the local structure of Li₂FeSiO₄ and how this changes during the first cycle and through subsequent cycles. It has been found that different synthesis methods and variations on reaction temperatures can have an effect on the initial polymorph synthesised. Three different, as synthesised polymorphs, have been previously reported with different space groups, monoclinic γ_s

with space group $P2_1/n$, orthorhombic γ_{II} with space group $Pmnb$ and orthorhombic β_{II} with space group $Pmn2_1$ [18]. Graphic representations of their structures are shown in Figure 3.1. Synthesis methods include solid state, hydrothermal, molten carbonate and sol-gel [19] [20] [21].

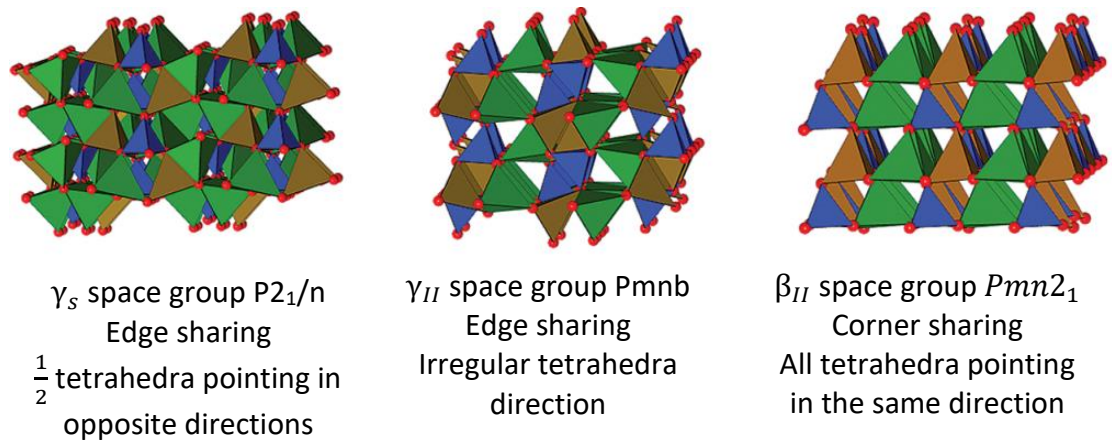


Figure 3.1: Diagrams of $\text{Li}_2\text{FeSiO}_4$ polymorphs (reprinted with permission [41])

This study uses $\text{Li}_2\text{FeSiO}_4$ with a $P2_1/n$ space group, however, it should be noted that during the first delithiation, a phase transition occurs which changes the materials polymorph and space group from γ_s $P2_1/n$ to inverse β_{II} $Pmn2_1$, this transition is irreversible upon further cycling. In successive lithiations and delithiations the structure alternates between orthorhombic inverse β_{II} and β_{II} as depicted in Figure 3.2.

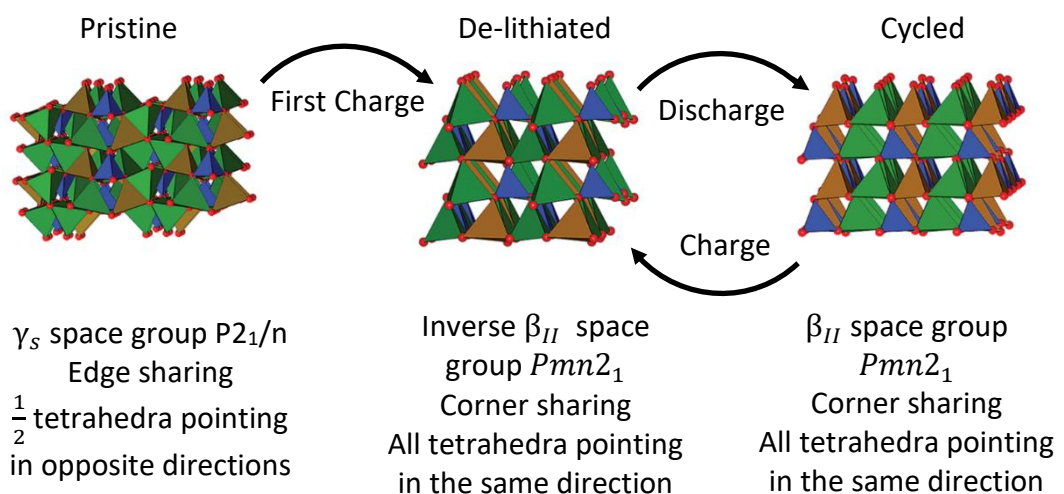


Figure 3.2: Diagrams of $\text{Li}_2\text{FeSiO}_4$ pristine and cycled structures (reprinted with permission [41])

Also mentioned is the materials reactivity to air, suggesting for optimal performance exposure to air must be limited. It should also be noted that Nytén et al. cycled the material between 2.0 and 3.7V, a much smaller voltage window than the accepted range today of 1.5 - 4.8V the smaller cycling window limits the lithium extraction to a maximum of one Li^+ per unit formula. Here no carbon coating or nanosizing of the material was employed. Instead, the issue of poor electronic and ionic conductivities was resolved by cycling $\text{Li}_2\text{FeSiO}_4$ at an elevated temperature of 60°C . This increase in conductivity allows for more accurate CV curves and improved cycling performance. However, the need for elevated temperature cycling would limit the materials use in a commercial battery without further improvements.

3.1 Synthesis and Characterisation

3.1.1 Solid State

$\text{Li}_2\text{FeSiO}_4$ was initially synthesised via a solid-state method following Masese et al. [22]. Stoichiometric amounts of Li_2CO_3 , SiO_2 and $\text{FeC}_2\text{O}_4 \cdot 2\text{H}_2\text{O}$ were added in a molar ratio of (1:1:1) with the addition of 10wt% carbon black. The mixture was ball milled under ethanol at 400rpm for 6hours then dried, pressed into a pellet and placed in a tube furnace under constant argon flux. The tube furnace was heated at a rate of $2^\circ\text{C}/\text{min}$ to 800°C , where it dwelled for 6 hours before cooling back to room temperature at a rate of $2^\circ\text{C}/\text{min}$. Owing to the materials air sensitivity the obtained material was immediately transferred into an argon glovebox for storage and further characterisation. However, upon characterisation of the material using XRD all samples were found to contain various impurities, including lithium silicates and iron oxides. These impurities would affect the electrochemical behaviour during cycling, but more importantly, they would greatly affect the proposed XAS experiment. XAS experiments require high purity materials as any impurities will distort both the XANES and EXAFS spectra. It was, therefore, decided to synthesise $\text{Li}_2\text{FeSiO}_4$ via a different method in order to reduce/remove these impurities. The method chosen was a two-step sol-gel method based on Brownrigg et al. [23].

3.1.1.1 XRD

The XRD spectrum for $\text{Li}_2\text{FeSiO}_4$ synthesised via the Solid-state method (Figure 3.3) indicates a crystalline sample, with sharp peaks corresponding to the disordered structure of the $\text{P2}_1/\text{n}$ space group. In addition to the $\text{Li}_2\text{FeSiO}_4$ compound, two common impurities associated with this synthesis, namely Fe_3O_4 and Li_2SiO_3 , are also identified. Due to the impurities identified in this sample, the sample is not suitable for XAS experiments. Even after repeating the synthesis several times with minor adjustments to the procedure impurities were still present. It was, therefore, decided to go down a different synthesis route, namely, sol-gel synthesis.

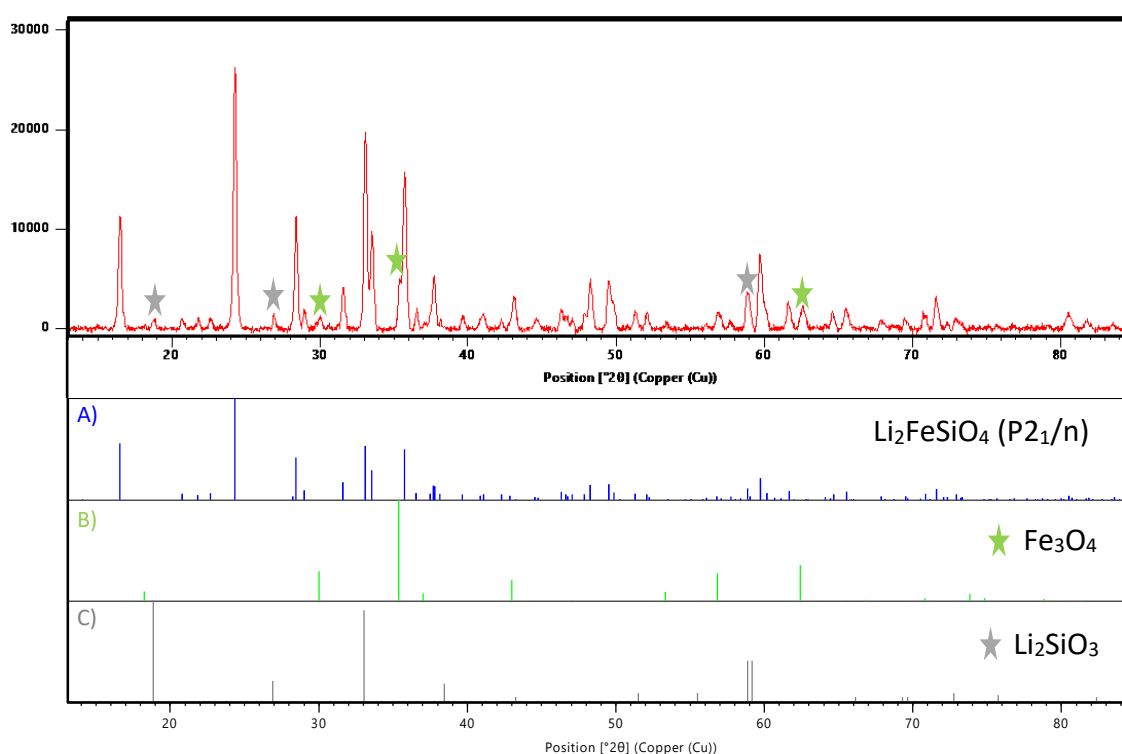


Figure 3.3: XRD of $\text{Li}_2\text{FeSiO}_4$ synthesised via solid state reaction with corresponding peak lists A) $\text{Li}_2\text{FeSiO}_4$ B) Fe_3O_4 C) Li_2SiO_3

3.1.2 Sol-Gel

Stoichiometric amounts of Fe(II)acetate , TEOS, $\text{Li(Ac)} \cdot 2\text{H}_2\text{O}$ and a small amount of acetic acid were added to a Teflon lined autoclave with Ethanol and heated at a temperature of 130°C for 12 hours, the autoclave was opened to reveal a sol-gel, which was dried in an oven at 80°C until a dry powder was formed. The powder was mixed with sucrose so that the resulting carbon weight is 10%. This mixture was ball milled thoroughly in acetone at 600rpm for 1 hour before being dried under vacuum. The resulting mixture was pressed into a pellet and calcined at 600°C for 10 hours

under a constant argon flux. The resulting material was transferred into an argon filled glovebox for storage and further characterisation.

3.1.2.1 Sol-Gel XRD

To ensure the sol-gel method produced a close to phase pure material, the amount of sucrose as well as the environmental parameters needed to be optimised. This was achieved by a “trial-and-error” approach, based on a recipe published by Brownrigg et al. [23]. In this project, the amount of sucrose, annealing temperatures and times as well as oxidising versus reducing environment during various drying stages have been varied. From the XRD (Figure 3.4) it is seen that by following Brownriggs recipe, high amounts of metallic Fe was produced. Following the same recipe but drying under air instead of vacuum resulted in Fe_3O_4 impurities (Figure 3.5).

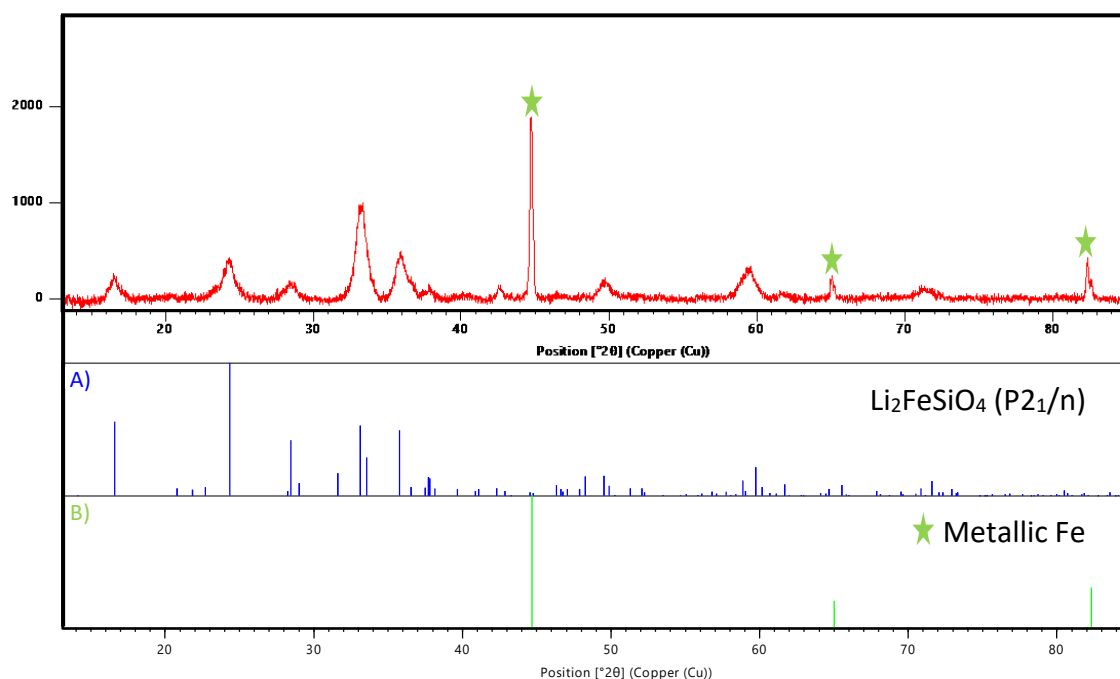


Figure 3.4: XRD of $\text{Li}_2\text{FeSiO}_4$ synthesised via Sol-Gel method with corresponding peak lists A) $\text{Li}_2\text{FeSiO}_4$ B) Metallic Fe

Once a balance was found, a close to phase pure $\text{Li}_2\text{FeSiO}_4$ was synthesised, XRD is shown in Figure 3.6. Whilst there are still impurities, these have been associated with Li_2SiO_3 , an electrochemically inactive material, whilst the sample from Figure 3.5 exhibits more Fe_3O_4 which is electrochemically active and will affect cycling performance.

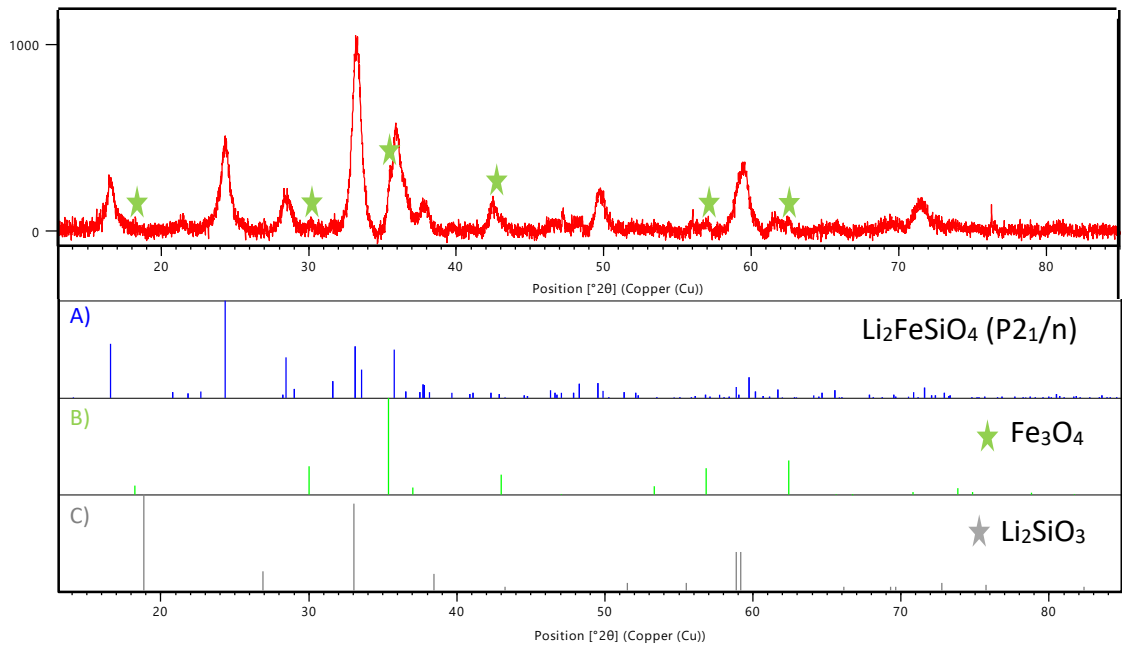


Figure 3.5: XRD of $\text{Li}_2\text{FeSiO}_4$ synthesised via Sol-Gel method with corresponding peak lists A) $\text{Li}_2\text{FeSiO}_4$ B) Fe_3O_4
 Synthesis was highly reproducible and materials synthesised following this procedure were used in all XAS measurements and cycling profiles. The resulting material exhibits a space-group $P2_1/n$, characterised by edge sharing LiO_4 and FeO_4 tetrahedra, where half of the LiO_4 tetrahedra are pointing in opposite directions. It should be noted that small levels of impurities were still present as indicated in Figure 3.6.

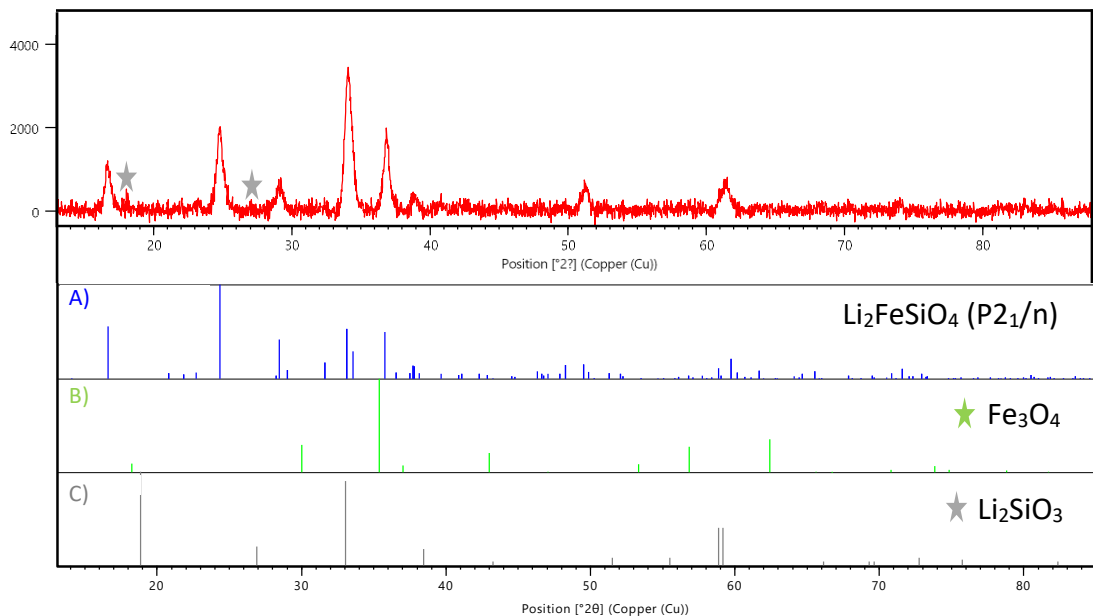


Figure 3.6: XRD of $\text{Li}_2\text{FeSiO}_4$ synthesised via Sol-Gel method with corresponding peak list for A) $\text{Li}_2\text{FeSiO}_4$ B) Fe_3O_4 C) Li_2SiO_3

3.1.3 SEM

SEM has been used to determine the morphology and gain information on particle size (Figure 3.8). However, SEM is difficult to perform on this material, due to the materials inherently low conductivity, which leads to overcharging. This leads to blurry images at high magnifications, making it difficult to determine detailed features, including morphology. Figure 3.7 shows SEM images of $\text{Li}_2\text{FeSiO}_4$ at low magnification (scale bar $100\mu\text{m}$). Indicating some agglomerating of particles (highlighted in orange).

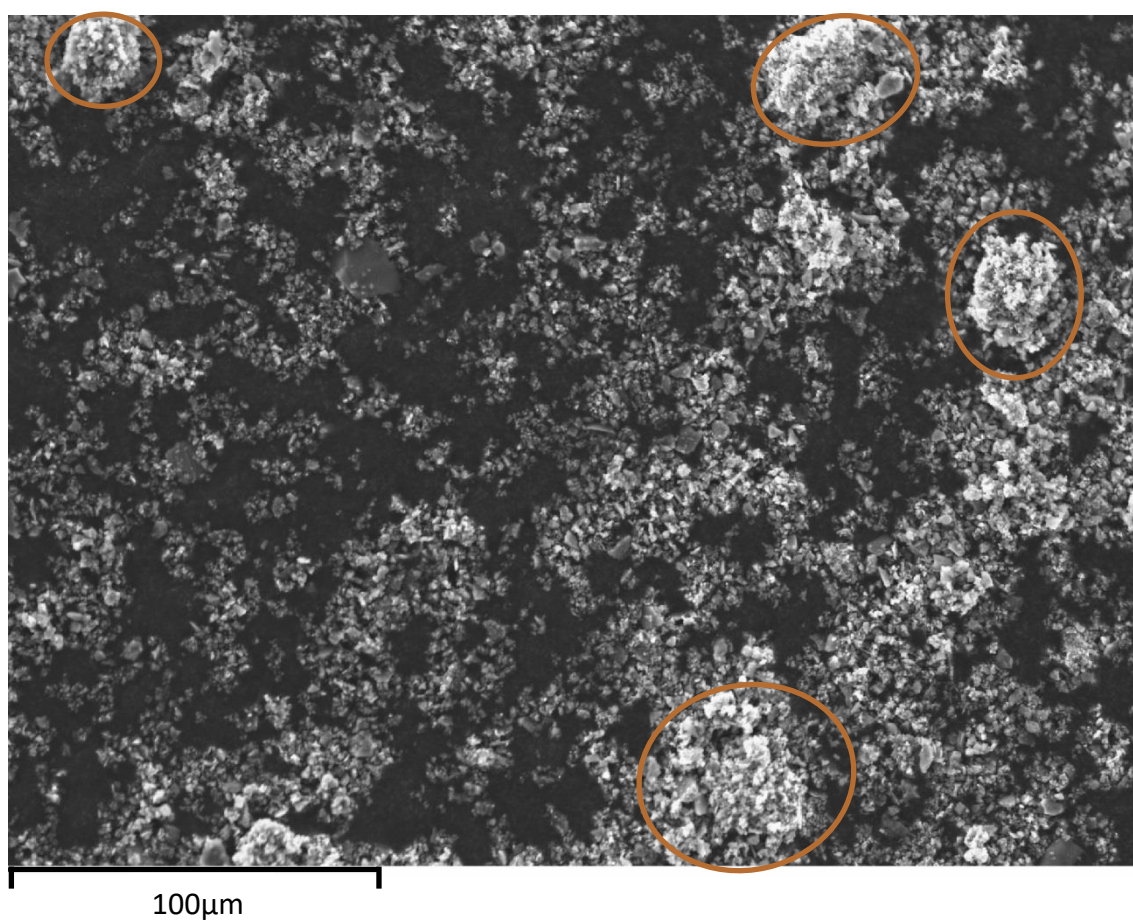


Figure 3.7: Low magnification SEM image of $\text{Li}_2\text{FeSiO}_4$

Increasing the magnification, the images are losing resolution, despite this, Figure 3.8 indicates that there is no regular particle morphology. Instead, irregularly shaped particles are observed, which might suggest that they are agglomerations of smaller particles. However, due to the poor resolution this cannot be fully confirmed.

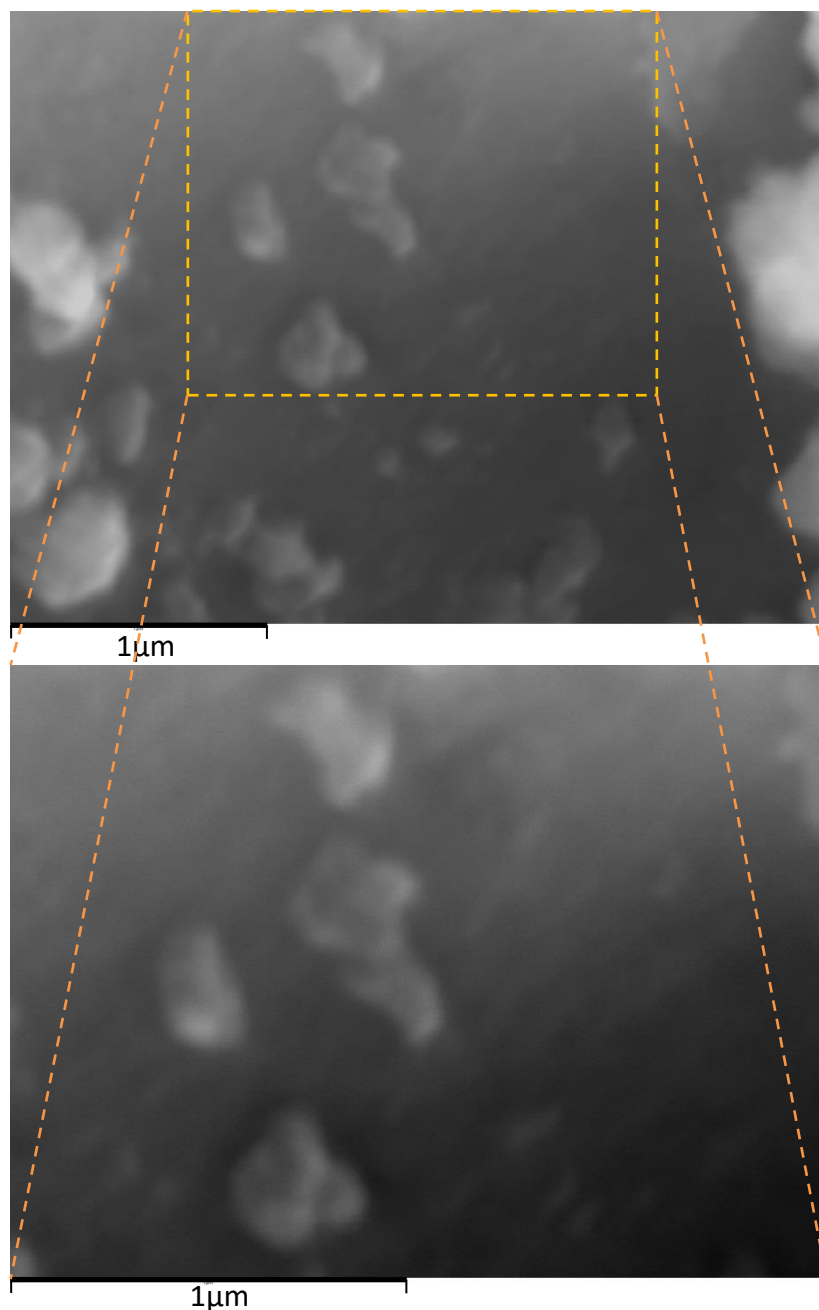


Figure 3.8: High magnification SEM images of $\text{Li}_2\text{FeSiO}_4$

Despite the relatively poor resolution, it is evident from that the individual particle size is sub-micrometre (Figure 3.7). This corresponds well with the sol-gel XRD patterns (Figure 3.6), where a broadening of the peaks is observed when compared to the XRD pattern developed for the solid-state synthesised material, which instead, shows sharp peaks (Figure 3.3). This phenomenon is regularly observed in XRD patterns of nano-materials.

3.2 Cycling

As previously mentioned $\text{Li}_2\text{FeSiO}_4$ has a theoretical capacity of 330mAhg^{-1} , corresponding to a complete removal and insertion of two Li^+ ions [24]. However, experimentally this is difficult to achieve [25]. Figure 3.9 shows a cycling profile of $\text{Li}_2\text{FeSiO}_4$ with a 1Li^+ reaction. This cycling profile is from $\text{Li}_2\text{FeSiO}_4$ synthesised using the solid-state method described in section 3.1.1.

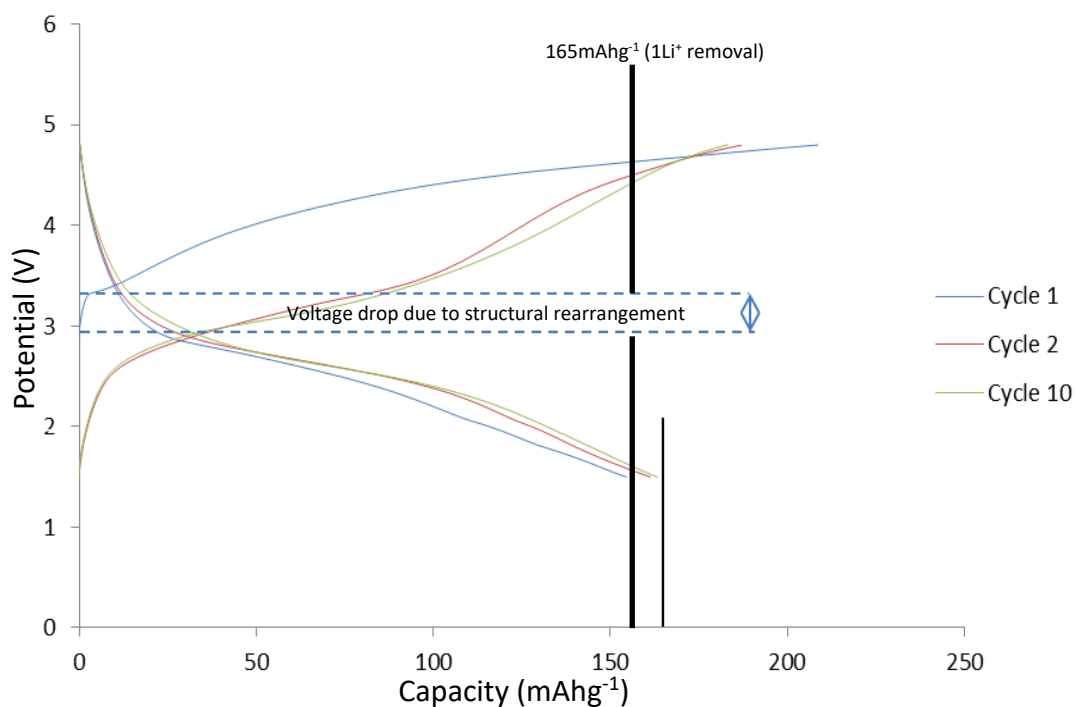


Figure 3.9: Galvanostatic cycling of $\text{Li}_2\text{FeSiO}_4$ showing a 1Li^+ extraction and insertion

The redox potential shift after the first cycle indicates that a structural rearrangement has taken place. Representing a phase transformation from the monoclinic $\text{P2}_1/\text{n}$ to the more stable orthorhombic $\text{Pmn}2_1$ structure [26]. To improve the performance of $\text{Li}_2\text{FeSiO}_4$ as a cathode material, a greater than 1Li^+ redox reaction should be achieved. It is, therefore a necessity to improve the materials ionic as well as electronic conductivity. As already discussed, this was achieved by carbon coating, whilst ionic conductivity has been improved by particle size reduction, using the sol-gel technique. This combination leads to a better performing material and higher capacities than when using the material derived from the solid-state synthesis method, as shown in Figure 3.10. A greater than 1Li^+ redox reaction has been achieved. It should also be mentioned this was achieved with room temperature cycling and not elevated temperature cycling, which will be discussed later in this chapter.

Figure 3.10 indicates that the capacity corresponding to a greater than 1Li⁺ removal/insertion is a reversible process across multiple cycles and not an additional capacity attributed to SEI formation or irreversible reactions, such as, the structural rearrangement of the material during the first cycle. As previously mentioned, the additional capacity, referring to the removal of >1Li⁺ per unit formula has been proposed to be attributed to the formation of a small amount of Fe⁴⁺ ions [5]. Brownrigg et al. [23] found no evidence of Fe⁴⁺ being formed, using in-situ XAS analysis. Instead, the latter study proposed that the additional capacity was linked to considerable electrolyte degradation, supported by the cycling curves and considerable gas formation in the pouch cells during cycling [27]. As capacities greater than 1Li⁺ have been achieved using this material, it was deemed suitable for the following XAS experiments investigating the potential Fe⁴⁺/oxygen edge debate.

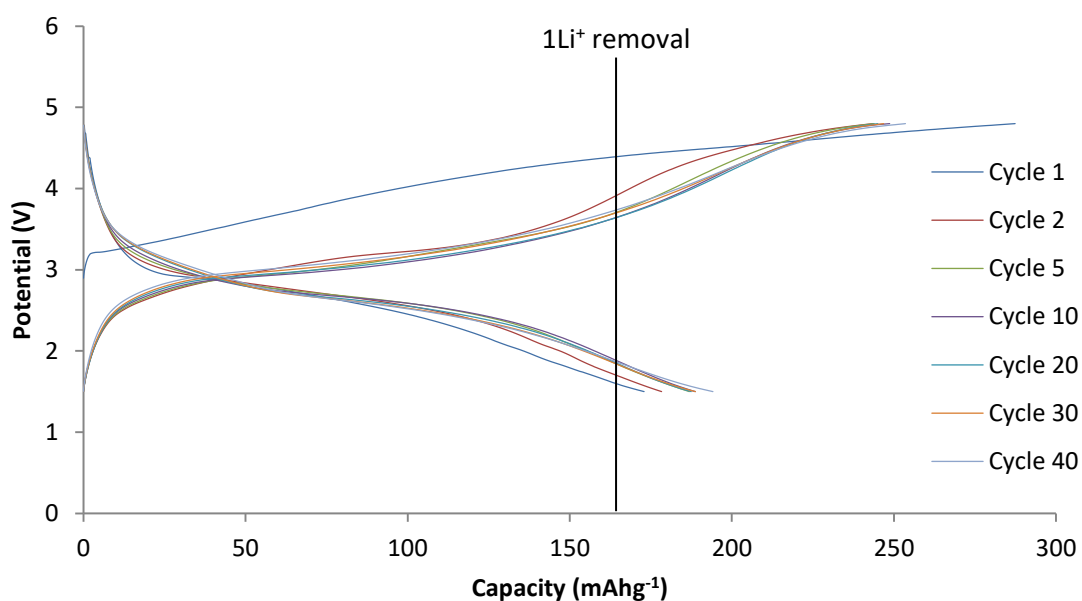


Figure 3.10: Room temperature cycling performance of Li₂FeSiO₄ synthesised via a sol-gel method showing a greater than 1Li⁺ removal

3.3 X-ray Absorption Spectroscopy (XAS)

As described in Chapter 2 X-ray Absorption Spectroscopy (XAS) measurements include an array of useful techniques that allows users to obtain information, including both, electronic as well as geometric structure e.g. oxidation states, bond distances and coordination numbers. Whilst structural information is useful in confirming how materials behave whilst cycling, for example, the structural rearrangements and changes in Fe-O bond distances during the initial cycles of $\text{Li}_2\text{FeSiO}_4$, this has been extensively researched by other groups. The focus of this study is to determine the redox reactions taking place which lead to the additional capacity observed in $\text{Li}_2\text{FeSiO}_4$ materials when cycled beyond the removal of 1Li^+ . There are three hypotheses proposed in the literature: i) access to the $\text{Fe}^{3+}/\text{Fe}^{4+}$ redox pair [5], ii) an oxygen redox reaction occurring [28] and iii) electrolyte degradation [23]. The conclusion of the Brownrigg et. al. study named the latter as the most probable hypotheses, owing to no visible Fe^{4+} observed in the XANES spectra and the shape of the electrochemical cycling curves, showing a noisy but steady increase in voltage after 4.2V. No such “noisy” cycling data was observed with the samples used in this study. However, in an early XANES experiment investigating Fe^{4+} it was observed that some samples were in a pre-oxidised state, that is to say, they were nearing the Fe^{3+} oxidation state before being cycled (pristine), shown in Figure 3.11.

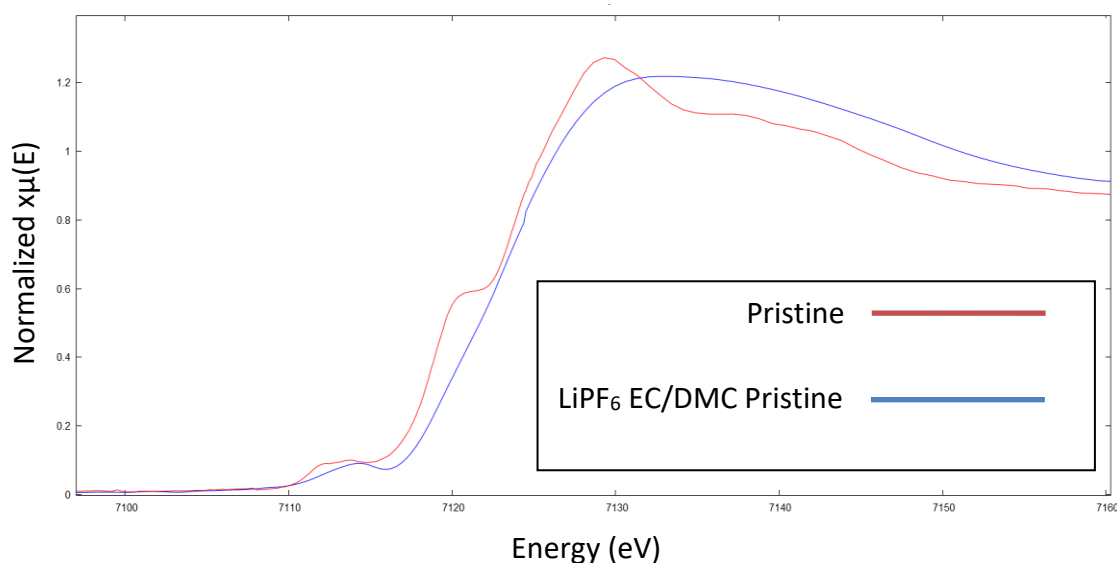


Figure 3.11: XANES data showing pre-cycling oxidation of $\text{Li}_2\text{FeSiO}_4$

Upon further investigation and research, it was found that a potential spontaneous reaction was occurring. According to Arthur et al. [28] LiPF₆ salt spontaneously reacts with Li₂FeSiO₄. However, not all LiPF₆ containing samples appeared to be pre-oxidised. As accurate oxidation state readings are essential when determining the mechanisms behind the additional capacity of Li₂FeSiO₄, this reaction was investigated further.

3.3.1 Electrolyte Effect

To allow further investigation of the possibility to achieve Fe⁴⁺ in Li₂FeSiO₄, the source of this spontaneous reaction should be determined to avoid unwanted reactions in future experiments. Hence, an electrolyte study was proposed whereby a variety of electrolytes commonly used in the literature were investigated to better understand the conditions necessary for the reaction to occur. This investigation was conducted using XANES measurements in pouch cells.

Two causes of the pre-cycling oxidation of the Fe²⁺ to Fe³⁺ ions were proposed. Firstly, it was proposed that the LiPF₆ salt or electrolyte react with the electrode material. Secondly, that a potential is formed over the electrode between the Li-metal and Li₂FeSiO₄ resulting in a cell self-charging effect. To investigate the electrolyte effect, pouch cells were assembled containing three different salts, namely lithium hexafluorophosphate (LiPF₆), lithium bis(trifluoromethanesulfonyl)imide (LiTFSI) and lithium bis(oxolato)borate (LiBOB). Two combinations of solvents (EC/DEC or EC/DMC in a 1:1 ratio) were used together with each of the salts. Two additional cells were made containing the LiPF₆ salt in both solvent combinations along with Li₂FeSiO₄ with no Li-metal present. This was to determine if a potential across the material was required. Table 3.1 shows all cells assembled, including a “pristine” sample.

Cell Number	Name	Salt	Solvents	vs Li metal
1	Pristine	None	None	No
2	LiPF ₆ DEC	LiPF ₆	EC/DEC	Yes
3	LiPF ₆ DMC	LiPF ₆	EC/DMC	Yes
4	LiPF ₆ DEC no Li	LiPF ₆	EC/DEC	No
5	LiPF ₆ DMC no Li	LiPF ₆	EC/DMC	No
6	LiTFSI DEC	LiTFSI	EC/DEC	Yes
7	LiTFSI DMC	LiTFSI	EC/DMC	Yes
8	LiBOB DEC	LiBOB	EC/DEC	Yes
9	LiBOB DMC	LiBOB	EC/DMC	Yes

Table 3.1: Cells assembled for the study of the Electrolyte Effect using XANES

All samples were scanned, but no changes in oxidation state were observed in any of the samples as shown in Figure 3.12 a). It should be noted that these were freshly prepared samples and so, to eliminate the possibility of a time dependant reaction, a follow-up experiment was conducted using the same samples after storage under argon for 14 days, the results of which are shown in Figure 3.12 b).

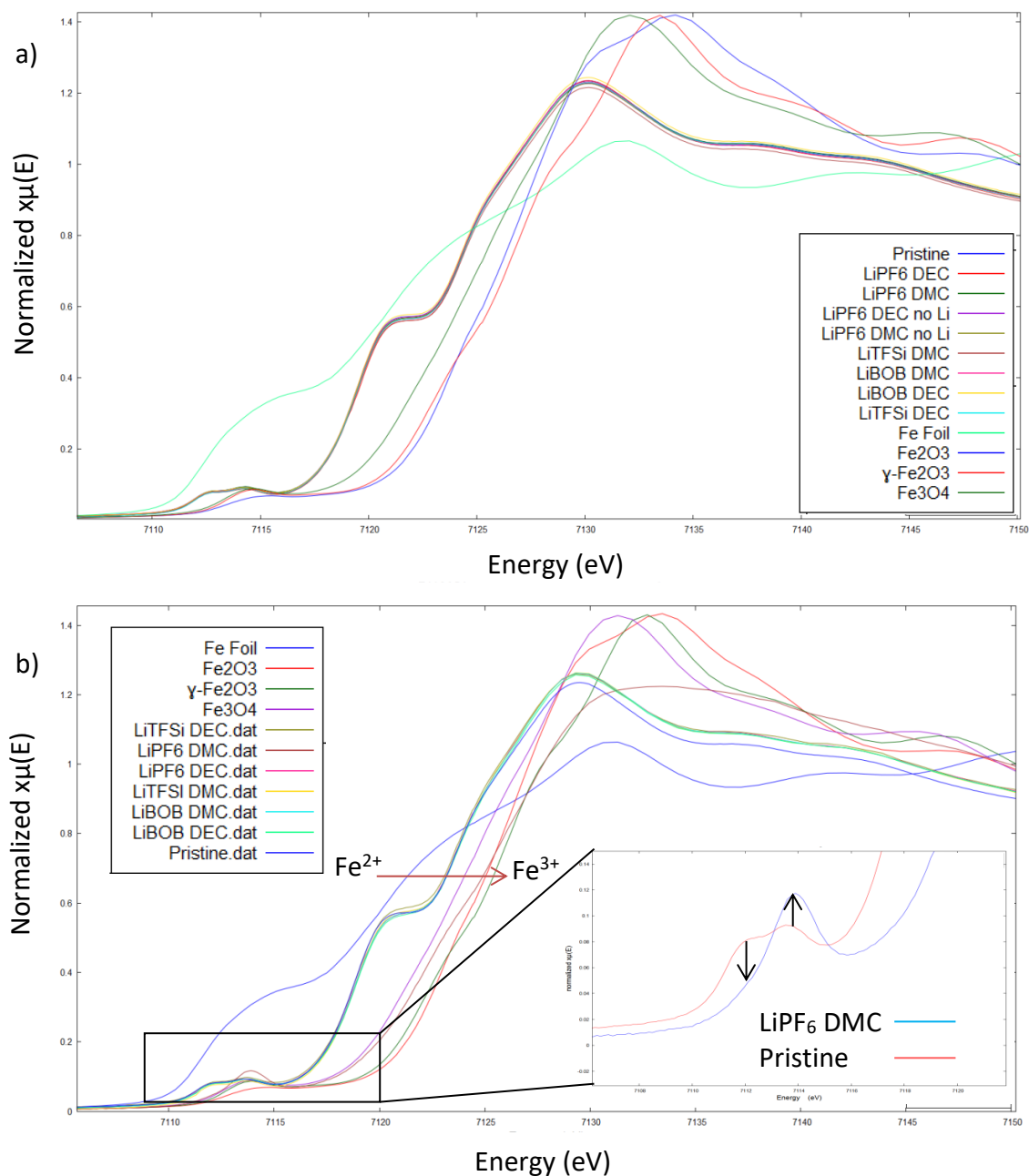


Figure 3.12: XANES data of the Electrolyte Effect study a) freshly prepared samples b) the same samples after 14 days storage under an argon atmosphere

Figure 3.12 b) indicates a clear shift in the Fe K-edge towards Fe³⁺ oxidation state in the sample based on LiPF₆ in EC/DMC electrolyte mounted as a half cell i.e. containing Li-metal anode.

This sample also shows a change in the pre-edge region (inset Figure 3.12). This change from a double peak to a well-defined singular peak is another indication of a change from Fe²⁺ to Fe³⁺ located in a tetrahedral environment according to Brownrigg et al. [23]. It should be noted that all samples were stored and transported identically. This study shows that whilst LiPF₆ does spontaneously react with Li₂FeSiO₄, as reported by Arthur et al. [28], it does so only under specific conditions. Namely, the reaction is solvent dependant (EC/DMC) and requires an OCV to be initiated (Li-metal must be present).

Following the results of this investigation it was decided that all further Li₂FeSiO₄ cells made would use the LiPF₆ in EC/DEC electrolyte as opposed to EC/DMC. Furthermore, all cells would be assembled as close to the experiment date as possible to further reduce the chance of a reaction taking place.

3.4 The Elusive Fe⁴⁺: In-Operando XANES

There is strong debate as to the origin of the additional capacity found in Li₂FeSiO₄. In particular, whether the additional capacity is associated with a further oxidation of iron from Fe³⁺ to Fe⁴⁺ or whether it can be attributed to another reaction or rearrangement, such as, a change in the oxygen oxidation state.

Both sides of the debate have supporting evidence to argue their point. Dongping et al. [5] and Kamon-in et al. [29] used in-situ XANES as evidence of Fe oxidation beyond Fe³⁺ along with other groups reporting a similar Fe³⁺/Fe⁴⁺ reaction via Mössbauer spectroscopy [30] [31] [14] However, it should be noted that the Fe⁴⁺ spectrum overlaps closely that of the Fe²⁺ and Fe³⁺ in Mössbauer measurements, as reported by Liivat et al. [32], where it was determined not possible to determine a definite presence of Fe⁴⁺. Furthermore, DFT calculations imply that an iron oxidation to Fe⁴⁺ within the Li₂FeSiO₄ structure would lead to major structural distortions attributed to the strong electrostatic repulsions between the highly oxidised Fe and Si cations, thus,

preventing a long-term reversible reaction of greater than 1Li^+ if attributing the additional capacity to $\text{Fe}^{3+}/\text{Fe}^{4+}$ redox couple. [33]

The contribution of oxygen in the reaction is supported not only by DFT calculations [34] where it is suggested a delithiation of $>1\text{Li}^+$ leads to a reorganization of the oxygen bonding, but also ex-situ XAS measurements on the O K-edge where a distinct change in the pre-edge is reported by Masese et. al. which proposes an oxygen contribution to a charge compensation mechanism [35]. However, due to the nature of the XAS technique used and the low energy of the oxygen K-edge this technique only gives surface and very shallow penetration of the electrode surface. This study utilises a different technique explained in Chapter 2 where a true representation of the bulk is observed.

3.4.1 Fe K-edge XANES

It has been shown that the material synthesised and used in this study is capable of a greater than 1 removal and reinsertion of lithium upon cycling between 1.5V and 4.8V. It is, therefore, imperative that we investigate the Fe oxidation state during this cycling. An in-operando technique is used, this allows for uninterrupted cycling and constant data acquisition. The pouch cells were prepared as described in Chapter 2.

Figure 3.13 A) shows the XANES data of the first charge cycle, indicating a clear progression in the Fe K-edge position from Fe^{2+} to Fe^{3+} . It should be noted that there is no indication of Fe-oxidation state progressing further than Fe^{3+} , as evidenced by the reference Fe_2O_3 reference samples also plotted. This is despite an initial charging capacity of greater than 300mAhg^{-1} as demonstrated by the electrochemical cycling profiles of this sample (Figure 3.14), corresponding to greater than 1Li^+ removal. It can also be seen that the aforementioned change in the pre-edge feature attributed to the formation of Fe^{3+} ions in a tetrahedral site is also seen in Figure 3.13 A) with a magnified image of this area shown in Figure 3.13 B).

A closer look at the Fe K-edge XANES during the first charge Figure 3.13 C) shows that no discernible increase in Energy is observed after the first couple of scans during the 4.8V hold. The overlapping scans suggest no further increase in Fe oxidation state is achieved during further cycling.

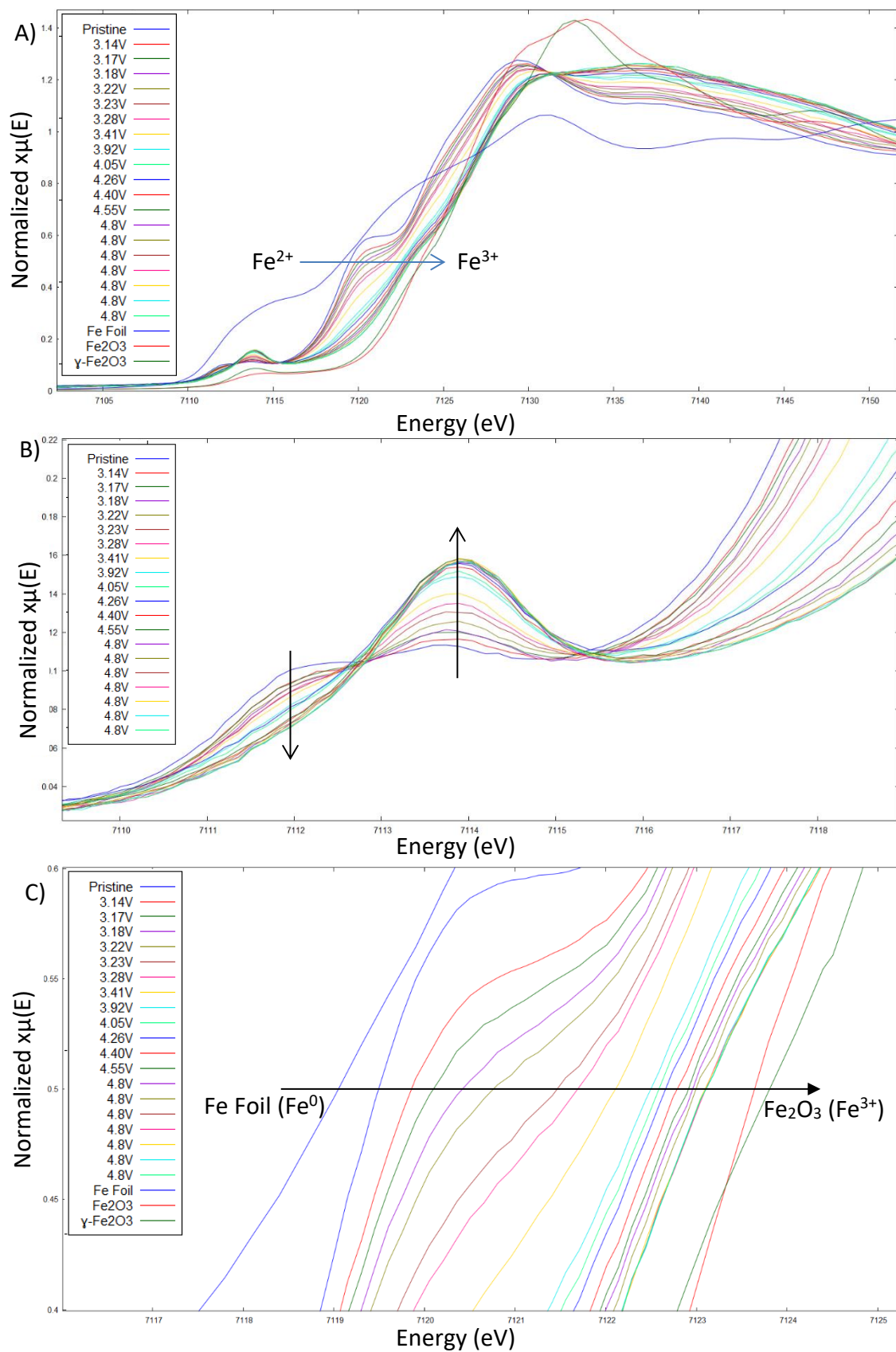


Figure 3.13: XANES data showing: A) a clear progressive change in oxidation state from Fe²⁺ to Fe³⁺ during the first charge B) A zoomed in image of the pre-edge feature showing the same progressive change from Fe²⁺ to Fe³⁺ C) a zoomed in image of the main Fe K-edge indicating no further progression beyond Fe³⁺ is achieved

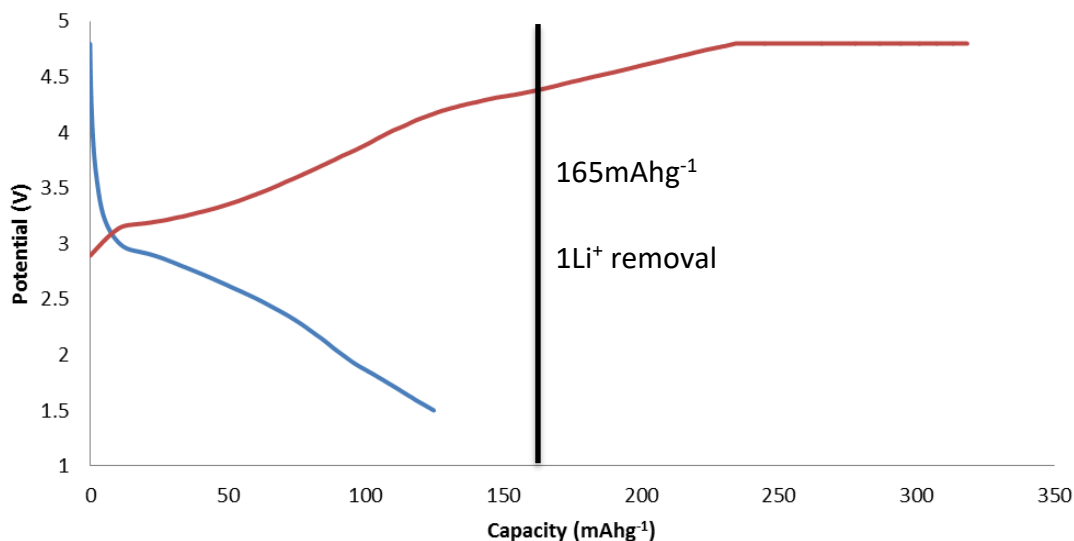
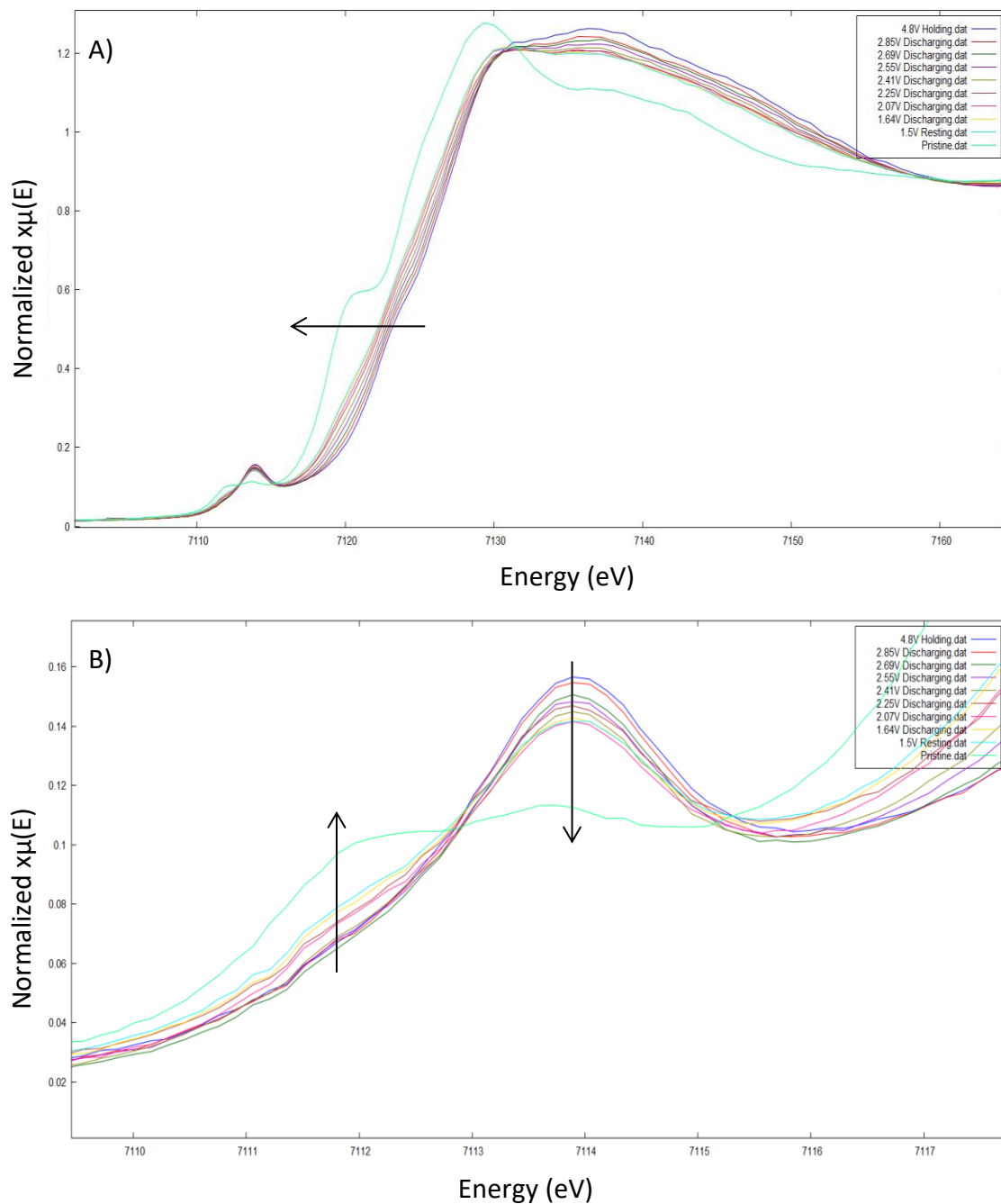


Figure 3.14: Galvanostatic cycling profile for $\text{Li}_2\text{FeSiO}_4$

It should be noted here, that the purpose of this XAS experiment was to search for evidence supporting the existence of Fe^{4+} within the sample upon charging. The charging was, therefore, carried out at the slow rate of $\frac{C}{6}$ (corresponding to 1Li^+ removal) and then further held to ensure that at least 1Li^+ was extracted, but also to allow for the greatest possibility of observing Fe^{4+} if this is a short lived (unstable) state. The discharge was deemed less important for the purpose of this experiment, and so was cycled at a higher rate, hence the low discharging capacity shown in Figure 3.14

The faster discharge rate also impacts the reversibility of the $\text{Fe}^{2+} \leftrightarrow \text{Fe}^{3+}$ redox reaction. Figure 3.15 A) shows a trend of decreasing Fe oxidation state towards Fe^{2+} , however, this is only achieved in part. This is further supported in Figure 3.15 B) where a partial reversal of the pre-edge feature can be seen.



**Figure 3.15: XAS data showing a partially reversed Fe oxidation state going from Fe^{3+} to Fe^{2+} upon first discharge
 A) main edge B) magnified pre-edge**

3.4.2 Oxygen K-Edge Contribution

So far it has been shown that the samples synthesised in this study are phase pure, their cycling performance goes beyond a 1Li^+ redox reaction, and that upon cycling no evidence supporting the existence of Fe^{4+} in this material has been found using XAS techniques. As previously mentioned, it has been proposed that additional capacity can be attributed to a reaction in the oxygen edge, which has been supported by XAS measurements using a soft x-ray surface probing technique. Whilst this is promising, it could also be argued that it does not give a true representation of the bulk material, and thus, we employ a different technique to Masese et al. [35] and Lu et al. [36]. The technique, described in Chapter 2, is a Raman based technique whereby the spectrum is collected via an energy loss. Simply put, the beam enters at a much higher elastic energy and the loss in energy from hitting the sample is measured to create a spectrum (as opposed to hitting the sample at the O K-edge energy of 536eV where sample penetration is very low) this allows a true representation of the bulk material.

Not only does this technique allow the observation of the oxygen K-edge but also other surrounding low energy edges including the Li K-edge and Fe L-edge. Here the Li K-edge was used to simply help ensure we were viewing our sample and not surrounding polymer pouches or glues. Whilst the Fe L-edges were used to follow changes in the Fe *d*-states.

Figure 3.16 shows A) C) the beamline setup and B) sample pouches. Due to the nature of this technique all measurements were taken ex-situ, as one measurement takes around 10 hours. The materials aforementioned air sensitivity was considered when designing sample holders for the measurements. Laminate aluminium pouches were assembled with windows cut out and pure aluminium foil windows were inserted where the sample was to be placed. This reduces oxygen interference from the pouches' polymer laminates. Laminates were vacuum sealed under a dry argon atmosphere (Argon glovebox) to reduce oxygen contamination of the active material.

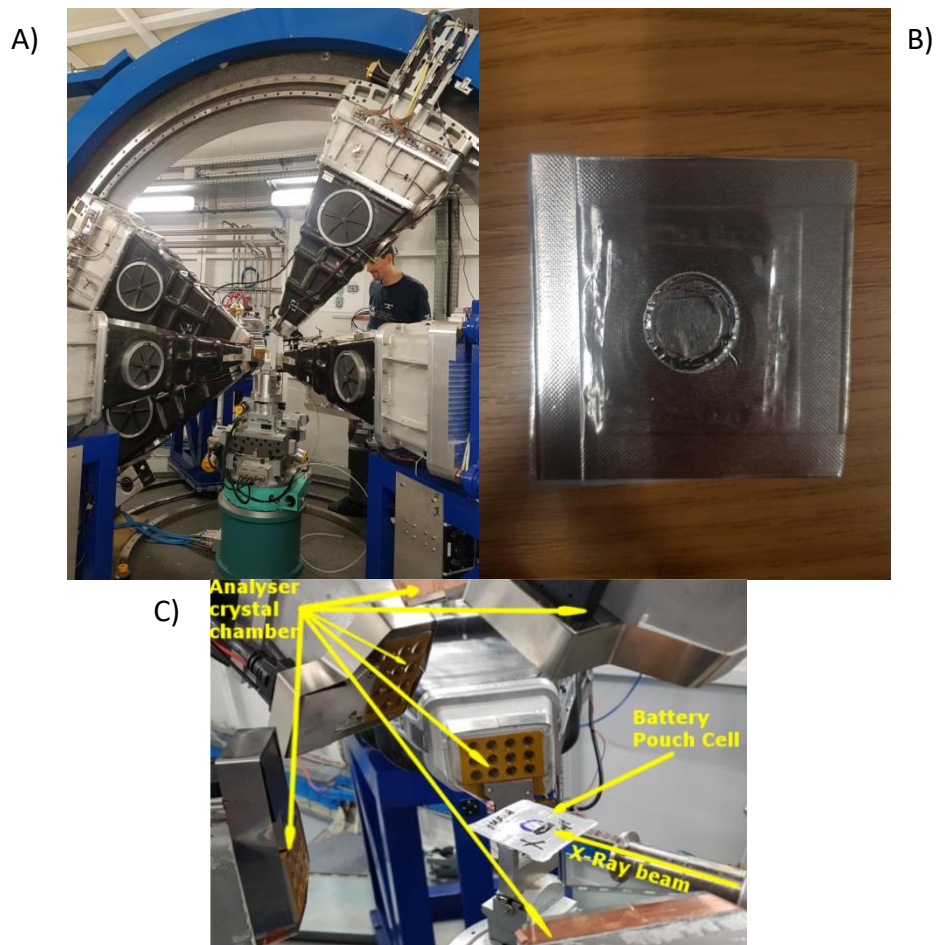


Figure 3.16: A) an image showing the beamline setup and position of moveable sensors B) An example of a sample pouch with aluminium windows C) A close up of sample holder and sensor position, as well as beam position

Once samples have been placed in the holder x and y position scans are used to determine the best position for the main data collection scans. These scans show us a “slice” of what we are hitting and thus, we can determine what the final beam position will be. Figure 3.17 below shows an example “slice” image of the y plane scan.

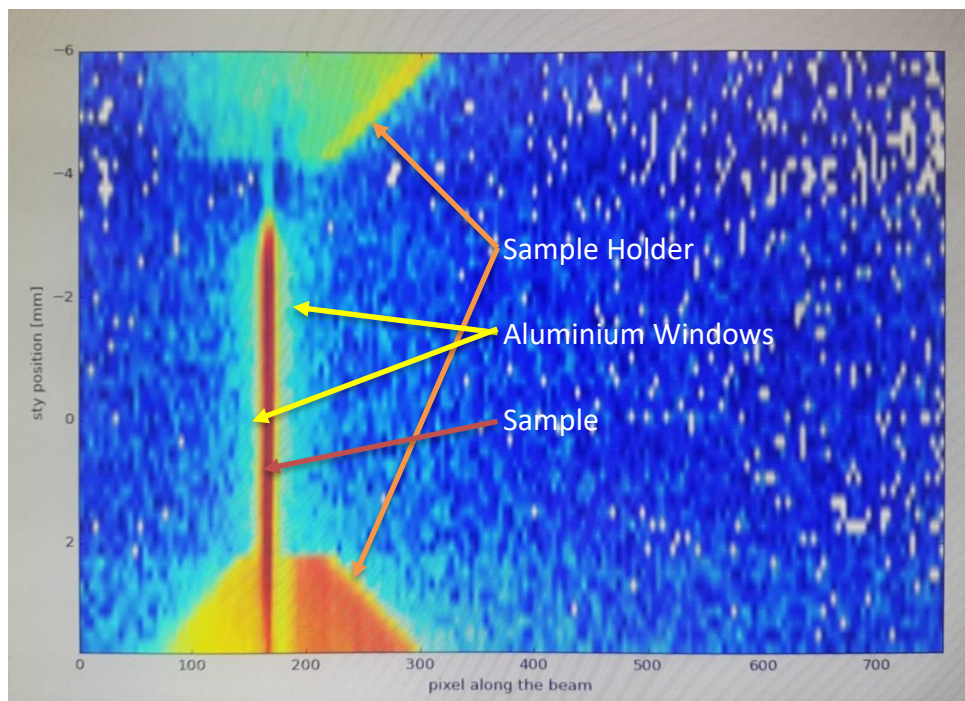


Figure 3.17: An image of a y-plane scan of the sample pouch and holder

From the scan in Figure 3.17 the holder, pouch, and sample can be clearly defined. The bright red strip is the sample, therefore, a beam position roughly central to this is chosen, and the procedure is then repeated for the x plane.

For this sample, it was found that a vertical orientation of the sample did not yield a high enough energy loss to properly observe detailed oxygen edge peaks. This may be down to the thin profile of the cast electrodes or the small quantity of sample deposited on the current collector. It was, therefore, decided to angle the samples so as to hit more of the bulk material as the beam passes. In addition to this, the sensors were spread out to gain a better representation of the exiting beam, including more sensors observing the low-q region. As depicted by Figure 2.10 in Chapter 2, low-q indicates the region where there is a low transfer of momentum imparted by the incident beam and, therefore, is evidenced by low scattering angles. To observe the low-q region, more detectors are placed rear-facing in respect to the direction of the incident beam (Figure 3.16 A) and C).

Figure 3.18 shows a representation of the state of charge each sample was cycled to when the sample was removed, washed and placed into the sample pouches. It is shown that cycling limits are equal to $>1\text{Li}^+$ removal and reinsertion, ensuring the potential of an oxygen contribution.

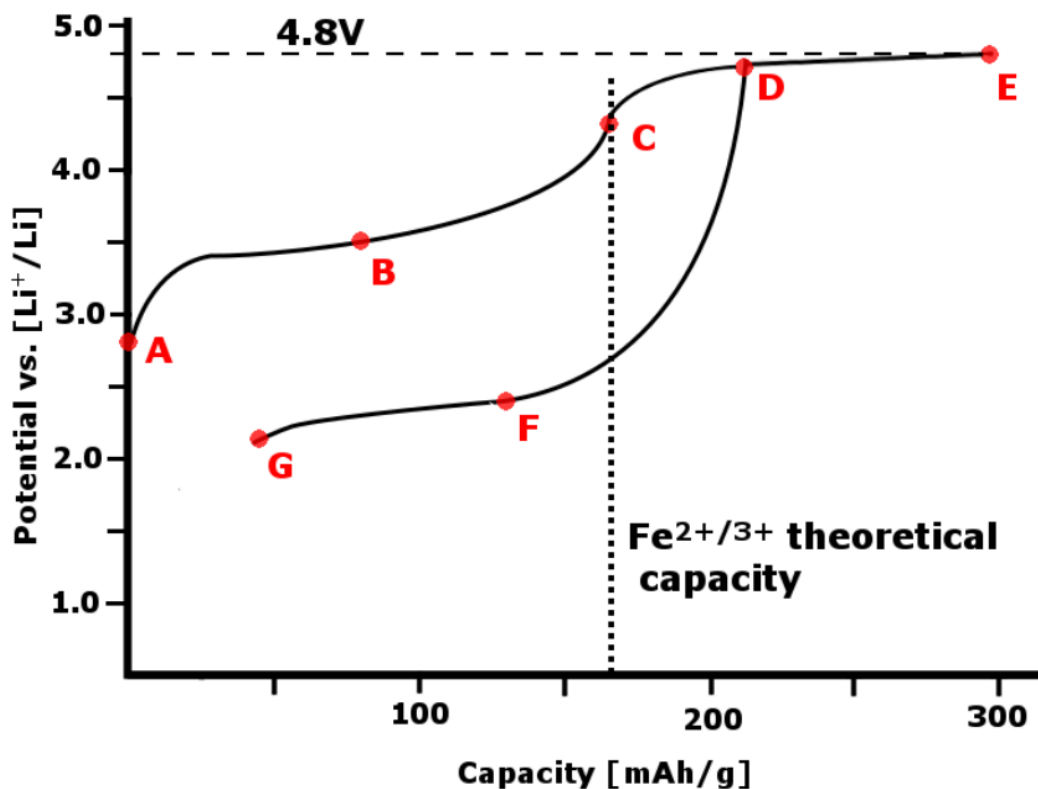


Figure 3.18: A graphical representation of $\text{Li}_2\text{FeSiO}_4$ samples' state of charge used for this experiment, dashed line denotes 1Li^+ removal

These points were chosen as it not only gives the extremes (pristine and fully charged/discharged) but also intermediate steps in an effort to determine if/or the oxygen edge is actively contributing to the reaction.

To ensure all features are observed during sample analysis Figure 3.19 shows an example of a full range scan separating the low-q and high-q detectors, as sometimes features present are masked in high-q or low-q regions. The energy range indicated in Figure 3.19 is the effective energy range, not the energy of the incident beam, which was in the region of 10keV , as described in Chapter 2.

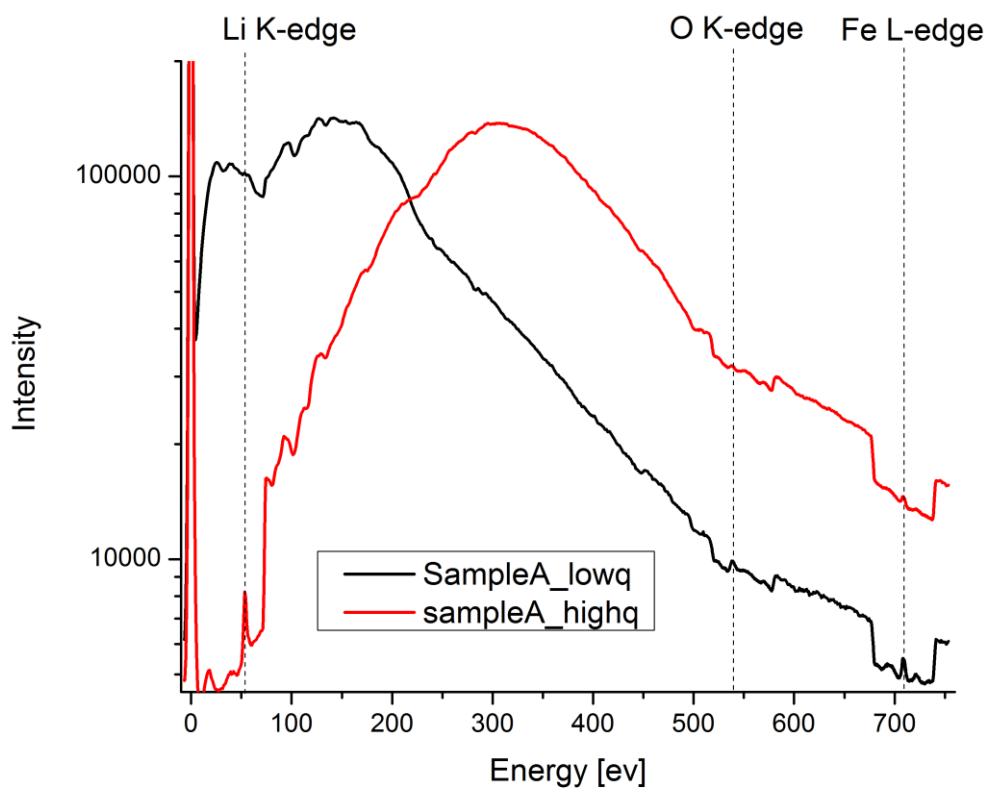


Figure 3.19: An example of the full-range XRS scan, with indicated Li, O and Fe edges

It can be seen from this scan that both lithium and iron are present; indicating the incident beam is targeting the sample. From the Li K-edge a larger and more clearly defined peak is reported in the high-q region compared to that of the low-q, whilst the Fe L-edge as well as the O K-edge show more defined peaks in the low-q region.

Firstly, we take a look at Fe L₃-edges. The observation of L-edges directly probes the spin-state and chemical bonding by monitoring the 2p_{3/2} → 3d transitions. Figure 3.20 follows this evolution during charge A) and discharge B). It is evident that the transition consists of two peaks, observed between 708 and 710eV. These two peaks are an observation of the 2d → 3d L-edge transition and, as indicated in Figure 3.20, correspond directly to the redox couple Fe²⁺ → Fe³⁺. The continued increase in the transition towards Fe³⁺ post charge (holding at 4.8V (sample E)) compared to the fully charged (sample D) can be attributed to Li₂FeSiO₄'s aforementioned slow kinetics, and potentially, some relaxation due to these samples being ex-situ.

The Fe L-edge's double peak feature can be directly compared to the Fe K-edge XANES pre-edge double peak feature in Figures 3.13 B) and 3.15 B) where the trends match closely. When looking at the discharge spectra, it can be seen that there is only a partial reversal of the Fe³⁺ → Fe²⁺. This can be attributed to two factors, firstly, the incomplete discharge, indicated by sample G in Figure 3.18 and secondly, the known structural rearrangement occurring during the first charge of Li₂FeSiO₄.

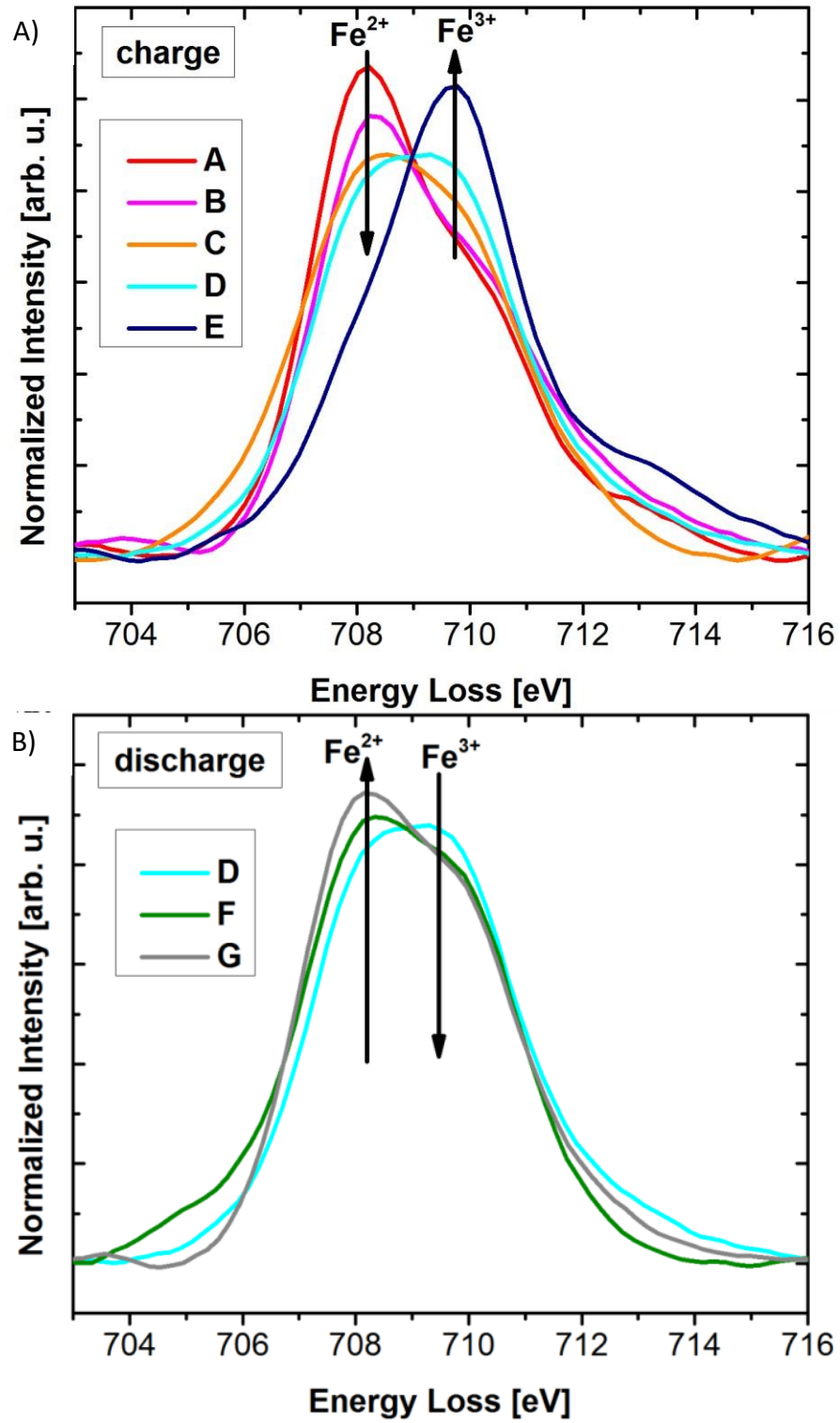


Figure 3.20: Fe L-edge XRS scans through $\text{Li}_2\text{FeSiO}_4$ first charge (A) and discharge (B)

Next, we take a look at the O K-edge spectra. Here, two main features are investigated. Firstly, the pre-edge feature at 531eV which corresponds to the O1s \rightarrow Fe3d and O2p orbital. Secondly, the broad main peak centred around 539eV, corresponding to O1s electron excitation above the Fermi level and hybridisation of O2p and Fe 42p orbitals according to Yoon et al. [37].

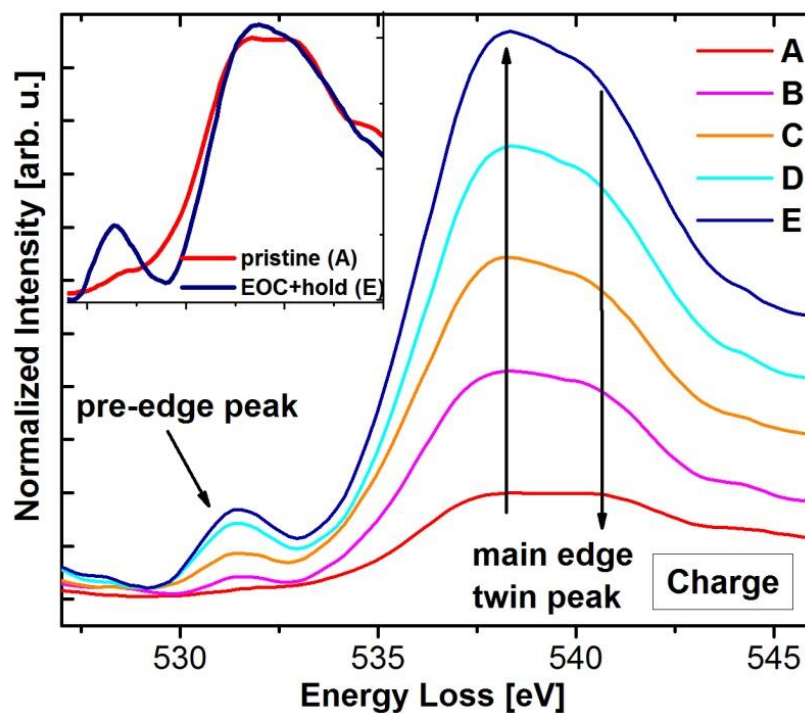


Figure 3.21: Oxygen edge XRS spectrum of $\text{Li}_2\text{FeSiO}_4$ during first charge

Figure 3.21 shows a steadily increasing pre-edge peak intensity upon charging of the material. This change in pre-edge upon Li^+ deintercalation reveals information about hole state distribution and the oxygen atoms' effective charge [37]. The increase in pre-edge intensity only partially agrees with Lu et al. [36], who observed an abrupt change in O K-edge pre-edge feature once the state of charge corresponded to a removal of $>1\text{Li}^+$ per formula unit, at this point they report a large increase in pre-edge peak intensity, prior to this, no change in the O K-edge was observed.

When looking at the oxygen main edge, no significant peak shift is observed. This indicates that the oxygen oxidation state remains unchanged during cycling, i.e. no direct oxygen redox reaction is taking place.

However, other changes in the main edge are observed. Namely, the main peak intensity increases and the broad twin-peak feature changes to a broad more singular feature. These changes are attributed to a change in the oxygen orbitals during Li^+ removal.

Upon discharge, a partial reversal of pre-edge peak intensity is observed shown in Figure 3.22. A reversal is expected due to the reinsertion of Li^+ . The reasoning behind the observation of only a partial reversal (when comparing sample G to pristine sample A) can be attributed to an incomplete discharge (Figure 3.18) suggesting not all Li^+ has been reinserted. Another potential contributing factor is the structural rearrangement known to take place during the first cycle.

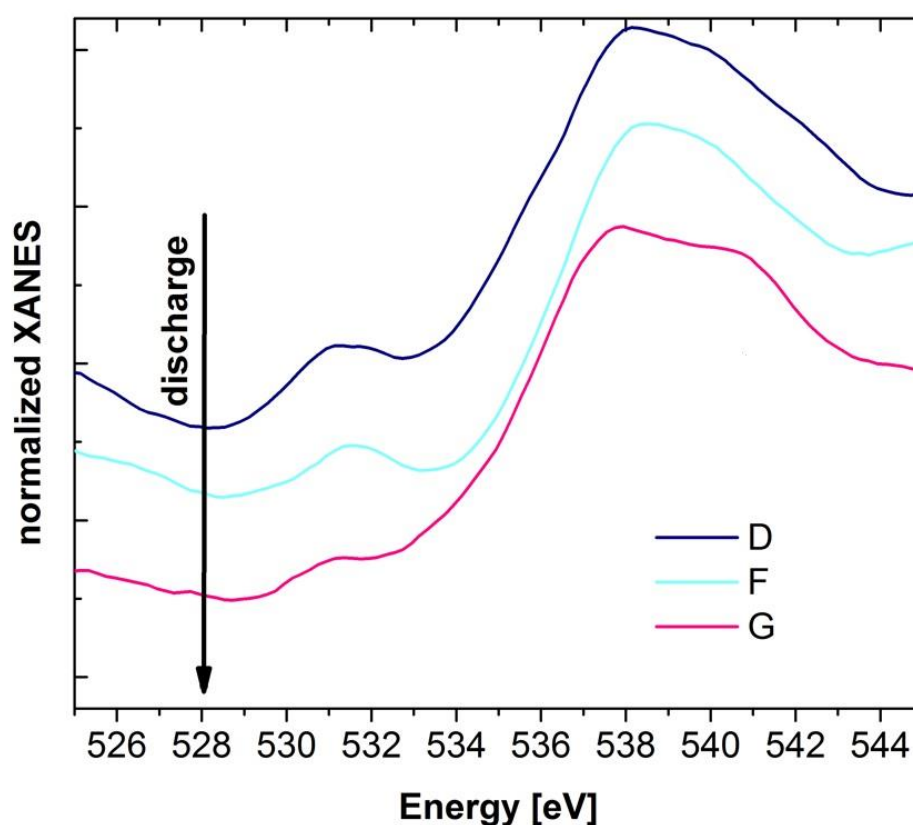


Figure 3.22: Oxygen edge XRS spectrum of $\text{Li}_2\text{FeSiO}_4$ during first discharge

This suggests – contrary to a previous publication [35] – that oxygen not only contributes the capacity of $\text{Li}_2\text{FeSiO}_4$ but does so throughout its cycling and not only after more than 1Li^+ has been removed per molecular unit as suggested by Masese et al. These graphs also indicate that the process is largely reversible, something not shown in Masese’s paper. In addition to the oxygen edge suggesting a continual

contribution upon cycling the Fe L-edge also suggests a continual contribution of iron throughout cycling and not only until the point $x=1$ in $\text{Li}_{2-x}\text{FeSiO}_4$. These findings are not only interesting and important in the field of understanding high capacity cathode materials but are also novel.

As a part of this work, FDMNES calculations have also been carried out to simulate the materials electronic configuration. A good likeness was achieved, further suggesting a gradual emptying and re-filling of 3d orbitals upon cycling [38].

Whilst the findings of this O K-edge XRS study do not definitively prove that oxygen is the source of additional capacity in $\text{Li}_2\text{FeSiO}_4$, it does suggest bulk material oxygen activity throughout cycling and a strong contribution as part of a charge compensation mechanism, preserving electronic and structural stability of $\text{Li}_2\text{FeSiO}_4$ during a $>1\text{Li}^+$ removal. In addition, this study, in combination with the in-operando Fe K-edge XANES and other works by various groups strongly suggest that Fe^{4+} is not the source of the additional capacity in $\text{Li}_2\text{FeSiO}_4$. Other potential sources of additional capacity which need to be further investigated include surface reactions as reported by Dominko et al. [39] and electrolyte degradation as reported by Brownrigg et al. [23].

3.5 Elevated Temperature Cycling

It was previously mentioned in this chapter that $\text{Li}_2\text{FeSiO}_4$ suffers from a low ionic conductivity. This can dramatically hinder the performance of $\text{Li}_2\text{FeSiO}_4$ as a cathode material. Despite using material with controlled nanoparticle size distribution in combination with carbon additives, the material still shows significantly lower ionic conductivity than other cathode materials, such as LiCoO_2 . Higher conductivity – in general – allows us to utilize a higher percentage of the materials theoretical capacity and cycle the material at a higher C-rate.

All the materials cycled in previous sections used cycle rates of $\frac{C}{6}$ or slower, allowing for the removal/insertion of $>1\text{Li}^+$ per unit formula. However, as C-rates increase the achievable capacity drops and polarisation increases, as shown in 3.23.

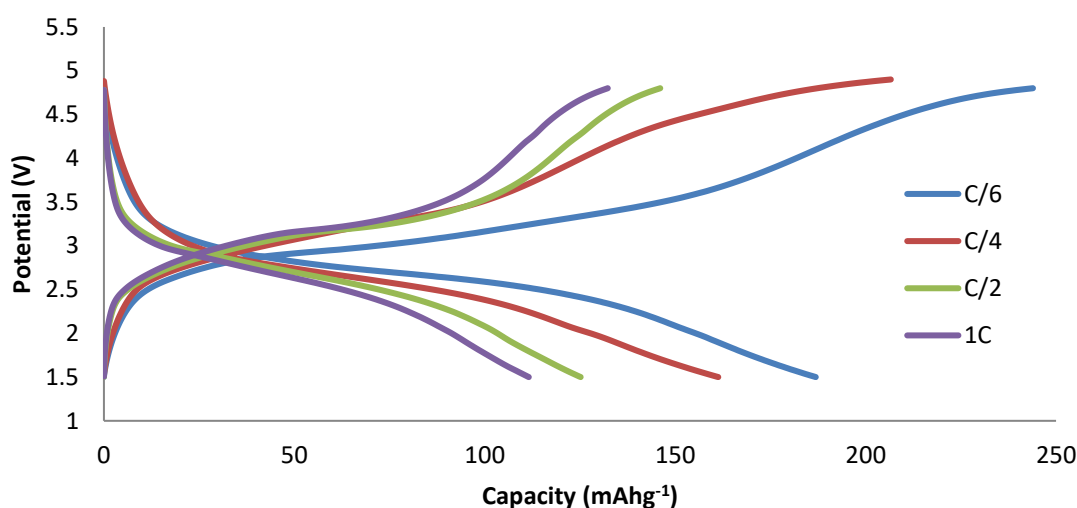


Figure 3.23: Galvanostatic cycling profiles of $\text{Li}_2\text{FeSiO}_4$ cycled at various rates

Another method regularly employed to improve ionic conductivity and thus, performance, is cycling at elevated temperatures. High temperatures pose a risk when cycling Li-ion batteries as the electrolytes are combustible. As a consequence, all elevated temperature cycling was undertaken using a moderate temperature of 55°C to limit electrolyte deterioration. The electrolyte used was standard 1M LiPF₆ in EC/DEC 1:1.

Figure 3.24 shows cycling curves at room temperature, the cell was then heated up in-operando partway through cycle 3. This is clearly visible by a sudden increase in voltage. This can be attributed to improved kinetics associated with elevated temperatures. It is well known that elevated temperatures increase ionic conductivity and, therefore, reduce internal resistivity in a material which, in turn, leads to a reduction in polarization, also observed in Figure 3.24.

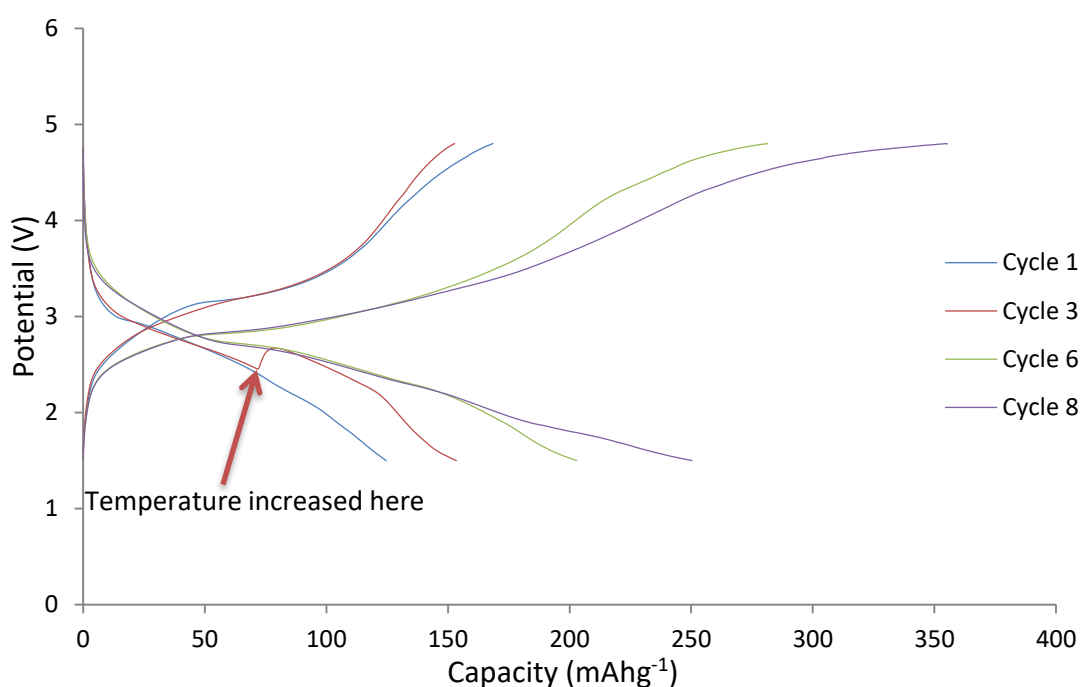


Figure 3.24 Room temperature vs elevated temperature Galvanostatic cycling curves for Li₂FeSiO₄

In addition to this, a marked increase in both charge and discharge capacities are observed. With discharge capacities increasing from around 125mAhg⁻¹ in the first cycle to an increased capacity of up to 250mAhg⁻¹ observed in cycle 8. It is clear that elevated temperature cycling improves the short-term battery performance dramatically, allowing for faster cycling and increased capacities. However, as

previously mentioned, the electrolyte will deteriorate over time if the system is exposed to these temperatures long-term. There is a potential to resolve this issue with the use of a temperature stable, solid polymer electrolyte, further discussed in Chapter 5. It should be noted that whilst additional capacities are observed due to enhanced kinetic properties, to keep the system at these temperatures requires additional energy, potentially negating the benefits in increased performance. This severely reduces the potential applications for a system like this.

3.6 Conclusion

In this chapter $\text{Li}_2\text{FeSiO}_4$ was investigated as a high capacity, affordable, environmentally benign cathode material. It has been shown that phase pure $\text{Li}_2\text{FeSiO}_4$ was synthesised via a sol-gel process. Electrochemical cycling of the phase pure material, yielded a capacity corresponding to a Li^+ removal of greater than 1 per unit formula when cycled between 1.5V and 4.8V. The origin of the increased capacity has been studied in detail using both XAS and XRS techniques. It has been proposed in literature that the additional capacity is associated with an $\text{Fe}^{3+}/\text{Fe}^{4+}$ redox couple [5] or related to an oxygen charge compensation mechanism [28].

Further to this, an “electrolyte effect” XANES study was conducted to ensure no unwanted, spontaneous reactions occurred during the investigation into a possible $\text{Fe}^{3+}/\text{Fe}^{4+}$ redox couple. This was undertaken when an early study and a report in literature suggested that, under certain conditions, $\text{Li}_2\text{FeSiO}_4$ reacted with the electrolyte, resulting in a pre-cycling oxidation from Fe^{2+} to Fe^{3+} . The study indicated that $\text{Li}_2\text{FeSiO}_4$ reacted with LiPF_6 salt, when in combination with EC/DMC solvents and was placed in a cell format vs Li-metal. It was also found that the reaction was somewhat time dependant, with no reaction occurring in the freshly prepared cells, however, with a reaction occurring in the cell stored for 14 days. As a result, all cells were prepared using 1M LiPF_6 in EC/DEC.

The in-operando XANES study conducted on this material showed a clear Fe K-edge progression, as expected, from Fe^{2+} to Fe^{3+} . Upon continued cycling, no further increase or shift in Fe K-edge oxidation state was observed. This strongly suggests that the presence of Fe^{4+} is not observed under current cycling conditions in $\text{Li}_2\text{FeSiO}_4$,

therefore, the additional capacity associated with a $>1\text{Li}^+$ removal ought to be attributed to some other reaction.

This claim is further supported by the ex-situ XRS study conducted to observe the O K-edge. This study yielded important information on the charge compensation contribution of oxygen in the cycling of $\text{Li}_2\text{FeSiO}_4$. It indicates that oxygen reversibly contributes throughout the materials cycling, not only after 1Li^+ is removed, this contradicts a study conducted by Masese et al. [35] using soft XAS probing, which, unlike the XRS technique employed in this study, is limited to surface observations.

In addition to the XAS studies conducted, a short study on the cycling of $\text{Li}_2\text{FeSiO}_4$ at elevated temperatures was conducted to observe and improve the materials kinetic properties. It was found that an elevated temperature leads to higher kinetics resulting in higher capacities and lower polarisation when compared to room temperature cycling. This suggests that the material needs further enhancement to improve its internal kinetics or that the material may be better suited to environments where elevated temperature cycling is preferable. However, as stated, this would require an intensive study on electrolyte materials.

Whilst this study does not conclusively determine the origin of the reaction occurring beyond 1Li^+ removal, it does contribute to the wealth of knowledge on this extensively researched subject and $\text{Li}_2\text{FeSiO}_4$ remains well-placed as a promising high capacity and environmentally benign cathode material.

3.7 References

- [1] N. Nitta, F. Wu, J. T. Lee and G. Yushin, "Li-ion battery materials: present and future," *Materials Today*, vol. 18, no. 5, pp. 252 - 264, 2015.
- [2] Z. Chen, S. Qiu, Y. Cao, J. Qian, X. Ai, K. Xie, X. Hong and H. Yang, "Hierarchical porous Li₂FeSiO₄/C composite with 2 Li storage capacity and long cycle stability for advanced Li-ion batteries," *Journal of Materials Chemistry A*, vol. 1, no. 16, pp. 4988 - 4992, 2013.
- [3] Z. Ding, D. Zhang, Y. Feng, F. Zhang, L. Chen, Y. Du, D. D. Ivey and W. Wei, "Tuning anisotropic ion transport in mesocrystalline lithium orthosilicate nanostructures with preferentially exposed facets," *NPG Asia Materials*, vol. 10, no. 7, 2018.
- [4] X. Lu, H. Wei, H.-C. Chiu, R. Gauvin, P. Hovington, A. Guerfi, K. Zaghib and G. P. Demopoulos, "Rate-dependent phase transitions in Li₂FeSiO₄ cathode nanocrystals," *Scientific Reports*, vol. 5, 2015.
- [5] D. Lv, J. Bai, P. Zhang, S. Wu, Y. Li, W. Wen, Z. Jiang, J. Mi, Z. Zhu and Y. Yang, "Understanding the High Capacity of Li₂FeSiO₄: In Situ XRD/XANES," *Chemistry of Materials*, vol. 25, pp. 2014-2020, 2013.
- [6] H. Hosono, K. Hayashi, T. Kamiya, T. Atou and T. Susaki, "New functionalities in abundant element oxides: ubiquitous element strategy," *Science and Technology of Advanced Materials*, vol. 12, 2011.
- [7] H. Hao, J. Zhang, X. Liu, T. Huang and A. Yu, "Mesoporous Li₂FeSiO₄/C as Cathode Material for Lithium Ion Battery," *International Journal of Electrochemical Science*, vol. 8, pp. 10976 - 10986, 2013.
- [8] R. Dominko, "Li₂MSiO₄ (M = Fe and/or Mn) cathode materials," *Journal of Power Sources*, vol. 184, no. 2, pp. 462 - 468, 2008.

- [9] P. Vajeeston, F. Bianchini and H. Fjellvag, "First-Principles Study of the Structural Stability and Dynamic Properties of Li₂MSiO₄ (M = Mn, Co, Ni) Polymorphs," *Energies*, vol. 12, p. 224, 2019.
- [10] Z. Zhang, X. Liu, L. Wang, Y. Wu, H. Zhao, B. Chen and W. Xiong, "Fabrication and characterization of carbon-coated Li₂FeSiO₄ nanoparticles reinforced by carbon nanotubes as high performance cathode materials for lithium-ion batteries," *Electrochimica Acta*, vol. 168, pp. 8 - 15, 2015.
- [11] H.-j. Guo, K.-x. Xiang, X. Cao, X.-h. Li, Z.-x. Wang and L.-m. Li, "Preparation and characteristics of Li₂FeSiO₄/C composite for cathode of lithium ion batteries," *Transactions of Nonferrous Metals Society of China*, vol. 19, no. 1, pp. 166 - 169, 2009.
- [12] S. Sun, C. M. Ghimbeu, C. Vix-Guterl, M.-T. Sougrati, C. Masquelier and R. Janot, "Synthesis of Li₂FeSiO₄/carbon nano-composites by impregnation method," *Journal of Power Sources*, vol. 284, pp. 574 - 581, 2015.
- [13] P. Vajeeston and H. Fjellvag, "First-principles study of structural stability, dynamical and mechanical properties of Li₂FeSiO₄ polymorphs," *RSC Advances*, vol. 7, pp. 16843 - 16853, 2017.
- [14] J. Yang, X. Kang, L. Hu, X. Gong and S. Mu, "Nanocrystalline-Li₂FeSiO₄ synthesized by carbon frameworks as an advanced cathode material for Li-ion batteries," *Journal of Materials Chemistry A*, vol. 2, pp. 6870-6878, 2014.
- [15] S. Shen, Y. Zhang, G. Wei, W. Zhang, X. Yan, G. Xia, A. Wu, C. Ke and J. Zhang, "Li₂FeSiO₄/C hollow nanospheres as cathode materials for lithium-ion batteries," *Nano Research*, vol. 12, no. 2, pp. 357 - 363, 2019.
- [16] P. Vajeeston, "Ionic conductivity enhancement by particle size reduction in Li₂FeSiO₄," *Materials Letters*, vol. 218, pp. 313 - 316, 2018.
- [17] A. Nyten, A. Abouimrane, M. Armand, T. Gustafsson and J. O. Thomas,

- “Electrochemical performance of $\text{Li}_2\text{FeSiO}_4$ as a new Li-battery cathode material,” *Electrochemistry communications*, vol. 7, pp. 156-160, 2005.
- [18] C. Sirisopanaporn, C. Masquelier, P. G. Bruce, A. R. Armstrong and R. Dominko, “Structural Dependence of the Electrochemistry of $\text{Li}_2\text{FeSiO}_4$ (supporting information),” *Journal of the American Chemical Society*, vol. 133, no. 5, pp. S1 - S11, 2011.
- [19] C. Sirisopanaporn, C. Masquelier, P. G. Bruce, A. R. Armstrong and R. Dominko, “Dependence of $\text{Li}_2\text{FeSiO}_4$ Electrochemistry on Structure,” *Journal of the American Chemical Society*, vol. 133, no. 5, pp. 1263 - 1265, 2011.
- [20] K. Gao, K. Wang and S. Li, “Optimum synthesis and electrochemical properties of $\text{Li}_2\text{FeSiO}_4$ cathode for lithium ion battery prepared by a molten salt assisted method,” *Polyhedron*, vol. 166, pp. 28 - 35, 2019.
- [21] A. A. Popovich, P. A. Novikov, A. O. Silin, N. G. Razumov and W. Q. Sheng, “Synthesis of a $\text{Li}_2\text{FeSiO}_4/\text{C}$ Nanocrystalline Cathode Material for Lithium-Ion Batteries,” *Applied Electrochemistry and Corrosion Protection of Metals*, vol. 87, no. 9, pp. 1268 - 1273, 2014.
- [22] T. Masese, T. Orikasa, K. Yamamoto, T. Ina, T. Minato, K. Nakanishi, T. Ohta, C. Tassel, Y. Kobayashi, H. Kageyama, H. Arai, Z. Ogumi and Y. Uchimoto, “Local structural change in $\text{Li}_2\text{FeSiO}_4$ polyanion cathode material during initial cycling,” *Solid State Ionics*, vol. 262, pp. 110-114, 2013.
- [23] A. W. Brownrigg, G. Mountjoy, A. V. Chadwick, M. Alfredsson, W. Bras, J. Billaud, A. R. Armstrong, P. G. Bruce, R. Dominko and E. M. Kelder, “In situ Fe K-edge X-Ray Absorption Spectroscopy study during cycling of $\text{Li}_2\text{FeSiO}_4$ and $\text{Li}_{2.2}\text{Fe}_{0.9}\text{SiO}_4$ Li ion battery materials,” *Journal of Materials Chemistry A*, vol. 3, pp. 7314 - 7322, 2015.
- [24] L. Li, E. Han, L. Dou, L. Zhu, C. Mi, M. Li and J. Niu, “Enhanced Electrochemical performance of $\text{Li}_2\text{FeSiO}_4/\text{C}$ as cathode for lithium-ion batteries via metal doping

- at Fe-site," *Solid State Ionics*, vol. 325, no. 1, pp. 30 - 42, 2018.
- [25] J. Ni, Y. Jiang, X. Bi, L. Li and J. Lu, "Lithium Iron Orthosilicate Cathode: Progress and Perspectives," *ACS Energy Letters*, vol. 2, no. 8, pp. 1771 - 1781, 2017.
- [26] A. R. Armstrong, N. Kuganathan, M. S. Islam and P. G. Bruce, "Structure and Lithium Transport Pathways in $\text{Li}_2\text{FeSiO}_4$ Cathodes for Lithium Batteries," *Journal of the American Chemical Society*, vol. 133, no. 33, pp. 13031 - 13035, 2011.
- [27] M. Alfredsson, *Private communication*, 2019.
- [28] T. Masese, C. Tassel, Y. Orikasa, Y. Koyama, H. Arai, N. Hayashi, J. Kim, T. Y. K. Mori, Y. Kobayashi, H. Kageyama, Z. Ogumi and Y. Uchimoto, "Crystal Structural Changes and Charge Compensation Mechanism during Two Lithium Extraction/Insertion between $\text{Li}_2\text{FeSiO}_4$ and FeSiO_4 ," *The Journal of Physical Chemistry*, vol. 119, pp. 10206-10211, 2015.
- [29] Z. Arthur, H.-C. Chiu, X. Lu, N. Chen, V. Emond, K. Zaghib, D.-T. Jiang and G. P. Demopolous, "Spontaneous reaction between an uncharged lithium iron silicate cathode and a LiPF_6 -based electrolyte," *ChemComm*, vol. 52, pp. 190 - 193, 2016.
- [30] O. Kamon-in, S. Buakeaw, W. Klysubun, W. Limphirat, S. Srilomsak and N. Meethong, "A Study of Transient Phase Transformation in LFS/C using insitu Time Resolved X-ray Absorption Spectroscopy," *Internation Journal of Electrochemical Science*, vol. 9, pp. 4257-4267, 2014.
- [31] L. Dongping, W. Wen, X. Huang, J. Bai, J. Mi, S. Wu and Y. Yang, "A novel $\text{Li}_2\text{FeSiO}_4/\text{C}$ composite: Synthesis, characterization and high storage capacity," *Journal of Materials Chemistry*, vol. 21, pp. 9506-9512, 2011.
- [32] X. Wu, X. Jiang, Q. Huo and Y. Zhang, "Facile synthesis of $\text{Li}_2\text{FeSiO}_4/\text{C}$ composites with triblock copolymer P123 and their application as cathode materials for lithium ion batteries," *Electrochimica Acta*, vol. 80, pp. 50-55, 2012.

- [33] A. Liivat, J. Thomas, J. Guo and Y. Yang, "Novel insights into higher capacity from the Li-ion battery cathode material $\text{Li}_2\text{FeSiO}_4$," *Electrochimica Acta*, vol. 223, pp. 109-114, 2017.
- [34] A. Saracibar, A. Van der Ven and M. E. Arroyo-de Dompablo, "Crystal Structure, Energetics, And Electrochemistry of $\text{Li}_2\text{FeSiO}_4$ Polymorphs from First Principles Calculations," *Chemistry of Materials*, vol. 24, pp. 495-503, 2012.
- [35] X. Lu, H.-C. Chiu, K. H. Bevan, D.-T. Jiang, K. Zaghbi and G. P. Demopoulos, "Density functional theory insights into the structural stability and Li diffusion properties of monoclinic and orthorhombic $\text{Li}_2\text{FeSiO}_4$ cathodes," *Journal of Power Sources*, vol. 318, pp. 136-145, 2016.
- [36] X. Lu, H.-C. Chiu, Z. Arthur, J. Zhou, J. Wang, N. Chen, D.-T. Jiang, K. Zaghbi and G. P. Demopoulos, "Li-ion storage dynamics in metastable nanostructured $\text{Li}_2\text{FeSiO}_4$ cathode: Antisite-induced phase transition and lattice oxygen participation," *Journal of Power Sources*, vol. 329, pp. 355 - 363, 2016.
- [37] W.-S. Yoon, M. Balasubramanian, K. Y. Chung, X.-Q. Yang, J. McBreen, C. P. Grey and D. A. Fischer, "Investigation of the Charge Compensation Mechanism on the Electrochemically Li-Ion Deintercalated $\text{Li}_{1-x}\text{Co}_{1/3}\text{Ni}_{1/3}\text{Mn}_{1/3}\text{O}_2$ Electrode System by Combination of Soft and Hard X-ray Absorption Spectroscopy," *Journal of the American Chemical Society*, vol. 127, no. 49, pp. 17479 - 17487, 2005.
- [38] M. Fehse, C. J. Sahle, M. P. Hogan, C. Cavallari, E. M. Kelder, M. Alfredsson and A. Longo, *Bulk Sensitive Soft X-Ray Edge Probing for Elucidation of Charge Compensation in Battery Electrodes*, Submitted for publication (2019).
- [39] R. Dominko, C. Sirisopanaporn, C. Masquelier, D. Hanzel, I. Arcon and M. Gaberscek, "On the Origin of the Electrochemical Capacity of $\text{Li}_2\text{Fe}_{0.8}\text{Mn}_{0.2}\text{SiO}_4$," *Journal of the Electrochemical Society*, vol. 157, no. 12, pp. 1309 - 1316, 2010.
- [40] D. Lv, J. Bai, P. Zhang, S. Wu, Y. Li, W. Wen, Z. Jiang, J. Mi, Z. Zhu and Y. Yang.

- [41] C. Eames, A. R. Armstrong, P. G. Bruce and M. S. Islam, "Insights into Changes in Voltage and Structure of $\text{Li}_2\text{FeSiO}_4$ Polymorphs for Lithium-Ion Batteries," *Chemistry of Materials*, vol. 24, pp. 2155 - 2161, 2012.

4 Negative Electrode - PEDOT:PSS

4.1 Introduction

Poly(3,4-ethylenedioxythiophene):poly(styrenesulfonate) (PEDOT:PSS) is a co-polymer with many useful properties, including being environmentally friendly, easily processable and readily available. Resulting in PEDOT:PSS being used in a vast array of industrial applications, among which include Organic Light Emitting Diodes (OLEDs), Photovoltaic (PV) cells and anti-static coatings [1] [2] [3]. It is also used as a mixed conductor i.e. the material is both electronically and ionically conductive. These properties make PEDOT:PSS a suitable candidate for the next generation of lithium-ion battery materials. Current battery electrodes consist of an active material combined with an electronically conducting additive (e.g. carbon black) and a binder (e.g. PVDF) coated onto a metallic current collector (copper and aluminium foils). The current setup means that whilst the active material may have a high theoretical capacity and stable redox reaction potentials the overall energy density of the battery is greatly reduced due to the required additives and assembly components. Reducing or removing these components is a vital step towards improving Li-ion battery energy density. PEDOT:PSS, with its intrinsic electronic conductivity removes the need for the carbon black conducting additive. In addition to this, PEDOT:PSS is a self-binding polymer that, if deposited correctly, has no need for additional binder, meaning 100% of the deposited electrode is active material. Finally, PEDOT:PSS can be made into self-standing flexible films [4]. This would theoretically give rise to the possibility of removing the current collector from the battery (as described in Section 1.6.4), a bulky, heavy and inactive material, which does not contribute to the capacity of the electrochemical cell.

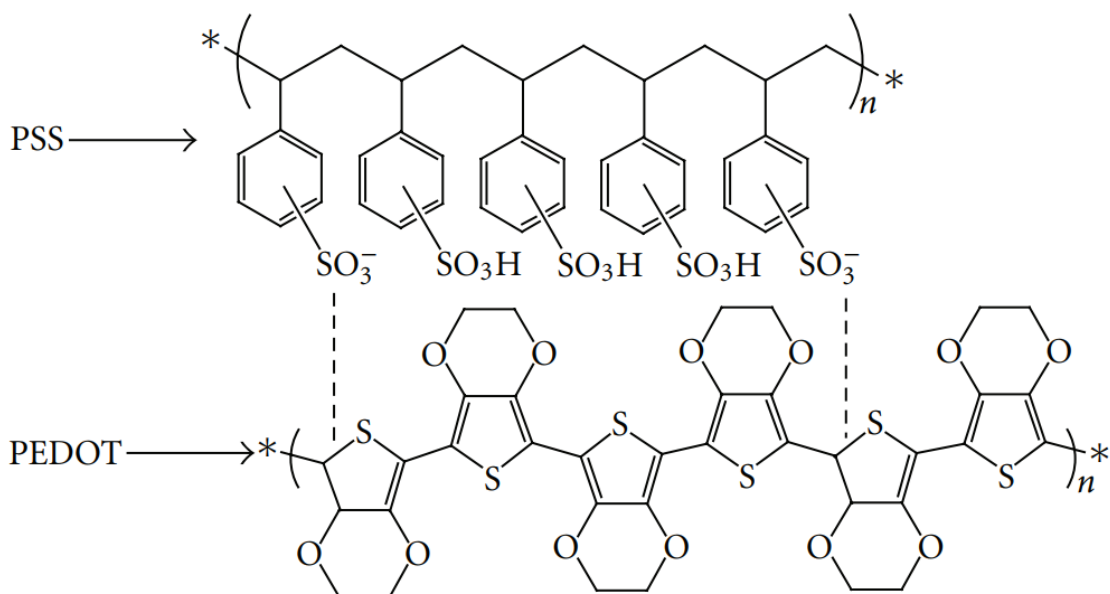


Figure 4.1: Chemical structure of PEDOT:PSS [7]

Figure 4.1 shows the chemical structure of PEDOT:PSS. Its electronic conductivity stems from the PEDOT polymer, which is a conjugated polymer. The ionic conductivity stems from the SO₃⁻ groups associated with PSS and their ability to attract Li⁺ ions. In addition to this, research has shown PEDOT:PSS to be both chemically stable [5] and biocompatible [6]. The latter property is essential for potential usage in bio-integrated electronic devices, where this material may be used as an electrode (see Chapter 6). The material is also soluble in aqueous solutions and its ability to form a suspension in water, allows for more environmentally friendly electrode manufacturing methods to be used. As discussed in Chapter 2, electrode slurries are regularly made using NMP as the solvent, a substance not only harmful to the environment but also costly to evaporate from the slurry because of its high boiling point. It is also expensive to recover the solvent during the manufacturing process. Using water as the main solvent removes these issues.

This chapter will focus on PEDOT:PSS electrodes manufactured using water as the solvent, but will also look at various deposition techniques and their feasibility for use in large scale production. Finally, the electrochemical performance will be compared using various deposition techniques and their reaction mechanisms discussed.

4.2 Deposition Methods

4.2.1 Tape Casting (Doctor Blade)

Firstly, PEDOT:PSS was deposited using the same approach as mentioned in chapter 2. The main difference when coating PEDOT:PSS is the use of aqueous solutions as the solvent as opposed to NMP, which means that PVDF is no longer a viable option as the binder, as PVDF is insoluble in water. Initially binderless slurries were cast, however, the resulting electrodes were brittle and flaky, resulting in poor cycling behaviour. This latter issue could be remedied by reducing the thickness of the deposited films, but in this study the thickness had to be reduced to the degree where the amount of deposited material was too low to sufficiently coat or wet the entire current collector. To improve the prepared coating a water-soluble binder: sodium carboxymethylcellulose (CMC) was added to aid with structural integrity and adhesion. As previously stated, PEDOT:PSS is electronically conductive, and so, no additional carbon conductive additive was added, therefore, no ball-milling step was required. As the PEDOT:PSS came as a ready-made suspension in aqueous solution (1.3 wt.%) the resulting slurry demonstrated poor viscosity reducing its potential to be directly cast using the Doctor Blade method. Instead, CMC was added to the as bought PEDOT:PSS suspension and dissolved fully before being heated and stirred via a magnetic stirrer for 2-3 hours. The latter steps were introduced to ensure a uniform suspension and to evaporate around 50% of the solvent, increasing viscosity. The resulting slurry was cast the same way as the NMP-based slurries, and the dried at 40°C under vacuum for 12 hours followed by a 70°C drying under vacuum. Figure 4.2 shows the wet slurry after casting and after drying.



Figure 4.2: PEDOT:PSS doctor blade coating A) wet B) after drying

There are many advantages with using the tape casting technique. When the slurry composition is formulated for this technique (viscosity, solvent compositions, binders) then the Doctor Blade technique can be used to create electrode castings of a homogenous appearance, and uniform thickness. The technique allows for roll-to-roll large area coverage with minimal material waste. The process is used as a “single pass” technique i.e. repeated layering is not necessary. Due to this single layer application process, there is a lower chance of a breakdown in the network controlling the conductive pathways in-between the cast layers and, therefore, minimising the chance of unnecessary electrode impedance created by adding more interfaces. Adhesion of electrodes are good even with thick electrodes due to the uniform slow-moving deposition of the slurry, allowing the binders to adhere to the foil and its neighbouring particles. Thicknesses of several hundred micrometres can be quickly achieved using this technique.

The Doctor Blade (tape casting) technique is limited in some respects. If thin layers are desired, Doctor Blades may not be an option, minimum electrode thickness is $>1\mu\text{m}$. In addition to this, if a specific shape of electrode is required then other techniques will be preferable, Doctor Blading is used for straight full coverage coatings no controllable patterning is used.

4.2.2 Spray-Coating

Spray-coating is a widely used coating technique in many fields from the automotive industry to art. It has also been previously used for Li-ion battery electrode deposition. [7] [8] Further, it is known to be used in photovoltaic (PV) cell research, spraying the layered components – of which PEDOT:PSS is among them [9] [10]. As a result, the spray coating technique may be used in the fabrication of polymeric lithium-ion electrodes. The reason the technique is attractive as a deposition method is that, like “Doctor Blading”, it can be used to cover large areas including roll-to-roll processes. Unlike “Doctor Blading”, spray coating can also be used to cover non-uniformly shaped surfaces and masks can be used to ensure selective coating areas. The spray coating technique can be tuned so that the desired deposition thickness is achieved. Multiple passes are often undertaken to increase thickness and improve homogeneity of the film. Lower viscosity slurries compared to “Doctor Blade” can often lead to surface tension issues resulting in non-uniform coatings, meaning that multiple passes are required to achieve a uniform film.

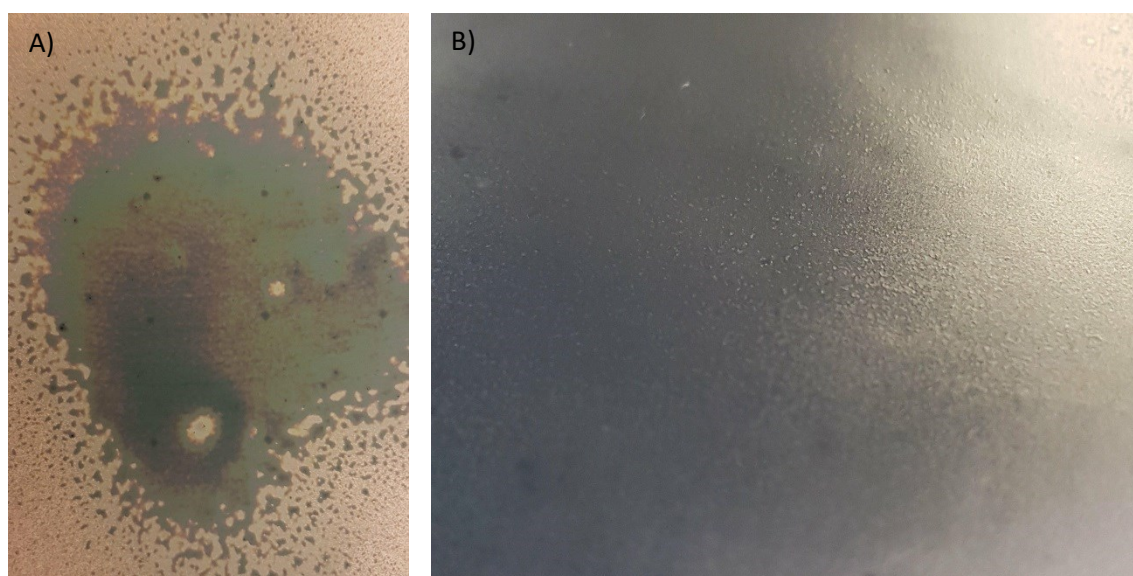


Figure 4.3: Spray-coated PEDOT:PSS on copper foil after A) one coat and B) final coat

The PEDOT:PSS adhesion to the copper current collector using this method was sufficient enough that no additional binder was needed. However, it should be noted that if the coating became too thick ($>20\mu\text{m}$), the surface was prone to flaking and delamination. The PEDOT:PSS suspension was used as bought (1.3 wt.% in H_2O) and sprayed using a standard compressed gas air brush. Figure 4.3 B shows the fully coated

copper foil with some visible minor pitting or flaking of the coatings. In addition, due to the low viscosity of the slurry and the aqueous solution used, surface wetting issues were found, resulting in non-uniform coatings (Figure 4.3 A) due to the high surface tension of the solution. The issue was remedied by multi-layer coatings. Multiple coatings (3-4 coatings) were required to achieve the desired sample loading, with ambient drying conditions after each coat, followed by a 70°C drying process under vacuum.

4.2.3 Inkjet Printing

Inkjet printing has been chosen as a finely tuneable deposition method. Capable of printing specific designs accurately on the micrometre scale, allowing not only large area coating as the previously mentioned coating methods but also allowing intricate electrode designs, which can be useful in bespoke and/or integrated batteries. Again, this method used the PEDOT:PSS suspension as bought (1.3 wt.% in H₂O) with no additional binder and was printed directly onto the copper foil using a standard inkjet printer (HP Deskjet 2130) shown in Figure 4.4 A. No additional binder was used due to the exceptional adherence to the copper without binder, the likely reasoning for this is that like the spray coating method, and unlike the “Doctor Blading” method, the PEDOT:PSS is deposited in a layer-by-layer fashion.

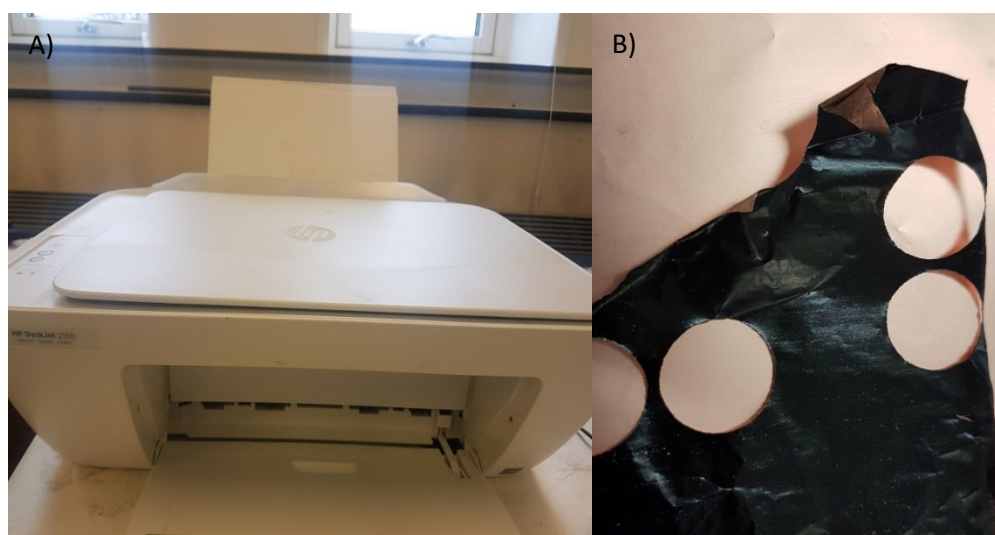


Figure 4.4: A) Inkjet printer used to deposit PEDOT:PSS onto copper foil B) coated copper foil

Approximately 30 layers were deposited with a 1-minute heat curing time at 70°C in-between each layer, Followed by a final drying at 70°C under vacuum. The adherence seems even better than that of the spray coating, likely due to a more uniform

deposition spread, and smaller quantities being deposited at a time, creating a uniform coating with a smooth, flat surface. Shown in Figure 4.4 B is the finished dried coating after long term storage and being handled multiple times. Further suggesting strong adherence of the ink to the substrate.

4.3 Results

PEDOT:PSS samples, deposited using each of the previously mentioned techniques was then characterised. SEM was used to examine film forming properties and uniformity. TGA and XRD were used to obtain the materials thermal stability characteristics, including the nature of the polymer after drying and ensure it is unaffected by the drying procedures used in this study.

4.3.1 Thermal Stability

Independent of the deposition technique a drying process was required. This means that the polymer films need to be thermally stable, at least above 70°C. In view of this a thermal stability study was undertaken using TGA and XRD before and after drying. It is commonly accepted that a materials thermal stability window can be determined by the point at which 5% mass loss occurs. To measure this, thermal gravimetric analysis (TGA) was employed to determine the stability of PEDOT:PSS.

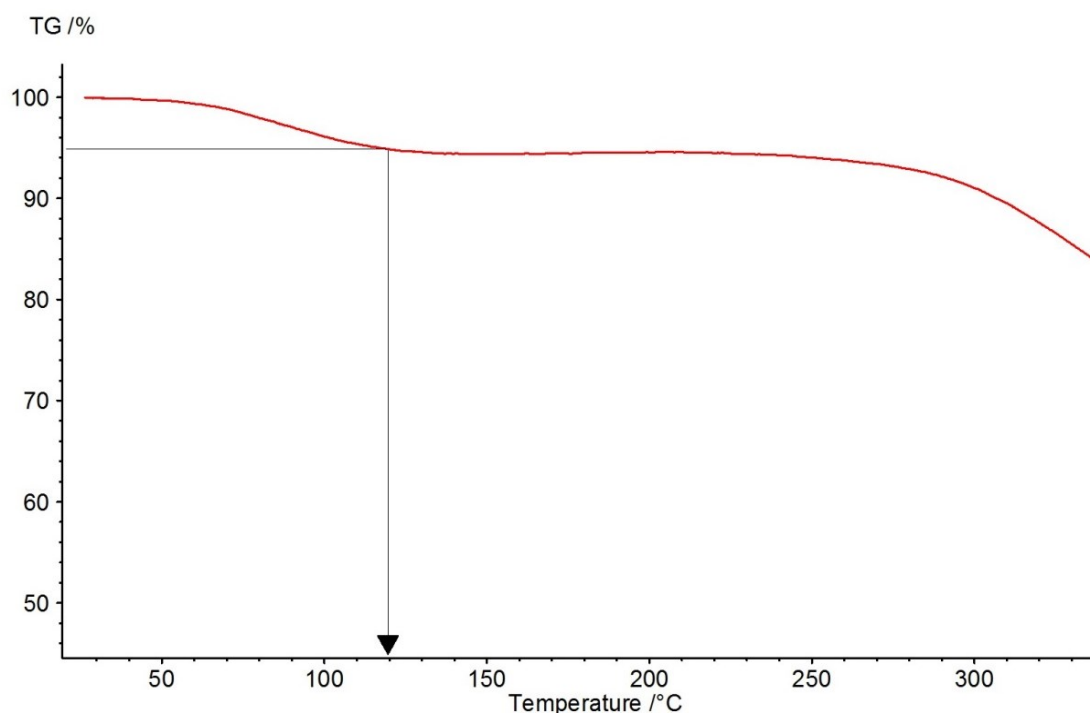


Figure 4.5: TGA of dried, pure PEDOT:PSS with an indicator showing 5% mass loss

Figure 4.5 shows a 5% mass decrease occurs at around 120°C. Normal cycling conditions are at room temperature and drying conditions are up to 70°C. PEDOT:PSS' stability up to 120°C not only ensures no thermal degradation of the PEDOT:PSS under normal cycling conditions, but also allows for elevated temperature cycling and therefore increases PEDOT:PSS' potential applications.

To further ensure PEDOT:PSS was not affected by the drying procedure used in the coating processes, X-ray diffraction (XRD) of the sample was collected. The as received PEDOT:PSS was dried at 70°C under vacuum and ground into a powder. The XRD spectra of PEDOT:PSS (Figure 4.6) demonstrates no sharp peaks, instead a spectrum of very broad peaks are observed. This can be easily attributed to the amorphous or semi-crystalline nature of the PEDOT:PSS polymer, indicating that no long range, periodic atomic arrangement is present. The identifiable broad peak at 17.5° is associated with the amorphous halo of PSS, whilst the peak found at 25° is attributed to the π - π stacking (d 010) of the PEDOT thiophene ring. This data fits well with literature [11] [12] [13].

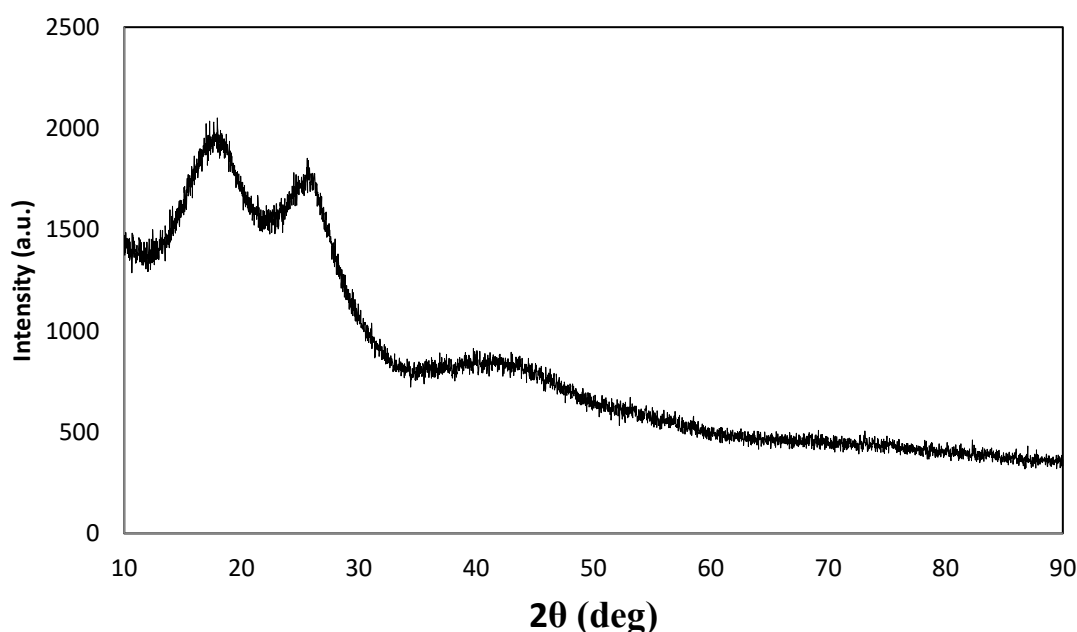


Figure 4.6: XRD of pure PEDOT:PSS

4.3.2 Chemical and Mechanical Properties of the Films

4.3.2.1 Doctor Blade

Scanning electron microscopy (SEM) was used to inspect the film forming properties and to estimate the adhesion of the active material to the copper substrate. Upon inspection of the SEM images, the PEDOT:PSS film deposited using the tape casting method (Figure 4.7 A) It can be seen that whilst the PEDOT:PSS adheres well to the copper foil it also cracks after handling. This is a phenomenon known as “mud-cracking”. Mud-cracking occurs under multiple conditions, most commonly during the drying process after film deposition. As solvent is removed the film may contract, creating tension within the film (known as capillary pressure), as the film continues to dry cracks are formed [14]. There is a film thickness, known as the critical thickness, where films thinner than this will exhibit no cracking. The most likely reason for the cracking observed in Figure 4.7 A is due to the thickness of the film (around 5 μ m) – when used in other applications, such as, photovoltaic cells the thickness is significantly less (typically <100nm) [15] [16]. From the elemental mapping of sulphur and copper it can be seen that whilst sulphur is uniformly distributed throughout the coating (Figure 4.7 B) the copper is most evident in-between the cracks of the film, indicating that the cracking is not just a surface effect but travels the full depth of the PEDOT:PSS coating to reveal the copper foil underneath (Figure 4.7 C).

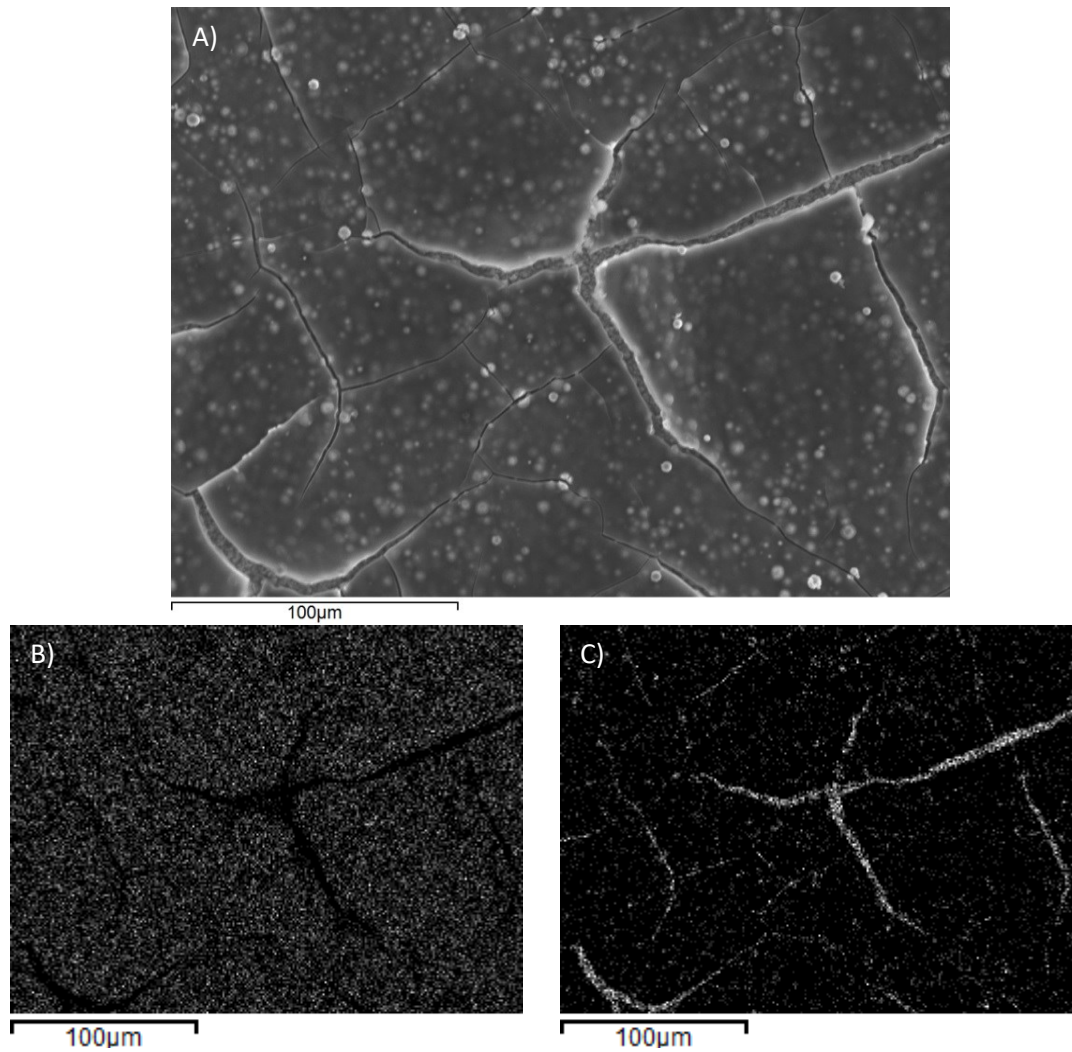


Figure 4.7: SEM image of A) doctor bladed PEDOT:PSS/CMC coating B) EDX sulfur mapping C) EDX copper mapping

When increasing the magnification (Figure 4.8 A) it can also be seen that there are bright “spots” in the coating. From elemental mapping (Figure 4.8 B and C) of sulphur showing darker voids and copper mapping showing brighter spots (marked by orange circles), It can be seen that copper particles are raised in small clusters during the coating process, i.e. when the doctor blade glides along the foil it pulls at the foil whilst depositing, creating a rough surface, with copper particles remaining in the dried film. Another explanation is that copper diffusion may occur due to the PEDOT:PSS’ acidic nature, other deposition methods will be observed for evidence of this. It is possible that added surface roughness may help with adherence to the copper foil.

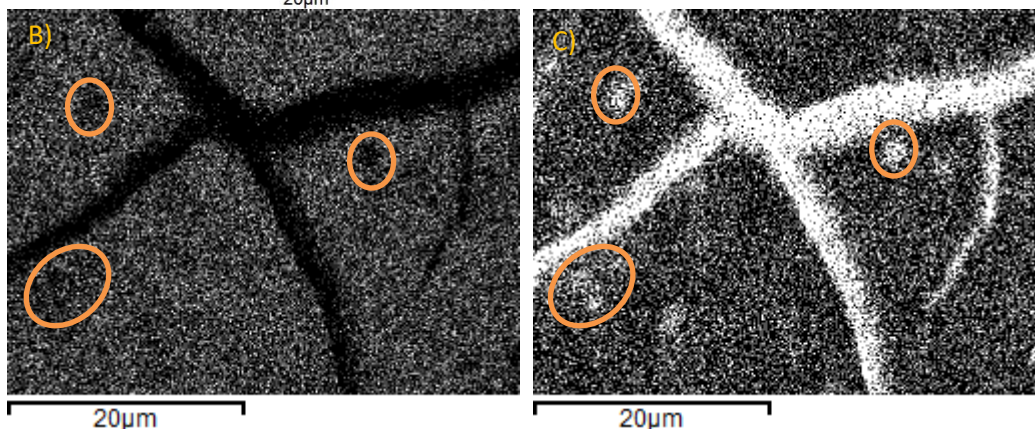
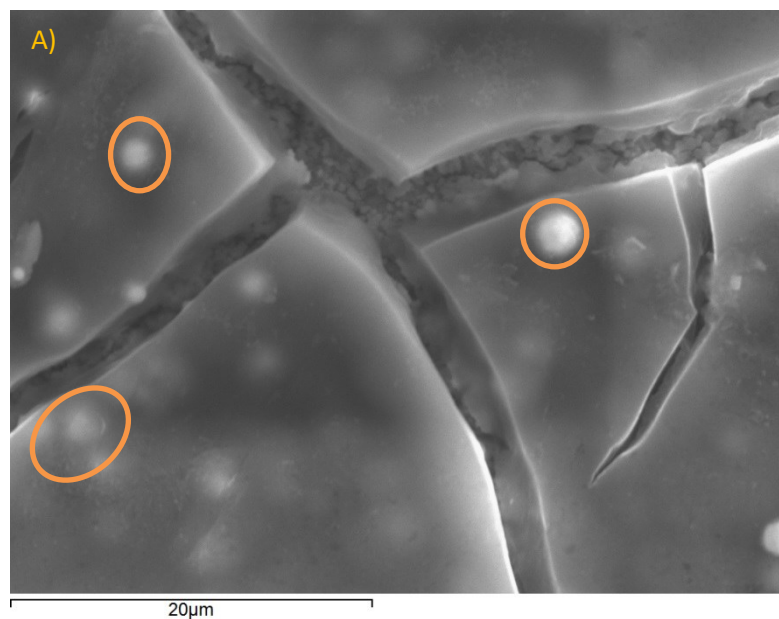


Figure 4.8: Magnified SEM image of A) Doctor Bladed PEDOT:PSS B) EDX mapping of Sulphur C) EDX mapping of Copper

4.3.2.2 Spray-Coating

Investigating the SEM images of the spray-coated PEDOT:PSS films (Figure 4.9 A), distinct topological differences in the morphology of the coatings are immediately visible, similar “mud-cracking” is observed, as seen in the “Doctor Blade” coatings (Figures 4.7 A and 4.8 A). However, the evidence of the copper clusters are significantly less obvious, nonetheless, elemental mapping does indicate the presence of copper spread across the film surface (Figure 4.9 B), though it appears more evenly distributed when compared to the doctor bladed sample. This suggests that the cause of the copper clustering is, in fact, due to the acidic nature of the PEDOT:PSS, a similar phenomenon of indium diffusion is observed in PEDOT:PSS coated ITO [17]. No aggressive dragging of material across the surface occurs during the spray-coating deposition technique, this may be the reason there is no obvious clustering as seen in the Figure 4.7 A and 4.8 A.

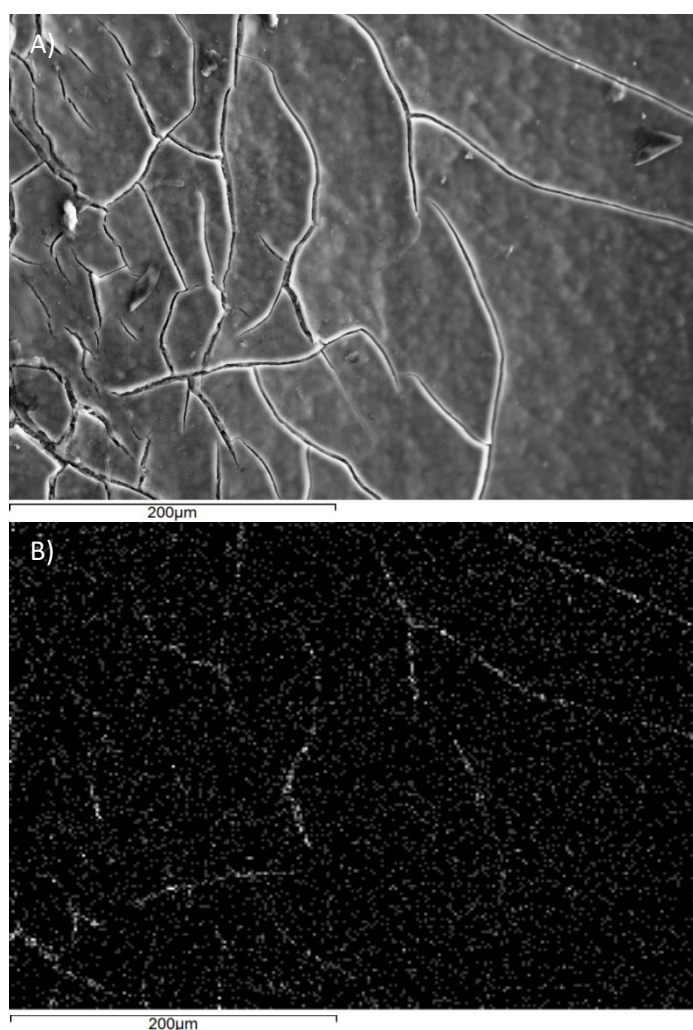


Figure 4.9: SEM image of A) spray coated PEDOT:PSS B) EDX copper mapping

However, the overall surface appearance is much rougher and “bumpy” than the “Doctor Blade” coatings. Comparing the magnified images (Figures 4.8 A and 4.10) the “Doctor Blade” coatings were smooth in appearance, apart from the copper clusters, whilst the whole surface of the spray-coated film is rough. This “roughening” is most likely due to the nature of spray coating, where droplets of the material is deposited, surface tension and other parameters cause agglomerations when dried and by depositing further layers, a film with a peak/trough topology is formed. This is evidenced in Figure 4.3 where it can be seen that the PEDOT:PSS agglomerates in patches when drying.

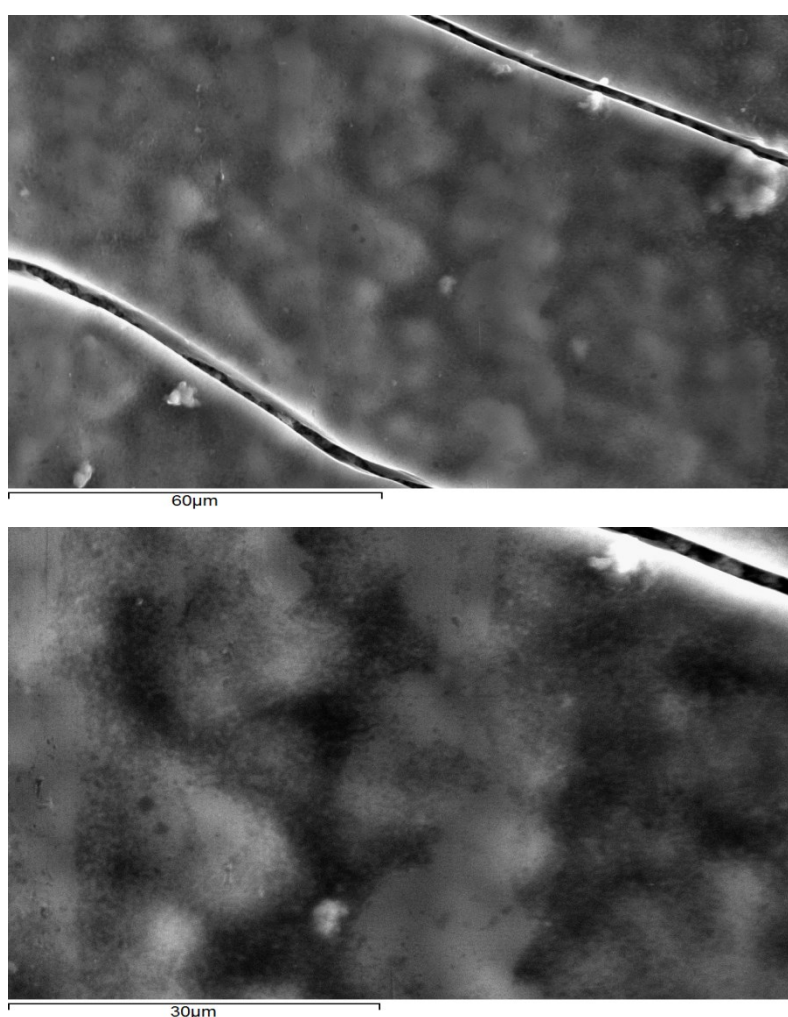


Figure 4.10: SEM images of spray-coated PEDOT:PSS at varying magnifications

The roughness of the surface can both help and hinder battery performance. On one hand, it increases surface area and, therefore, increases contact with electrolyte – improving ionic contact. On the other hand, as previously mentioned, the rough surface may lead to flaking of the coating resulting in delamination, resulting in loose

material which can no longer contribute to the battery capacity, or worse, potentially lead to short circuiting.

4.3.2.3 Inkjet Printing

The SEM image of the inkjet printed PEDOT:PSS films (Figure 4.11), again shows a different morphology to both the “Doctor Blade and spray-coated samples. It should be noted that this sample was the most handled and longest stored sample of the three (around 8 - 10 months between coating and SEM images being taken) and so cracking of the film would be expected. It should also be noted that whilst there appears to be a larger number of cracks, they are finer in diameter ($<1\mu\text{m}$) than with the other two deposition techniques ($2\text{-}5\mu\text{m}$). However, other than the cracking – also seen in the other deposition methods – the film has a smooth surface with little evidence of “bumping” or copper clustering.

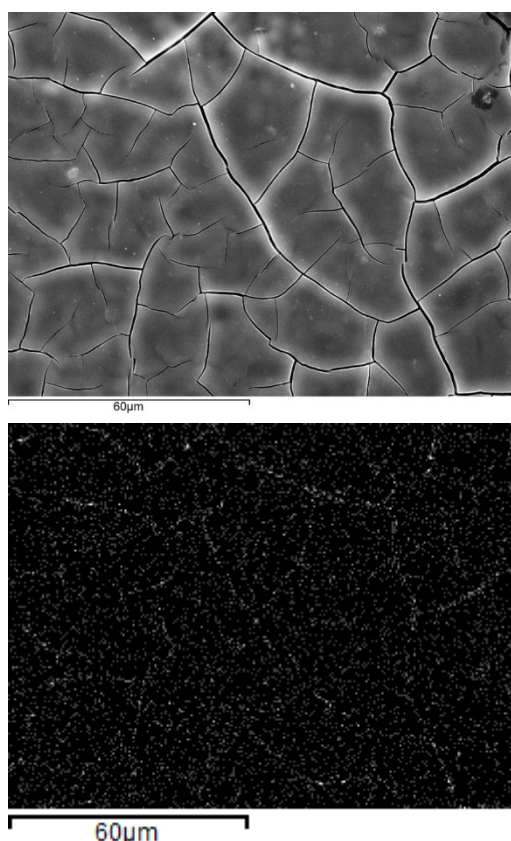


Figure 4.11: SEM image of inkjet printed PEDOT:PSS film

Similarly to the spray coating technique, there appears to be an even distribution of copper across the film suggesting copper diffusion has occurred. The presence of copper without large clusters can be attributed to the non-invasive deposition

technique, where no scraping or pulling of the material is involved. Despite the inkjet printer producing droplets, (an attribute discussed as a negative point of the spray-coating technique) the coating appears to be even throughout the films. This has been attributed to the inkjet printing techniques' smaller droplet size (inkjet printing droplet sizes are typically between 15-150 μm [18]) and more uniform spacing between droplets when compared to the spray-coating technique. In addition, the amount of material deposited per layer is significantly less than the spray-coating technique, so whilst there may still be a peak/trough topology the appearance is far less pronounced.

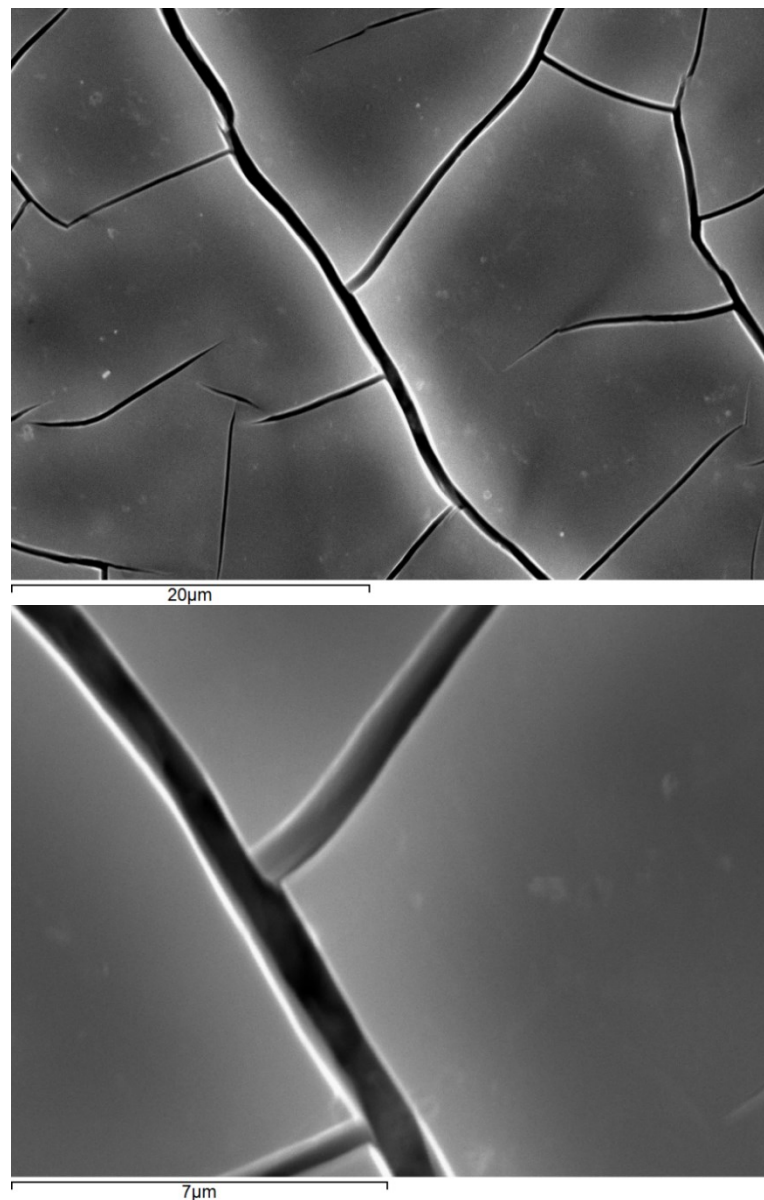


Figure 4.12: SEM images of inkjet printed PEDOT:PSS film, at varying magnifications

Instead, magnified SEM images of the ink-jet printed films shown in Figure 4.11, illustrate that the surface is smooth, even at high magnification. This deposition technique, with its smooth surface appears to give the coating good adhesion, as even when crumpled, the coating adheres to the copper foil without flaking or delamination. This may be due to the large amount of layering involved with this technique. To achieve a coating with this thickness ($\approx 4\mu\text{m}$) PEDOT:PSS was deposited layer-by-layer with a drying stage in between each coating. A total of 30 layers were deposited. Thin, even layers deposited on top of each other, appears to give strength to the structure similar to bricks in a wall.

4.3.3 Electrochemical Properties of the Films

4.3.3.1 Deposition Dependent Galvanostatic Battery Cycling

To determine if PEDOT:PSS has potential as an anode material in Li-ion batteries, PEDOT:PSS has been cycled vs lithium metal discs in half cells. All cells were cycled between 0.05 – 3V at a rate of $100\text{mA}\text{g}^{-1}$ to ensure consistency throughout the results. All cells used Celgard polymer separator and a standard 1M LiPF_6 in EC/DEC electrolyte. As pure PEDOT:PSS has not been previously researched as a viable candidate for an anode material in the literature, there is little in terms of cycling statistics. However, one report using PEDOT:PSS as a conductive additive in Silicon anode based Li-ion batteries shows an initial discharge capacity of around $60\text{mA}\text{h}\text{g}^{-1}$ [19]. It also proposes a Li trapping mechanism, which further reduces the capacity by around $50\text{mA}\text{h}\text{g}^{-1}$ after the first cycle, with successive cycles the material achieves just $10\text{mA}\text{h}\text{g}^{-1}$. Reports of cycling similar materials (conductive polymers) suggest capacities for conjugated polymers to be around 70 – $150\text{mA}\text{h}\text{g}^{-1}$ [20] [21].

4.3.3.1.1 Manufacturing Dependent Electrochemical Performance

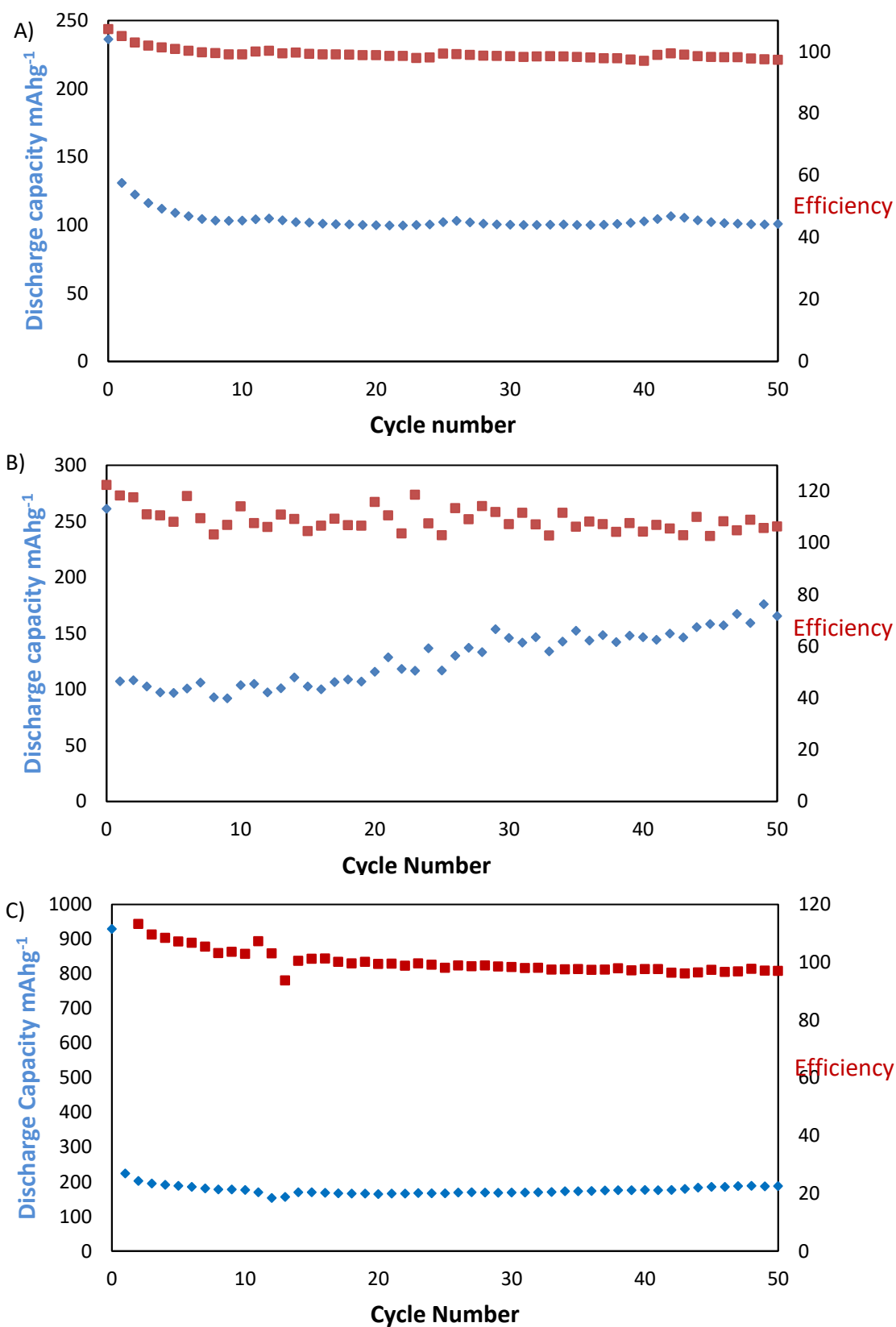


Figure 4.13: Discharge Capacities and Coulombic Efficiencies across 50 cycles of A) Doctor Blade B) spray-coted C) Inkjet Printed PEDOT:PSS films cycled between 3.1V and 0.01V

Figure 4.13 A) B) and C) show discharge capacities of each different deposition method and their respective coulombic efficiency. From the graphs it can be seen that, depending on the deposition technique used, significantly different cycling performances are observed for the PEDOT:PSS cells. Electrochemical performances of each technique are discussed and then compared.

4.3.3.1.2 Doctor Blade

Using the Doctor Blade technique, a PEDOT:PSS consisting of a film with a thickness of around $5\mu\text{m}$ was cast, the film experienced mud-cracking (as shown in the SEM images (Figure 4.7)), however, strong adhesion to the current collector was observed with the addition of a small amount of CMC binder. In addition, stable discharge capacities, sitting around the 100mAhg^{-1} are observed across 50 cycles (Figure 4.13 A). Also shown, is the high coulombic efficiency performance, with efficiency in the 98-100% region. Additionally, it can be seen that there is an initial drop in capacity after the first cycle which is being attributed to lithium trapping, discussed further in Section 4.3.4.

4.3.3.1.3 Spray-Coating

The spray-coated film, instead, shows a more complex behaviour compared to the doctor blade coated sample (Figure 4.13 B). The film was coated using multiple passes of the spray coater to achieve a thickness similar to the doctor blade sample. Again, mud-cracking was observed, however, as previously mentioned, this technique used no additional binder, therefore the film is prone to flaking. It is immediately noticeable that the cycling behaviour is more “erratic” and show a clear trend of increasing capacity during repeated discharges. Starting from around 100mAhg^{-1} and steadily increasing towards 180mAhg^{-1} as the cycle number increases. In addition, the efficiency is not only erratic but also consistently above 100% indicating more lithium is being inserted than is being removed, suggesting that either side reactions are taking place or a continued trend of lithium trapping occurs even after the initial cycle. This needs further investigation, but was out of the scope of this project, which focused on battery performance based on the processing of different coating techniques.

4.3.3.1.4 Inkjet Printing

Finally, the discharge capacities of the first 50 cycles of PEDOT:PSS deposited via inkjet printing were analysed. From Figure 4.13 C it is obvious that the capacities of both the initial cycle and the following cycles are significantly higher than those of the doctor bladed and the spray-coated electrodes. Of course, the spray-coated discharge capacity was steadily increasing and nearing these values; however, the capacity of the inkjet printed electrode demonstrated improved stability, similar to the doctor blade coated electrodes but with almost double the capacity. It can also be seen from the efficiency that values, whilst not quite as consistent as the doctor bladed, still sit in the 97-100% range. The initial cycle indicates a much larger amount of lithium trapping than the other methods with a value of around 700mAhg^{-1} ($\approx 350\%$ of reversible capacity) being trapped, compared to around $100\text{-}150\text{mAhg}^{-1}$ ($100\text{-}150\%$ of reversible capacity) of the other two techniques.

4.3.3.1.5 Comparison of Electrochemical behaviours

When comparing the cycling between the three coating methods it can be seen that with regards to capacity, the doctor blade method has the lowest performance giving a capacity of around 100mAhg^{-1} which, when taking the 15% binder into consideration gives a capacity of just 87mAhg^{-1} , the next lowest performing method would be the spray-coating method, which is deposited without binder and, therefore, gave a total capacity range between $100\text{-}180\text{mAhg}^{-1}$. However, the capacity values are erratic and steadily increasing with efficiencies well above 100%. This can cause issues with long-term cycling due to side reactions and/or lithium trapping. Finally, the preferred deposition, resulting in the highest discharge capacities along with stable coulombic efficiency values, is the inkjet printed electrode without binder, exhibiting capacities of around 200mAhg^{-1} and efficiencies in the order of 97-100%.

It should be noted that, whilst spray coated films may have exhibited improved performance characteristics with the addition of a binder, the aim of this project was to develop a binder-free coating technique as an alternative to the doctor blade technique. Not only did the inkjet printed film exhibit the highest electrochemical performance characteristics, it also exhibited strong adhesion characteristics, with no evidence of delamination despite heavy handling and long-term storage, it is proposed

that this is due to the coating being deposited in a controlled layer-by-layer fashion resulting in a stable particle network with high area of contact without the need for a binder.

In addition to this, we propose a potential mechanism for the first cycle irreversible capacity loss or “lithium trapping” as well as an explanation of the different performance characteristics of the various deposition techniques. One potential mechanism responsible for lithium trapping is an ion exchange between the protons H^+ found in the PSS chains and lithium ions Li^+ , this can lead to hydrogen evolution. A similar ion exchange has been intentionally produced when using PSS containing polymers in separators for Li-S batteries [22] where it was used to hinder poly-sulphide movement through the functionalised separator, also observed was a reduction in Li^+ ion mobility through the separator.

4.3.4 Chemical Reaction Mechanism and “Lithium Trapping”

4.3.4.1 Cyclic Voltammetry (CV)

In addition to a comparison between deposition techniques’ performance, electrochemical techniques were used to gain a better understanding of the electrochemical reactions taking place upon cycling PEDOT:PSS. Cyclic voltammetry (CV) was used to explore the potentials at which the reactions occur during cycling as well as the nature of those reactions. The “Doctor Blade” coated samples were placed into coin cells vs lithium metal, using $LiPF_6$ EC/DEC electrolyte. The scan rate used was $0.05mVs^{-1}$ across the same potential window used during galvanostatic battery cycling i.e. 0.05 – 3.0V. Figure 4.14 shows two distinct voltage peaks where the redox reactions take place – 0.75V and 1.6V on discharge and 1.2V and 2.55V on charge. It can also be seen from the profile that the peaks, whilst clear, are also small and broad – indicating either small plateaus or plateaus which are not well defined in the galvanostatic cycling, which would result in a sloped battery cycling curve rather than a flat plateau. This is further discussed further in section 4.3.4.2.

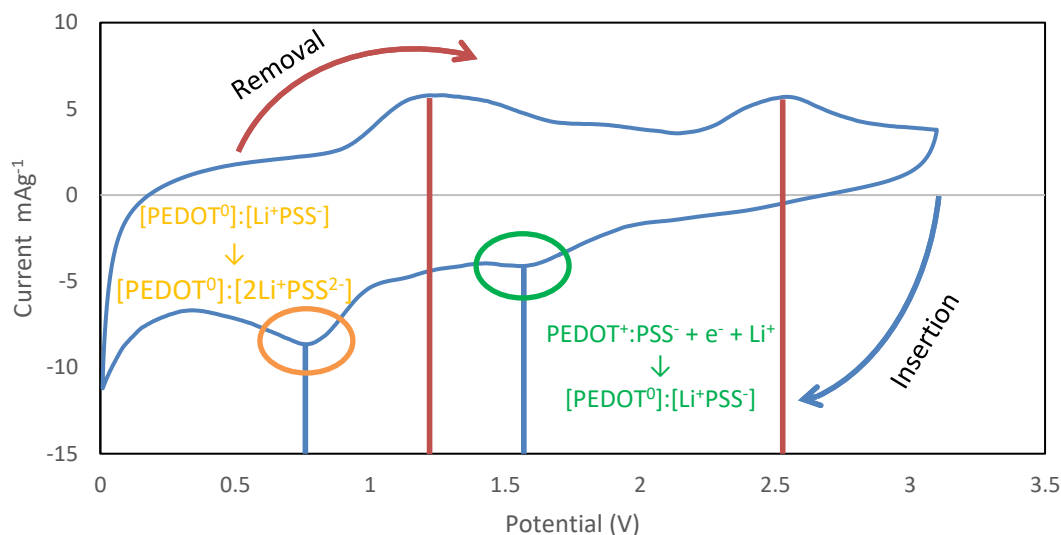


Figure 4.14: CV curve of PEDOT:PSS vs Li/Li (scan rate 0.05mV s⁻¹)

Following the CV curves' two reaction pairs, the proposed mechanism occurring is as follows: During discharge, the initial peak (1.6V) corresponds to the insertion of electrons into PEDOT⁺, reducing it to PEDOT⁰, to maintain charge balance, Li⁺ ions are inserted to the PSS⁻ as described by reaction equation (4-1). This reaction has previously been proposed in the literature [23] showing the reversible nature of inserting and removing Li⁺ ions from the PEDOT:PSS polymer.



The second peak (0.75V), instead, is being proposed as an additional Li⁺ insertion into the now [Li⁺PSS⁻], and additionally an electron for charge balancing, thus creating a radical, as shown in Figure 4.15. Upon charging these reactions are reversed.

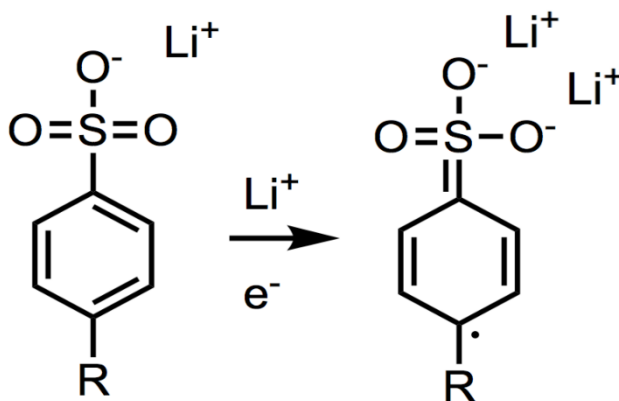


Figure 4.15: Schematic diagram of the proposed second lithium insertion mechanism into PSS

4.3.4.2 Galvanostatic Cycling Curves

A PEDOT:PSS cycling curve is shown in Figure 4.16 and upon closer inspection, it can be seen to correspond to the reactions identified in the CV curve (Figure 4.13). The plateaus corresponding to these CV peaks have been indicated on the graph. However, from the sloped nature of the cycling curve it is proposed that reactions are taking place throughout the voltage range and not simply at the redox voltages established from the CV curve. Again, this corresponds well to the CV curves' broad peaks. The location and sloped nature of these plateaus occur at the same locations, independent of the deposition method used

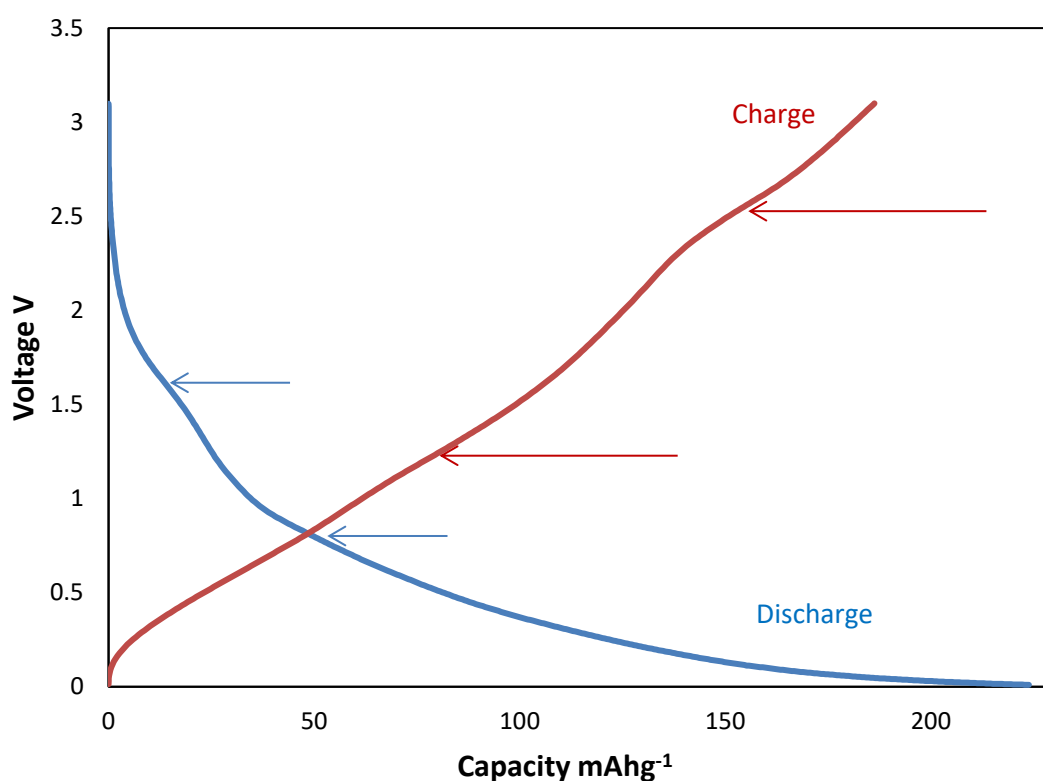


Figure 4.16: A typical PEDOT:PSS cycling curve with redox plateaus indicated

Figure 4.17 shows the cycling behaviour of PEDOT:PSS over multiple cycles, indicating a stable discharge capacity over 50 cycles. The large discharge capacity exhibited on the initial discharge (insertion of Li^+), is observed on every PEDOT:PSS cell regardless of coating method. This high initial capacity and subsequent loss of capacity on the second cycle could be attributed to several factors. A large drop in the initial capacity is often due to Surface Electrolyte Interface (SEI) formation. When the growth of thick SEI layers are observed, it appears in the initial cycling. As once a stable interface has formed it blocks the access of electrolyte to the active material putting a halt on further growth, however, no SEI layer was observed in the SEM images discussed in section 4.3.5, in addition to this, PEDOT:PSS is known to be stable versus standard electrolytes as it is often used as a protective layer on active materials to reduce side reactions and also to suppress SEI growth [24].

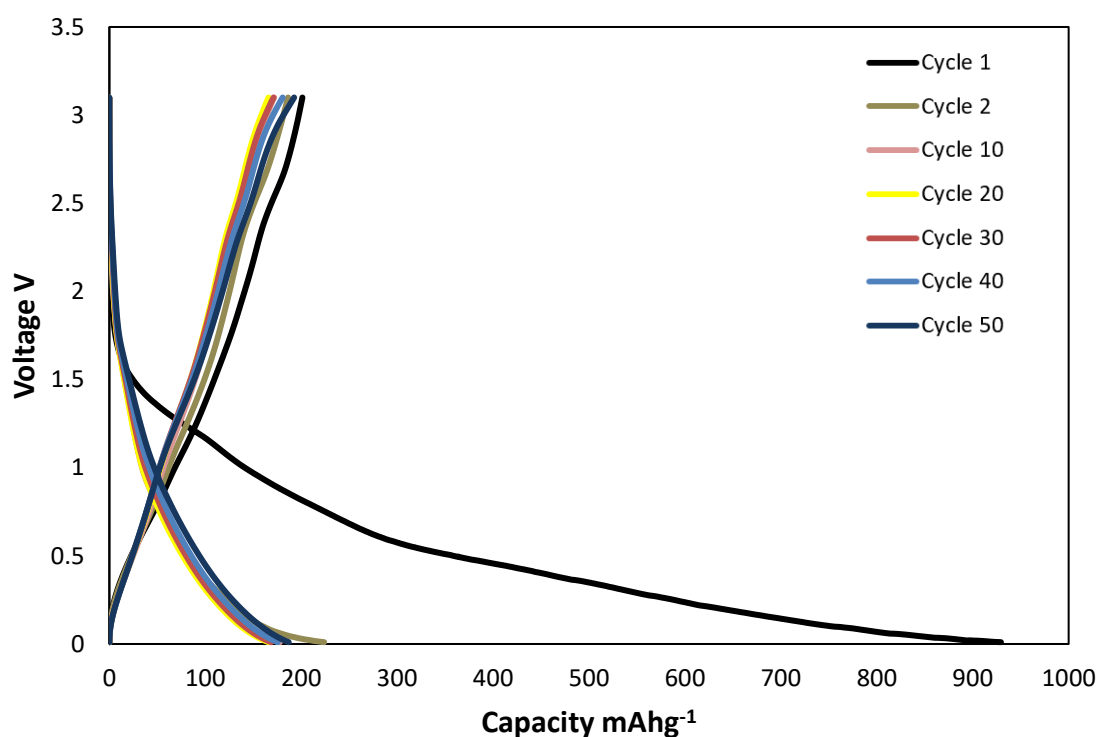


Figure 4.17: Multiple cycling curves of PEDOT:PSS

Another potential reason would be electrolyte degradation, however this would be seen to continue through further cycling, not only the initial cycle, it would also be expected to exhibit a 'noisy' cycling curve where this reaction is taking place, which is not the case here. Another possible reason is lithium trapping, proposed by Higgins et.

al. [19] where Li^+ ions are inserted into a material and the process is not fully reversible so that there are Li^+ ions trapped in the material and can no longer be utilised in the cycling of the material. This has also been observed in other studies of PEDOT:PSS cycling by Higgins et al. [19] where a capacity loss of 50mAhg^{-1} after the initial cycle was observed, this corresponded to a capacity loss of 83% in the successive cycles, not dissimilar to the capacity drop observed in the Inkjet printed sample from this study. The irreversible ionic reaction in PEDOT:PSS is also supported by Plieth et al. [25] and Huang et al. [26]. Figure 4.18 shows the CV curves of the first cycle (where “lithium trapping” is proposed) and the subsequent cycle (where stable cycling is observed).

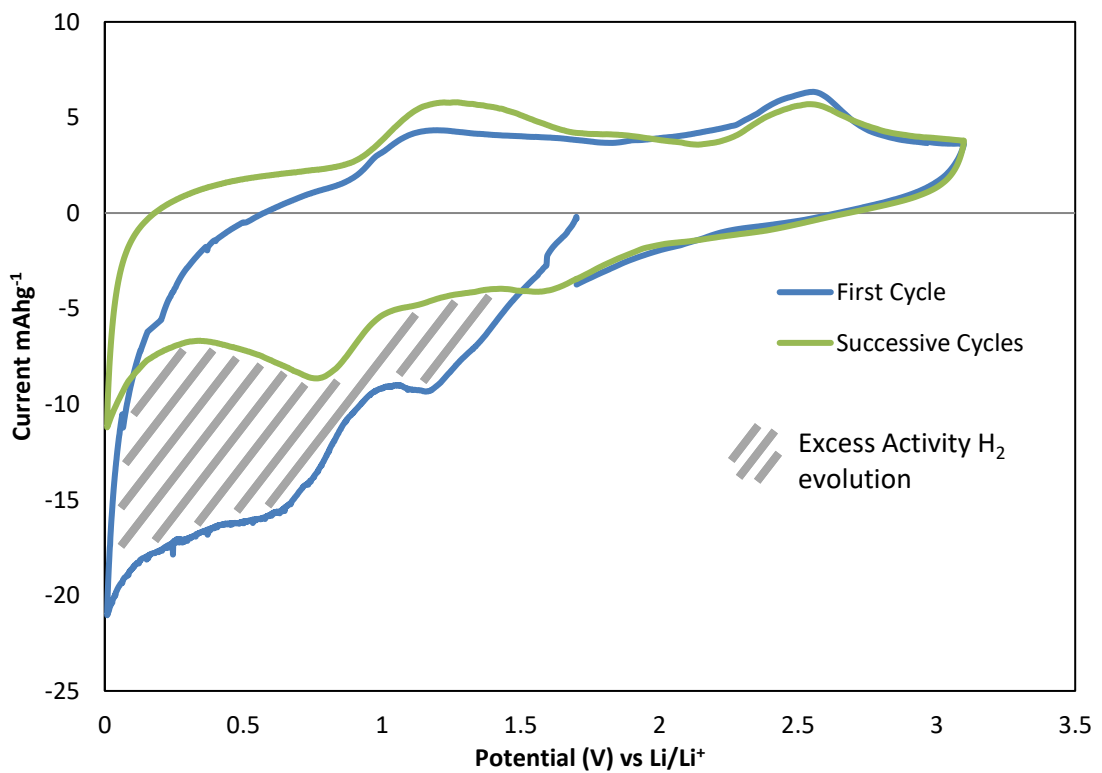


Figure 4.18: CV curves of initial (blue) and subsequent (green) PEDOT:PSS cycles

Upon closer inspection of the CV curves, it is evident that the current density is significantly larger in the first cycle when compared to the subsequent cycle (it should be noted that all successive cycles exhibit CV curves with current density matching each other). This corresponds well to the galvanostatic cycling curves and the proposed “lithium trapping” mechanism, whereby an ion exchange is occurring between H^+ and Li^+ in the $[\text{SO}_3^- \text{H}^+]$ groups. This ejection of H^+ paired with the charge balancing electrons leads to the formation of H_2 during the initial discharge, this

process is irreversible under regular cycling conditions, hence the association with “lithium trapping”.

To further support the lithium trapping theory, Quantum Mechanical modelling indicates strong phase separation between PEDOT and PSS [27]. The model indicates highly concentrated regions of closely packed PSS⁻ with open channels sitting amongst them supporting the potential for high ion mobility. The model also suggests that, as multiple PSS sit next to each other, Li⁺ ions are likely to “hop” between PSS sites rather than travel towards the Li-metal, hence becoming trapped. This phase separation phenomenon in PEDOT:PSS has been previously observed and reported in literature [28].

4.3.4.3 FTIR

In addition to reports of “lithium trapping” and the Quantum mechanical modelling suggesting Li⁺ prefers to remain in the PSS⁻ network, FTIR is used to give further insight into this mechanism. An FTIR spectrum of pure and lithiated PEDOT:PSS is shown in Figure 4.19 along with a representation of the PSS monomer indicating the preferred Li⁺ site in Figure 4.20.

From the FTIR, a peak at 705cm⁻¹ in the pristine PEDOT:PSS corresponds to an S-OH stretch, in the lithiated spectrum. This peak seems to split into two separate peaks at 719 and 669cm⁻¹. As Li⁺ interacts with the PSS⁻ monomer an interaction occurs with the S-O bond, the additional mass associated with the introduction of Li⁺ ions results in a frequency downshift – corresponding to the 669cm⁻¹ peak – where the Li⁺ stabilises the single bond. Whilst the 719cm⁻¹ corresponds to the sulphate bonds not interacting with the Li⁺ due to localised S-O double bonds, instead indicates the weaker long bond between PSS and PEDOT.

Upon closer inspection of these peaks (Figure 4.19 inset) it can be seen that the 705cm^{-1} peak in the pristine material is a broad peak which seems to also incorporate the peak at the 719cm^{-1} location. The bonding proposed is as follows:

1. Pristine:

705cm^{-1} PSS⁻—H⁺ short bonds – dominating

719cm^{-1} PSS⁻-----PEDOT⁺ weaker long bonds

2. Lithiated:

719cm^{-1} PSS⁻-----PEDOT⁺ weaker long bonds

669cm^{-1} PSS⁻—Li⁺ short bonds replacing H⁺

} Equal weighting

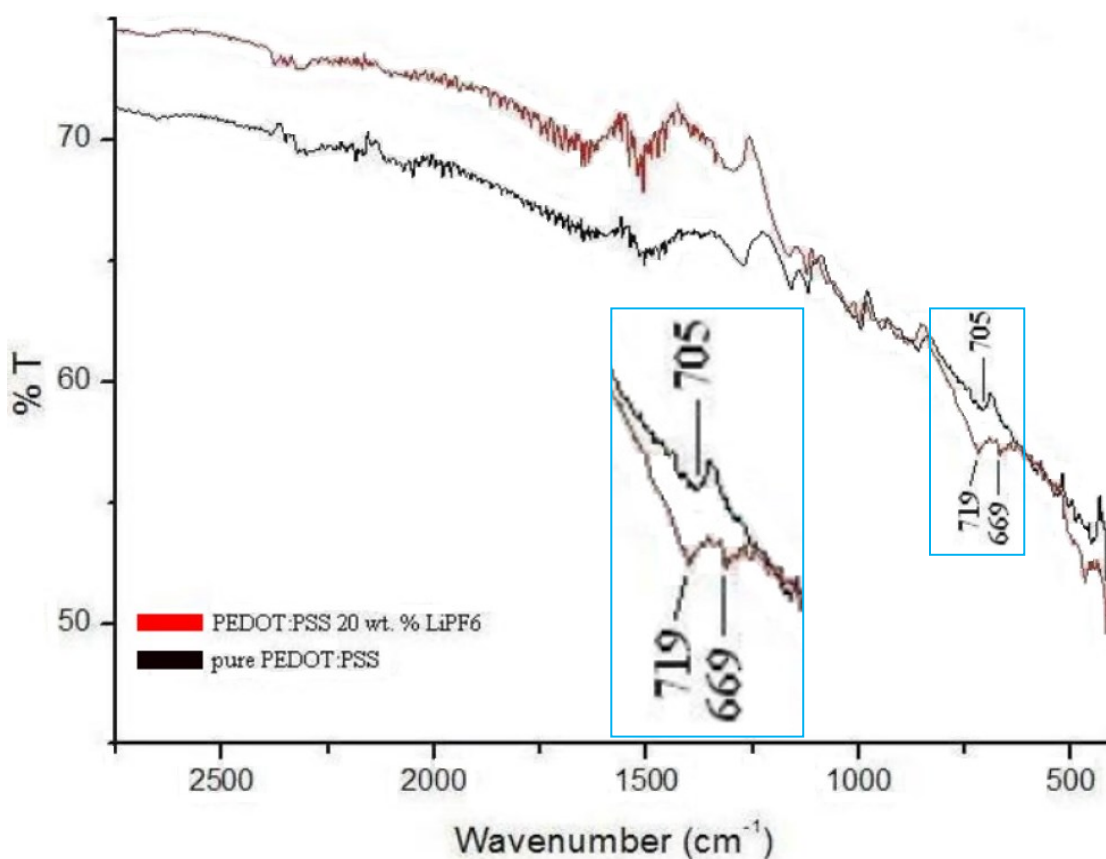


Figure 4.19: FTIR spectrum of pure and lithiated PEDOT:PSS (reprinted with permission [27])

It was suggested that the 669cm^{-1} may correspond to water, however, (no peaks were observed at 3000cm^{-1} and above corresponding to O-H stretching [27]) and no sharp peaks between 1600 and 1680cm^{-1} corresponding to H₂O bending was observed, therefore, it is deemed an unlikely cause for the splitting of the peak in pure PEDOT:PSS.

The model in Figure 4.18 indicates preferred Li^+ bonding to the single bonded oxygen in the SO_3^- groups. This matches the location of H^+ within the SO_3^- groups and corresponds well to literature [23].

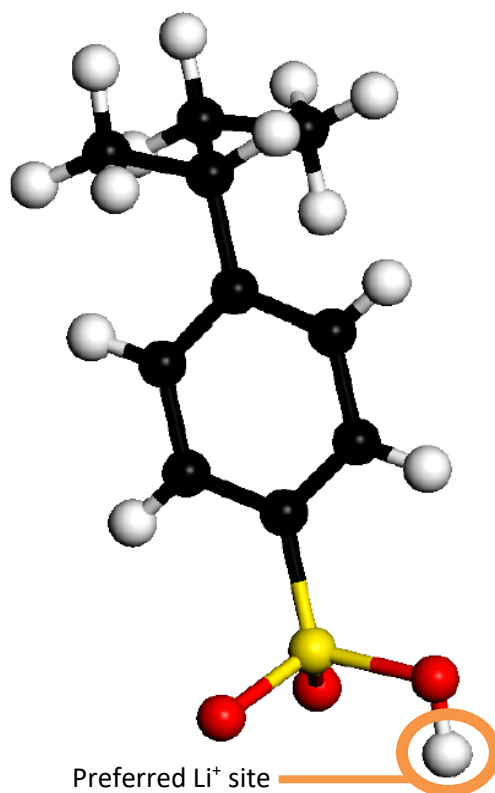


Figure 4.20: Model of PSS monomer indicating preferred Li^+ site

4.3.4.4 Proposed Mechanism – Deposition Dependent Reactions

As for the reason behind varying performance depending on deposition technique, it is proposed that the first reaction (stated in section 4.5.1) where electrons are inserted into PEDOT and Li^+ are inserted into vacant PSS^- sites, takes place consistently, due to the uninhibited electron network provided by the conducting polymer itself, meaning that electrons can always fill the available holes provided by PEDOT. This is supported by the fact the first plateau is a very similar size independent of deposition technique (Figure 4.21). However, the second reaction stated, where additional electrons are inserted into PSS to form a radical and additional Li^+ are attracted to these sites, are more difficult and have a greater reliance on both conductive network and electrolyte access to PSS sites. Hence this reaction step is limited by Li^+ ion access network, i.e. this reaction is controlled by the amount of contact area the film has with the ion-donating electrolyte and the electronic conductive network provided by the PEDOT. This is supported by the large difference in the second plateau size dependent on deposition technique (Figure 4.21)

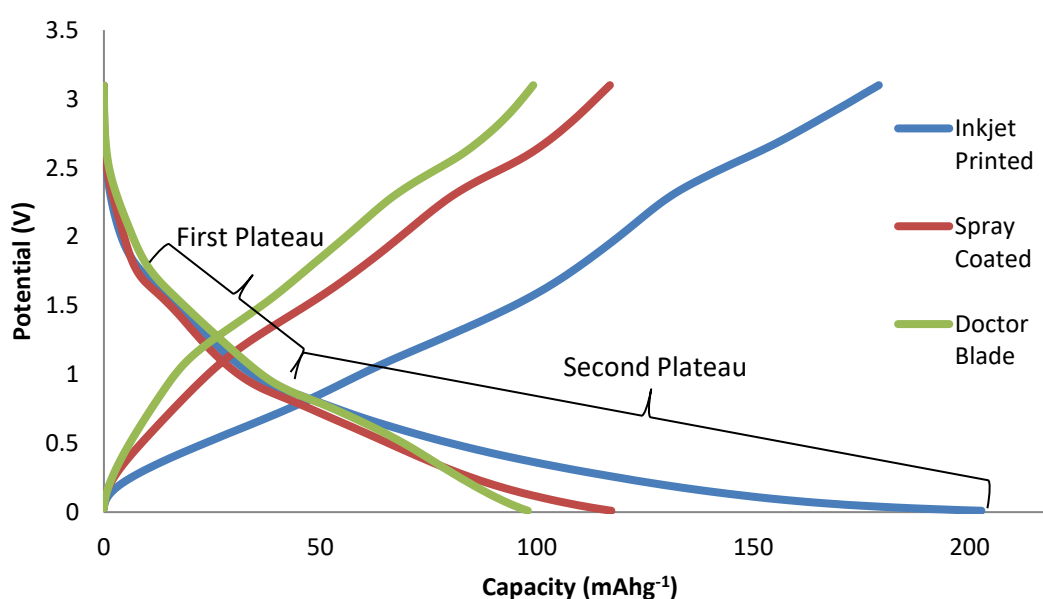


Figure 4.21: Galvanostatic cycling profiles of Inkjet Printed, Spray Coated and Doctor Blade cast PEDOT:PSS, indicating first and second reaction plateaus

Figure 4.22 A, B, C and D show the basic principle of the mechanism behind the proposed explanation. With the doctor bladed sample (Figure 4.22 A), a single pass deposition technique resulted in a thick film with ionic contact only at the surface of the film. It is known that upon ion insertion and removal into PEDOT:PSS, swelling and contraction is observed, however, due to the additional CMC binder used, the film stays intact. This leads to stable cycling performance but limited capacities.

Looking at the spray coated sample (Figure 4.22 B), a similar principle is observed, the area of PEDOT:PSS in contact with electrolyte is restricted to the surface. However, upon repeated insertion/removal of lithium ions, resulting in repeated swelling and contracting, it is proposed that the aforementioned flaking in the film occurs, with no binder to hold the flakes in place, they can move, revealing additional layers of PEDOT:PSS underneath the surface (Figure 4.22 C), this process is repeated, hence the rising capacities shown in Figure 4.13 B. In addition, this would explain the “erratic” cycling behaviour, as a constant change in available Li^+ sites in every cycle dependant on how the film has swelled/contracted in the previous cycle, this may also give rise to additional H_2 formation as new layers of accessible $[\text{PSS}^-\text{H}^+]$ sites are revealed, this matches the coulombic efficiency values exhibited by the spray coated material.

When looking at the Inkjet printed sample (Figure 4.22 C), it is shown that the multi-layered, droplet-type structure allows for deeper electrolyte penetration giving higher amounts of surface contact between PEDOT:PSS and electrolyte, allowing a larger amount of the Li^+ sites to be utilised. In addition, the brickwork-like structure allows for swelling and contracting without the flaking as observed in the spray-coated film. Together, these attributes result in higher capacities and matched with good coulombic efficiency values.

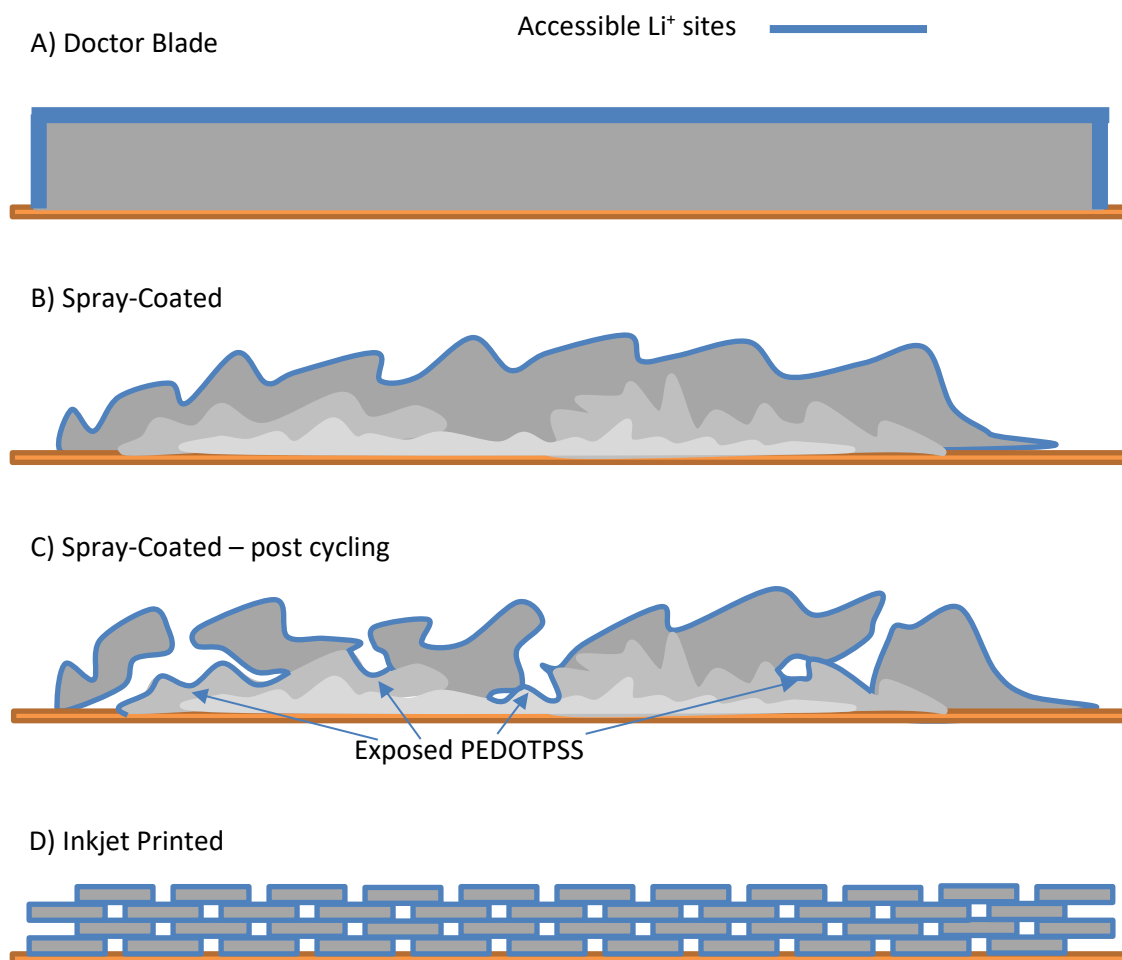


Figure 4.22: Schematic diagram of the proposed mechanism for performance variations in A) Doctor Blade B) Spray Coated C) Spray Coated post-cycling D) Inkjet Printed PEDOT:PSS films

4.3.5 Post Mortem SEM

To further determine whether the first cycle capacity loss is due to SEI formation, as well as to determine the impact cycling has on the structural integrity of the PEDOT:PSS coating, post-cycling SEM images have been taken. Half cells assembled as coin cells were cycled to various stages: pristine, 1st discharge, 20 cycles and 100+ cycles. They were then returned to a glovebox and decrimped, the electrodes were removed and SEM images collected. Figure 4.23 shows the different electrodes, pristine and after various amounts of cycles. It can be seen that whilst there have been extensive cycling differences between samples; there is no noticeable difference between the SEM images of the different electrodes. This indicates not only good structural integrity of the films, but also good cycling and chemical stability. These

results support the proposal that the first cycle capacity loss is not due to thick SEI formation, though thin SEI formation cannot be ruled out completely, however, a more probable explanation is, in fact, a result of the aforementioned Li^+ trapping. Another possible explanation for the high capacity exhibited in the first cycle is polymeric rearrangement, that is to say, PEDOT:PSS has rearranged itself creating the effect of additional capacity, the rearranged PEDOT:PSS then becomes stable and no further additional capacity is observed.

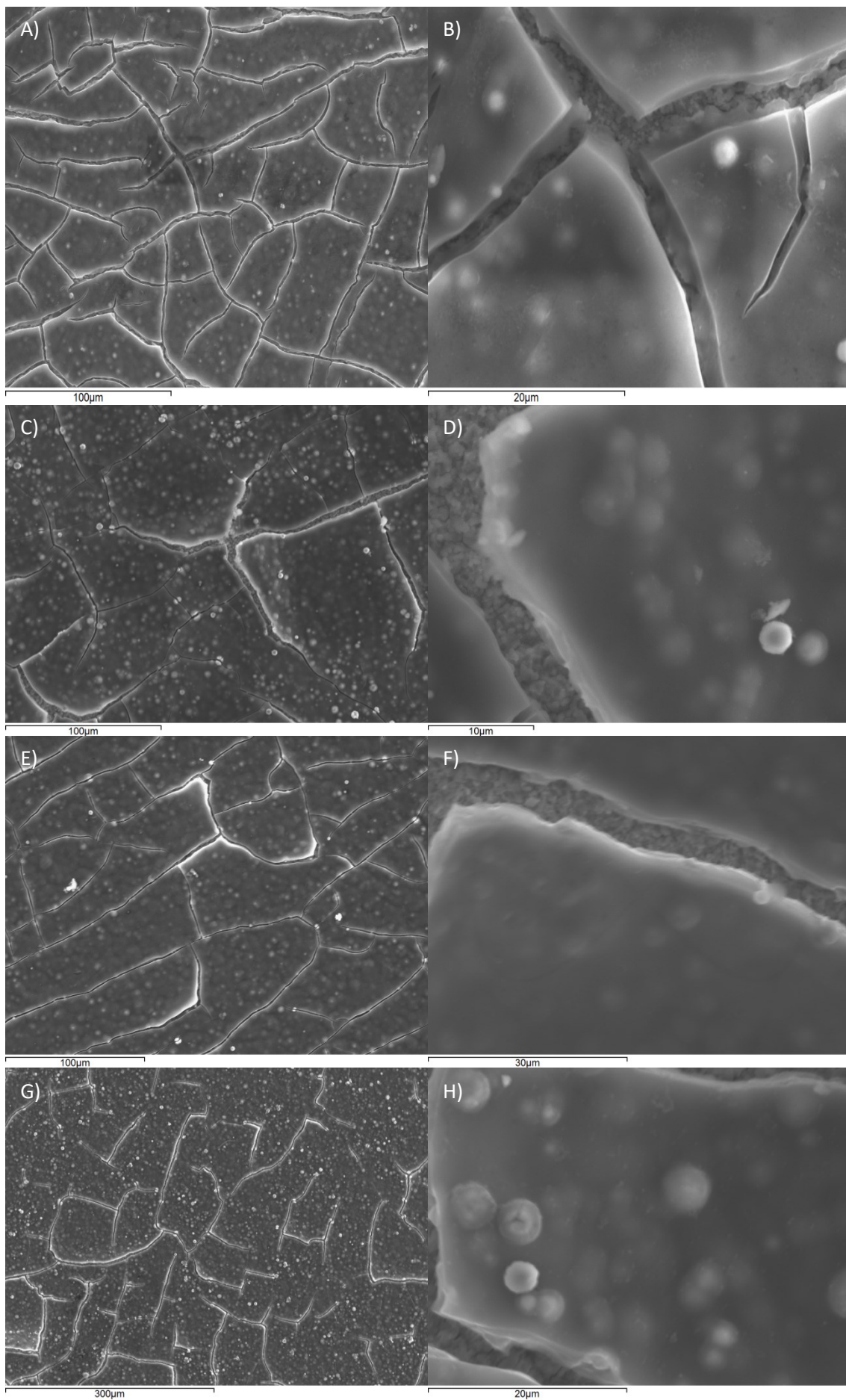


Figure 4.23: SEM images of post-mortem PEDOT:PSS cells A) B) pristine C) D) after 1st discharge E) F) after 20 cycles G) H) after 100+ cycles

4.4 Conclusion

PEDOT:PSS was investigated as a potential candidate for an anode material in lithium-ion batteries. The intention was to create a binder-free electrode film with strong adhesion properties and electrochemical performance. Two deposition techniques were proposed and compared to a standard Doctor Blade deposition technique commonly used in Li-ion battery manufacturing. Techniques used in this study were doctor blade coating, spray coating and inkjet printing. All techniques used an environmentally friendly solvent (water), and no additional additives (conducting carbon or binder) were used other than CMC binder in the doctor bladed sample.

SEM was conducted to observe film-forming and adhesion properties, along with elemental mapping to observe elemental distribution. It was found that copper diffusion was occurring in all samples, likely due to the acidic nature of PEDOT:PSS. CV was conducted to determine at which voltages redox reactions were taking place to give a better insight into the mechanics behind cycling PEDOT:PSS.

It was found that electrochemical performance was heavily influenced by the deposition technique used, not only in capacities, but also coulombic efficiencies. With “erratic” performance being shown in spray coated films, which also exhibited flaking due to the uneven deposition and lack of binder. In contrast, inkjet printed films demonstrated strong adhesion to the current collector along with strong electrochemical performance and coulombic efficiency values.

Whilst PEDOT:PSS films exhibit lower capacities than conventional anode materials such as graphite (theoretical capacity 372mAhg^{-1} and experimentally $\approx 330\text{mAhg}^{-1}$ [29]) their capacities remain stable around 200mAhg^{-1} . In addition, the material may be of further convenience when applying the material to flexible battery systems due to the polymers inherent flexibility.

A mechanism has been proposed, to explain the lithium trapping observed by others in the literature but not explained. It is proposed that an irreversible/not easily reversible ion exchange mechanism occurs during the first cycle. Where protons are replaced by

Li^+ ions and H_2 is formed. In addition, an explanation of the varying performance due to deposition technique has been proposed.

Overall, PEDOT:PSS was successfully deposited using inkjet printing as a binder-free film with strong adhesion properties, it exhibited strong electrochemical performance and simple processability without the use of harsh solvents. Placing it well as a candidate for further investigation in polymer electrode Li-ion batteries.

Further investigations should include a deeper exploration into the reaction mechanisms proposed, including simulation work and utilising techniques such as NMR, XAS and XPS to gain a better understanding of the interactions with PEDOT:PSS upon cycling.

4.5 References

- [1] G.-F. Wang, X.-M. Tao and R.-X. Wang, "Fabrication and characterization of OLEDs using PEDOT:PSS and MWCNT nanocomposites," *Composites Science and Technology*, vol. 68, no. 14, pp. 2837 - 2841, 2008.
- [2] B. Xu, S.-A. Gopalan, A.-I. Gopalan, N. Muthuchamy, K.-P. Lee, J.-S. Lee, Y. Jiang, S.-W. Lee, S.-W. Kim, J.-S. Kim, H.-M. Jeong, J.-B. Kwon, J.-H. Bae and S.-W. Kang, "Functional solid additive modified PEDOT:PSS as an anode buffer layer for enhanced photovoltaic performance and stability in polymer solar cells," *Scientific Reports*, vol. 7, 2017.
- [3] I. F. Perepichka and D. F. Perepichka, *Handbook of Thiophene-Based Materials: Applications in Organic Electronics and Photonics*, Chichester: John Wiley & Sons Ltd, 2009.
- [4] Y. Liu, B. Weng, J. M. Razal, Q. Xu, C. Zhao, Y. Hou, S. Seyedin, R. Jalili, G. G. Wallace and J. Chen, "High-Performance Flexible AllSolid-State Supercapacitor from Large Free-Standing GraphenePEDOT/PSS Films," *Scientific Reports*, vol. 5, 2015.
- [5] M. Asplund, T. Nyberga and O. Inganas, "Electroactive polymers for neural interfaces," *Polymer Chemistry*, vol. 1, pp. 1341-1520, 2010.
- [6] M. Berggren and A. Richter-Dahlfors, "Organic Bioelectronics," *Advanced Materials*, vol. 19, no. 20, 2007.
- [7] L. Zolin, J. Nair, D. Beneventi, F. Bella, M. Destro, P. Jagdale, I. Cannavaro, A. Tagliaferro, D. Chaussy, F. Geobaldo and C. Gerbaldi, "A simple route toward next-gen green energy storage concept by nanofibres-based self-supporting electrodes and a solid polymeric design," *Carbon*, vol. 107, pp. 811-822, 2016.
- [8] N. Singh, C. Galande, A. Miranda, A. Mathkar, W. Gao, A. L. M. Reddy, A. Vlad and P. M. Ajayan, "Paintable Battery," *Scientific Reports*, vol. 2, p. 481, 2012.
- [9] N. Chaturvedi, S. K. Swarmi and V. Dutta, "Spray deposition of poly(3-hexylthiophene) and [6,6]-phenyl-C61-butyric acid methyl ester blend under electric field for improved interface and organic solar cell characteristics," *Thin Solid Films*, pp. 82-87, 2016.
- [10] N. Scarratt, J. Griffin, T. Wang, Y. Zhang, H. Yi and A. Iraqi, "Polymer-based solar cells having an active area of 1.6 cm² fabricated via spray coating," *APL Materials*, vol. 3, 2015.
- [11] D. Yoo, J. Kim and J. H. Kim, "Direct synthesis of highly conductive poly(3,4-ethylenedioxythiophene):poly(4-styrenesulfonate) (PEDOT:PSS)/graphene composites and their applications in energy harvesting systems," *Nano Research*, pp. 717 - 730, 2014.
- [12] H. Lee, Y. Kim, H. Cho, J.-g. Lee and J. H. Kim, "Improvement of PEDOT:PSS linearity via

- controlled addition process," *RSC Advances*, vol. 9, 2019.
- [13] J. Kim, C. Park, S. Im, H. Lee and J. H. Kim, "Effect of molecular weight distribution of PSSA on electrical conductivity of PEDOT:PSS," *RSC Advances*, vol. 9, p. 4028, 2019.
- [14] M. Murray, "Cracking in coatings from colloidal dispersions An industrial perspective," AkzoNobel RD & I, Wilton UK, 2009.
- [15] F. Zhi-Hui, H. Yan-Bing, S. Quan-Min, Q. Li-Fang, L. Yan, Z. Lei, L. Xiao-Jun, T. Feng, W. Yong-Sheng and X. Rui-Dong, "Polymer solar cells based on a PEDOT:PSS layer spin-coated under the action of an electric field," *Chinese Physics B*, vol. 19, no. 3, 2010.
- [16] P. Singh, S. K. Srivastava, B. Sivaiah, P. Prathap and C. M. S. Rauthan, "Enhanced photovoltaic performance of PEDOT:PSS/Si solar cells using hierarchical light trapping scheme," *Solar Energy*, vol. 170, pp. 221 - 233, 2018.
- [17] M.-C. Chen, Y.-S. Chiou, J.-M. Chiu, A. Tedla and Y. Tai, "Marked improvement in the stability of small molecule organic photovoltaics by interfacial modification using self-assembled monolayers to prevent indium diffusion into the active layer," *Journal of Materials Chemistry A*, vol. 1, 2013.
- [18] H. Ujiie and E. M. Freire, "Ink jet printing technology (CIJ/DOD)," in *Digital Printing of Textiles*, Woodhead Publishing, 2006, pp. 29 - 52.
- [19] T. Higgins, S. Park, P. King, C. Zhang, N. McEvoy, N. Berner, D. Daly, A. Shmeliov, U. Khan, G. Duesberg, V. Nicolosi and J. Coleman, "A Commercial Conducting Polymer as Both Binder and Conductive Additive for Silicon Nanoparticle-Based Lithium-Ion Battery Negative Electrodes," *ACS NANO*, pp. 3702 - 3713, 2016.
- [20] J. F. Mike and J. L. Lutkenhaus, "Recent Advances in Conjugated Polymer Energy Storage," *Journal of Polymer Science, Part B: Polymer Physics*, vol. 51, pp. 468 - 480, 2013.
- [21] N. C. Perez, *Innovative Poly(3,4-ethylenedioxythiophene) Materials for Electrochemical Energy Storage*, Vizcaya: University of the Basque Country UPV/EHU, 2017.
- [22] J. M. Conder, Asymmetrically Functionalized Separator for Lithium-Sulfur Battery with Polysulfide Barrier Properties, ETH Zürich, 2016.
- [23] A. Arena, N. Donato and G. Saitta, "Electrical characterization of solid-state heterojunctions between PEDOT:PSS and an anionic polyelectrolyte," *Microelectronics Journal*, vol. 38, no. 6 - 7, pp. 678 - 681, 2007.
- [24] J. Lee and W. Choi, "Surface Modification of Over-Lithiated Layered Oxides with PEDOT:PSS Conducting Polymer in Lithium-Ion Batteries," *JES*, vol. 162, no. 4, pp. 734 - 748, 2015.

- [25] W. Plieth, A. Bund, U. Rammelt, S. Neudeck and L. Duc, "The role of ion and solvent transport during the redox process of conducting polymers," *Electrochimica Acta*, vol. 51, no. 11, pp. 2366 - 2372, 2006.
- [26] J.-H. Huang, D. Kekuda, C.-W. Chu and K.-C. Ho, "Electrochemical characterization of the solvent-enhanced conductivity of poly(3,4-ethylenedioxythiophene) and its application in polymer solar cells," *Journal of Materials Chemistry*, vol. 19, pp. 3704 - 3712, 2009.
- [27] M. Woods, *A Novel Approach to Design an Integrated Antenna-Battery System*, Canterbury: University of Kent, 2015.
- [28] A. V. Volkov, K. Wijeratne, E. Mitraka, U. Ail, D. Zhao, K. Tybrandt, J. W. Andreasen, M. Berggren, X. Crispin and I. V. Zozoulenko, "Understanding the Capacitance of PEDOT:PSS," *Advanced Functional Materials*, vol. 27, 2017.
- [29] R. Dash and S. Pannala, "Theoretical Limits of Energy Density in Silicon-Carbon Composite Anode Based Lithium Ion Batteries," *Scientific Reports*, vol. 6, 2016.
- [30] J. Li, H. Zhang, J. Liu and H. Qi, "Influence of Alkaline Treatment with Ammonia Water on the Properties of PEDOT: PSS Films," *International Journal of Photoenergy*, vol. 2012, no. 1, 2012.
- [31] J. Li, J. Liu, C. Gao, J. Zhang and H. Sun, "Influence of MWCNTs Doping on the Structure and Properties of PEDOT:PSS Films," *International Journal of photoenergy*, 2009.
- [32] M. O. P. Kara and M. W. Frey, "Effects of Solvents on the Morphology and Conductivity of Poly(3,4-ethylenedioxythiophene):Poly(styrenesulfonate) Nanofibers," *Applied Polymer Science*, vol. 131, 2014.

5 Solid State Electrolyte – PEGDA PEM

5.1 Introduction

Lithium ion batteries are one of the most dominant battery technologies for use in modern electronics. This is due to their suitability in “high drain” applications, ability to recharge multiple times with very good efficiency and their high energy density. Their use spans from small consumer electronics, such as mobile phones, to electric vehicles and grid applications. Frost and Sullivan have reported a dramatic increase in electric vehicle demand over the next few years, from \$381.9 million in 2013 to an estimated \$7.6 billion by 2020. [1]

One of the key research areas in Li-ion battery technology is their safety, due to their potential to combust. Needless to say, the expected growth in a single sector of an even larger market has fuelled the need for research in this area. The research finds limitations in the current technology and attempts to improve upon it. One of these major limitations is the liquid electrolyte. Liquid electrolytes are currently used due to the convenience of their high ionic conductivity (approx. $\approx 10^{-2} \text{Scm}^{-1}$) [2, 3]. However, these electrolytes are highly flammable and are prone to leaking from their battery casings, potentially causing battery fires and explosions. When their intended use is in consumer electronics and electric vehicles this is a major hazard. With Electric Vehicles in particular, where road collisions are inevitable and, therefore, a real possibility of damaging the batteries. Liquid electrolytes are also reliant on a separator, and ensuring that dendrites formed are not able to grow through/punch holes into this separator, therefore causing a short circuit.

5.2 Why Solid State

Safety issues are among the major reasons researchers are actively looking towards solid state batteries. This means removing the liquid electrolyte and polymer separator used in traditional Li-ion batteries, replacing it with a solid-state electrolyte. This immediately removes one of conventional Li-ion batteries’ problems – cell leakage whilst also reducing the chances of fires and explosions by using heat and flame-resistant materials as the solid-state electrolyte. There are many candidates that have

been investigated in literature, stemming from three main categories: glass, ceramic and polymeric. These have been discussed in Chapter 1, however, the chosen system for this study is a polymer electrolyte.

5.3 What is a Polymer Electrolyte

Polymer electrolytes (PE) can be categorised by 3 main types: 1) Ionic Liquid PE 2) Gel PE and 3) Solid PE. Each type has its advantages and disadvantages briefly explained here.

- 1) Ionic Liquid based PEs incorporate ionic liquids (room temperature molten salts) into a polymer network. The role of the ionic liquid is to act as plasticiser – reducing the polymer hosts' crystallinity – and provide free charge carriers increasing ionic conductivity. Ionic liquids require no additional solvent to assist with ion dissociation.
- 2) Gel polymer electrolytes (GPEs) are a type of intermediate between liquid electrolyte and full solid electrolyte. The idea is that a liquid electrolyte is incorporated with a polymer host matrix to give structural support to the electrolyte. GPEs have high ionic conductivities, good interfacial contact between electrolyte and electrode, however, separators are still necessary when using GPEs.
- 3) Solid polymer electrolytes (SPEs) are solvent free (the polymer matrix acts as solvent to the lithium salts) fully solid electrolytes where the polymer host contributes not only to the structural integrity of the electrolyte but also to the ionic conductivity and ion dissociation within its matrix. Due to their solid nature, additional separators are not necessary when using SPEs.

When referring to polymer electrolytes it is, henceforth, referring to solid polymer electrolytes unless expressly stated.

5.4 Polymer Electrolytes and Ionic Conductivity

Solid polymer electrolytes have been extensively researched in recent years, though the concept dates back over 40 years to the 1970's [4]. Polymer-salt complexes – as they were then referred, were vastly researched in many disciplines including the electrochemical community by forerunners in the field, such as Michel Armand [5] for use in energy storage. Early systems proposed involved a binary system of a lithium salt e.g. LiPF_6 and a polymer host, often, poly(ethylene oxide) (PEO). These systems, whilst paving the way for decades of promising research, are internally flawed. Ionic conductivities at room temperature is in the region of 10^{-6} Scm^{-1} far lower than the

accepted “superionic” range of $\geq 10^{-3} \text{ Scm}^{-1}$ and further still from liquid electrolytes which sit in the 10^{-2} Scm^{-1} range. To increase Li-ion diffusion it was found that by heating the PEO and other polymer-based electrolytes, ionic conductivities are significantly increased, approaching and exceeding the superionic threshold. This was a breakthrough that allowing the continuation of research into polymer electrolytes, but for polymers to be used in a commercial setting the room temperature conductivity issues would need to be solved. This requires knowledge of what is limiting ionic conductivity within a polymer electrolyte system i.e. an understanding of the lithium ion transport mechanisms is crucial before formulating a successful electrolyte candidate.

5.5 Lithium ion Transport Mechanism in Solid Polymer Electrolytes

When looking at ionic conductivity in solid electrolytes there are a wide variety of transport mechanisms that ought to be considered i.e. transport mechanisms in crystalline solids are different from amorphous systems. Ion mobility in crystalline structures usually occurs due to defects within their structure. These defects are often intentional to promote ion movement, they allow mechanisms, such as, vacancy transport and interstitial movement. Vacancy transport is where an ion in a crystalline lattice can “jump” or “hop” from its current site into an ionic vacancy, also referred to as a “hole”, one example of a defect in the lattice network (depicted in Figure 5.1 A). When an ion hops from its current site into a vacant site, another vacancy is created in its original site, allowing continued vacancy transport. When this process is repeated it contributes to ionic conductivity due to a net movement of charge. Interstitial movement is where ions move from irregular sites (not part of the normal crystalline structure) to either another irregular site (direct interstitial) or pushes out another ion from a regular site and takes its place, with the removed ion continuing the interstitial migration (indirect interstitial) (depicted in Figure 5.1 B and C respectively). These migration methods suggest that for high conductivity a system must have a large defect:charge-carrier ratio so as to allow free movement of ions.

It should be noted that the vacancy transport mechanism often requires elevated temperatures to be observed due to the higher activation energies required when

compared to the interstitial mechanism. A common place to observe vacancy transport is in Solid Oxide Fuel Cells (SOFCs) [6] [7].

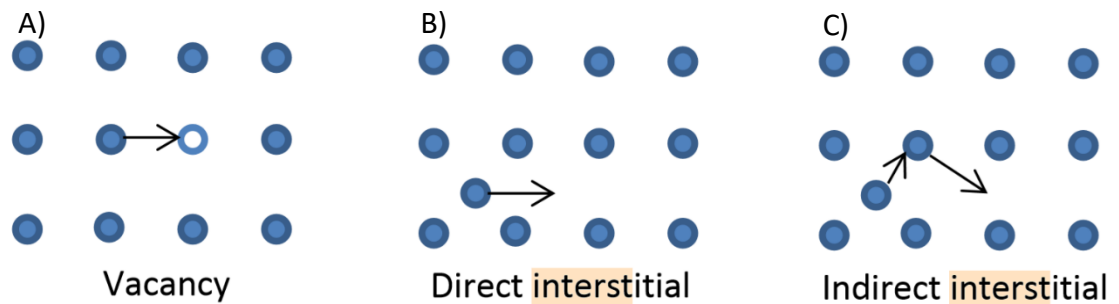


Figure 5.1: A diagram depicting the most common ion transport mechanisms found in crystalline materials (reprinted with permission [6])

In amorphous systems, defects are less common and more irregular in position, due to the lack of a long range, regular, lattice structure. Hence an additional ionic transport mechanism in the form of ion migration occurs, this is where a charge carrier with enough energy to overcome its binding energy takes the place of another ion, which in turn, continues the process, resulting in a net conductivity [8]. Polymer electrolytes can have attributes of both crystalline and amorphous mechanisms. Molecular dynamics simulations have suggested that ionic conductivity in solid polymer electrolytes occurs, with varying contributions, via three main methods: 1) Li^+ motion along polymer chains 2) Li^+ motion together with polymer chain movement and 3) Li^+ hopping between neighbouring polymer chains. [9] When discussing ionic conductivity in solid polymer electrolytes, ion hopping is often referred to as the dominant mechanism, often overlooking the other mechanisms involved. However, systems designed to increase ionic conductivity into the accepted superionic regions take the other methods into consideration when choosing the polymer host for the electrolyte, for example, choosing polymers with low glass transition temperatures T_g . The glass transition temperature is the temperature at which the molecules transform from a disordered but still relatively ridged and brittle structure with very low mobility to a more supple and mobile structure as temperatures increase above T_g . This allows for segmental motion and thus, an increased ionic conductivity linked to polymer chain motion. [10]

In addition to the aforementioned ionic conduction mechanisms and discussions on glass transition temperatures, it has been well understood that ionic conductivity largely occurs in the amorphous regions of solid polymer electrolytes [11]. This suggests that an amorphous solid polymer electrolyte (SPE) is preferable to a SPE with crystalline or semi-crystalline phase. Amorphous regions in a polymer electrolyte can be created in many ways, including the addition of nanoparticles, nanowires, block polymers and other fillers. These “fillers” act to disrupt the repeating chain structure of crystalline polymer networks creating or enhancing the size of amorphous regions and, thus, facilitating charge carrier mobility [12].

Sometimes, fillers are used in such quantities that they can be considered as polymer/ceramic composites or polymer blends [13]. In such composites, fillers are used not only to enhance ionic conductivity by disrupting the polymer network, but to also promote Li-salt dissociations, increasing charge carrier mobility. Additionally, fillers can create pathways through the host polymer by which Li⁺ ions can travel. Fillers in larger quantities can also be used to enhance solid electrolytes thermal stability and mechanical properties [14].

Another commonly used method to enhance solid polymer electrolytes properties is the addition of plasticizers. Plasticizers often come in the form of non-volatile solvents or low molecular weight polymers. ethylene carbonate (EC), propylene carbonate (PC) PEG-200, dibutylphthalate (DBP) and polyethyleneglycol dimethylether (PEGDME) have all been used as plasticizers in solid polymer electrolytes [15] [16]. Their role varies from creating amorphous regions in the polymer matrix and promoting ion pair dissociation to reducing glass transition temperatures and, therefore, increasing segmental motion within the polymer matrix which, again, promotes ionic conductivity, or a combination of all aspects.

The addition of plasticizers into a polymer electrolyte is one of the simplest, yet effective methods of increasing ionic conductivity. Whilst the addition of small molecule plasticizers comes with many advantages, their addition can also reduce performance in terms of mechanical properties, so a balance must be found in order to maintain the electrolytes stability. Among the vast array of plasticizers used in solid

polymer electrolyte research, succinonitrile (SCN) has been found to not only successfully promote ionic conductivity, but many cases, to do so whilst also maintaining mechanical properties, [17] [18] improving thermal stability and improving interfacial contact between electrolyte/electrode. These properties are owed to SCNs high melting point of 60°C which allows SCN to be used safely as a plasticizer without the detrimental effects of liquid plasticizers. SCN is the plasticizer used in the solid polymer electrolyte in this study.

5.6 Selecting a Host Polymer

As previously mentioned, poly(ethylene oxide) (PEO) is the most commonly used host polymer in solid polymer electrolyte research. This is due to PEOs' low glass transition temperature T_g , high stability vs lithium metal, a strong ability to dissolve lithium salts and a flexible macromolecular backbone, enabling ionic transport. [19] [20] However, PEOs high crystallinity prevents ion migration and thus, leads to low ionic conductivity and low Li^+ transference numbers at room temperature, thus, lowering the rate capabilities of batteries made using a PEO electrolyte [21]. Synthesising SPE using a PEO backbone, with high room temperature conductivity, requires the addition of a large amount of lithium salt which often sacrifices mechanical stability, creating brittle electrolyte layers, therefore limiting its potential applications [22]. Plasticisers have also been used in an attempt to both increase ionic conductivity and reduce the brittle nature of binary PEO polymer-salt electrolytes.

Multiple studies have incorporated SCN plasticiser into PEO/Li-salt polymer electrolyte membranes (PEMs) and have shown promising increases in ionic conductivity values [23] [24] [25]. However, these PEMs often suffer from weak mechanical properties, such as poor elasticity and waxy characteristics [26] [23]. This is attributed to the fact PEO is a linear polymer, to improve ionic conductivity values, large amounts of SCN are often required and thus, can have detrimental effects [27] [28]. To overcome this, many groups have looked at alternative host polymers, including PEO or derivatives such as C-PEGDE, PEGDMA, PEEC and PEGDA [29] [30] [31] [32].

This study takes a look at poly(ethylene glycol) diacrylate (PEGDA) as the host polymer due to its well documented characteristics. Properties utilised in this project include:

An ability to cross-link via UV photopolymerization, an ability to dissociate lithium ions from its salt and, due to its cross-linking ability, enhanced mechanical properties over standard PEO-based and other PEMs [28] [32] [33] [34]. It holds all the positive characteristics of polymer electrolytes and is, therefore, the most easily processable out of the aforementioned solid electrolyte categories as it does not require high temperature deposition or sintering. It has been shown that, like PEO, binary polymer-salt electrolytes exhibit low room temperature ionic conductivity, [35] so SCN was chosen as plasticiser to assist with ionic conductivity and lithium ion dissociation [36].

5.7 Aims

The aim of this chapter is to explore a PEGDA based ternary system as a solid-state electrolyte. Using known characterisation techniques to understand the electrolytes conductive, mechanical and thermal properties, whilst also testing the electrolyte electrochemically to gain an understanding of its stability and performance. Galvanostatic cycling of both half-cells and full cells is used to explore the electrolytes suitability to real-world systems, with the potential for integration into wearable electronics and other devices.

5.8 Synthesis

The materials used in the synthesis of the solid polymer electrolyte are as follows. Polyethylene glycol diacrylate molecular weight 8000 (PEGDA8000) was purchased from Alfa Aesar, Bis(trifluoromethane) sulfonimide lithium salt (LiTFSI) $\geq 99\%$, Succinonitrile 99% (SCN) and Phenylbis(2,4,6 – trimethylbenzoyl)phosphine oxide 97% (photoinitiator) were purchased from Sigma Aldrich. The LiTFSI salt was dried under vacuum at 120°C overnight before being transferred to an argon filled glovebox. The other chemicals were used as purchased.

The synthesis route used in this study has been widely used in UV-curable solid polymer electrolyte research. [37] [38] [39] [40] All PEM synthesis took place inside an argon filled glovebox. For this study, solid PEGDA8000, LiTFSI and SCN with a ratio of 25/30/45 wt.%, were mixed together to form a liquid, this was then stirred vigorously until all constituents were fully dissolved. The photoinitiator was added at a ratio of 1-2% with respect to the weight of PEGDA8000, stirring continued until fully dissolved.

The resulting clear gel-like liquid was then deposited on the desired substrate (glass for free standing membranes or directly onto electrodes for cell assembly) once deposited as desired, the liquid was then cured using UV light until solid. The resulting membranes are clear with a soft rubber-like texture. Figure 5.2 shows a schematic of the process.

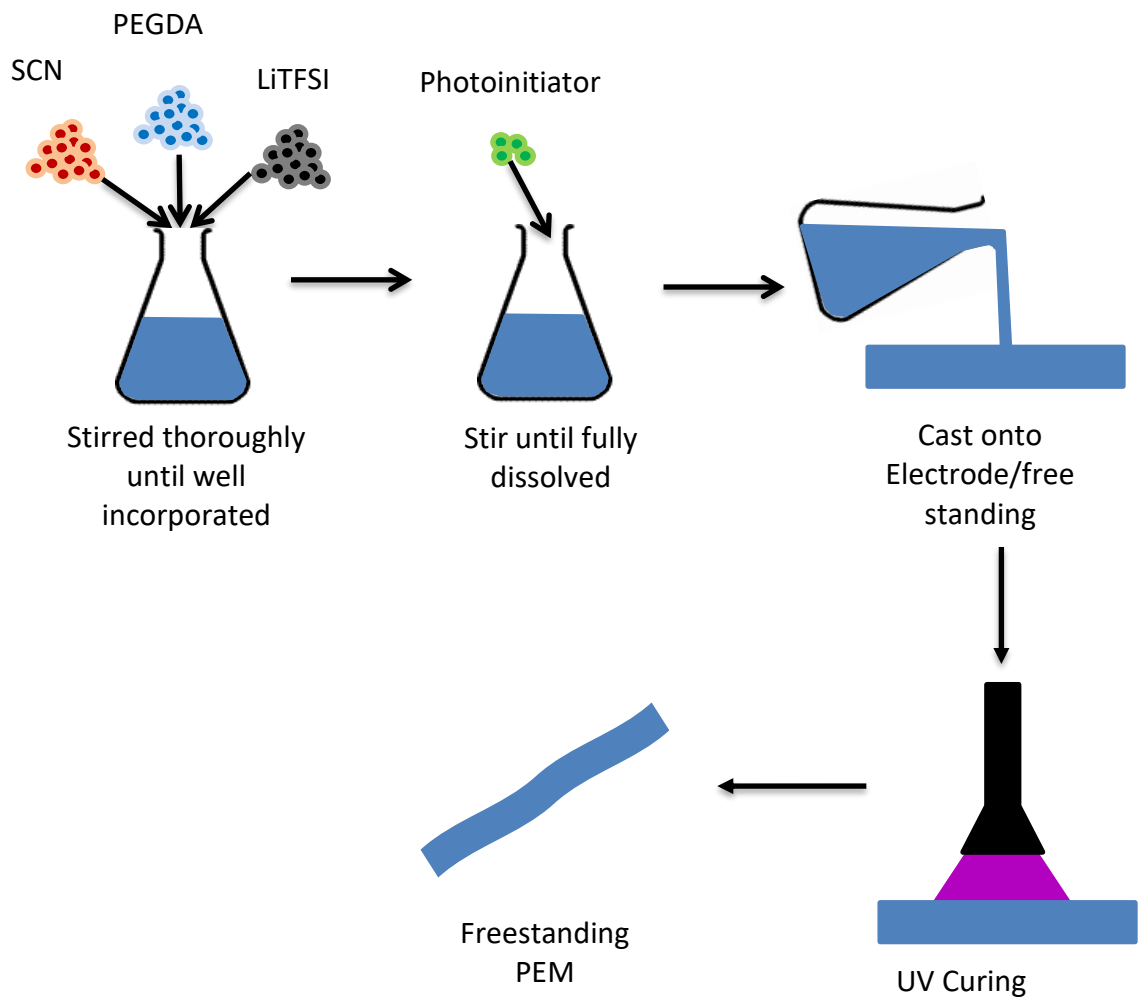


Figure 5.2: Schematic diagram of the PEGDA PEM synthesis process

5.9 Characterisation

5.9.1 XRD

Figure 5.3 shows the XRD spectra for the individual components of the PEM. It can be seen that all constituent components of the PEM have at least one distinctive peak, indicating crystallinity. The SCN XRD shows a plastic crystal structure – as evidenced by the amorphous “hump” paired with the sharp crystalline peak.

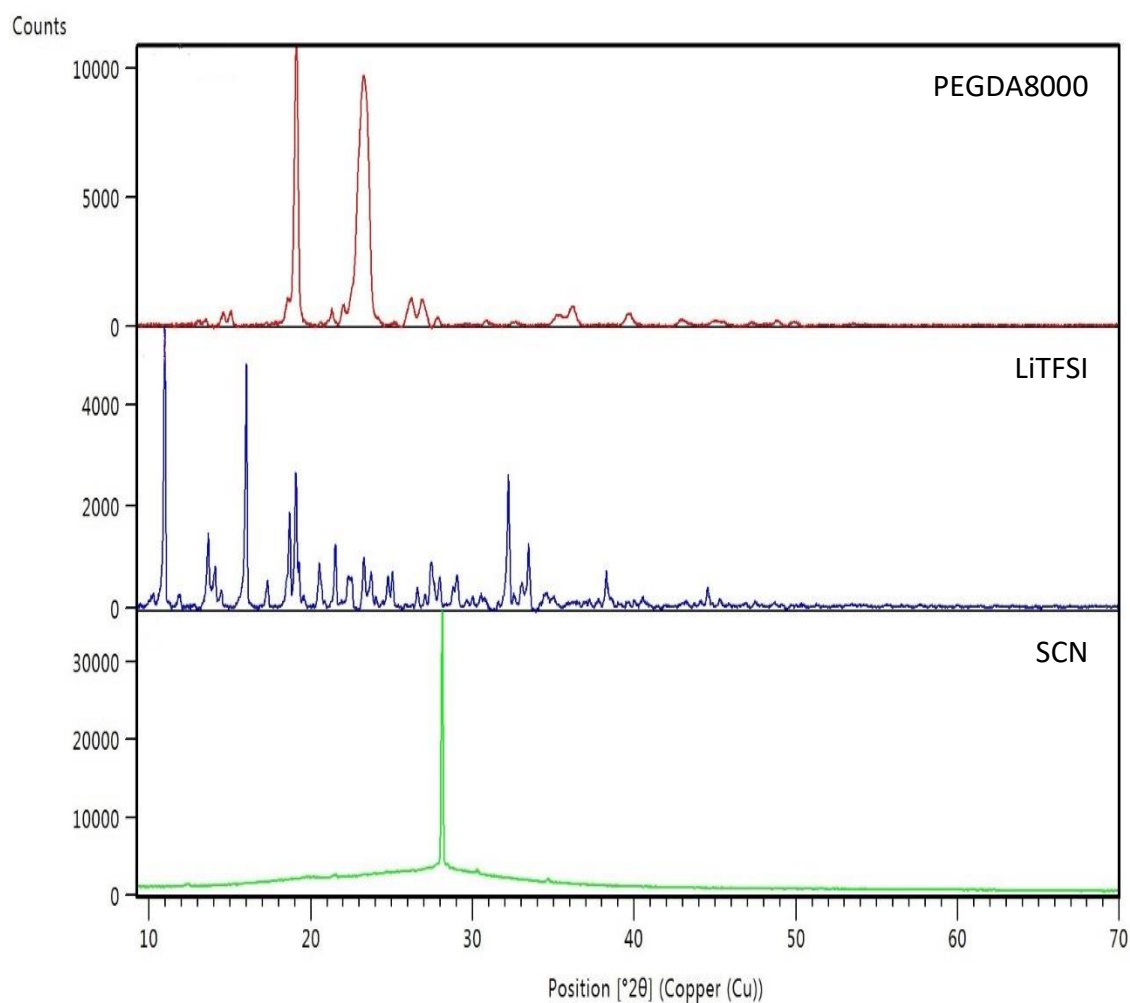


Figure 5.3: XRD spectra for the PEGDA PEM's constituent components (PEGDA8000, LiTFSI and SCN)

After mixing and UV curing, the PEM, PEGDA8000/LiTFSI/SCN (25/30/45 wt.%). The main feature, a singular broad peak around $2\theta = 20^\circ$ is recorded in the XRD (Figure 5.3). This is often referred to as the 'amorphous halo'. The broadness of the peak suggests the nature of the PEM is amorphous. As previously mentioned, this is often a target when designing SPEs as ionic conductivity is considered to take place in the amorphous regions of SPEs. When comparing the XRD pattern of the PEM (Figure 5.4) with the individual components (Figure 5.3) no identifiable peaks are present that correspond to its constituent chemicals suggesting the components are fully complexed. This is not to say that the sample is entirely amorphous, however, like many polymers, the main bulk is of an amorphous nature. Further characterisation will give a better indication to the PEMs true nature.

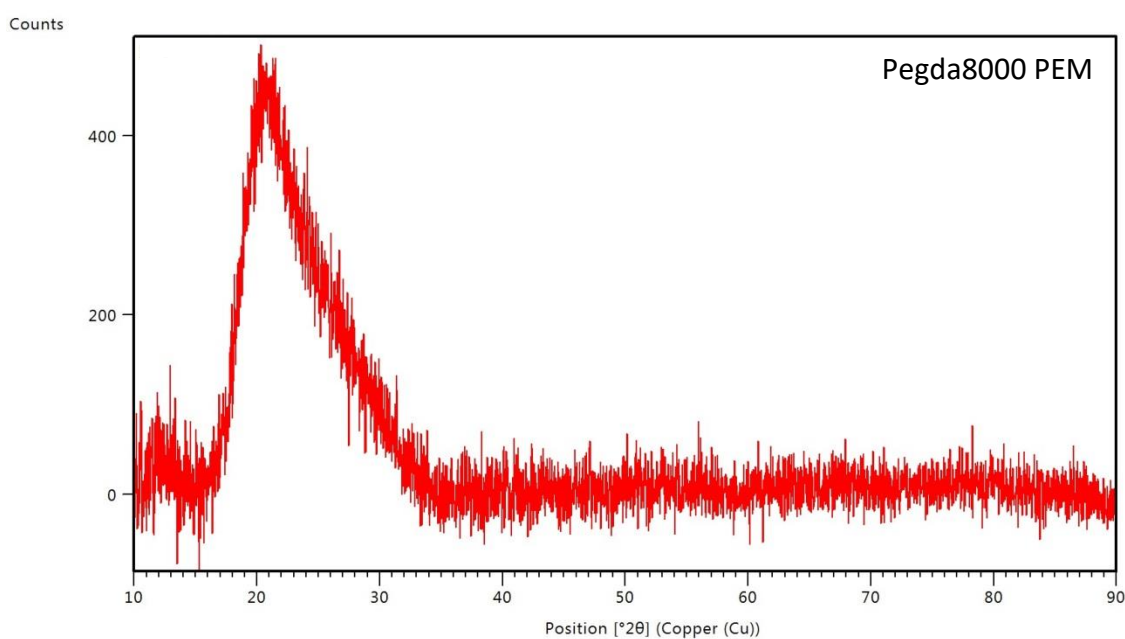


Figure 5.4: XRD pattern of Pegda PEM

5.9.2 TGA

Thermo Gravimetric Analysis (TGA) is widely used in battery analysis to better understand the materials' thermal properties, cycle life degradation, electrode degradation, electrolyte degradation and safety properties. There are a few well-known examples of thermal runaway occurring in lithium-ion batteries so TGA studies have played an important role in understanding this. Electrolyte degradation and combustion is another major safety factor to consider and TGA is widely used to analyse electrolytes' thermal properties. Here TGA is used to determine the PEGDA PEMs thermal stability and then compare with a standard liquid electrolyte.

Figure 5.5 shows TGA results for each of the PEMs constituent components. It can be seen that the thermal stability of SCN is the lowest, at a temperature of around 150°C whilst PEGDA8000 and LiTFSI demonstrate higher thermal stabilities, with decomposition temperatures of 375°C and 380°C respectively.

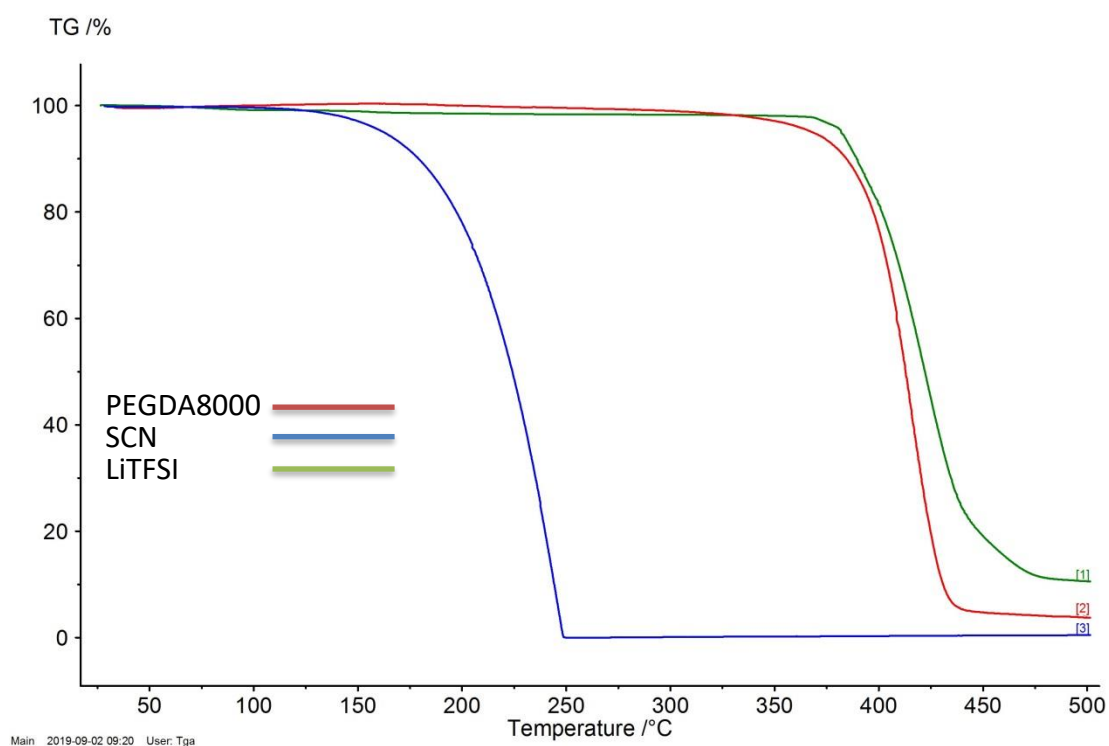


Figure 5.5: TGA results for PEM constituent components PEGDA8000, SCN and LiTFSI

It is commonly accepted that a thermal stability window for PEMs can be determined by the point at which 5% mass loss occurs. From the TGA measurement, (Figure 5.6) it can be seen that the sample is stable at temperatures up to 152°C, close to the decomposition temperature of pure SCN. This temperature is above standard battery applications. However, it should be noted that a battery's internal temperature increases when under load i.e. the battery is charging or discharging, this is caused by the chemical reactions happening within the cell, high currents and the cells' internal resistance. A batteries' electrolyte should, therefore, be able to cope with a range of temperatures without degradation. Temperature rises of 5-15°C above ambient temperature are well documented for low to moderate ($\leq 1C$) charging rates [41] [42]. Whilst temperature increases in excess of 20°C have been observed at high charging rates ($<5C$) [41] [43]. A thermal stability of 152°C suggests that the PEGDA based PEM is also suitable for elevated temperature cycling.

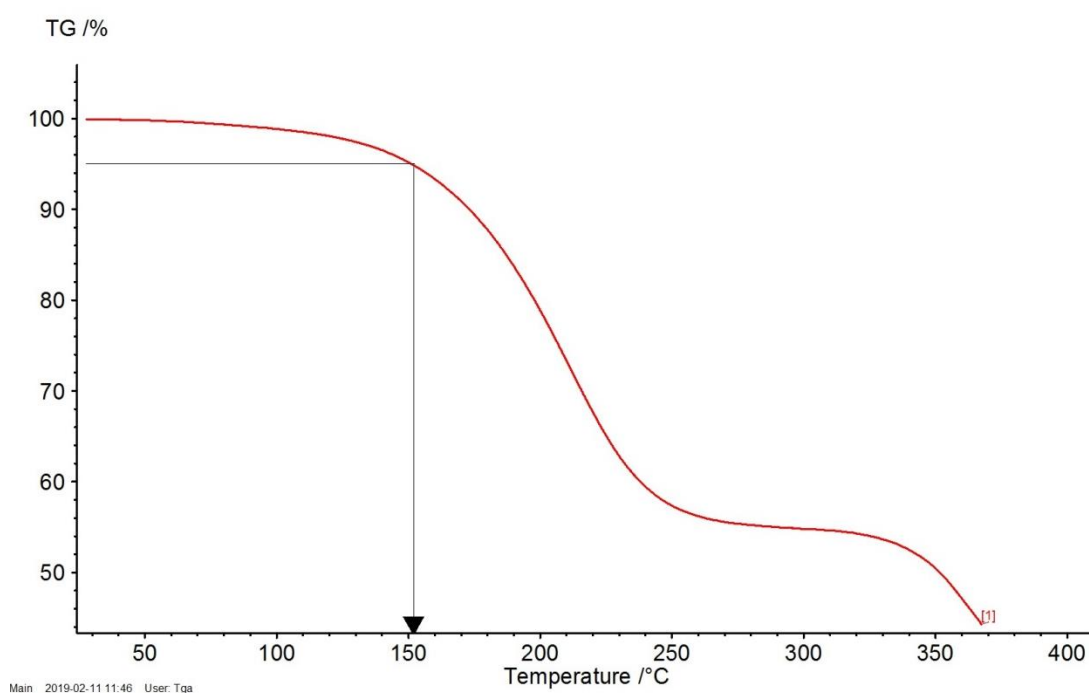


Figure 5.6: TGA results for PEGDA8000 based PEM with a 5% mass loss indication

The first mass loss occurs at around 150°C and corresponds to the degradation of SCN, it can be seen that the mass% falls by around 45% suggesting no SCN is present at temperatures beyond 250°C. The second mass loss, starting at around 330-350°C, is instead attributed to the degradation of PEGDA8000.

The main item to look at is the first degradation to occur (SCN) as this sets the PEMs thermal stability window. This can then be directly compared to standard electrolytes used today (1M LiPF₆ in EC/DEC). Figure 5.7 shows TGA of the liquid electrolyte alongside this study's PEM. It is apparent that the thermal stability of the liquid electrolyte is significantly inferior to the PEMs, with a mass loss occurring steadily from initial recording to a 5% mass loss at around 75-80°C, approximately half of the temperature of the PEMs stability window. LiPF₆ in EC:DEC based liquid electrolytes have been extensively studied for a better understanding of their thermal properties and its components formed during decomposition. These include LiF, PF₅, CO₂, POF₃, HF and carbonates [44] [45]. The first mass loss is usually attributed to a combination of LiF, POF₃, HF and PF₅ formation [46] where LiF, POF₃ and HF are formed in the presence of moisture within the electrolyte or cell and LiF and PF₅ are typically formed at temperatures above 80°C.

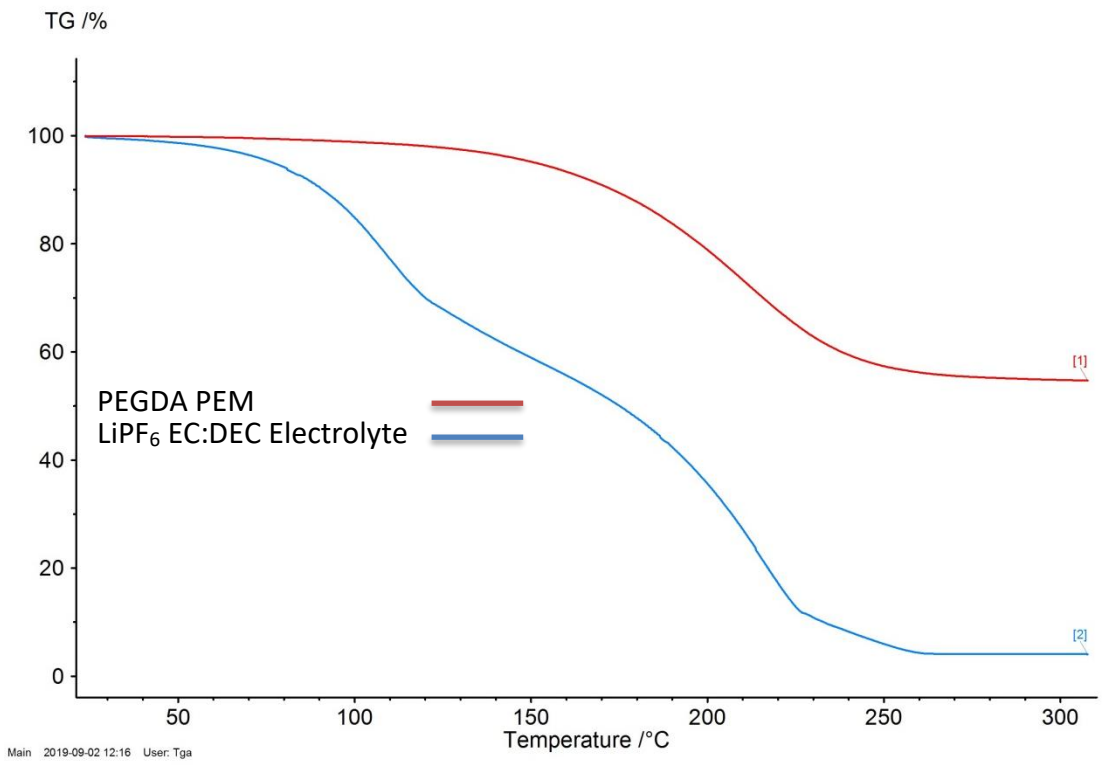


Figure 5.7: TGA results of PEGDA PEM vs LiPF₆ liquid electrolyte

5.9.3 DSC

To further understand the nature of the PEGDA8000 PEM, differential scanning calorimetry (DSC) was conducted, as shown in Figure 5.8. The broad sloped region is attributed to the PEMs glass transition temperature (T_g). As previously mentioned, the glass transition temperature is the temperature above which an amorphous materials properties transition from a rigid immobile state to a more mobile state. Here it can be seen that T_g has an onset of -75.3°C with its' mid-point at -68.7°C . With a T_g so low the PEM will always be operating at temperatures above this, a typical cycling environment will be at room temperature. The larger the gap between T_g and cycling temperature the higher the structures mobility will be and, therefore, the higher the potential conductivity will be.

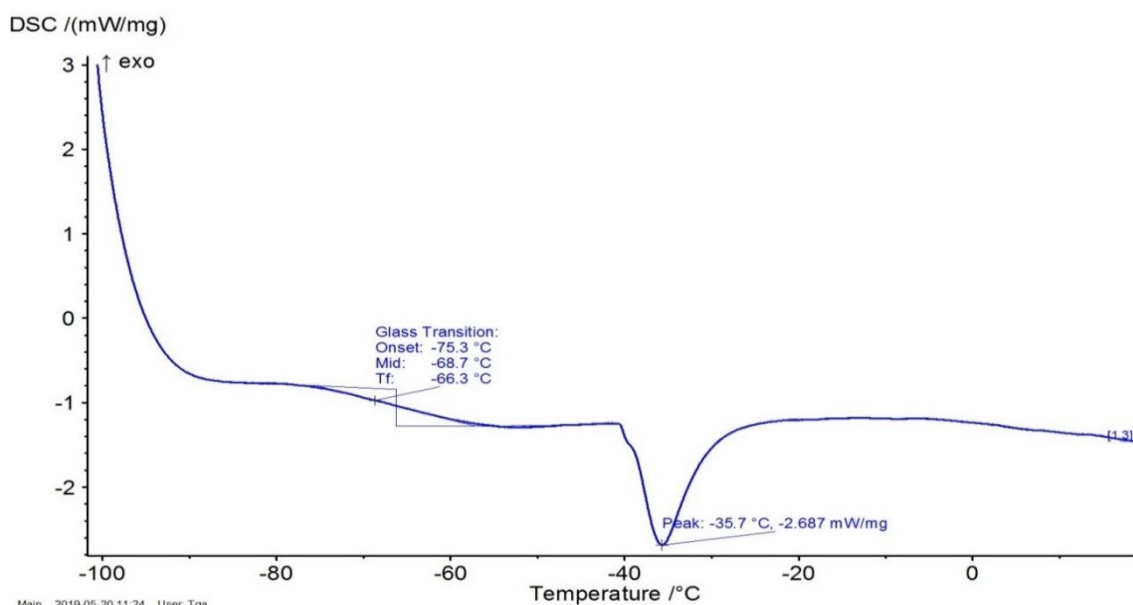


Figure 5.8: DSC scan for PEGDA PEM

Other than the T_g slope, there is another sharp feature indicated in Figure 5.8 which can be attributed to the SCN crystal to plastic-crystal phase change. This suggests that the PEM is not fully amorphous as this transition would not appear in the DSC curves. In addition to this, it suggests that the amount of SCN currently present in the PEM is higher than the amount soluble in the polymer network. This has previously been reported by Ruixuan He [47], showing a disappearance of this transition peak with a reduction of SCN in the PEM network. It is also suggested by the same group, that PEMs close to the coexistence envelope of isotropic and plastic crystalline regions can have polymerisation-induced crystallisation occurring during the PEM fabrication [40].

5.10 Mechanical Properties

It has been suggested that solid state batteries will pave the way for pioneering work on battery design. Previous barriers and design constraints will be overcome, allowing for 3D architecture, flexible, roll-able and even stretchable batteries to become a reality. For this to happen, electrolytes need to have the same degree of freedom as the battery design itself. The thermal properties of the PEGDA8000 PEM have been discussed, but this is of limited use if the PEM is brittle. Even a simple rolled cell design – common in consumer electronics (AA cells), would prove difficult with a brittle electrolyte.

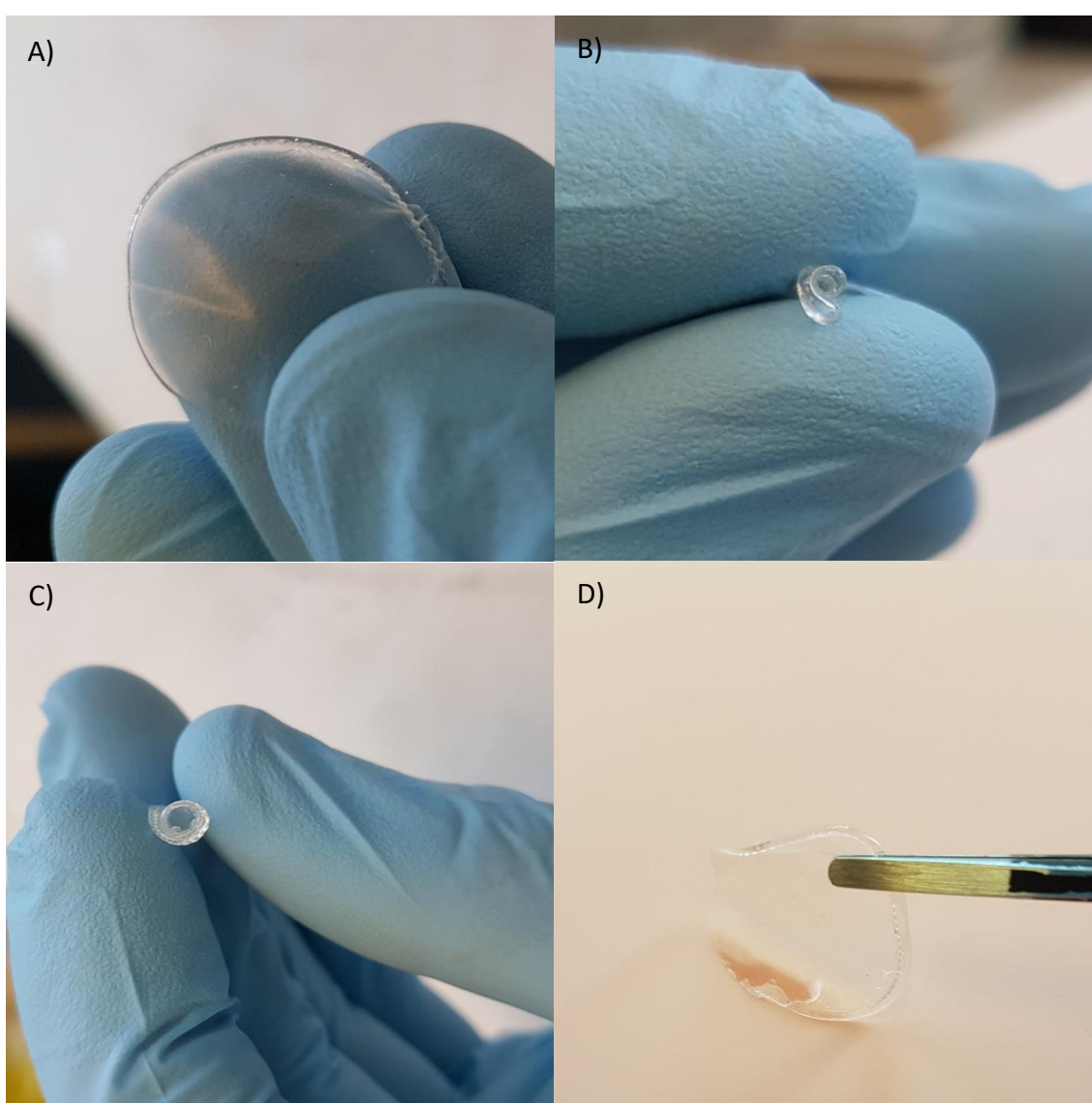


Figure 5.9: Freestanding PEGDA PEM being flexed, rolled and twisted

Figure 5.9 A-D, show free standing PEMs being flexed, rolled and twisted. It can be seen that the polymer electrolyte is supple and easily flexed. In addition, the figures demonstrate the PEMs' elasticity, returning to its original form, post flexing. This is an essential attribute of PEMs in terms of battery lifetime and potential abuse the battery may be subjected to by consumers. The PEMs ability to repeatedly flex ties in well with potential applications in flexible electronics.

Aside from the PEGDA8000 PEMs ability to flex, an attribute commonly found in polymer electrolytes, it is also stretchable. The stretching capability of the PEM is demonstrated in Figure 5.10. Whilst not entirely novel [48] [49] it is certainly a desirable attribute to have as it further reduces restrictions in cell designs and potential applications. It should be noted that all stretch testing was done by manually stretching, using two pairs of tweezers and reading from a ruler. Figure 5.10 shows the extent of stretching from the PEM's original size, it should be noted that after each of these stretches the tension was released and the PEM returned to its original size. It can be seen that the PEM has the ability to stretch to more than double its length. Further testing showed the PEM can be repeatedly stretched to over 200% of its original length without suffering irreversible deformation. The springy nature of the electrolyte allows it to return to its original size and shape quickly. Upon stretching even further, the PEM tears. This typically happens at the point which the PEM is stretched to 230% (an average of 5 different samples of the same composition).

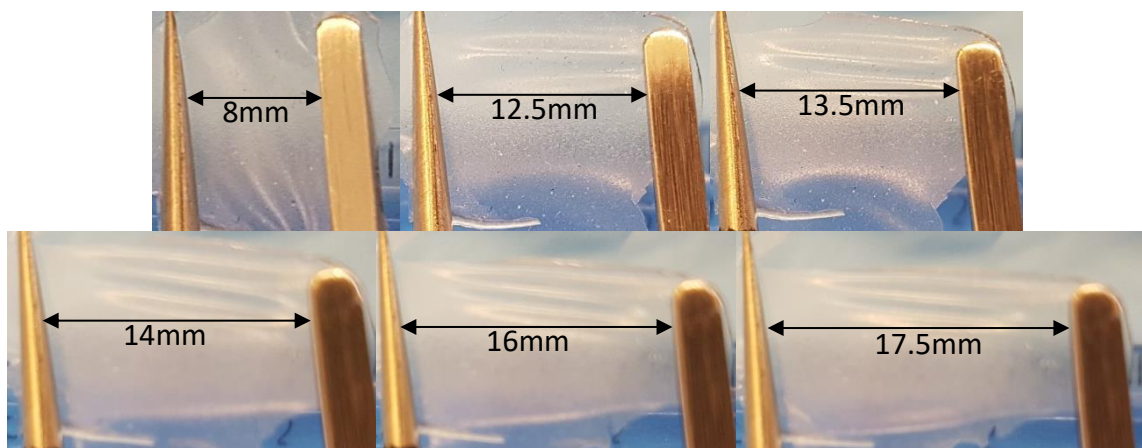


Figure 5.10: PEGDA PEM being stretched

5.11 Conductivity (Impedance Spectroscopy)

Electrochemical Impedance Spectroscopy (EIS) was used on a stainless steel/PEM/stainless steel cell to determine the PEMs conductivity at room temperature. The conductivity of a sample can be determined using the following equation:

$$\sigma = \frac{1}{\rho} \quad (5-1)$$

Where σ is conductivity and ρ is resistivity. To find the resistivity of a sample the following equation is used:

$$\rho = R \frac{A}{l} \quad (5-2)$$

Where R is the total resistance, A is the sample area and l is the sample thickness. To determine the total resistance impedance spectroscopy has been used. Impedance spectroscopy can be used to determine a samples' impedance (complex resistance) from which the total resistance can be determined. It is often difficult to distinguish between ionic and electrical conductivity, however, as the PEM would create a short circuit within a lithium-ion cell were it to conduct electrically, it has been considered negligible for this experiment.

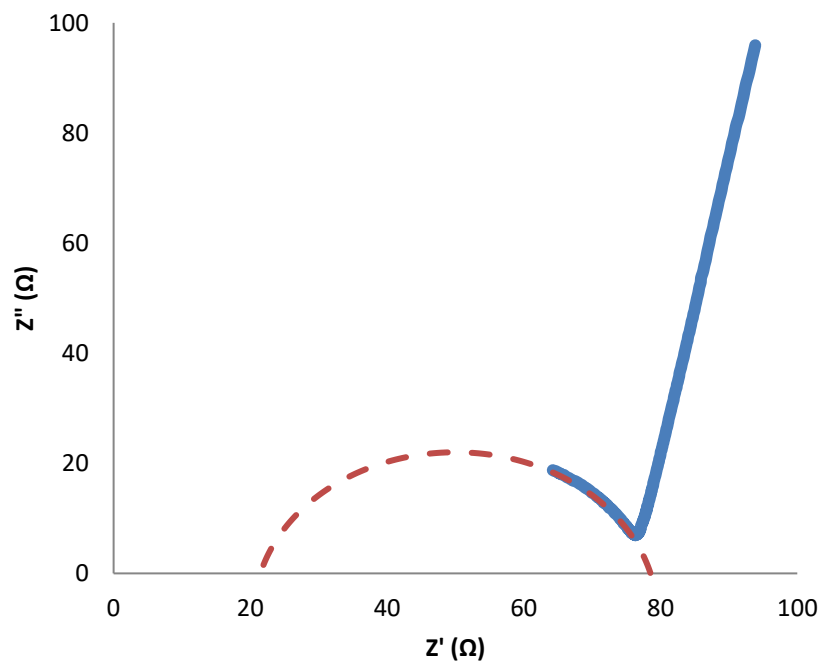


Figure 5.11: EIS spectrum of PEGDA8000 PEM

Figure 5.11 shows the EIS spectra, with the dashed line representing total resistance (R_{bulk}) determined by the intersection of the real resistance (Z') axis. Using equations 5-1 and 5-2, a conductivity value of $1.4 \times 10^{-3} \text{Scm}^{-1}$ was determined. This value places the PEGDA8000 PEM well within the “superionic” region and sits strongly among other similar systems, He et.al. reported a lower molecular weight PEGDA ternary system with a room temperature conductivity up to $1.0 \times 10^{-3} \text{Scm}^{-1}$ whilst Lu et. al. reports a room temperature conductivity of $1.6 \times 10^{-4} \text{Scm}^{-1}$ for a polysulfone-PEO copolymer ternary system (PSF-PEO)/LiTFSI/SCN [36] [50].

The “spur” or “tail” on the graph occurs due to the polarisation effect taking place on the stainless steel (SS) electrodes due to the mobility of lithium ions. It confirms both the ionically blocking nature of the SS electrodes and the ionic nature of the PEM.

5.12 Electrochemical Stability vs Li/Li⁺

Aside from high ionic conductivity, the PEM must also be electrochemically stable vs lithium to be used in a cell. If the PEM breaks down or reacts with lithium in the regular potential window then it limits its applications as an electrolyte. To test the electrochemical stability of the PEM a Li/PEM/SS cell was made and a linear sweep CV curve was generated with a scan rate of 1mVs^{-1} . The current response is monitored and a sharp rise in current is observed when PEM oxidation or other reaction occurs.

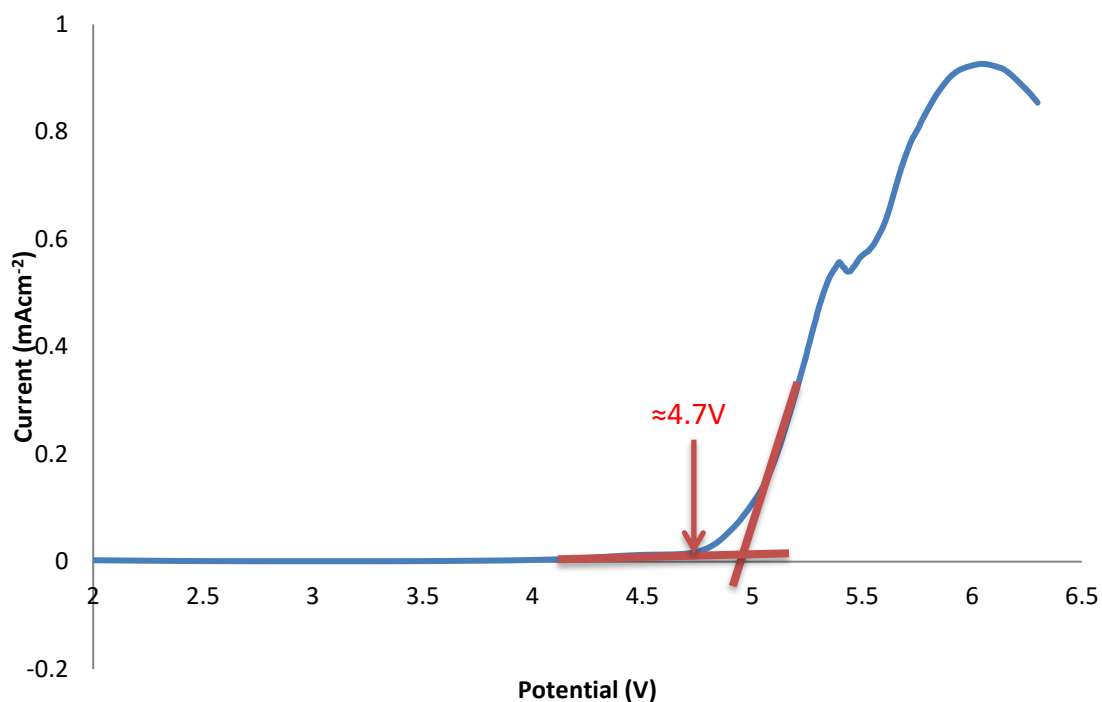


Figure 5.12: Electrochemical stability window of PEGDA8000 PEM

Figure 5.12 shows a flat profile from 2V until well into the 4V region, a sharp rise is then observed at around 4.7V indicating a reaction between the lithium and the PEM. It can therefore be stated that PEM: PEGDA8000/LiTFSI/SCN (25/30/45 wt.%) is electrochemically stable up to 4.7V. This allows for the PEM to be used with a multitude of cathode materials including $\text{LiNi}_{0.33}\text{Mn}_{0.33}\text{Co}_{0.33}\text{O}_2$ (NMC) or LiCoO_2 (LCO), two materials widely used in industry today. As a comparison, carbonate based liquid electrolytes are electrochemically stable up to a voltage of $\approx 4.2\text{V}$, beyond this potential, the electrolytes undergo various forms of decomposition including gas evolution and ROH formation which, in turn, can lead to LiPF_6 hydrolysis, POF_3 formation and eventually HF formation [51] [52].

5.13 SEM

A scanning electron microscopy (SEM) image of the bulk UV cured PEGDA8000 PEM (Figure 5.13) shows a smooth surface. Also, elemental mapping was carried out to determine the distribution of the components in the PEM. EDX mapping of elements carbon, oxygen, fluorine and sulphur show a homogenous distribution of all elements ruling out “highly concentrated zones” due to poor mixing. This distribution is ideal, a homogenous membrane indicates that performance (thermal, mechanical and conductivity) should be consistent throughout the PEM.

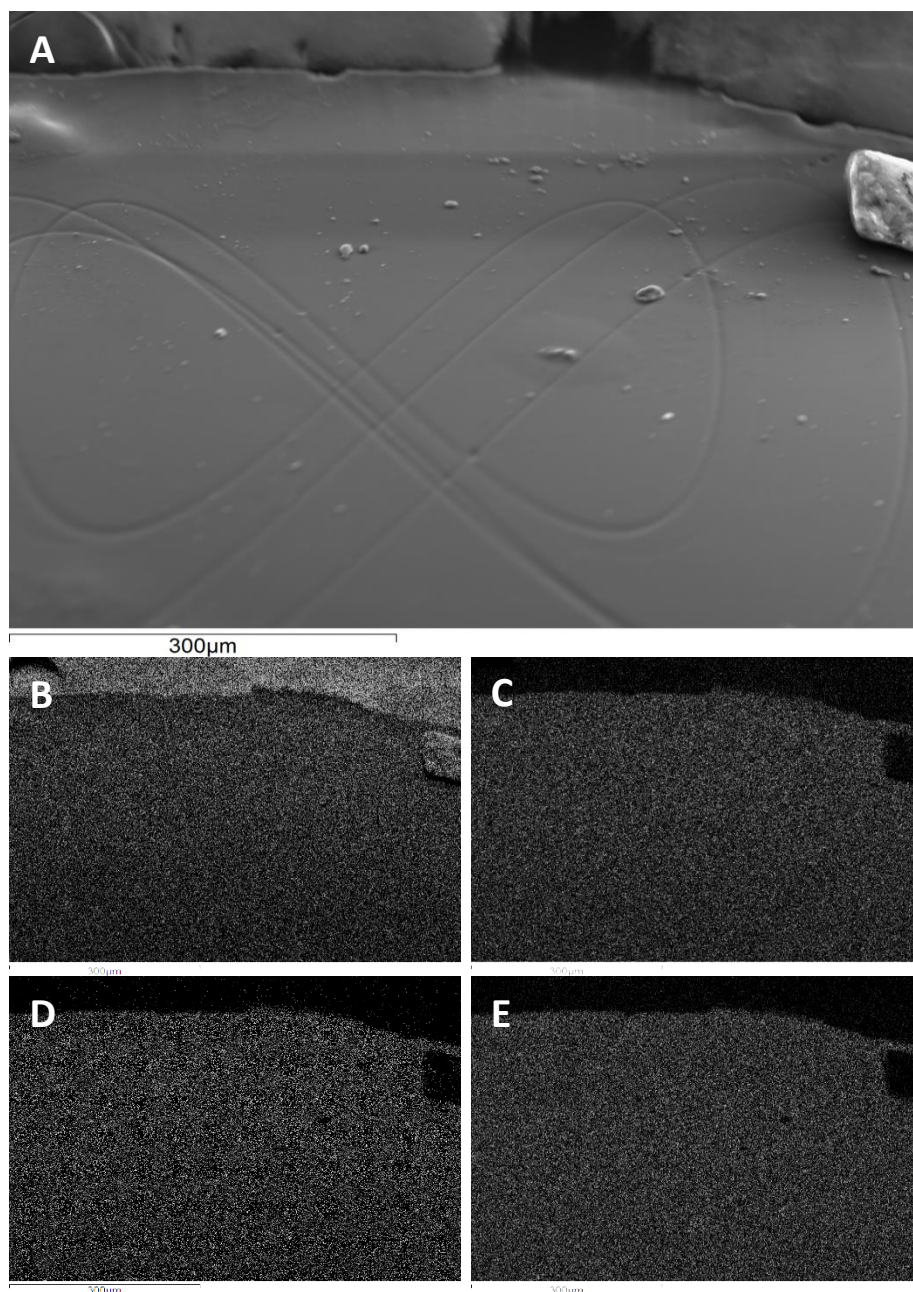


Figure 5.13: A) SEM image of PEGDA8000 PEM B)C)D)E) EDX elemental mapping of carbon, oxygen, fluorine and sulphur respectively

In addition, SEM has also been used to show layer thickness of the thin films, as deposited before cycling. A cross sectional view of an LNMO electrode on aluminium foil with PEGDA8000 PEM cast over the top of the active material is shown in Figure 5.14. It should be noted that the electrode was prepared as described in Chapter 2, i.e. the electrode was pressed using a pellet press and then the PEM was cast directly on top of the electrode. Around 30 seconds was given to allow the electrolyte to soak into the electrode material before it was subjected to UV curing. It can be seen that the Al thickness is around 10µm, the cathode 26µm and the PEM 30µm.

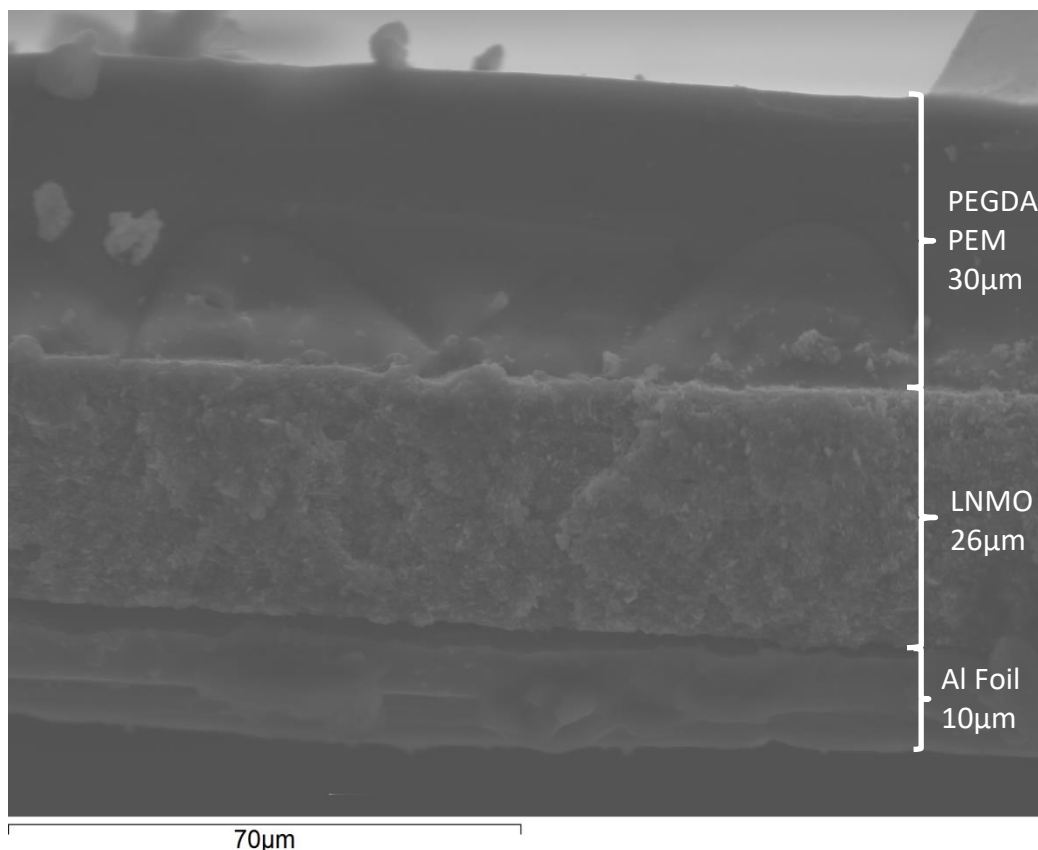


Figure 5.14: Cross-sectional SEM image of PEGDA8000 PEM cast onto an LNMO electrode on an aluminium foil current collector

The layers are well distinguished and it can be seen that there is no obvious separation between the LNMO and PEM layers indicating good interfacial contact between cathode and electrolyte. It should also be noted that whilst layers are fairly uniform throughout the length of the sample, the PEM was deposited by hand and so control over layer thickness is somewhat limited. In the long term, it is important to control the thickness of the electrolyte to improve energy density and to reduce waste. In its current form a huge volume is taken up by the PEM, especially considering the same deposition is required on the anode side, making the total PEM thickness $\approx 60\mu\text{m}$. As an example, the polymer separator typically used in conventional Li-ion batteries is between $2\text{-}5\mu\text{m}$, making the current PEM setup over a factor of 10 thicker.

The electrode/electrolyte interface is an important aspect when designing a PEM. The electrolyte should seamlessly coat all electrode material so that there are no breaks in ionic pathways allowing full utilisation of the available electrode material. To achieve this, not only does the PEM have to adhere well to the electrode material but it also has to penetrate the full depth of the electrode layer. In liquid electrolytes this is

simple, as the liquid easily accesses all crevices, with solid electrolytes though, this is one of the major limitation factors. As previously mentioned, the PEGDA8000 PEM is in liquid form before UV curing, thus allowing the potential of penetrating deeper into the cast electrodes. In this study, SEM measurements were utilised to give evidence of PEM penetration through electrode layers are shown in Figure 5.15. A higher magnification of the electrode/electrolyte interface shows, not only good contact throughout the interface, but also that the electrolyte mixes with the electrode and penetrates the electrode to a certain extent. It is difficult to gauge how far it is penetrating due to the close packing of the electrode material. However, using EDX mapping it can be seen that there is penetration further into the electrode than just the surface.

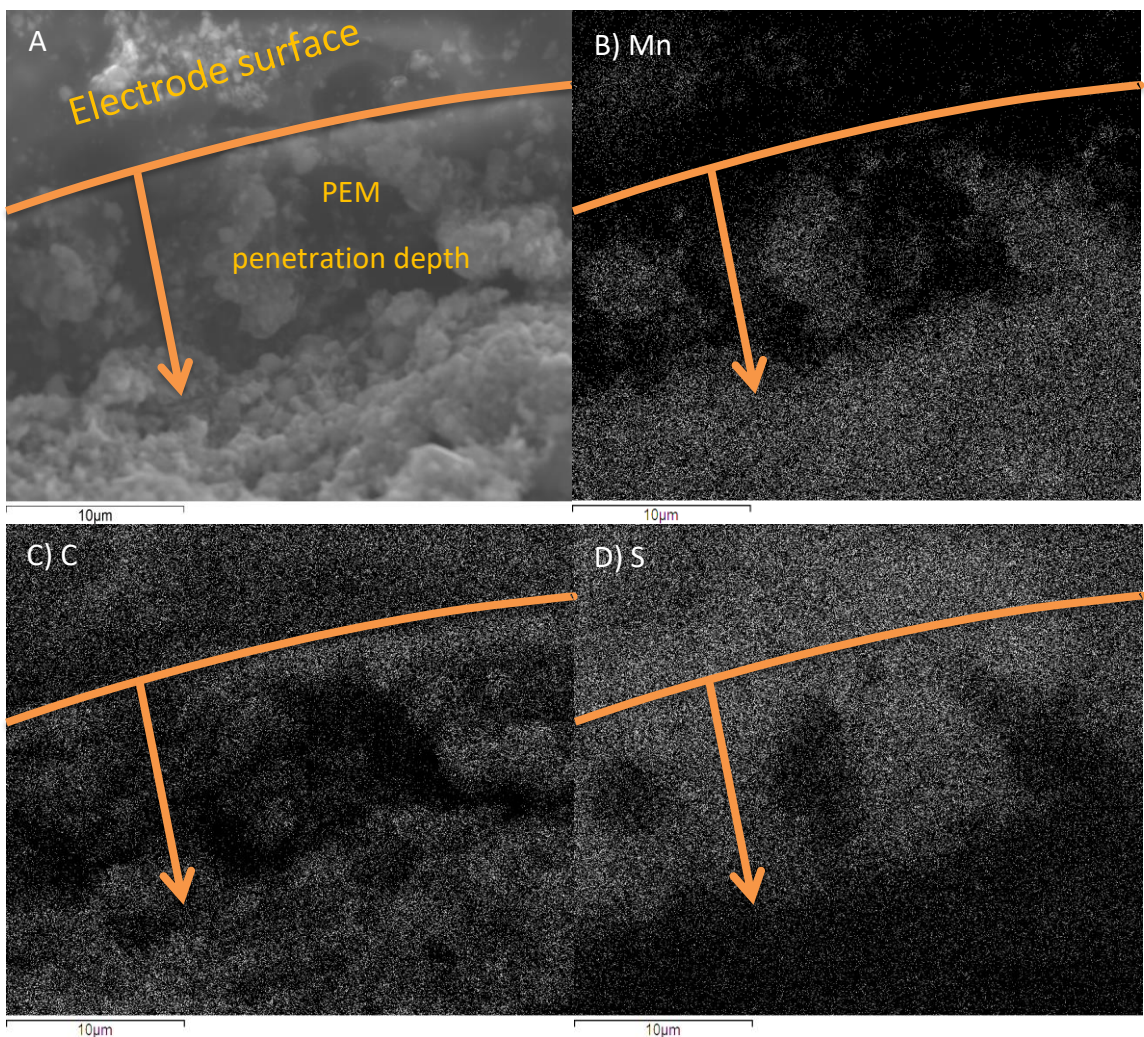


Figure 5.15: A) high magnification SEM image of PEGDA8000 PEM/LNMO electrode interface B)C)D) EDX mappings of manganese, carbon and sulphur respectively

An orange marker has been used to indicate where the electrolyte/electrode interface begins. The orange arrow represents the main penetration depth (approx. 10 μ m). From looking at the sulphur mapping it can be seen that there is electrolyte penetration well beyond the electrode surface, and whilst faint, there is also some sulphur present in the bottom right corner of the image. As LNMO contains no sulphur, it can be concluded, whilst penetration is severely limited, there is some electrolyte reaching deeper into cast electrodes. To enhance performance further, not only is a more controlled deposition technique required, but also a better degree of control over electrode porosity. It is evident from the close packing of the electrode that there is very low porosity, likely due to post casting electrode processing i.e. electrode pressing in a pellet press. Applying pressure to electrodes to improve electronic conductivity within the electrode, under normal circumstances, does not cause an issue when using liquid electrolytes. However, perhaps due to the SPE higher viscosity, this electrode pressing should be switched out for another pressing method. In industry, a calendaring machine is used to accurately control electrode thickness and porosity. This equipment is not currently available in the lab.

5.14 Galvanostatic Cycling

When discussing an electrolyte, it is ultimately, its cycling performance which determines its potential application in commercial devices. The electrolyte must, not only be stable i.e. not degrade at the desired working voltages and temperatures, but it must also allow redox reactions to occur repeatedly as the battery is cycled.

Electrodes were made, processed (as described in Chapter 2) and pressed in a pellet press to be returned to an argon filled glovebox where they were coated with PEGDA8000 PEM, which was then UV cured. Coin-cells were assembled as both full and half-cells.

Firstly, a full-cell consisting of a $\text{Li}_2\text{FeSiO}_4$ (LFS) cathode and $\text{Li}_4\text{Ti}_5\text{O}_{12}$ (LTO) anode was assembled. The first cycle of the LFS/LTO full-cell using PEGDA8000 PEM is depicted in Figure 5.16. LFS was chosen as it is a major part of this study; LTO was chosen to lower the working voltage of the cell and ensure cycling was kept under the PEMs degradation voltage (Figure 5.12). Also, LTO is well known as a standard material with strong stability characteristics. LTO has been previously been cycled with PEMs of similar compositions and should, therefore, cycle stably with the PEM [40].

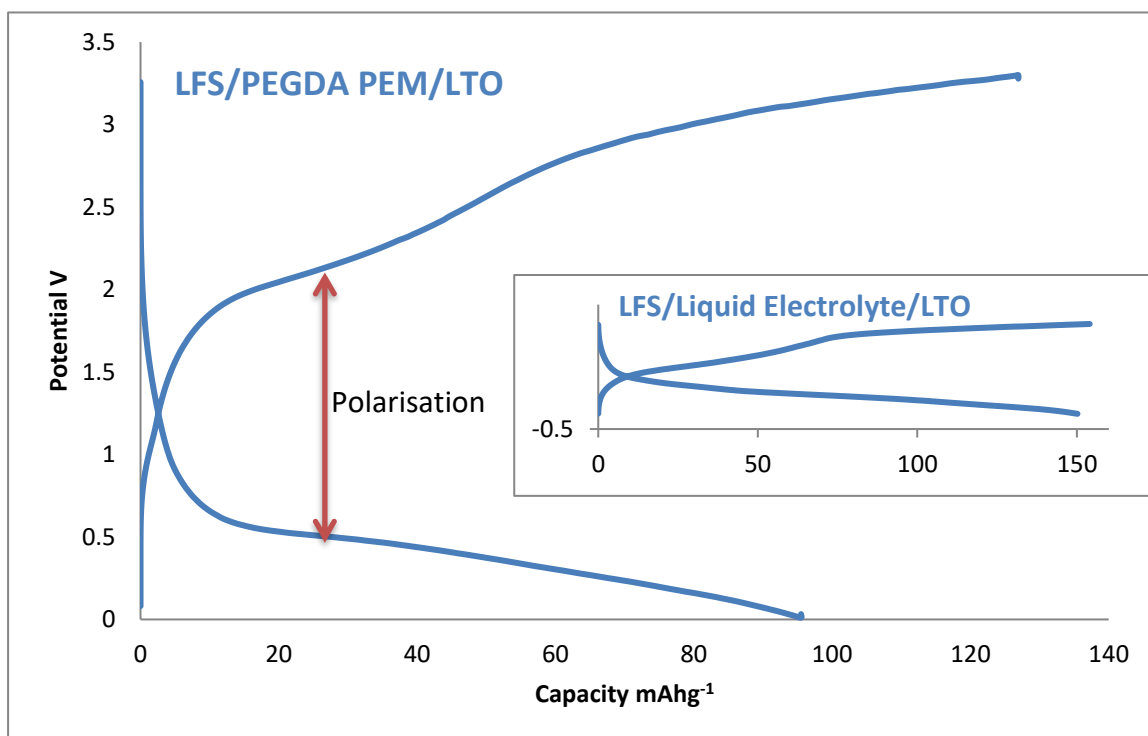


Figure 5.16: Cycling profile of LFS/PEGDA PEM/LTO full cell at room temperature. Inset: Cycling profile of LFS/LTO using LiPF_6 EC/DEC liquid electrolyte

It can be seen (Figure 5.16) that the cell cycling performance is poor i.e. there is evidence of large polarisation within the cell, as well as low discharge capacities. Polarisation occurs when conductive networks break down, creating internal resistance within the cell. In conventional cells, this is normally due to a poor electronic network within the electrode materials, however, as observed in the inset cycling curve (Figure 5.16) these same electrodes cycle well using liquid electrolyte (LiPF₆ EC:DEC). The polarisation is greatly reduced, achieved capacities are higher and apparent overcharging is reduced. It is, therefore, most likely an ionic conductivity issue. As previously mentioned LFS has a rather poor ionic conductivity, this coupled with a significantly lower electrolyte conductivity (an order of magnitude lower than conventional electrolytes) results in a poorly cycling battery. It should be noted that the cycling profile shown in Figure 5.16 was from a battery cycling at room temperature, however, increasing temperature did not improve cycling performance in this material.

It should be noted, that whilst cycling performance was poor, all expected plateaus were observed, the cycling profile is of the correct form but cell performance is limited. This suggests that the redox reactions are taking place correctly, however internal resistivity remains high and a change of electrode material may rectify this.

It was, therefore, decided to replace the positive electrode for further cycling using the PEM. The material chosen were LiFePO₄ (LFP), keeping Li₄Ti₅O₁₂ (LTO) as the negative electrode. These materials were chosen for their well-known stability characteristics and very flat plateaus, also due to the fact they were successfully cycled with PEMs of similar compositions, albeit as half cells [40] [52].

Firstly, a half-cell was assembled using LFP. Figure 5.17 shows the initial cycles of LFP vs Li/Li⁺ using a C-rate of $\frac{C}{3}$. It can be seen that, compared to LFS, the material exhibits an improved cycling performance, with acceptable capacities (theoretical capacity of LFP = 175mAhg⁻¹), stable plateaus and low polarization, as evidenced by the 0.2V difference between charge and discharge plateaus. This cycling was undertaken at room temperature. It can be seen that there is an overcharge of around 20mAhg⁻¹, which results in a low coulombic efficiency. Whilst a small overcharge is common; an

overcharge of this magnitude indicates an internal issue. Overcharge can occur for a multitude of reasons, i.e. the origin of an overcharge issue can stem from side reactions, SEI formation and lithium trapping. A likely cause here, lithium trapping, i.e. a removal of lithium from the cathode, which is not replaced upon charging due to the lithium getting “stuck”. There are a few places this can occur: (I) lithium ions may have migrated into the solid electrolyte from the cathode and become trapped, or (II) the lithium ions have reached the lithium metal anode, and are unable to migrate back to the cathode. This can be resulting from a breakdown in the ionic conductive network, making the reverse reaction unfavourable. An example of how this can happen is when lithium is inserted or extracted from a material, the material can expand or contract, this can be detrimental to surface contact between the electrode and the electrolyte meaning that the kinetics behind the reinsertion of lithium are hindered. In the case of the PEGDA based PEM, surface contact should be consistent due to the rubber consistency of the PEM assisted by the pressure within the coin cell, ensuring good contact regardless of expanding and contracting materials. Nonetheless, a drop in ionic conductivity from other sources can affect the reversibility of the redox reaction.

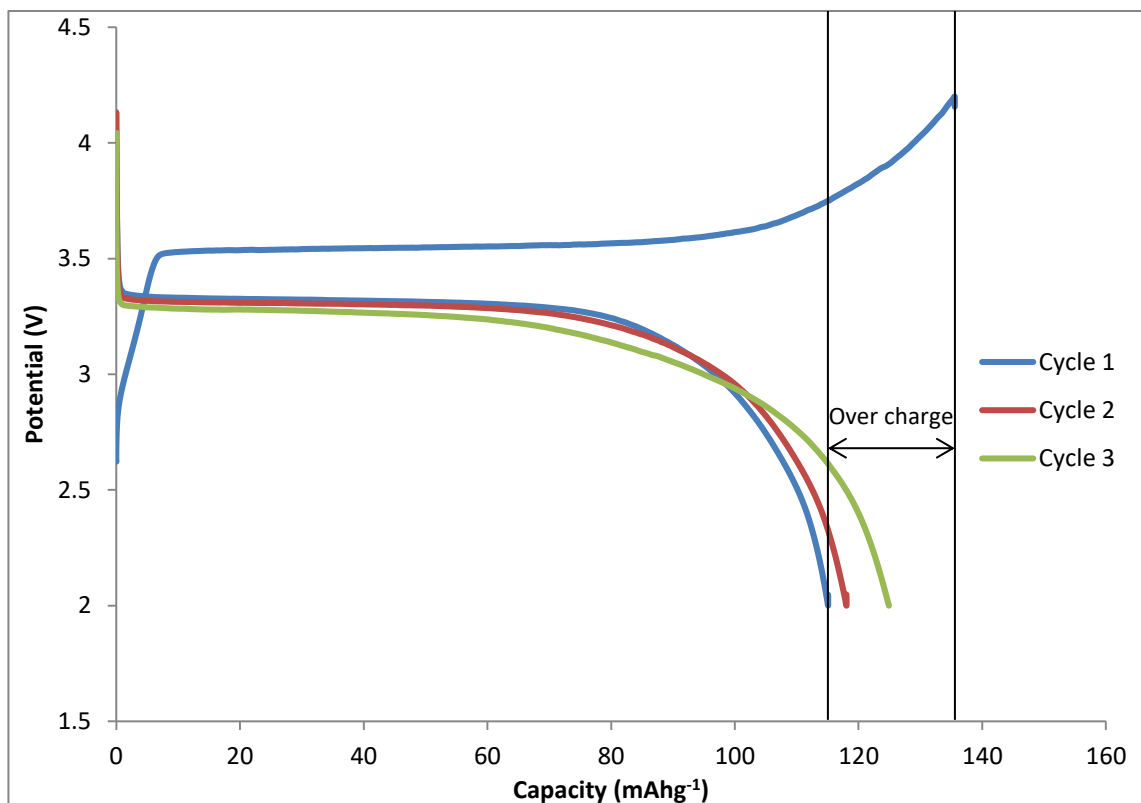


Figure 5.17: Initial cycling profile for LFP/PEM/Li half-cell at room temperature

One way to improve the samples ionic conductivity is to increase the cycling temperature. It was shown using TGA that the PEM is stable at elevated temperatures up to 152°C. For this experiment a more modest cycling temperature of 60°C was selected. The initial cycle of LFP at 60°C, again at a C-rate of $\frac{C}{3}$, is presented in Figure 5.18 A). It can be seen there is a marked improvement in performance when compared to the room temperature cycling profile. Not only is there a lower degree of polarisation, owing to a decrease in the battery's internal resistance, as a result of the improved ionic conductivity due to the elevated temperature, but also a large increase in discharge capacity, from 115mAhg⁻¹ to 152mAhg⁻¹.

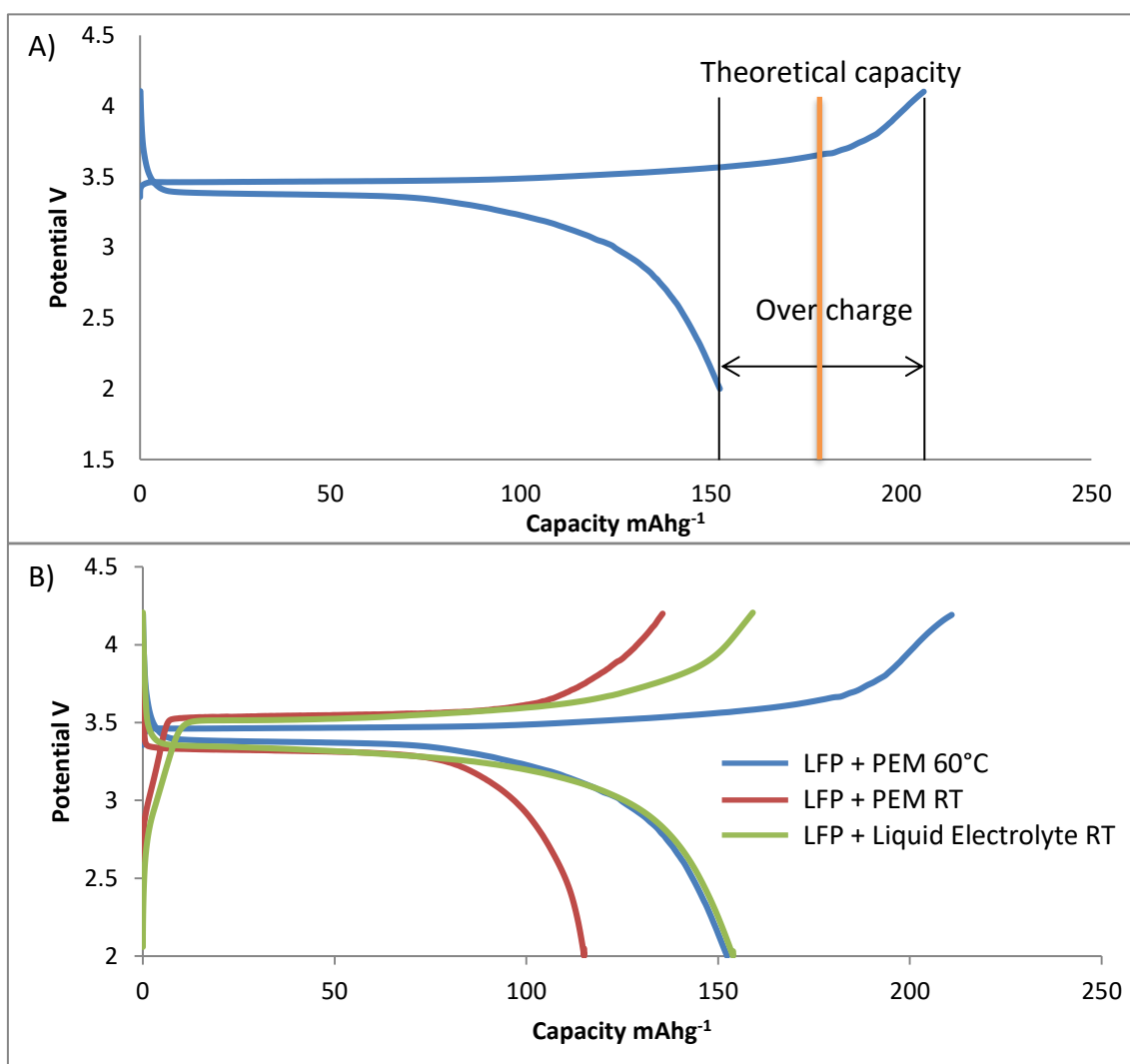


Figure 5.18: A) Initial cycling profile of LFP/PEM/Li half-cell at 60°C and B) A comparison of galvanostatic cycling performance of LFP half-cells using PEGDA8000 PEM at room temperature (red) and at 60°C (blue) and using liquid electrolyte at room temperature (green)

However, there is still a large overcharging observed, which indicates that the overcharging is not due to low ionic conductivity. Furthermore, the charging plateau extends beyond the theoretical capacity of LFP, suggesting that the origin of the overcharge issue is due to side reactions and/or SEI formation. It should be noted that the amount of overcharge observed is increased at elevated temperatures compared to room temperature.

Despite the issues with overcharging, the cycling performance of the PEM is promising. A comparison between the initial cycles at room temperature and 60°C using the PEM and a room temperature cell using conventional liquid electrolyte are shown in Figure 5.18 B). The cycling profiles indicate good performance of the PEM with high capacities, particularly at elevated temperatures, where the achieved capacity is directly comparable to conventional LFP half-cells using a liquid electrolyte (LiPF₆ in EC:DEC).

All of these factors point towards a strongly performing PEM, however, for use in consumer electronics, the PEM must not only perform in half cells vs Li⁺ but also as full cells using both an anode and cathode.

Figure 5.19 A) shows initial cycling profiles of an LFP/PEM/LTO full cell battery. It shows that whilst initial capacity is low, it does increase in the second cycle. It should also be noted that these capacities correspond to a room temperature, full-cell, all-solid-state battery cycling at a rate of 1C. In addition to this battery's impressive discharge capacities, Figure 5.19 A) also shows flat and stable plateaus, at voltages that correspond to the redox reactions expected with such a cell. However, it can be seen that the over charge is still evident throughout all cycles, but most prominent in the first cycle. This is another indicator of an SEI formation in the first cycle, along with other side reactions occurring in successive cycles.

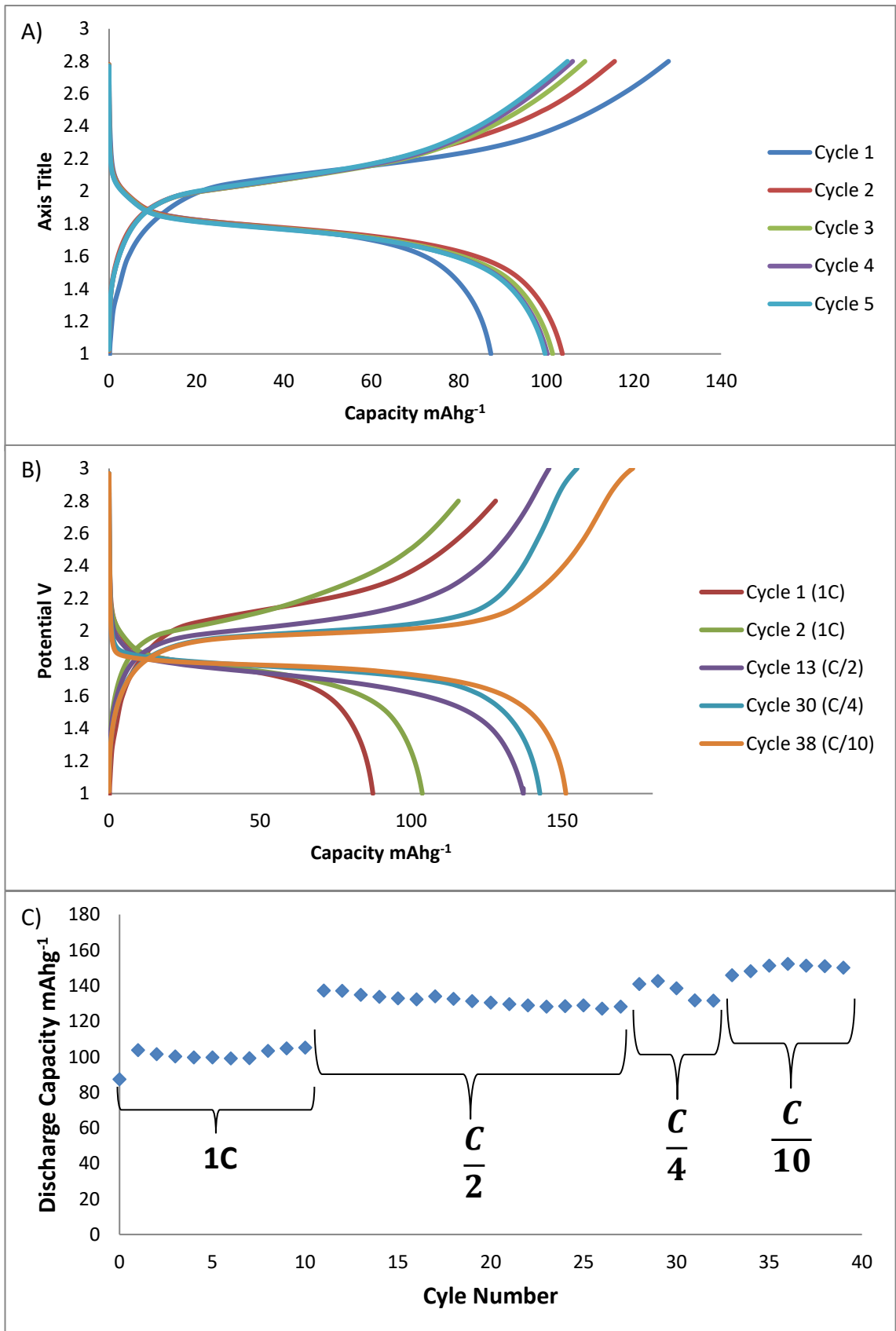


Figure 5.19: A) First 5 cycle curves of LFP/PEM/LTO full cell, cycled at a C-rate of 1C B) Cycling profiles of various cycles of a LFP/PEM/LTO full cell at various rates C) Discharge capacities of all cycles of LFP/PEM/LTO full cell at various C-rates

This is further supported when looking at Figure 5.19 B), which shows a larger number of cycles at various C-rates. It is shown that the overcharge feature continues for all 40 cycles, however, the discharge capacities do not decrease by the corresponding amount, meaning that the overcharge is due to a different reaction in addition to the regular redox. Also shown in Figure 5.19 B) is that the discharge capacities climb with slower C-rates, as expected, reaching as high as 151mAhg^{-1} at room temperature with a C-rate of $\frac{C}{10}$. The stable voltage plateaus and high discharge capacities are indicative of stable cycling performance.

The discharge capacities vs cycle number for all cycles of the full cell, including C-rate indicators are presented in Figure 5.19 C). The high capacities and stable cycling for at least 40 cycles are impressive for an all-solid-state battery and suggests that the PEM is well suited for further investigation as a potential liquid electrolyte replacement.

5.15 Conclusion

This chapter has explored PEGDA8000 as a host polymer for the use for an all-solid-state polymer electrolyte membrane. The PEM exhibited the ability to be cured using a UV photo-polymerisation technique, thus allowing good and consistent interfacial contact with electrode materials as deposited in liquid phase before UV curing to solidify. The resulting membrane retained good interfacial contact post-curing, as evidenced by SEM images. SEM was also carried out to observe electrolyte penetration depths and homogeneity of the PEM.

TGA and DSC was carried out to explore the PEMs thermal stability and determine its glass transition temperature T_g . It was found that thermal stabilities were in excess of 150°C , placing the PEGDA8000 PEM above LiPF_6 EC:DEC liquid electrolyte for thermal properties. Whilst T_g was found to be $\approx -70^\circ\text{C}$, indicating that normal operating conditions would be well above the PEMs glass transition temperature, therefore, enabling a larger degree of structural mobility which, in turn, promotes ionic conductivity within the PEM.

In addition, the PEMs mechanical attributes were tested. Free-standing PEMs were folded, rolled and twisted with no visible signs of tearing and always returning to the

PEMS original shape with no signs of deformation. The PEM also exhibits the ability to be repeatedly stretched, with tests showing single direction stretching in excess of 200% its original length.

Ionic conductivity was further explored using impedance spectroscopy. It was found that the PEMs ionic conductivity was $1.4 \times 10^{-3} \text{Scm}^{-1}$, placing the PEGDA8000 PEM well within the accepted "superionic" region. This is another indicator of strong performance potential as a solid-state polymer. This was further backed, by a CV sweep, indicating the PEM exhibits an electrochemical stability window up to 4.7V, allowing for its potential use in high voltage Li-ion cells.

Galvanostatic cycling of the PEM indicates strong performance across multiple cycles in both half-cell (LFP/PEM/Li) and full-cell (LFP/PEM/LTO) configurations. The overcharging observed in all PEM cycling requires further investigation, and whilst capacities are lower and polarisation higher when compared to a comparable liquid electrolyte cell, due to slower kinetics and incomplete electrode penetration of the PEM, the cycling curves show promising performance characteristics, such as, flat and stable redox plateaus and good reversibility, at various cycle rates.

This, in combination with the thermal and mechanical properties, place the PEGDA8000 PEM in good stead for further exploration as a viable alternative to the liquid electrolyte in consumer electronics and integrated devices.

It has been stated that the PEGDA based PEM deserves continued research as a viable alternative to conventional liquid electrolytes, however, there are some key areas that need further exploration. Firstly, the origin of the overcharge issue needs addressing, and will likely need a suppression mechanism for long term cycle life (several hundred cycles). In addition, an electrode porosity study should be undertaken to investigate the correlation with electrode porosity/electrolyte penetration/cycling performance. By controlling electrode porosity, an increase in electrode penetration may be achieved, which would allow for better interfacial contact between electrode and electrolyte, thus promoting a complete ionic network.

5.16 References

- [1] F. a. Sullivan, "<https://www.frost.com/sublib/display-report.do?id=M98E-01-00-00-00>," Frost and Sullivan, 19 May 2014. [Online]. [Accessed 06 June 2017].
- [2] S. Zhang, K. Xu and T. Jow, "Study of LiBF₄ as an electrolyte salt for a li-ion battery," *Journal of the Electrochemical society*, vol. 149, pp. 586-590, 2002.
- [3] M. Dahbi, F. Ghamouss, F. Tran-Van and D. A. M. Lemordant, "Comparative study of EC/DMC LiTFSi and LiPF₆ electrolytes for electrochimica istorage," *Journal of Power Sources*, vol. 196, pp. 9743-9750, 2011.
- [4] D. E. Fenton, J. M. Parker and P. V. Wright, "COMPLEXES OF ALKALI-METAL IONS WITH POLY(ETHYLENE OXIDE)," *Polymer*, vol. 14, no. 11, pp. 589 - 589, 1973.
- [5] M. B. Armand, J. M. Chabagno and M. Duclot, "Poly-ethers as solid electrolytes," in *Fast Ion Transport in Solids, Electrodes and Electrolytes*, Amsterdam, North Holland Publishers, 1979, pp. 131 - 136.
- [6] M. P. Hogan, Experimental and Modelling Study of Ionic Conductivity in Lithium Phosphate and Silicate Glasses, Kent: University of Kent, 2014.
- [7] M. Bertuzzo, INTERSTITIAL OXIDE-ION CONDUCTIVITY IN NOVEL MELILITE-TYPE SOLID OXIDE FUEL CELLS, Kent: University of Kent, 2018.
- [8] P. Yao, H. Yu, Z. Ding, Y. Liu, J. Lu, M. Lavorgna, J. Wu and X. Liu, "Review on Polymer-Based Composite Electrolytes for Lithium Batteries," *Frontiers in Chemistry*, vol. 522, no. 7, 2019.
- [9] O. Borodin and G. D. Smith, "Mechanism of Ion Transport in Amorphous Poly(ethylene oxide)/LiTFSI from Molecular Dynamics Simulations," *Macromolecules*, vol. 39, pp. 1620 - 1629, 2006.
- [10] Q. Zhang, K. Liu, F. Ding and X. Liu, "Recent advances in solid polymer electrolytes

for lithium batteries," *Nano Research*, vol. 10, no. 12, p. 4139–4174, 2017.

- [11] D. Dolodnitsky, E. Strauss, E. Peled and S. Greenbaum, "Review—On Order and Disorder in Polymer Electrolytes," *Journal of The Electrochemical Society*, vol. 162, no. 14, pp. 2551 - 2566, 2015.
- [12] K. J. Siczek, "Chapter Seven - Electrolytes," in *Next-Generation Batteries with Sulfur Cathodes*, Academic Press, 2019, pp. 79 - 115.
- [13] F. Croce, L. Persi, B. Scrosati, F. Serraino-Fiory, E. Plichta and M. A. Hendrickson, "Role of the ceramic fillers in enhancing the transport properties of composite polymer electrolytes," *Electrochimica Acta*, vol. 46, pp. 2457 - 2461, 2001.
- [14] M. Marcinek, J. Syzdek, M. Marczewski, M. Piszcz, L. Niedzicki, M. Kalita, A. Plewa-Marczewska, A. Bitner, P. Wieczorek, T. Trzeciak, M. Kasprzyk, P. Lezak, Z. Zukowska, A. Zalewska and W. Wieczorek, "Electrolytes for Li-ion transport – Review," *Solid State Ionics*, vol. 276, pp. 107 - 126, 2015.
- [15] S. V. Ganesan, K. K. Mothilal and T. K. Ganesan, "The role of zirconium oxide as nano-filler on the conductivity ,morphology, and thermal stability of poly(methyl methacrylate)–poly(styrene-co-acrylonitrile)-based plasticized composite solid polymer electrolytes," *Ionics*, vol. 24, pp. 3845 - 3860, 2018.
- [16] T. Jose Benedict, S. Banumathi, A. Veluchamy, R. Gangadharan, A. Zulfiyar Ahamad and S. Rajendran, "Characterization of plasticized solid polymer electrolyte by XRD and AC impedance methods," *Journal of Power Sources*, vol. 75, pp. 171 - 174, 1998.
- [17] W. Zha, F. Chen, D. Yang, Q. Shen and L. Zhang, "High-performance Li_{6.4}La₃Zr_{1.4}Ta_{0.6}O₁₂/Poly(ethylene oxide)/Succinonitrile composite electrolyte for solid-state lithium batteries," *Journal of Power Sources*, vol. 397, pp. 87 - 94, 2018.
- [18] L.-Z. Fan, Y.-S. B. A. J. Hu and J. Maier, "Succinonitrile as a Versatile Additive for

- Polymer Electrolytes," *Advanced Functional Materials*, vol. 17, pp. 2800 - 2807, 2007.
- [19] A. R. Polu and H.-W. Rhee, "Nanocomposite solid polymer electrolytes based on poly(ethylene oxide)/POSS-PEG (n = 13.3) hybrid nanoparticles for lithium ion batteries," *Journal of Industrial and Engineering Chemistry*, vol. 31, pp. 323 - 329, 2015.
- [20] D. Devaux, R. Bouchet, D. Glé and R. Denoyel, "Mechanism of ion transport in PEO/LiTFSI complexes: Effect of temperature, molecular weight and end groups," *Solid State Ionics*, vol. 227, pp. 119 - 127, 2012.
- [21] Y. Jiang, X. Yan, Z. Ma, P. Mei, W. Xiao, Q. You and Y. Zhang, "Development of the PEO Based Solid Polymer Electrolytes for All-Solid State Lithium Ion Batteries," *Polymers*, vol. 10, no. 11, p. 1237, 2018.
- [22] Y.-J. Li, C.-Y. Fan, J.-P. Zhang and X.-L. Wu, "A promising PMHS/PEO blend polymer electrolyte for all-solid-state lithium ion batteries," *Dalton Transactions*, vol. 47, p. 14932 – 14937, 2018.
- [23] P. Walke, K. M. Freitag, H. Kirchhain, M. Kaiser, L. v. Wullen and T. Nilges, "Electrospun Li(TFSI)@Polyethylene Oxide Membranes as Solid Electrolytes," *Journal of Inorganic and General Chemistry*, vol. 644, pp. 1863 - 1874, 2018.
- [24] A. Pierre-Jean, Y. Abu-Lebdeh, A. Abouimrane and M. Armand, "The plastic-crystalline phase of succinonitrile as a universal matrix for solid-state ionic conductors," *Nature Materials* 3, pp. 476 - 481, 2004.
- [25] M. Echeverri, N. Kim and T. Kyu, "Ionic Conductivity in Relation to Ternary Phase Diagram of Poly(ethylene oxide), Succinonitrile, and Lithium Bis(trifluoromethane)sulfonimide Blends," *Macromolecules*, vol. 45, pp. 6068 - 6077, 2012.
- [26] G. Fu, S. Buddhiranon, N. Kim, A. Seko, K. Adachi, Y. Tsukahara and T. Kyu, "Effects

of molecular complexation on phase equilibria in mixtures of urea/polyethylene glycol derivatives and electrochemical performance of urethane based polymer electrolyte membranes for solid-state lithium ion battery," *Polymer*, vol. 159, pp. 64 - 74, 2018.

[27] Z. Xue, D. He and X. Xie, "Poly(ethylene oxide)-based electrolytes for lithium-ion batteries," *Journal of Materials Chemistry A*, vol. 3, no. 38, pp. 19218 - 19253, 2015.

[28] J. Cao, R. He and T. Kyu, "Fire retardant, superionic solid state polymer electrolyte membranes for lithium ion batteries," *Current Opinion in Chemical Engineering*, vol. 15, pp. 68 - 75, 2017.

[29] Y. Cui, X. Liang, J. Chai, Z. Cui, Q. Wang, W. He, X. Liu, Z. Liu, G. Cui and J. Feng, "High Performance Solid Polymer Electrolytes for Rechargeable Batteries: A Self-Catalyzed Strategy toward Facile Synthesis," *Advanced Science News*, vol. 4, p. 1700174, 2017.

[30] B. Oh, W. I. Jung, D.-W. Kim and H. W. Rhee, "Preparation of UV Curable Gel Polymer Electrolytes and Their Electrochemical Properties," *Bulletin of the Korean Chemical Society*, vol. 23, no. 5, pp. 683 - 687, 2002.

[31] Y.-C. Jung, M.-S. Park, D.-H. Kim, M. Ue, A. Eftekhari and D.-W. Kim, "Room-Temperature Performance of Poly(Ethylene Ether Carbonate)-Based Solid Polymer Electrolytes for All-Solid-State Lithium Batteries," *Scientific Reports*, vol. 7, 2017.

[32] G. Fu, J. Dempsey, K. Izaki, K. Adachi, Y. Tsukahara and T. Kyu, "Highly conductive solid polymer electrolyte membranes based on polyethylene glycol-bis-carbamate dimethacrylate networks," *Journal of Power Sources*, vol. 359, pp. 441 - 449, 2017.

[33] C. Piedrahita, V. Kusuma, H. B. Nulwala and T. Kyu, "Highly conductive, flexible polymer electrolyte membrane based on poly(ethylene glycol) diacrylate-co-thiosiloxane network," *Solid State Ionics*, vol. 322, pp. 61 - 68, 2018.

- [34] M. Ueno, N. Imanishi, K. Hanai, T. Kobayashi, A. Hirano, O. Yamamoto and Y. Takeda, "Electrochemical properties of cross-linked polymer electrolyte by electron beam irradiation and application to lithium ion batteries," *Journal of Power Sources*, vol. 196, pp. 4756 - 4761, 2011.
- [35] C. T. Elmore, M. E. Seidler, H. O. Ford, L. C. Merrill, S. P. Upadhyay, W. F. Schneider and J. Schaefer, "Ion Transport in Solvent-Free, Crosslinked, Single-Ion Conducting Polymer Electrolytes for Post-Lithium Ion Batteries," *Batteries*, vol. 4, no. 2, 2018.
- [36] R. He and T. Kyu, "Effect of Plasticization on Ionic Conductivity Enhancement in Relation to Glass Transition Temperature of Crosslinked Polymer Electrolyte Membranes," *Macromolecules*, vol. 49, no. 15, pp. 5637 - 5648, 2016.
- [37] B. Wang, H. Lou, H. Xu, J. Zhao, Q. Wang, Q. Shi and Y. Deng, "High voltage, solvent-free solid polymer electrolyte based on a star-comb PDLLA-PEG copolymer for lithium ion batteries," *RSC Advances*, vol. 8, pp. 6373 - 6380, 2018.
- [38] J. R. Nair, C. Gerbaldi, M. Destro, R. Bongiovanni and N. Penazzi, "Methacrylic-based solid polymer electrolyte membranes for lithium-based batteries by a rapid UV-curing process," *Reactive & Functional Polymers*, vol. 71, pp. 409 - 411, 2011.
- [39] M. Willgert, M. H. Kjell, E. Jacques, M. Behm, G. Lindbergh and M. Johansson, "Photoinduced free radical polymerization of thermoset lithium battery electrolytes," *European Polymer Journal*, vol. 47, pp. 2372 - 2378, 2011.
- [40] R. He, M. Echeverri, D. Ward, Y. Zhu and T. Kyu, "Highly conductive solvent-free polymer electrolyte membrane for lithium-ion batteries: Effect of prepolymer molecular weight," *Journal of Membrane Science*, vol. 498, pp. 208 - 217, 2016.
- [41] S. Goutam, J.-M. Timmermans, N. Omar, P. V. D. Bossche and J. V. Mierlo, "Comparative Study of Surface Temperature Behavior of Commercial Li-Ion Pouch Cells of Different Chemistries and Capacities by Infrared Thermography," *Energies*, vol. 8, no. 8, pp. 8175 - 8192, 2015.

- [42] J. D. Hoog, J. Jaguemont, M. Abdel-Monem, P. V. D. Bossche, J. V. Mierlo and N. Omar, "Combining an Electrothermal and Impedance Aging Model to Investigate Thermal Degradation Caused by Fast Charging," *Energies*, vol. 11, no. 4, 2018.
- [43] X. Fleury, M. H. Noh, S. Genies, P. X. Thivel, C. Lefrou and Y. Bultel, "Fast-charging of Lithium Iron Phosphate battery with ohmic-drop compensation method: Ageing study," *Journal of Energy Storage*, vol. 16, pp. 21 - 36, 2018.
- [44] C. L. Campion, W. Li and B. L. Lucht, "Thermal Decomposition of LiPF₆-Based Electrolytes for Lithium-Ion Batteries," *The Electrochemical Society*, vol. 152, no. 12, pp. A2327 - A2334, 2005.
- [45] H. Yang, G. V. Zhuang and P. N. Ross Jr, *Thermal Stability of LiPF₆ Salt and Li-ion Battery Electrolytes Containing LiPF₆*, California: eScholarship, 2006.
- [46] Y. Wang, J. Qui, J. Peng, J. Li and M. Zhai, "One-step radiation synthesis of gel polymer electrolytes with high ionic conductivity for lithium-ion batteries," *Journal of Materials Chemistry A*, no. 24, 2017.
- [47] R. He, STUDIES ON IONIC CONDUCTIVITY AND ELECTROCHEMICAL STABILITY OF PLASTICIZED PHOTOPOLYMERIZED POLYMER ELECTROLYTE MEMBRANES FOR SOLID STATE LITHIUM ION BATTERIES, Akron: The University of Akron , 2016.
- [48] L. Porcarelli, C. Gerbaldi, F. Bella and J. R. Nair, "Super Soft All-Ethylene Oxide Polymer Electrolyte for Safe All-Solid Lithium Batteries," *Scientific Reports*, vol. 6, 2016.
- [49] Y. Li, K. W. Wong, Q. Dou, W. Zhang, L. Wang and K. Ng, "A highly elastic and flexible solid-state polymer electrolyte based on ionic liquid-decorated PMMA nanoparticles for lithium batteries," *New Journal of Chemistry*, no. 21, 2017.
- [50] Q. Lu, J. Fang, J. Yang, G. Yan, S. Liu and J. Wang, "A novel solid composite polymer electrolyte based on poly(ethylene oxide) segmented polysulfone copolymers for rechargeable lithium batteries," *Journal of Membrane Science*, pp. 105 - 112,

2013.

- [51] A. Gueguen, D. Streich, M. He, M. Mendez, F. F. Chesneau, P. Novak and E. J. Berg, "Decomposition of LiPF₆ in High Energy Lithium-Ion Batteries Studied with Online Electrochemical Mass Spectrometry," *Journal of The Electrochemical Society*, vol. 163, no. 6, pp. 1095 - 1100, 2016.
- [52] R. Imhof and P. Novak, "Oxidative Electrolyte Solvent Degradation in Lithium-Ion Batteries: An In Situ Differential Electrochemical Mass Spectrometry Investigation," *The Electrochemical Society*, vol. 146, no. 5, pp. 1702 - 1706, 1999.
- [53] H. Bai, J. Hu, Y. Duan, T. Kozawa, M. Naito, J. Zhang and S. Dong, "Surface modification of Li_{1.3}Al_{0.3}Ti_{1.7}(PO₄)₃ ceramic electrolyte by Al₂O₃-doped ZnO coating to enable dendrites-free all-solid-state lithium-metal batteries," *Ceramics International*, vol. 45, no. 12, pp. 14663 - 14668, 2019.
- [54] Y. Deng, C. Eames, B. Fleutot, R. David, J.-N. Chotard, E. Suard, C. Masquelier and M. S. Islam, "Enhancing the Lithium Ion Conductivity in Lithium Superionic Conductor (LISICON) Solid Electrolytes through a Mixed Polyanion Effect," *ACS Applied Material Interfaces*, vol. 9, no. 8, pp. 7050 - 7058, 2017.
- [55] S. Song, B. Chen, Y. Ruan, J. Sun, L. Yu, Y. Wang and J. Thokchom, "Gd-doped Li₇La₃Zr₂O₁₂ garnet-type solid electrolytes for all-solid-state Li-Ion batteries," *Electrochimica Acta*, vol. 270, pp. 501 - 508, 2018.
- [56] Y. Inaguma, C. Liqun, M. Itoh, T. Nakamura, T. Uchida, H. Ikuta and M. Wakihara, "High ionic conductivity in lithium lanthanum titanate," *Solid State Communications*, vol. 86, no. 10, pp. 689 - 693, 1993.
- [57] J.-F. Wu and X. Guo, "Origin of the low grain boundary conductivity in lithium ion conducting perovskites: Li₃xLa_{0.67-x}TiO₃," *Physical Chemistry Chemical Physics*, vol. 19, no. 8, 2017.
- [58] X. Li, J. Liu, M. N. Banis, A. Lushington, R. Li, M. Cai and X. Sun, "Atomic layer

deposition of solid-state electrolyte coated cathode materials with superior high-voltage cycling behavior for lithium ion battery application,” *Energy & Environmental Science*, vol. 7, no. 2, 2014.

[59] X. Han, Y. Gong, K. Fu, X. He, G. T. Hitz, J. Dai, A. Pearse, B. Liu, H. Wang, G. Rubloff, Y. Mo, V. Thangardurai, E. D. Wachsman and L. Hu, “Negating interfacial impedance in garnet-based solid-state Li metal batteries,” *Nature Materials*, vol. 16, pp. 572 - 579, 2017.

[60] “Three-Dimensional Bicontinuous Nanocomposite from a Self-Assembled Block Copolymer for a High-Capacity All-Solid-State Lithium Battery Cathode,” *Chemistry of Materials*, vol. 28, pp. 4453 - 4459, 2016.

[61] Q. Zhang, W. Jiang, Z. Zhou, S. Wang, X. Guo, S. Zhao and G. Ma, “Enhanced electrochemical performance of Li₄SiO₄-coated LiFePO₄ prepared by sol-gel method and microwave heating,” *Solid State Ionics*, vol. 218, pp. 31 - 34, 2012.

[62] R. He, *STUDIES ON IONIC CONDUCTIVITY AND ELECTROCHEMICAL STABILITY OF PLASTICIZED PHOTOPOLYMERIZED POLYMER ELECTROLYTE MEMBRANES FOR SOLID STATE LITHIUM ION BATTERIES*, Akron: University of Akron, 2016.

[63] B. V. Lotsch and J. Maier, “Relevance of solid electrolytes for lithium-based batteries: A realistic view,” *Journal of Electroceramics*, vol. 38, no. 2-4, pp. 128 - 141, 2017.

[64] A. Varzi, R. Raccichini, S. Passerini and B. Scrosati, “Challenges and prospects of the role of solid electrolytes in the revitalization of lithium metal batteries,” *Journal of Materials Chemistry A*, vol. 4, pp. 17251 - 17259, 2016.

[65] P. Murmann, R. Scmitz, S. Nowak, N. Ignatiev, P. Sartori, I. Cekic-Laskovic and M. Winter, “Electrochemical Performance and Thermal Stability Studies of TwoLithium Sulfonyl Methide Salts in Lithium-Ion Battery Electrolytes,” *Journal of the Electrochemical Society*, vol. 162, no. 9, pp. 1738 - 1744, 2015.

- [66] K. Mori, T. Kasai, K. Iwase, F. Fujisaki, Y. Onodera and T. Fukunaga, "Structural origin of massive improvement in Li-ion conductivity on transition from $(\text{Li}_2\text{S})_5(\text{GeS}_2)(\text{P}_2\text{S}_5)$ glass to $\text{Li}_{10}\text{GeP}_2\text{S}_{12}$ crystal," *Solid State Ionics*, vol. 301, pp. 163 - 169, 2017.
- [67] "Ion Conduction in Superionic Glassy Electrolytes: An Overview," *Journal of Materials Science & Technology*, vol. 29, no. 3, pp. 193 - 208, 2013.
- [68] L. L. Van-Jodin, A. Claudel, C. Secouard, F. Sabary, J.-P. Barnes and S. Martin, "Role of the chemical composition and structure on the electrical properties of a solid state electrolyte: Case of a highly conductive LiPON," *Electrochimica Acta*, vol. 259, pp. 742 - 751, 2018.
- [69] H. W. Kim, P. Manikandan, Y. J. Lim, J. H. Kim, S.-c. Nam and Y. Kim, "Hybrid solid electrolyte with the combination of $\text{Li}_7\text{La}_3\text{Zr}_2\text{O}_{12}$ ceramic and ionic liquid for high voltage pseudo-solid-state Li-ion batteries," *Journal of Materials Chemistry A*, vol. 43, 2016.
- [70] K. B. Dermenci, E. Cekic and S. Turan, "Al stabilized $\text{Li}_7\text{La}_3\text{Zr}_2\text{O}_{12}$ solid electrolytes for all-solid state Li-ion batteries," *International Journal of Hydrogen Energy*, vol. 41, no. 23, pp. 9860 - 9867, 2016.
- [71] X. Yu, J. Bates, G. Jellison and F. Hart, "A stable thin-film lithium electrolyte: lithium phosphorus oxynitride," *Journal of the Electrochemical Society*, vol. 144, no. 2, pp. 524 - 532, 1997.
- [72] Y. Lai, Z. Sun, L. Jiang, X. Hao, M. Jia, L. Wang and F. Liu, "Rapid sintering of ceramic solid electrolytes $\text{LiZr}_2(\text{PO}_4)_3$ and $\text{Li}_{1.2}\text{Ca}_{0.1}\text{Zr}_{1.9}(\text{PO}_4)_3$ using a microwave sintering process at low temperatures," *Ceramics International*, vol. 45, no. 8, pp. 11068 - 11072, 2019.
- [73] K. Nie, Y. Hong, J. Qui, Q. Li, X. Yu, H. Li and L. Chen, "Interfaces Between Cathode and Electrolyte in Solid State Lithium Batteries: Challenges and Perspectives," *Frontiers in Chemistry*, vol. 6, no. 616, 2018.

- [74] J. L. Schaefer, Y. Lu, S. S. Moganty, P. Agarwal, N. Jayaprakash and L. A. Archer, "Electrolytes for high-energy lithium batteries," *Applied Nanoscience*, vol. 2, no. 2, pp. 91 - 109, 2012.
- [75] S. Berg, T. Kelly, I. Porat, B. Moradi-Ghadi and H. Ardebili, "Mechanical deformation effects on ion conduction in stretchable polymer electrolytes," *Applied Physics Letters*, vol. 113, 2018.
- [76] P. Lv, J. Yang, G. Liu, H. Liu, S. Li, C. Tang, J. Mei, Y. Li and D. Hui, "Flexible solid electrolyte based on UV cured polyurethane acrylate/succinonitrile-lithium salt composite compatibilized by tetrahydrofuran," *Composites Part B: Engineering*, vol. 120, pp. 35 - 41, 2017.
- [77] S. Chen, J. Wang, Z. Wei, Z. Zhang, Y. Deng, X. Yao and X. Xu, "One-pot synthesis of crosslinked polymer electrolyte beyond 5V oxidation potential for all-solid-state lithium battery," *Journal of Power Sources*, vol. 431, pp. 1 - 7, 2019.
- [78] C. Li, Y. Huang, X. Feng, Z. Zhang and P. Liu, "High electrochemical performance poly(ethylene oxide)/2,4-toluene diisocyanate/polyethylene glycol as electrolytes for all-solid-state lithium batteries," *Journal of Membrane Science*, vol. 587, 2019.
- [79] Z. Wang, S. Chen, Z. Huang, Z. Wei, L. Shen, H. Gu, X. Xu and X. Yao, "High conductivity polymer electrolyte with comb-like structure via a solvent-free UV-cured method for large-area ambient all-solid-state lithium batteries," *Journal of Materiomics*, vol. 5, no. 2, pp. 195 - 203, 2019.
- [80] M. Sasikumar, A. Jagadeesan, M. Raja, R. Hari Krishna and P. Sivakumar, "The effects of PVAc on surface morphological and electrochemical performance of P(VdF-HFP)-based blend solid polymer electrolytes for lithium ion-battery applications," *Ionics*, vol. 25, no. 5, pp. 2171 - 2181, 2019.
- [81] D. E. Fenton, J. M. Parker and P. V. Wright, "COMPLEXES OF ALKALI-METAL IONS WITH POLY(ETHYLENE OXIDE)," *Polymer*, vol. 14, no. 11, p. 589, 1973.

- [82] M. B. Armand, J. M. Chabagno and M. J. Dulcot, "Fast ion transport in solids: electrodes and electrolytes," P. Vashista, J. N. Mundy and G. K. Shenroy, Eds., New York, United States: Elsevier North Holland, 1979, p. 131.
- [83] A. Arya and A. L. Sharma, "Insights into the use of polyethylene oxide in energy storage/conversion devices: a critical review," *Journal of Physics D: Applied Physics*, vol. 50, 2017.
- [84] W. H. Meyer, "Polymer Electrolytes for Lithium-Ion Batteries," *Advanced Materials*, vol. 10, no. 6, 1998.
- [85] J. F. Le Nest, S. Callens, A. Gandini and M. Armand, "A new polymer network for ionic conduction," *Electrochimica Acta*, vol. 37, no. 9, pp. 1585 - 1588, 1992.
- [86] R. Khurana, J. L. Schaefer, L. A. Archer and G. W. Coates, "Suppression of Lithium Dendrite Growth Using Cross-Linked Polyethylene/Poly(ethylene oxide) Electrolytes: A New Approach for Practical Lithium-Metal Polymer Batteries," *Journal of the American Chemical Society*, vol. 136, pp. 7395 - 7402, 2014.
- [87] H. Saxena, B. Bhattacharya, N. A. Jadhav, V. K. Singh, S. Shukla, M. Dubey and P. K. Singh, "Multiwall carbon-nanotube-doped ion conducting polymer electrolyte for electrochemical application," *Journal of Experimental Nanoscience*, vol. 9, no. 5, pp. 444 - 451, 2014.
- [88] Y.-T. Kim and E. S. Smotkin, "The effect of plasticizers on transport and electrochemical properties of PEO-based electrolytes for lithium rechargeable batteries," *Solid State Ionics*, vol. 149, pp. 29 - 37, 2002.
- [89] L. Liu, X. Qi, S. Yin, Q. Zhang, X. Liu, L. Suo, H. Li, L. Chen and Y.-S. Hu, "In Situ Formation of a Stable Interface in Solid-State Batteries," *American Chemical Society Energy Letters*, vol. 4, no. 7, pp. 1650 - 1657, 2019.
- [90] H. Graebe, A. Netz and A. Kwade, "A Solvent-Free Electrode Coating Technique for All Solid State Lithium Ion Batteries," in *Symposium on Plasma Nano Science and*

Technology held during the 231st Meeting of the Electrochemical-Society (ECS), New Orleans, 2017.

- [91] V. Gregorio, N. Garcia and P. Tiemblo, "Solvent-Free and Scalable Procedure to Prepare PYR13TFSI/LiTFSI/PVDF–HFP Thermoplastic Electrolytes with Controlled Phase Separation and Enhanced Li Ion Diffusion," *Membranes*, vol. 9, no. 50, 2019.
- [92] Y. Lin, Y. Cheng, J. Li, J. D. Miller, J. Liu and X. Wang, "Biocompatible and biodegradable solid polymer electrolytes for high voltage and high temperature lithium batteries," *RSC Advances*, vol. 7, no. 40, 2017.
- [93] E. Yulianti, Deswita, Sudaryanto and Mashadi, "Study of solid polymer electrolyte based on biodegradable polymer polycaprolactone," *Malaysian Journal of Fundamental and Applied Sciences*, vol. 15, no. 3, pp. 467 - 471, 2019.

6 Integrated Design

6.1 The Concept

As mentioned in Chapter 1, in recent years, the emergence of bio-integrated, close to skin and wearable technologies has resulted in the need for body-conformable products to be developed. These products should be low profile, lightweight, safe and minimally invasive. Whilst the concept is not new – both, electronics and energy storage research groups have investigated it in depth, often referencing each other for potential applications. However, these investigations rarely result in an integrated product, combining the two areas of research. This study presents a fully integrated battery antenna system (IBAS), where battery and antenna become one product, each dependant on the other to function.

This work is a collaborative effort between The University of Kent EDA and SPS groups and University of Rome Tor Vergata, stemming from early modelling and simulation works presented [1] [2].

6.2 The Antenna

The antenna chosen for this project is a nested slot line antenna, whose design is a modified version of an antenna originating from a previous publication within the group [3]. This design was selected due to its ability to function on-skin (or very close-to-skin) which is difficult to achieve with acceptable read ranges. The antenna design used in this study is depicted in Figure 6.1.

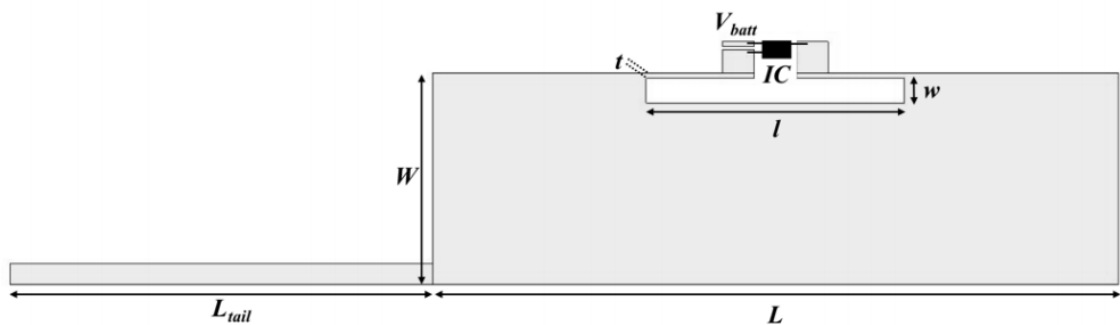


Figure 6.1: Layout of the nested slot line RFID antenna
Size in mm: $L = 65$, $W = 20$, $l = 25$, $w = 2.2$, $t = 0.5$; and $L_{tail} = 40$ (reprinted with permission [8])

The design of the antenna is such that an electric field is induced in the slot, creating a thin current loop. Due to the narrow slot width (when compared to the driving frequency wavelength) and the fact that the current is not confined by the loop, it spreads across the conductive plate allowing for better radiation efficiencies. This is what allows the antenna to be used on-skin. In addition, the design also allows intimate integration with a layered battery design.

6.3 Battery Integration

As mentioned in Chapter 1, a battery consists of three main components, the anode, the cathode and the electrolyte. The anode and cathode materials are deposited on the “current collectors” – metallic foils used as an electrically conducting medium allowing for efficient battery cycling. It is well understood that metallic components in close proximity of an antenna can cause a mismatch in antenna impedance, resulting in decreased performance and read ranges. However, the common foil used as the negative current collector in a battery is copper, which is also the material commonly employed in RFID slot antenna designs. In addition, slot antennas consist of large area planes to assist in antenna radiation. By utilising this metallic copper plane as a current collector for the negative electrode in a battery, the intimate, truly integrated battery antenna system (IBAS) is conceptualised.

There are, however, other metallic components within a battery that can affect impedance matching. Namely, the battery casing and the positive current collector. Battery casings normally consist of rigid metallic casings (such as those found in coin cell designs) or flexible laminated polymer/metallic barrier sheets (such as those found in pouch cells). Both of these options were deemed unsuitable for the IBAS design, and so, a Mylar sheet was opted for as the system casing, avoiding unnecessary interference from metallic components, whilst still protecting the skin from exposure to electrolyte and avoid moisture uptake within the cell. The positive current collector (aluminium foil) was an unavoidable metallic component; however, it was found that a good matching and minimal performance loss, was possible when avoiding the antennas slot region with the aluminium.

The battery chemistry chosen for the IBAS consists of a PEDOT:PSS anode and a $\text{LiNi}_{0.5}\text{Mn}_{1.5}\text{O}_4$ (LNMO) cathode. PEDOT:PSS was chosen due to its processability, flexibility, and biocompatibility, as mentioned in Chapter 4. LNMO was chosen due to its characteristics as a high voltage cathode material, allowing the created cell to exhibit higher potentials. It should be noted that, during initial prototyping of the IBAS a vacuum sealer was unavailable, so the battery voltages during use were lower than the theoretical chemistry in a vacuum sealed cell. The reason for the poor battery performance is associated with the greatly increased cell impedance, stemming from potential contact issues and potentially mobile electrodes. To combat the potential for lower than expected voltages, LNMO was chosen as the cathode material. This is due to its high redox potential (4.7V), ensuring that even with a high impedance, the cell voltage was high enough to power the antennas chip.

6.4 The IBAS

The IBAS is designed to be assembled in a layered fashion, as depicted in Figure 6.2. It can be seen that the layout closely resembles a standard “single layer” pouch cell, with the addition of the antenna design etched into the copper current collector. This “single layer” design allows for efficient manufacturing and assembly, as no winding and minimal stacking is required. In addition, the “single layered” nature of the IBAS allows for it to flex and conform to body.

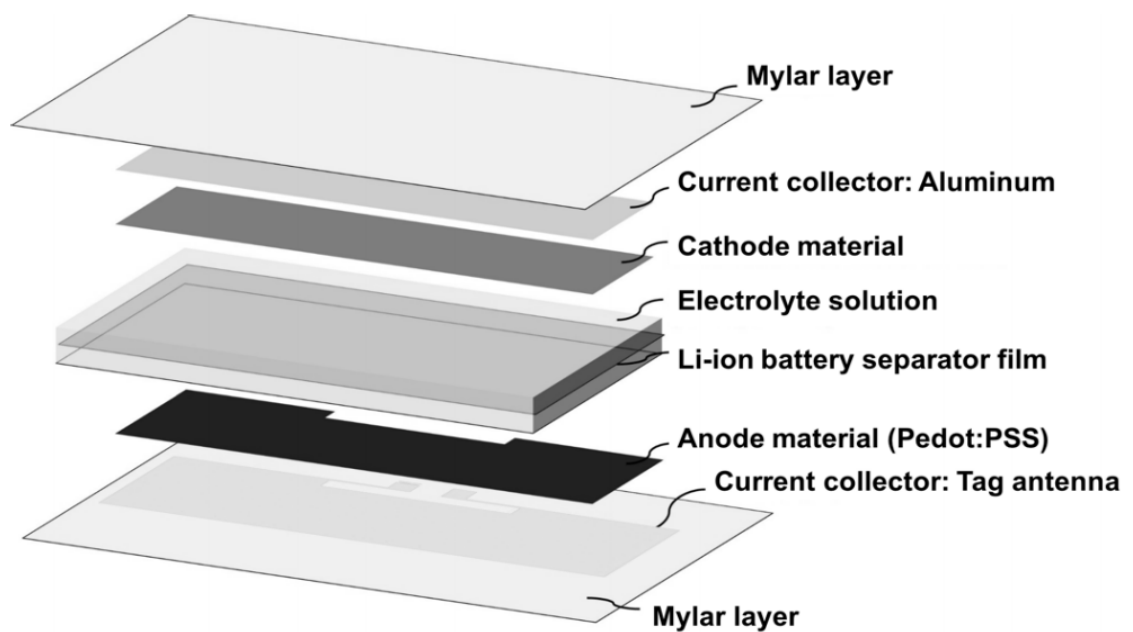


Figure 6.2: Schematic view of the IBAS layers (reprinted with permission [8])

Various techniques have been employed in the formation of each of the IBAS layers, all of which can be adapted to large scale production and roll-to-roll assembly. The antenna was made using a sheet of copper coated mylar sheet, and the design was created using an established copper masking and etching technique. The chip was then soldered onto the antenna, which was then further coated with PEDOT:PSS anode material, using a masking and spray coating technique as mentioned in Chapter 4. Separately, aluminium foil was coated with the LNMO cathode material using a standard doctor blading technique (as no shaping was required), this was then cut to size and adhered to a plain mylar sheet for the outer casing. Celgard separator was cut to size, and all materials were aligned and stacked by hand. Hot-melt glue was added to the edges of the system and heat sealed under argon in a glovebox, electrolyte was added prior to the final seal. Figure 6.3 shows the antenna-side process, along with the final prototype on body.

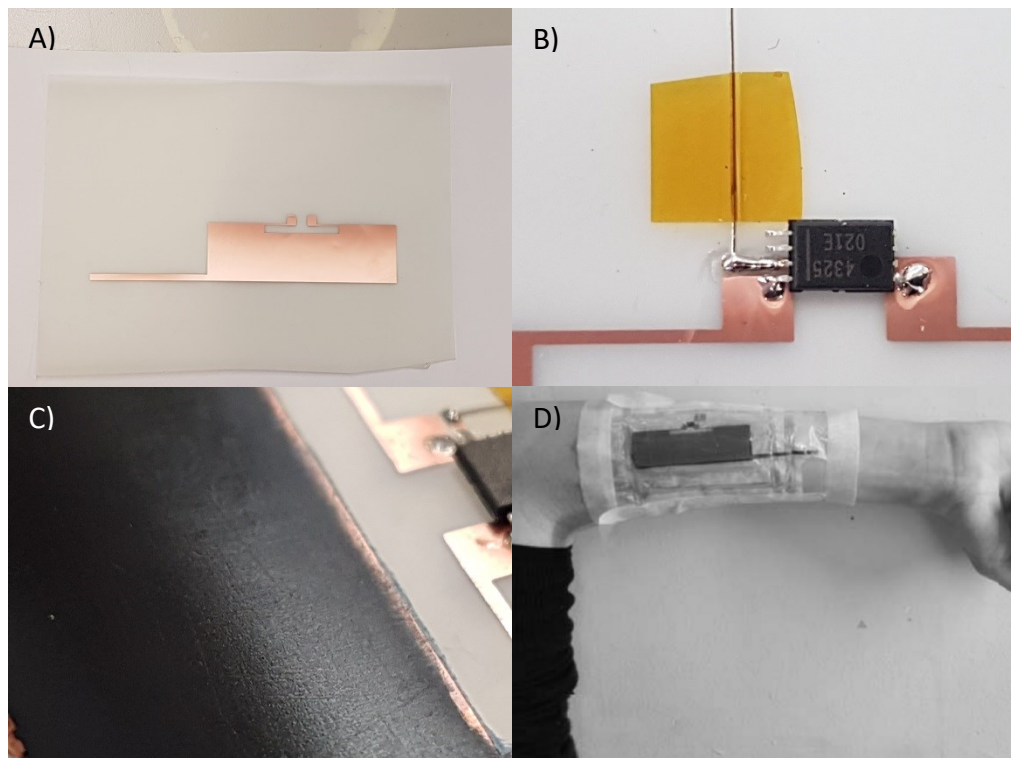


Figure 6.3: IBAS prototype stages A) antenna etching B) Chip soldering C) spray coated PEDOT:PSS D) final product on body for testing (reprinted with permission [8])

The chip chosen for the IBAS was the EM4325-TSSOP8 RFID IC [4]. This was selected due to its ability to work in both passive mode (no battery power) and BAP mode (battery assisted power mode), and its integrated thermal sensor, which allows close-to-skin sensing, having been used in previous epidermal sensing applications [5] [6].

6.5 IBAS Performance

For performance testing of the IBAS, forward and backward read distances were extrapolated by assuming a maximum realised gain and input power $G_r P_{in} = 3.2W$ EIRP (being the maximum allowed via European regulations) and from data gathered using a Voyantic Tagformance UHF RFID measurement system [7]. The results, shown in Figure 6.4, indicate at 870MHz the maximum theoretical read-ranges are: $d_{forward} = 6.9m$ and $d_{backward} = 1.3m$. This indicates a significant bottleneck on the backward link; however, these distances demonstrate that the tags performance is sufficient for use as a short-range epidermal data logger, allowing data transfer by interrogating base stations which can be placed in regularly visited locations such as doorways.

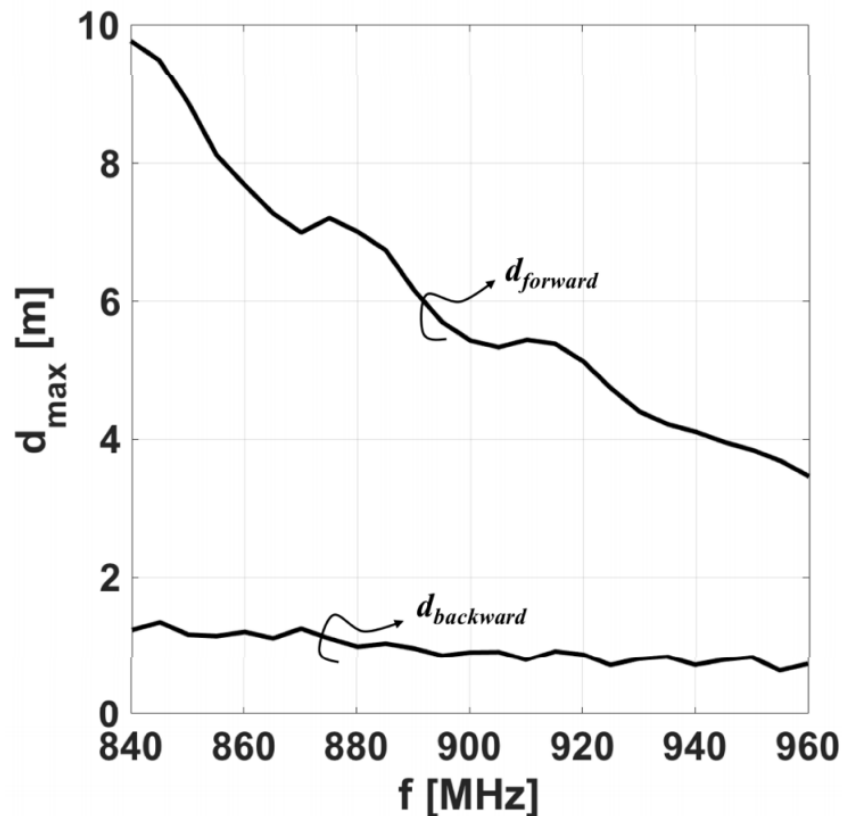


Figure 6.4: Theoretical read distances using a 3.2W EIRP interrogating power (reprinted with permission [8])

In addition to read distances, the tags' turn-ON powers were measured as a function of frequency, shown in Figure 6.5. Measurements were taken of the tag in passive mode, BAP mode, utilising the integrated battery and BAP mode using a standard 1.5V coin cell battery. The large difference observed between passive and BAP modes are as expected, due to the chip's different sensitivities in varying modes (-8dBm in passive vs -28dBm in BAP). Also observed is the directly comparable performance of the IBAS vs coin-cell readings. This allows the conclusion that the integrated battery is powering the antenna as desired and is not affecting the antenna performance negatively when compared to a coin cell battery.

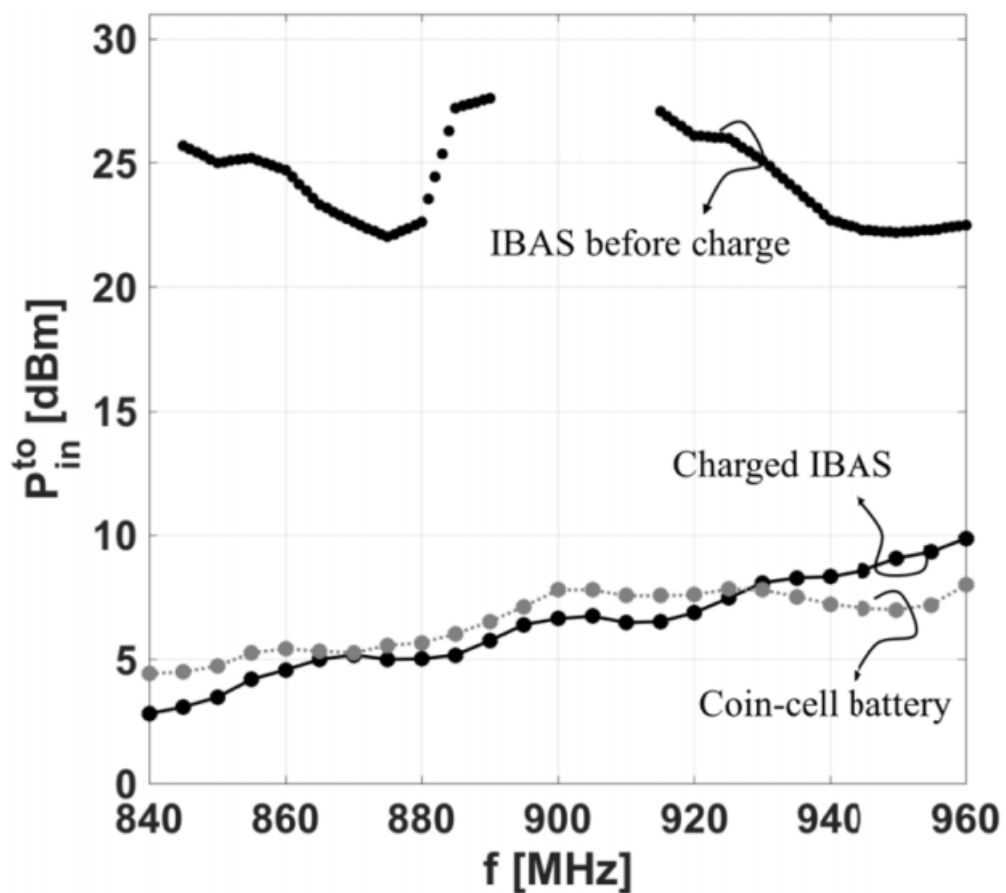


Figure 6.5: IBAS turn-ON powers for passive, BAP integrated and BAP coin-cell (reprinted with permission [8])

6.6 Battery Cycling

As previously mentioned, the chemistries chosen for the IBAS battery was PEDOT:PSS/LNMO. Figure 6.6 shows the charging profile of the IBAS battery, exhibiting all the expected plateaus of the LNMO cathode material, the redox reactions have been noted on the graph. However, the demonstrated voltages in this battery are somewhat different to the expected voltages which would arise from combining PEDOT:PSS and LNMO. You would expect the resultant potential to be equal to the cathode potential (4.2V and 4.7V) minus the anode voltage (between 1.5V and 0V), however, this is not observed. This phenomenon could be associated with a surface charging mechanism, similar to that described in Chapter 4, or lithium plating occurring, however, this was not observed in PEDOT:PSS vs lithium metal cells. Understanding this mechanism requires a larger in-depth study into these materials and the reactions associated with them. It should be mentioned that the IBAS was clamped and pressed during the charge to reduce impedance issues arising from poor contact etc. during the charge. However, when in use, the battery had no assistance with this and fully powered the IBAS.

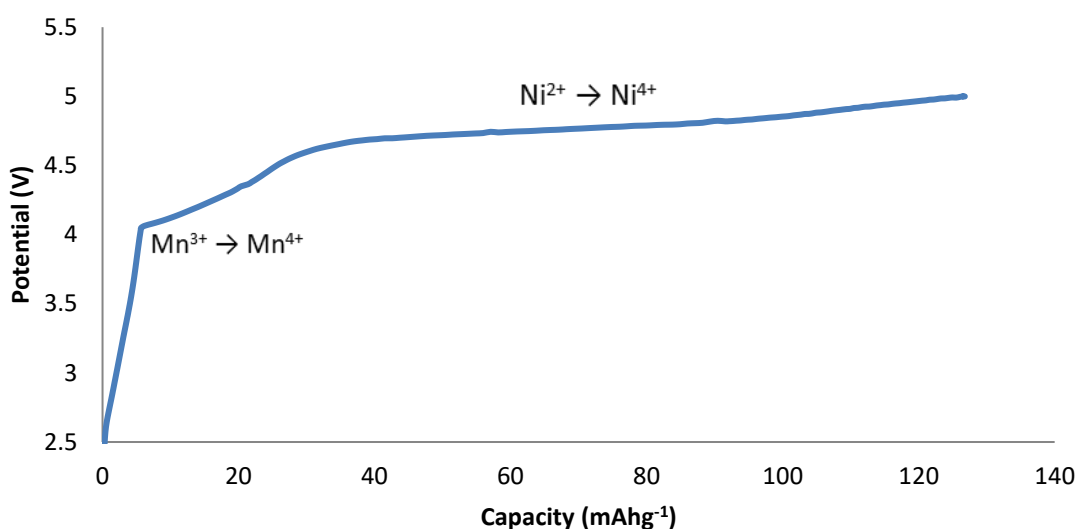


Figure 6.6: IBAS battery first charge curve

Whilst the IBAS discharge could not be observed in-use, another pouch cell using the same chemistry was assembled to test expected performance, the cycling curves are shown in Figure 6.7. It should be noted that this cell was vacuum sealed to give a more realistic performance overview of a fully working IBAS.

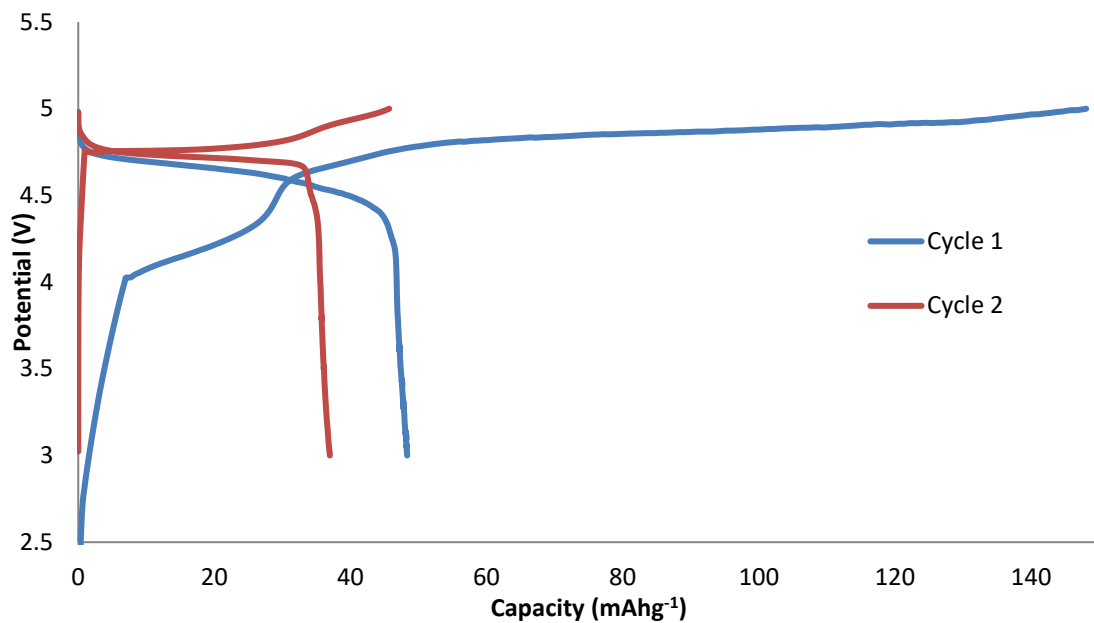


Figure 6.7: Cycling data for a PEDOT:PSS vs LNMO pouch cell

It can be seen that the first charge profile of the pouch cell closely resembles that of the IBAS, and with what is expected of an LNMO cathode. The cell achieves close to theoretical capacity in the first charge, indicating that almost all of the lithium has been removed from the cathode and brought to the anode. However, there is a significantly smaller discharge plateau, reaching only a third of LNMO's theoretical capacity. This has been attributed to the lithium trapping, as discussed in Chapter 4. The cell capacity was anode limited, to the extent that, if the PEDOT:PSS achieved 100mAhg^{-1} (as expected via doctor blade coated samples) then the capacity would be 50mAhg^{-1} with respect to LNMO, this fits well with the observed capacities. The second cycle exhibits only one plateau (4.7V), this is due to not reinserting enough lithium into LNMO to engage the manganese redox reaction. It can be seen that whilst capacities are severely limited by the anode (which can be remedied by adjusting loading levels during electrode deposition), the potential is stable, making it suitable to power the IBAS.

6.7 Conclusion

It has been demonstrated that, via the use of integrated design with an array of deposition and etching techniques it is possible to produce a truly integrated, multidisciplinary product which has promising performance characteristics whilst also

reducing design restrictions normally associated with battery powered antenna systems.

The product design allows for a significant reduction in thickness, the IBAS total thickness is sub-millimetre – whilst standard coin-cells are greater in thickness than 1mm alone, without accounting for additional thickness from the antenna and packaging. In addition, as previously mentioned, metallic components from coin cells would interfere with battery performance, often requiring the battery to be located with an offset to the antenna (either raised off of the antenna or placed beside the antenna), further increasing the product footprint.

Not only does the IBAS allow for reduced dimensions of the final system but also reduces weight. By using the antennas copper plane as a dual functioning antenna-current collector, and removing the metallic casings frequently used in battery manufacturing, the weight of the final IBAS is significantly reduced compared to a similar system without the mentioned integration.

The close proximity of the antenna to skin also allows for close-to-skin epidermal sensing capabilities; products designed to be worn close-to-skin should be comfortable, light weight and minimally invasive. The IBAS design and use of Mylar as the barrier material allows for a comfortable user experience. The Integrated design also allows the system to be flexible and body conformable, an attribute often lost when hard casing or multilayer batteries are incorporated into products.

The IBAS performance characteristics have been shown to compare strongly vs a conventional coin-cell battery. This further demonstrates that the integrated battery in the IBAS is functioning as desired, an integrated power supply, which does not detract from the systems primary function – a data-logging RFID antenna.

It should be noted that the IBAS presented is the first functioning prototype and made use of a mixture of known (LNMO) and novel (PEDOT:PSS) battery chemistries. Since this system, further improvements to the system have been employed via the use of antenna design tweaks, standard battery chemistries (LFP/graphite) and a vacuum sealer, the forward read ranges have seen an increase from 1.3m to >3m. These

improvements suggest promise for further exploration into IBAS systems and wearable integrated sensor systems.

The IBAS is not a finalised system, whilst it has been established that it is capable of emitting and receiving signals via the use of the antenna, none of the chips inbuilt sensors have been explored thus far. Future systems would include exploration of these sensors and other integrated sensors such as thermal, ECG, accelerometers and gas sensors. In addition to including the use of sensors, design tweaks will be necessary to allow to greater read and write distances, to enable their use in a real-world scenarios.

In regards to battery chemistries, an in-depth look into the mechanisms behind the novel chemistries is required to establish the reason for higher than expected voltage plateaus when combining PEDOT:PSS and LNMO. This would involve an array of techniques from XPS to investigate surface artefacts and properties, such as chemical and electronic states, as well as binding energies, to NMR to explore PEDOT:PSS diffusion properties. Exploration into the proposed surface charging phenomenon and lithium plating would be essential and may involve both experimental and simulation works.

6.8 References

- [1] M. Woods and J. Batchelor, "Low-profile slot antenna integrated with a thin polymer non-metallic battery," in *Loughborough Antennas and Propagation Conference*, Loughborough, 2013.
- [2] M. A. Woods, O. O. Rakibet, P. R. Young, R. Luck, M. L. Alfredsson and J. C. Batchelor, "Integrated Antenna-Battery for Low-profile Short Range Communications," in *Antennas and Propagation, EuCAP, European Conference on Antennas and Propagation*, The Hague, 2014.
- [3] M. A. Ziai and B. J. C, "Temporary On-Skin Passive UHF RFID Transfer Tag," *IEEE TRANSACTIONS ON ANTENNAS AND PROPAGATION*, vol. 59, no. 10, pp. 3565 - 3571, 2011.
- [4] "E M microelectronic," [Online]. Available: <https://www.emmicroelectronic.com/product/epc-and-uhf-ics/em4325>. [Accessed 09 10 2019].
- [5] S. Milici, S. Amendola, A. Bianco and G. Marrocco, "Epidermal RFID Passive Sensor for Body Temperature Measurements," *IEEE RFID Technology and Applications Conference*, pp. 140 - 144, 2014.
- [6] S. Amendola, G. Bovesecchi, A. Palombi, P. Coppa and G. Marrocco, "Design, Calibration and Experimentation of an Epidermal RFID Sensor for Remote Temperature Monitoring," *IEEE SENSORS JOURNAL*, vol. 16, no. 19, pp. 7250 - 7257, 2016.
- [7] "Voyantic Tagformance," [Online]. Available: <https://voyantic.com/products/tagformance-lite>. [Accessed 10 10 2019].
- [8] M. C. Caccami, M. P. Hogan, M. Alfredsson, G. Marrocco and J. C. Batchelor, "A Tightly Integrated Multilayer Battery Antenna for RFID Epidermal Applications,"

IEEE TRANSACTIONS ON ANTENNAS AND PROPAGATION, vol. 66, no. 2, pp. 609 - 617, 2018.

7 Conclusions and Future Works

7.1 Conclusions

In this thesis, multiple methods have been employed to explore different avenues for improving Li-ion batteries in the field of printed and flexible electronics. The three main components of a Li-ion battery were investigated, for ways to improve on current technologies, in terms of desirable attributes, such as, enhanced capacity, safety, processability, environmental benignity and integration into electronic systems. A combination of techniques were used to establish reaction mechanisms, film forming properties, galvanostatic cycling performance, as well as electrochemical and thermal stability windows.

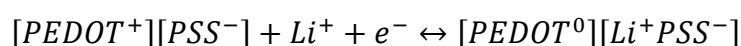
$\text{Li}_2\text{FeSiO}_4$ is investigated as a high capacity, affordable and environmentally benign cathode material. The investigation incorporated a large amount of synchrotron experiments, firstly exploring a spontaneous “electrolyte effect” to which it was found that a specific combination of salt and electrolyte (LiPF_6 in EC/DMC), along with a potential being created between electrode and Li-metal, results in a pre-cycling Fe oxidation from $\text{Fe}^{2+} \rightarrow \text{Fe}^{3+}$. This allowed for a correct combination of salt and solvent to be used in further experimental works.

Further to the electrolyte study, a combination study was conducted utilising both XANES and XRS techniques to investigate the origin of the additional capacity in $\text{Li}_2\text{FeSiO}_4$ associated with the removal of $>1\text{Li}^+$ per unit formula. The two most commonly referred to origins are the $\text{Fe}^{3+}/\text{Fe}^{4+}$ redox or an oxygen contribution. The XANES study established that no Fe^{4+} was observed during the in-operando experiment, despite a $>1\text{Li}^+$ removal. Instead, the bulk sensitive XRS study, revealed a continuous and reversible O K-edge contribution. Lastly, an elevated temperature galvanostatic cycling study was conducted revealing greatly improved kinetics, resulting in significantly larger capacities.

PEDOT:PSS is explored as a polymeric anode material, for its suitability in novel applications such as printed electronics. The study included using a variety of manufacturing techniques to establish their suitability for roll-to-roll processing and

integrated electronics applications. It was found that galvanostatic cycling performance was heavily dependent on the deposition technique used, with capacities ranging from 100mAhg⁻¹ to 200mAhg⁻¹. This is explained using a proposed surface sensitive reaction where Li⁺ ions can only react with accessible material surfaces.

Electrochemical and other characterisation techniques were used to explore the reaction mechanisms taking place within the polymer during cycling and 3 mechanisms were proposed. Firstly, the reaction:



Was determined for the first cycling plateau. Secondly, a second Li⁺ injection into the [Li⁺PSS⁻] groups, which forms a radical is associated with the second cycling plateau.

Lastly, an ion exchange mechanism is proposed to explain the “lithium trapping” phenomenon, observed in the initial discharge of PEDOT:PSS irrespective of deposition technique. Whereby Li⁺ replaces H⁺ within the PEDOT:PSS, stabilising the S-O single bond and effectively getting “stuck” within the PSS, this process instigates the formation of H₂ during the initial discharge.

Overall ink-jet printed PEDOT:PSS films, using an aqueous solvent and no additional binder, exhibited the best processability, film forming properties and electrochemical performance.

A PEGDA based solid-state polymer electrolyte was explored due to its facile processability and ability to change from liquid state to solid state via a simple UV curing procedure, allowing its use in printed batteries and other manufacturing. The thesis presents impressive cycling results for an all-solid-state full-cell battery. The PEM exhibited strong thermal and mechanical stability characteristics as well as high ionic conductivity and electrochemical stability window vs Li-metal. This places the PEM in good stead for its application into integrated electronics, as well as potential applications in high temperature environments or high voltage chemistries.

Galvanostatic cycling was conducted on both half-cell and full-cell configurations where it was established that cycling performances were good, with capacities nearing

those of similar cells using liquid electrolytes, however, performance was dependant on cycle rate and the type of cell chemistry used. SEM gave further insight to this, suggesting that performance limitations may be due to limited penetration into the cast electrodes, suggesting a greater control over electrode porosity is required for optimal performance.

Overall, the PEMs flexibility, stretchability, electrochemical stability and galvanostatic performance were found to be good and suitable for further exploration and potential integration into electronic devices.

The first iteration of the integrated battery antenna system (IBAS), showed that, through careful design and multipurpose components, battery powered antenna systems can be created without compromising on either form or function.

The battery uses the antenna body itself, as a current collector, allowing for not only a reduction in product dimensions, but also a reduction in product weight and costs associated with the removal of the additional current collector. Antenna performance using the integrated battery was directly compared to when using a conventional coin cell. The Li-ion battery used in the IBAS was found to match the performance of the commercial coin cell. But using the integrated battery the system becomes body conformable, low profile and light weight. This approach can be adapted to other systems suggesting promise in further exploration of the IBAS and other integrated battery systems.

7.2 Future Works

The materials and technologies explored in this thesis are, by no means, complete. Further exploration into these technologies is essential to gain a full understanding of their reaction mechanisms, their manufacturing, their product design and integration, as well as their potential in the Li-ion battery market.

For $\text{Li}_2\text{FeSiO}_4$, further methods of improving the materials kinetics should be explored, this may include material doping, or a larger scale investigation into the elevated temperature cycling where significantly higher capacities were observed.

Further to this, XAS and XRS studies should be continued, including using materials cycled at elevated temperatures and XRS studies using a greater number of sample points to gain a fuller understanding of the Fe⁴⁺/O K-edge debate. This may also include the need for a simulation study or alternative techniques such as XPS, soft X-ray of the O K-edge and Mössbauer.

For PEDOT:PSS, further exploration into the reaction mechanisms proposed, including the “lithium trapping” should be investigated. This may include simulation studies to investigate the proposed ion exchange mechanism, or the surface sensitive XPS technique to explore the proposed surface dependant Li⁺ ion insertion. Other techniques which can yield useful information regarding lithium insertion and reaction mechanisms include NMR and XAS.

Regarding PEGDA, a detailed composition dependent study should be explored, to find the optimum electrolyte composition for cell performance. A large-scale study into deposition techniques and electrode porosity should be conducted to establish the PEMs suitability for large scale production and performance improvement.

For the IBAS there are multiple ways to further investigate the system. Incorporating sensors into the system can allow for epidermal and environmental sensing within a body conformable package. Alternative battery chemistries can be explored and the use of a vacuum sealer in the assembly is essential.

Furthermore, it should be proposed that all sections of this thesis could be combined into a single package, creating an IBAS which incorporates Li₂FeSiO₄ as the cathode, the PEGDA PEM as the electrolyte and PEDOT:PSS as the anode. As an extension to the works presented in this thesis, further exploration into the field of Li-ion battery integration into printable, flexible, and elastic electronics is recommended.